Institut für Angewandte Physik

Fachrichtung Physik

Fakultät Mathematik und Naturwissenschaften
Technische Universität Dresden

Terahertz oscillation and stimulated emission from planar microcavities

Dissertation

zur Erlangung des

akademischen Grades

Doctor rerum naturalium

(Dr. rer. nat.)

vorgelegt von

Robert Gehlhaar

geboren am 10. März 1978 in Dresden

Dresden

2007

Eingereicht am 17. April 2007

1. Gutachter: Prof. Dr. Karl Leo

2. Gutachter: Prof. Dr. Manfred Helm

3. Gutachter: Prof. Dr. David Lidzey

Verteidigt am 17. Juli 2007

LHA GYAL LO

Abstract

In the past decades, the miniaturization in optics led to new devices with structural sizes in the range of the light wavelength, where the photonic modes are confined and the number of states is limited. In the smallest microcavities, i.e. micrometer sized optical resonators, the propagation of only one mode is permitted that is simultaneously amplified internally. This particularly strong enhancement of the electric field is directly related to the quality factor of the cavity. By introducing an optical dipole into a high-Q microcavity, the spontaneous emission is amplified at the cavity mode frequency enabling stimulated emission in an inverted system. Although some of theses cavity effects can only be understood by quantum electrodynamic theory, most mechanisms are accessible by classical and semi-classical approaches.

In this thesis, one-dimensional planar microcavities with quality factors up to 4500 have been fabricated by physical vapor deposition of dielectric thin films and organic active materials. A new cavity design based on anisotropic dielectric mirrors grown by oblique angle deposition microcavities with two energetically shifted orthogonally polarized modes is presented. The application of these anisotropic structures for terahertz difference signal generation is demonstrated in spectrally and time resolved transmission experiments, where optical beats with repetition rates in the terahertz range are observed.

Optically pumped organic vertical cavity surface emitting lasers (VCSELs) have been realized by applying an organic solid state laser compound and high reflectance distributed Bragg reflectors. These lasers combine a very low laser threshold with small beam divergence and good stability. A transfer of the anisotropic design towards an organic VCSEL results in the generation of two perpendicularly polarized laser modes with a splitting adjustable by the fabrication conditions. The observation of an oscillation of two laser modes in a photomixing experiment proves a phase coupling mechanism. This demonstrates the potential of the anisotropic cavity design for a passive or active component in a terahertz radiation source or frequency generator.

Furthermore, microcavities with two and three coupled resonators are investigated. By the application of time-resolved transmission experiments, spatial oscillations of the internal electric field - photonic Bloch oscillations - are successfully demonstrated. In combination with the anisotropic microcavities, this is a second concept for the modulation of transmitted light with terahertz frequencies.

All experiments are accompanied by numerical or analytical models. Transmission experiments of continuously incident light and single laser pulses are compared with transfer matrix simulations and Fourier transform based approaches. For the modeling of emission experiments, a plane wave expansion method is successfully used. For the analysis of the organic VCSEL dynamics, we apply a set of rate equations that explains the gain switching process.

Contents

1 Introduction

Photonics are a major driver of the technological development in the 21st century [1]. It may continue the line, started by the mechanical engines and continued by electricity and electronics in the past centuries. A commonly used photonic device is the laser, which was invented already half a century ago and very early became an established instrument in research and industry. Lasers control and amplify light in a resonator with a usually macroscopic dimension. In the most simple resonator specification, a laser consists of an active medium in between two planar mirrors. Optical resonators with sizes on the scale of the photon wavelength are the ultimate goal in miniaturization of devices for guidance, manipulation, and amplification of light. These so-called microcavities are demonstrated in several configurations as, e.g., micropillars, microdisks, microspheres, or microtoroids [2]. Already in 1946, Purcell observed an enhanced transition between oscillator states, if the transition frequency correlates with the resonance frequency of the cavity. Microcavities apply this effect in the form of the vertical-cavity surface-emitting laser, which was invented in 1977 and is now widely used in optical fiber networks [3].

Beside their commercial applications, microcavities are still a focus of interest in science. For instance, the strong optical confinement allows for the generation of cavity polaritons. These quasi-particles are a coherent superposition of an exciton and a photon. In theory, a polariton based laser would fulfill a long-cherished dream of a thresholdless source of coherent radiation [4]. Semiconductor polaritons have been demonstrated first in inorganic microcavities in 1992 [5], and later in 1998 also in organic structures [6].

There is an opportunity for organic semiconductors to substitute their inorganic counterparts in certain lighting, memory, and light harvesting applications. Organic light emitting diodes (OLEDs) have already entered the market with their advantage of low production costs, mechanical flexibility and nearly unlimited number of potential material configurations. Organic semiconductor lasers have been first demonstrated in 1996 [7] and are implemented in microcavities in the same year [8]. However, an application as active medium within organic VCSELs is highly demanding since the high excitation density drastically decreases the stability of common organic molecules.

The most fascinating feature of the devices investigated within this thesis is the combination of a rather simple way of fabrication and the generation of optical effects as coherent light emission and terahertz signal beating. The demands on the fabrication process concerning quality and precision control are rather high and have to be taken into account. Nevertheless, high quality microcavities and even organic VCSELs with excellent optical properties can be made within a standard high vacuum process. With a knowledge of the important parameters, we can build a microlaser by a precise arrangement of common dielectric oxides as SiO_2 and TiO_2, and an organic dye composite.

Within this framework, we have studied planar microcavities in several different modifications. All structures have the same design in common, where two mirrors surround a solid medium with a thickness in the order of the wavelength of light. At the beginning, the work is focussed on the fabrication of high quality resonators. For this purpose, we have improved the deposition process to enable the production of very high reflective mirrors. The first structures containing such distributed Bragg reflectors (DBRs) are filled with a dielectric material and are called passive microcavities. These devices confine light incident from the outside. Their optical properties are studied by reflection and transmission measurements in linear or picosecond time-resolved regimes. We demonstrate the accumulation of photons between the two mirrors in experiment and theoretical models. By the introduction of an structural anisotropy, we generate a transmission signal with a beating in the terahertz frequency range. Such a terahertz signal generation is also investigated in coupled microcavities, which consist of two resonator layers and an additional mirror to separate them.

Another class of microresonators investigated contains organic dyes that interact with incident light and are therefore called active microcavities. These microcavities can be distinguished by the internal coupling mechanism of light and matter. In the strong-coupling regime, a strong interaction of the organic material and the photon mode is resulting in the creation of polaritons. If the light-matter interaction is weak, the influence of the microcavity on the emission from the dyes prevails (weak-coupling regime). Here, the Purcell effect leads to an enhanced spontaneous emission rate, which is later used for the ultimate goal of the fabrication of an organic VCSEL. This laser system is studied and modeled in several experiments and provides one of the lowest lasing thresholds of organic microlasers. A terahertz beating, similar to that in passive structures, is also detected in the emission of organic VCSELs with anisotropic DBRs.

This thesis is separated in seven Chapters. In the following Chapters 2 and 3, the fundamentals of thin film optics and their influence on planar microcavities and light emission are discussed. Chapter 4 is dedicated to the experimental methods of sample fabrication and optical characterization as well as to the applied materials. In Chapter 5, we start the presentation of the results of this work with a focus on the passive structures. The following Chapter 6 is concentrated on the description of experimental results and theoretical modeling of the active microcavities working in the weak- and the strong-coupling regime. This Chapter is concluded by the reports on organic microlasers. Chapter 7 summarizes the results of this thesis and presents an outlook on future investigations.

2 Light propagation in stratified media

This Chapter is focussed on the basic modeling concepts of the linear optical properties of stratified media. Beginning with the effects at a single boundary, it continues with a description of the transfer matrix algorithm, to explain the interference of light in multilayer optical thin films. At the end, the transfer matrix method is applied in the characterization of distributed Bragg reflectors and microcavities.

2.1 Reflection and refraction at a single boundary

In quantum mechanics light has wave and particle properties. Following the explanation of reflection and refraction in stratified media in Ref. [9–11], light is considered as a propagating electromagnetic wave with a harmonic time dependence of the electric field $\mathbf{E}$ and the magnetic field $\mathbf{H}$:

$$\begin{aligned} \mathbf{E}(\mathbf{r},t) &= \mathbf{E}(\mathbf{r})\mathrm{e}^{i\omega t}, && (2.1)\\ \mathbf{H}(\mathbf{r},t) &= \mathbf{H}(\mathbf{r})\mathrm{e}^{i\omega t}, && (2.2) \end{aligned}$$

where $\mathbf{r}$ is the position vector in Cartesian coordinates, t is the time, and ω the circular frequency.

For an isotropic, linear and time independent medium, the Helmholtz equation describes the electric field $\mathbf{E}$ of an electromagnetic wave by :

$$\nabla^2\mathbf{E}(\mathbf{r},t) + k(\mathbf{r})^2\mathbf{E}(\mathbf{r},t) = 0, \tag{2.3}$$

$$k(\mathbf{r}) = \frac{\omega n(\mathbf{r})}{c} = \frac{2\pi n(\mathbf{r})}{\lambda}, \tag{2.4}$$

where $n(\mathbf{r}) = \sqrt{\epsilon(\mathbf{r})\mu(\mathbf{r})}$ is the complex refractive index with $\epsilon(\mathbf{r})$ as the dielectric constant and the magnetic permeability $\mu(\mathbf{r})$, c the speed of light and the wavelength λ. For dielectric materials, $\epsilon(\mathbf{r})$ is a real number, but in case of a conductor it becomes complex and depends on the specific conductivity σ by $\epsilon = \epsilon' + i4\pi\sigma/\omega$. The wave vector $\mathbf{k}$ points in the direction of propagation with the unit vector $\mathbf{e}_k$:

$$\mathbf{k}(\mathbf{r}) = k(\mathbf{r})\mathbf{e}_{k(\mathbf{r})}. \tag{2.5}$$

Since $\mathbf{H}$ can be directly calculated from $\mathbf{E}$ via

$$\mathbf{H} = \sqrt{\frac{\epsilon}{\mu}}\,\mathbf{e_k} \times \mathbf{E}, \tag{2.6}$$

we only consider the electric field in the further description.

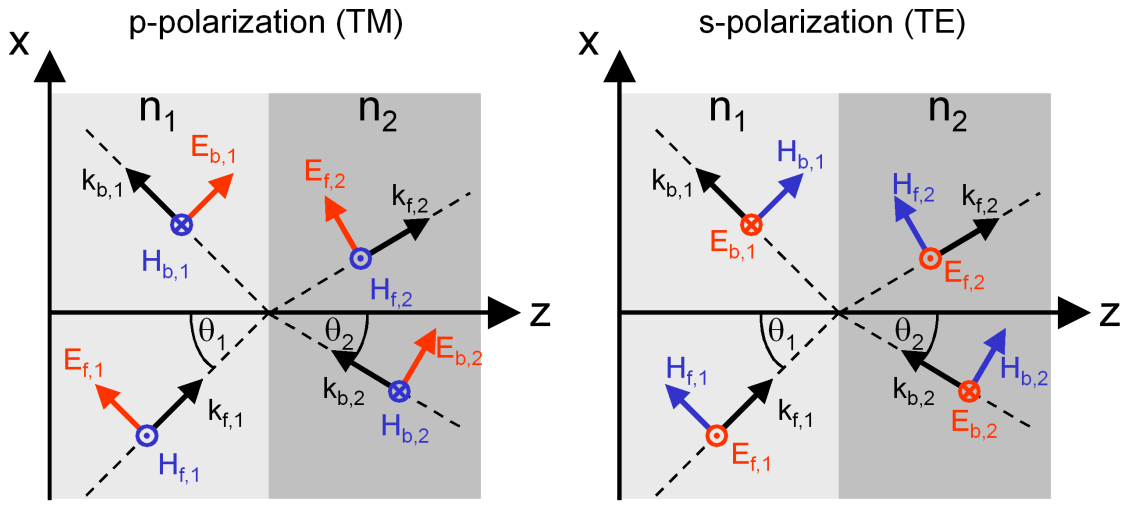

Figure 2.1: Reflection and refraction of an electromagnetic wave at an optical boundary.

In the following, the behavior of a planar wave at an optical boundary is discussed. Two homogeneous, semiinfinite media have an interface at the position $z = 0$, with refractive indices of n_1 and n_2 (Fig. 2.1). In general, the refractive index is a complex number, with a real part describing the refraction ratio of a medium and air, and an imaginary part, which characterizes the absorption or gain of light in the corresponding medium. The plane of the boundary is assumed to have infinite extensions in x- and y-direction. The electric field can have components in arbitrary direction. Without loss of generality, all calculations can be performed, assuming two perpendicular polarizations. In case of transversal magnetic (TM) or p-polarization, the electric field oscillates in the x-z-plane and the magnetic field is for all possible angles of incidence parallel to the boundary. For transversal electric (TE) or s-polarization, the electric field is oscillating in the x-y-plane. The separation in TE and TM polarization is allowed for linear media and all polarizations are modeled by an appropriate superposition of the two solutions. The terms of s- and p-polarization are directly connected to the coordinates of a layered system. If there is no layer present, the polarization directions have no physical significance.

In a homogeneous medium Eq. (2.3) has two solutions, a forward and a backward traveling wave:

$$\mathbf{E}_f(\mathbf{r},t) = E_f \,\mathrm{e}^{i\omega t-\mathbf{kr}}\,\mathbf{e}_{\perp k}, \tag{2.7}$$

$$\mathbf{E}_b(\mathbf{r},t) = E_b \,\mathrm{e}^{i\omega t+\mathbf{kr}}\,\mathbf{e}_{\perp k}. \tag{2.8}$$

In both cases, the electric field is perpendicular to the wave vector. The boundary conditions from the Maxwell equations on the tangential components of the electric and magnetic field vectors require that E_x, E_y, H_x and H_y are continuous at the interface at $z = 0$.

2.1.1 Reflection and transmission of the TE (s) wave

Imposing the continuity of E_y and H_x at the interface leads to

$$\begin{aligned} E_{f,1s} + E_{b,1s} &= E_{f,2s} + E_{b,2s}, && (2.9)\\ \sqrt{\frac{\epsilon_1}{\mu_1}}(E_{f,1s} - E_{b,1s})\cos\theta_1 &= \sqrt{\frac{\epsilon_2}{\mu_2}}(E_{f,2s} - E_{b,2s})\cos\theta_2, && (2.10)\end{aligned}$$

where θ_1 and θ_2 are the angles of the wave vectors k_1 and k_2, respectively, with the normal to the interface. In a matrix representation, the two equations can be rewritten as

$$D_{1s}\begin{pmatrix} E_{f,1s} \\ E_{b,1s}\end{pmatrix} = D_{2s}\begin{pmatrix} E_{f,2s} \\ E_{b,2s}\end{pmatrix}, \tag{2.11}$$

where

$$D_{is} = \begin{pmatrix} 1 & 1 \\ \sqrt{\frac{\epsilon_i}{\mu_i}}\cos\theta_i & -\sqrt{\frac{\epsilon_i}{\mu_i}}\cos\theta_i \end{pmatrix}, \qquad i = 1, 2. \tag{2.12}$$

The matrix D_{is} is called the dynamical matrix of the s wave for the medium i ($i = 1, 2$). The reflection and transmission coefficients of light incident from medium 1 ($E_{b,2s} = 0$) for the boundary are defined as

$$r_s = \left(\frac{E_{b,1s}}{E_{f,1s}}\right), \qquad t_s = \left(\frac{E_{f,2s}}{E_{f,1s}}\right). \tag{2.13}$$

Most materials can be assumed as non-magnetic in the optical range, which means a magnetic permeability equal unity: $\mu_1 = \mu_2 = 1$. From the definitions (2.13) and the boundary conditions (2.9, 2.10), one obtains

$$r_s = \frac{n_1\cos\theta_1 - n_2\cos\theta_2}{n_1\cos\theta_1 + n_2\cos\theta_2} \tag{2.14}$$

and

$$t_s = \frac{2n_1 \cos\theta_1}{n_1 \cos\theta_1 + n_2 \cos\theta_2}. \tag{2.15}$$

2.1.2 Reflection and transmission of the TM (p) wave

Imposing the continuity of E_x and H_y at the interface leads to

$$\begin{aligned} (E_{f,1p} + E_{b,1p}) \cos\theta_1 &= (E_{f,2p} + E_{b,2p}) \cos\theta_2, & (2.16)\\ \sqrt{\frac{\epsilon_1}{\mu_1}}(E_{f,1s} - E_{b,1s}) &= \sqrt{\frac{\epsilon_2}{\mu_2}}(E_{f,2s} - E_{b,2s}). & (2.17) \end{aligned}$$

Again, in the matrix representation these two equations can be rewritten as

$$D_{1p} \begin{pmatrix} E_{f,1p} \\ E_{b,1p} \end{pmatrix} = D_{2p} \begin{pmatrix} E_{f,2p} \\ E_{b,2p} \end{pmatrix}, \tag{2.18}$$

where

$$D_{ip} = \begin{pmatrix} \cos\theta_i & \cos\theta_i \\ \sqrt{\frac{\epsilon_i}{\mu_i}} & -\sqrt{\frac{\epsilon_i}{\mu_i}} \end{pmatrix}, \qquad i = 1, 2. \tag{2.19}$$

The matrix D_{ip} is called the dynamical matrix of the p wave for the medium i ($i = 1, 2$). For light incident from medium 1 ($E_{b,2s} = 0$), the reflection and transmission coefficients of the boundary are given as

$$r_p = \left(\frac{E_{b,1p}}{E_{f,1p}}\right), \qquad t_p = \left(\frac{E_{f,2p}}{E_{f,1p}}\right). \tag{2.20}$$

From the definitions (2.20) and the boundary conditions (2.16, 2.17), one obtains

$$r_p = \frac{n_1 \cos\theta_2 - n_2 \cos\theta_1}{n_1 \cos\theta_2 + n_2 \cos\theta_1} \tag{2.21}$$

and

$$t_p = \frac{2n_1 \cos\theta_1}{n_1 \cos\theta_2 + n_2 \cos\theta_1}, \tag{2.22}$$

where again $\mu_1 = \mu_2$ is assumed. The Equations (2.14), (2.15), (2.21) and (2.22) are commonly called Fresnel formulas, r_s and r_p are the Fresnel reflection coefficients and t_s and t_p the Fresnel transmission coefficients. These equations are valid for any two media, even for total reflection and absorbing materials.

2.1.3 Reflectance and transmittance

The Fresnel formulas give the ratios of the amplitudes of the reflected or transmitted wave to the incident wave. The energy flow per unit time in direction of the wave propagation is given by the time averaged Poynting vector $\mathbf{S}$:

$$\mathbf{S} = \frac{c}{4\pi}\sqrt{\frac{\epsilon}{\mu}}\,E^2\,\mathbf{e}_k. \tag{2.23}$$

As a consequence of the Maxwell equations, the tangential components of the energy flow are unaffected by the boundary. Thus, for the determination of the reflected and transmitted energy, we only consider the normal component of the Poynting vectors with respect to the boundary surface. The reflectance and transmittance are defined as

$$R_s = \left|\frac{\mathbf{e}_z \cdot \mathbf{S}_{b,1s}}{\mathbf{e}_z \cdot \mathbf{S}_{f,1s}}\right|, \qquad R_p = \left|\frac{\mathbf{e}_z \cdot \mathbf{S}_{b,1p}}{\mathbf{e}_z \cdot \mathbf{S}_{f,1p}}\right|, \tag{2.24}$$

$$T_s = \left|\frac{\mathbf{e}_z \cdot \mathbf{S}_{f,2s}}{\mathbf{e}_z \cdot \mathbf{S}_{f,1s}}\right|, \qquad T_p = \left|\frac{\mathbf{e}_z \cdot \mathbf{S}_{f,2p}}{\mathbf{e}_z \cdot \mathbf{S}_{f,1p}}\right|, \tag{2.25}$$

where the unit vector perpendicular to the boundary surface is expressed by $\mathbf{e}_z$. In accordance with the definition, the reflectance and transmittance are related to the Fresnel coefficients by

$$R_s = |r_s|^2, \tag{2.26}$$

$$R_p = |r_p|^2, \tag{2.27}$$

$$T_s = \frac{n_2 \cos\theta_2\,|t_s|^2}{n_1 \cos\theta_1}, \tag{2.28}$$

$$T_p = \frac{n_2 \cos\theta_2\,|t_p|^2}{n_1 \cos\theta_1}. \tag{2.29}$$

2.2 Multilayer structures

Within the framework of this thesis, different optical multilayer structures are investigated concerning their reflectance, transmittance, and other optical properties. These, at first glance complicated, systems can be theoretically analyzed by a fast algorithm, the transfer matrix method. This procedure is an often used numerical technique in the modeling of one-dimensional problems. In this section, we describe the application of this method in thin film optics. Extensive treatment of the theoretical background can be found in literature [9–14].

A multilayer stack of N homogeneous layers is embedded between two semi-infinite media (Fig. 2.2 a). The light enters the structure from the medium with the refractive index n_0, which is referred to as the ambient medium. The opposite medium with n_s may be regarded as the substrate.

Due to the layer homogeneity along the x,y-plane, there exist again two solutions for the electric field amplitude, a forward and a backward traveling wave. In the

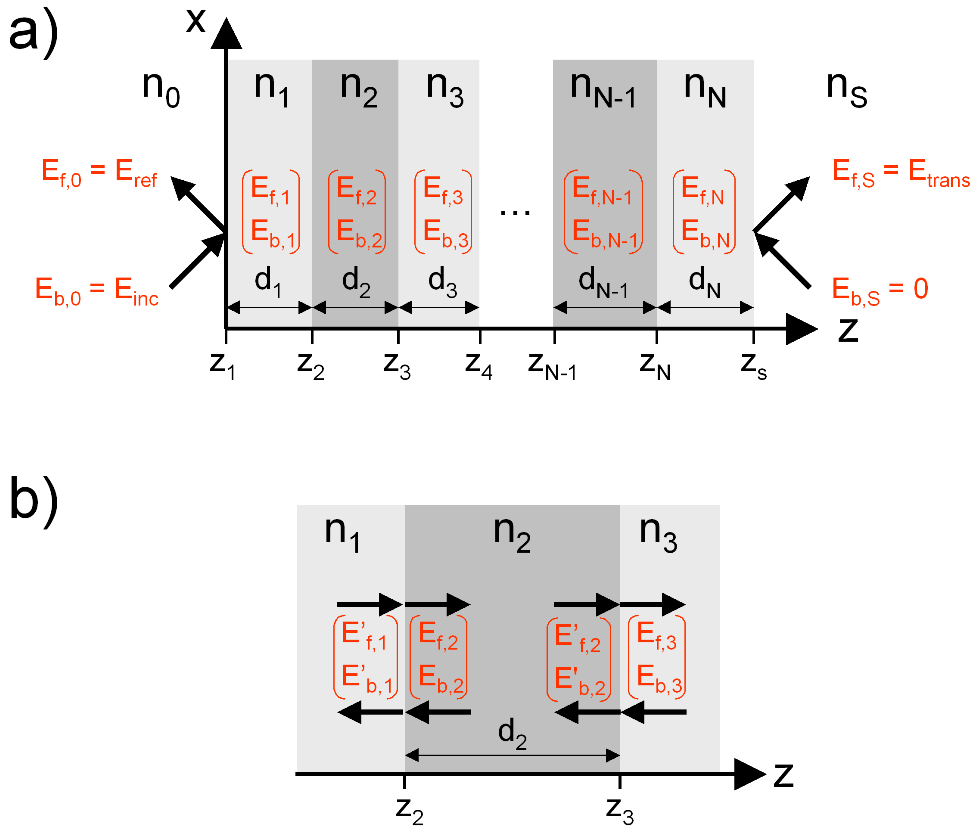

Figure 2.2: A multilayer stack (a) and a single layer (b) as used in the transfer matrix model.

first step, the optical properties of a single layer are considered (Fig 2.2 b). The amplitudes of the forward and backward propagating waves are represented as column vectors. At a boundary, these vectors are linked by the dynamic matrices introduced in Sec. 2.1.1 and Sec. 2.1.2. The column vectors are related by

$$\begin{pmatrix} E'_{f,1} \\ E'_{b,1} \end{pmatrix} = D_1^{-1} D_2 \begin{pmatrix} E_{f,2} \\ E_{b,2} \end{pmatrix} \equiv D_{12} \begin{pmatrix} E_{f,2} \\ E_{b,2} \end{pmatrix}, \tag{2.30}$$

$$\begin{pmatrix} E_{f,2} \\ E_{b,2} \end{pmatrix} = P_2 \begin{pmatrix} E'_{f,2} \\ E'_{b,2} \end{pmatrix} = \begin{pmatrix} \mathrm{e}^{i\phi_2} & 0 \\ 0 & \mathrm{e}^{-i\phi_2} \end{pmatrix} \begin{pmatrix} E'_{f,2} \\ E'_{b,2} \end{pmatrix}, \tag{2.31}$$

$$\begin{pmatrix} E'_{f,2} \\ E'_{b,2} \end{pmatrix} = D_2^{-1} D_3 \begin{pmatrix} E_{f,3} \\ E_{b,3} \end{pmatrix} \equiv D_{23} \begin{pmatrix} E_{f,3} \\ E_{b,3} \end{pmatrix}. \tag{2.32}$$

P_2 is the propagation matrix of the layer 2 and gives the phase shift between the two interfaces of the layer, where the phase ϕ_2 is without loss of generality given by

$$\phi_2 = k_{2x} d_2 = \frac{2\pi}{\lambda} n_2 d_2 \cos\theta_2. \tag{2.33}$$

The matrices D_{12} and D_{23} are the so-called transmission matrices of the respective interface and can be rewritten formally by applying the Fresnel coefficients of Equations (2.14), (2.15), (2.21), and (2.22) as

$$D_{12} = \frac{1}{t_{12}} \begin{pmatrix} 1 & r_{12} \\ r_{12} & 1 \end{pmatrix}. \tag{2.34}$$

D_{23} is similar to D_{12}, only the subscript indices need to be replaced. From the Equations (2.30), (2.30) and (2.32) the transfer of the electric field from layer 1 into layer 3 is represented by

$$\begin{pmatrix} E'_{f,1} \\ E'_{b,1} \end{pmatrix} = D_1^{-1} D_2 P_2 D_2^{-1} D_3 \begin{pmatrix} E_{f,3} \\ E_{b,3} \end{pmatrix}. \tag{2.35}$$

The same procedure can now be applied for the multilayer stack. Here the transmission and reflection properties can be calculated by multiplying the corresponding matrices for each layer:

$$\begin{pmatrix} E'_{f,0} \\ E'_{b,0} \end{pmatrix} = D_0^{-1} \left(\prod_{i=1}^{N} D_i P_i D_i^{-1} \right) D_s \begin{pmatrix} E_{f,s} \\ E_{b,s} \end{pmatrix} \equiv D_0^{-1} \widetilde{M} D_s \begin{pmatrix} E_{f,s} \\ E_{b,s} \end{pmatrix} \equiv M \begin{pmatrix} E_{f,s} \\ E_{b,s} \end{pmatrix}, \tag{2.36}$$

where $\widetilde{M}$ is the characteristic matrix of all layers and M is the characteristic matrix of the complete structure including the ambient material and the substrate. In a 2×2 representation the characteristic matrix has the form of

$$M = \begin{pmatrix} M_{11} & M_{12} \\ M_{21} & M_{22} \end{pmatrix}. \tag{2.37}$$

In the case of a lossless ambient medium with a real refractive index n_0, the reflectance of the system is given by

$$R = |r^2| = \left| \frac{M_{21}}{M_{11}} \right|^2. \tag{2.38}$$

Accordingly, the transmittance can be calculated with a component of the characteristic matrix, if the surrounding media are both lossless. Then the transmittance T can be modeled as

$$T = \frac{n_s \cos\theta_s}{n_0 \cos\theta_0} |t^2| = \frac{n_s \cos\theta_s}{n_0 \cos\theta_0} \left| \frac{1}{M_{11}} \right|^2. \tag{2.39}$$

In the general description of the transfer matrix algorithm so far, the polarization is neglected. If necessary, the polarization dependent characters can be adapted to the respective mode. With the accurate knowledge of the layer and experimental parameters of thickness d, complex refractive index n, angle of incidence θ_0 and polarization, the optical properties of an optical thin film structure can be accurately simulated.

It has to be stated that the results of the transfer matrix algorithm are steady state solutions, where light is incident with an constant intensity in time. For a pulsed regime, the transfer matrix method should be used only with special precautions.

Within the framework of this thesis, the transfer matrix calculations and fittings are performed by the commercial software FilmWizard[1].

2.3 Distributed Bragg reflector

A distributed Bragg reflector (DBR) is a multilayer structure consisting of pairs of dielectric films with alternating high (H) and low (L) refractive index and quarter wave optical thickness (QWOT) at a certain design wavelength λ_d, where $n_H d_H = n_L d_L = \frac{1}{4}\lambda_d$. In a DBR, the periodic layers with structure sizes of the order of the light wavelength form the simplest example of a one-dimensional photonic crystal [15]. In accordance with Eq. (2.36), the characteristic matrix of a DBR with outermost high index layers has the form

$$M = \begin{pmatrix} M_{11} & M_{12} \\ M_{21} & M_{22} \end{pmatrix} = D_0^{-1} \left[D_H P_H D_H^{-1} D_L P_L D_L^{-1} \right]^N D_H P_H D_H^{-1} D_s = D_0^{-1} \widetilde{M}_{(HL)^N H} D_s, \tag{2.40}$$

where $(2N+1)$ is the number of the layers in the stack and $\widetilde{M}_{(HL)^N H}$ represents the characteristic matrix of the DBR without the ambient and the substrate elements. The DBR is embedded in the ambient medium with the refractive index n_0 and the substrate with n_s as the index of refraction. For the design wavelength and normal incidence, the phase shift within the dielectric quarter wave layers $\phi_{H,L} = \frac{1}{2}\pi$ simplifies the propagation matrix to

$$P_{H,L} = \begin{pmatrix} i & 0 \\ 0 & -i \end{pmatrix}. \tag{2.41}$$

---

[1] SCI Scientific Computing International, http://www.sci-soft.com

After some matrix manipulation in Eq. (2.40) and by applying Eq. (2.38), the maximum reflectance at the design wavelength of the DBR can be obtained:

$$R_{max} = \left(\frac{1 - \frac{n_s n_0}{n_H^2} \left(\frac{n_L}{n_H} \right)^{2N}}{1 + \frac{n_s n_0}{n_H^2} \left(\frac{n_L}{n_H} \right)^{2N}} \right)^2 . \tag{2.42}$$

This result shows the strong influence of the number of pairs N on the optical performance of the mirror. With increasing number of layers, the reflectance converges to unity. With a large refractive index ratio n_L/n_H, this approach occurs already with a comparably low number of film pairs. Figure 2.3 a presents the reflectance of DBRs with a different number of layer pairs N. The refractive indices are chosen to agree with experimental values for TiO_2 and SiO_2 layers on a glass substrate. The layers are assumed to be perfectly dielectric so the influence of absorption is neglected and the refractive index is a real number. With this assumption a structure with 13 layers provides a maximum reflectance of $R_{max} > 0.99$. In a real structure, the absorption in the layers has to be reduced as far as possible in order to get a high maximum reflectance. Another channel for energy dissipation is the scattering at rough surfaces or impurities, which is not taken into account in transfer matrix calculations. With a 21 layer structure of TiO_2 and SiO_2 a maximum reflectance of $R_{max} > 99.6\,\%$ has been realized experimentally (Fig 2.3 b). The high reflectance

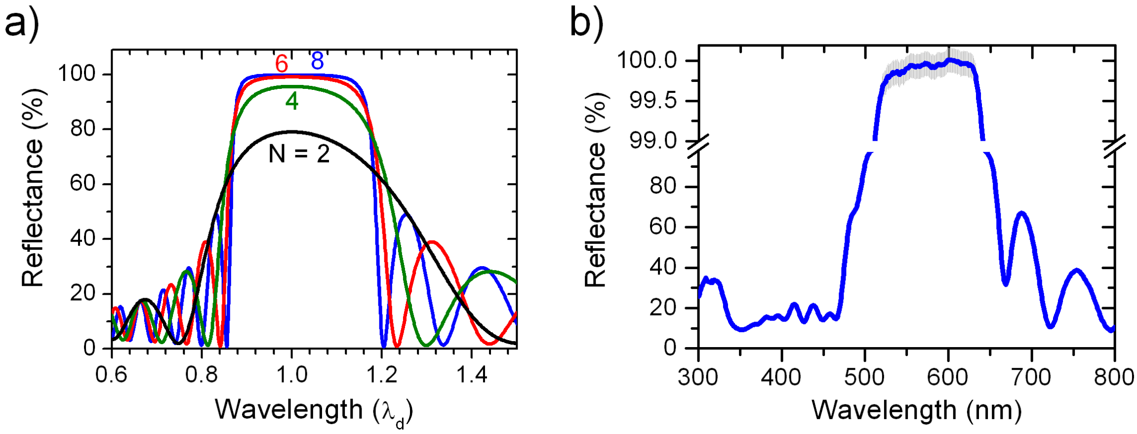

Figure 2.3: (a) Simulated reflectance at normal incidence of DBRs with a different number of layer pairs N as a function of the design wavelength λ_d. Alternating $\lambda/4$-layers of high ($n_H = 2.2$) and low ($n_L = 1.45$) refractive index are stacked on a substrate ($n_S = 1.5$) in an ambience of air ($n_0 = 1$). The maximum reflectance for the DBR with $N = 8$ is 99.84 %. The maximum reflectance is strongly dependent on the number of layers ($2N+1$). (b) Experimental normal incidence reflectance of a 21 layer DBR made of SiO_2 and TiO_2. The gray bars in the stop-band represent the random error of the measurement. The maximum reflectance is above 99.6 %.

of a DBR is exclusively the result of interference in the perfectly matched layers, whereas a metal mirror is based on the high absorption of the bulk. Unfortunately, the interference effects only a certain wavelength range around the design wavelength of the dielectric mirror. This area of high reflectance is the so-called stop-band of the DBR. The stop-band width Δg depends only on the ratio of the refractive indices of the high and low refractive materials and is given from Ref. [10, 12] by

$$\Delta g = \frac{4}{\pi} \sin^{-1} \left(\frac{n_H - n_L}{n_H + n_L} \right). \tag{2.43}$$

With an increasing number of mirror layers, the edges of the stop-band steepen. Outside of the this area, the reflected waves are not phase-matched with the incident wave and the structure becomes transparent.

Another optical property of thin film structures based on interference effects is the angle and polarization dependence. With increasing angle of incidence, the stop-band and the transmission modes shift to shorter wavelengths and the TE and TM modes of the same wavelength interact in a different way with the DBR. This effect will be discussed in the next Section (Sec. 2.4).

Due to the periodic nature of a DBR, a phase delay and a finite delay of reflection occurs. The delay is directly connected with a storage of energy within the layer stack. The quantity of delay time or energy storage is expressed by the penetration depth. This depth is of particular interest in microcavity structures, where the cavity length has a comparable size. Thus, the cavity round trip time and delay are of the same magnitude. An exact analytical expression for the reflection phase delay τ_r of a lossless mirror is given in Ref. [16] by

$$\tau_r = \frac{1}{2 f_d} \left(\frac{n_{LI}}{n_{HI}} \right) \frac{n_H}{n_H - n_L}, \tag{2.44}$$

with the design frequency $f_d = c/\lambda_d$ and the refractive indices of the high (n_{HI}) and low (n_{HI}) refractive materials at the side of incidence. Although strictly valid only for an infinite number of layers, this equation is reliable for DBRs with more than 3 periods. For a 21-layer TiO_2/SiO_2-DBR with a design wavelength of $\lambda_d = 800\,\mathrm{nm}$, the phase delay time is in the lower femtosecond range ($\tau_r = 1.8\,\mathrm{fs}$). While the phase delay has an influence on the round trip time in a cavity, the energy penetration depth L_e is related to the amount of light stored in the mirror at the incident side. In laser modeling, the knowledge of the intensity of light in the active medium is highly important. Especially in designs with dielectric mirrors and a very small active medium length, L_e is not negligible. For an infinite number of layers, the energy and phase penetration depth are equal and can be calculated with Eq. (2.44) by

$$L_e = \frac{c\tau_r}{2\,n_0}. \tag{2.45}$$

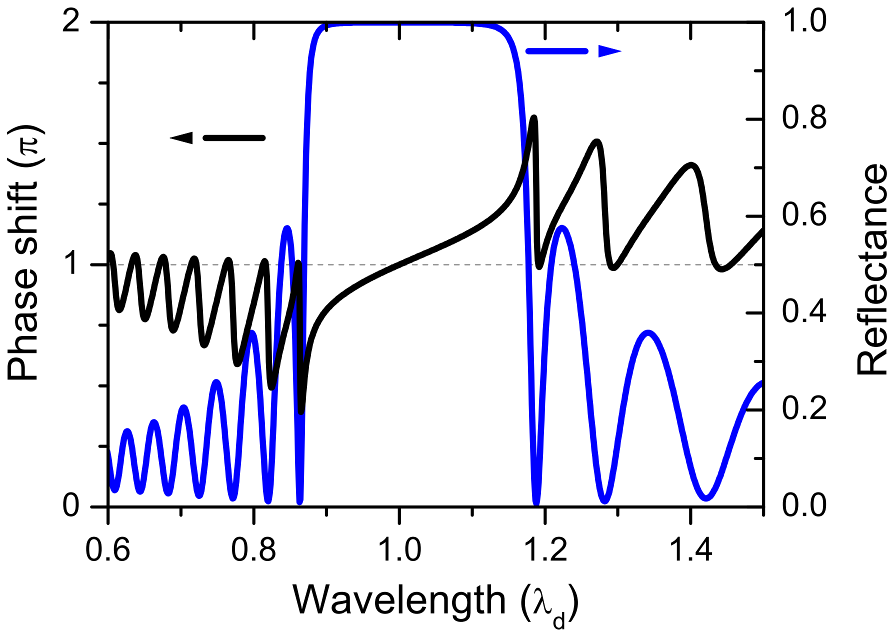

Figure 2.4: Phase shift spectrum (black) for a 21 layer DBR ((H L)10 H) of dielectric media with the indices of refraction $n_0 = 1$, $n_s = 1.5$, $n_H = 2.2$ and $n_L = 1.45$ as a function of the design wavelength λ_d. The blue line is the corresponding reflectance curve.

Unlike metal mirrors, there is a strong dispersion of the phase shift ϕ associated with Bragg reflection. With the power reflectance R in Eq. (2.38) the phase reflectance r of a mirror can be defined by

$$r = \sqrt{R}\,\mathrm{e}^{-i\phi}. \tag{2.46}$$

At the design wavelength, the reflected phase ϕ is shifted by 180° and the dispersion is zero (Fig. 2.4). For the wavelength coinciding with the stop-band center, the reflection delay is minimized. For all other wavelengths, especially outside of the stop-band, the light penetrates deeply into the structure.

2.4 Single microcavity

In 1897 Ch. Fabry and A. Perot described a new interferometer type based on multiple reflections between two parallel plates [17–19]. In comparison with two-beam interferometers, the spectral resolution is much higher, thus improving the measurement accuracy. If the separation between the two mirrors is in the range of a few micrometers or even below, that means in the range of the wavelength of light, this interferometer is called a microcavity. Not only due to the recent increasing interest in microcavities, the Fabry-Perot interferometer is nowadays more widely used than it was in its over 100 years history before.

In the following, we consider a microcavity, which consists of two DBRs with $(2N+1)$ layers with outermost high index layers and a cavity layer with an optical thickness $n_c d_c = \frac{1}{2}\lambda_d$ in between. The characteristic matrix can be formulated in accordance with the Equations (2.36) and (2.40) as

$$M = \begin{pmatrix} M_{11} & M_{12} \\ M_{21} & M_{22} \end{pmatrix} = D_0^{-1} \widetilde{M}_{(HL)^N H} D_c P_c D_c^{-1} \widetilde{M}_{(HL)^N H} D_s. \tag{2.47}$$

At the design wavelength and for normal incidence the phase shift reads $\phi_c = k_c d_c = \pi$ within the cavity layer. This results in the same form of the propagation matrix P_c and the characteristic matrix $\widetilde{M}_c$ of the cavity layer with

$$P_c = \widetilde{M}_c = \begin{pmatrix} -1 & 0 \\ 0 & -1 \end{pmatrix}. \tag{2.48}$$

As a consequence, the contribution of the DBRs in the characteristic matrix M of the whole structure vanishes and the reflectance is that of the single boundary between the ambient medium and the substrate, with

$$R = \left(\frac{n_0 - n_s}{n_0 + n_s} \right)^2. \tag{2.49}$$

This means that a cavity layer with a thickness of a multiple of $n_c d_c = m\frac{1}{2}\lambda_d$ cancels the high reflectance of the two DBRs and the structure is - if the layers have no absorbance - highly transparent at the design wavelength. The transmission becomes unity, if the device is completely symmetric, which means an equal reflectance of the two DBRs. In a more general explanation, the microcavity contains a mode, if the round trip phase shift ϕ_m follows the resonance condition

$$\phi_m = \phi_c - \left(\frac{\phi_1 + \phi_2}{2} \right) = \pm\, m\pi, \qquad m = 0, 1, 2, \dots\,, \tag{2.50}$$

where ϕ_1 and ϕ_2 are, in accordance with Equation (2.46), the phase shifts of the two surrounding mirrors. In the above explained example, the phase shifts of the two DBRs are $\phi_{1,2} = \pi$, thus fabricating a transmission mode at the design wavelength. To create a resonance, the cavity thickness d_c is not necessarily required to be exactly a multiple of half the design wavelength λ_d of the DBRs. In such a case, the dispersion of a DBR (see Fig. 2.4) or any other mirror has to be taken into account and the resonance wavelength is shifted with respect to the design wavelength of the cavity layer. In a system where the two mirrors have equal transmittance, the transmission at the cavity mode wavelength is maximized and approaches unity if there are no losses in the structure and ambient medium and substrate have equal indices of refraction [12]. Figure 2.5 a presents the reflectance spectrum of a $\lambda/2$-microcavity with two dielectric mirrors of 4.5 periods. The stop-band around the design wavelength is divided by a drop in reflection. The minimum reflectance of the cavity mode is $\sim 4\%$, which corresponds to the reflectance of a single ambient-substrate boundary. At the cavity frequency, the phase of transmitted light is shifted by 180°, whereas by a strong phase dispersion a jump of 180° occurs between the edges of the cavity mode.

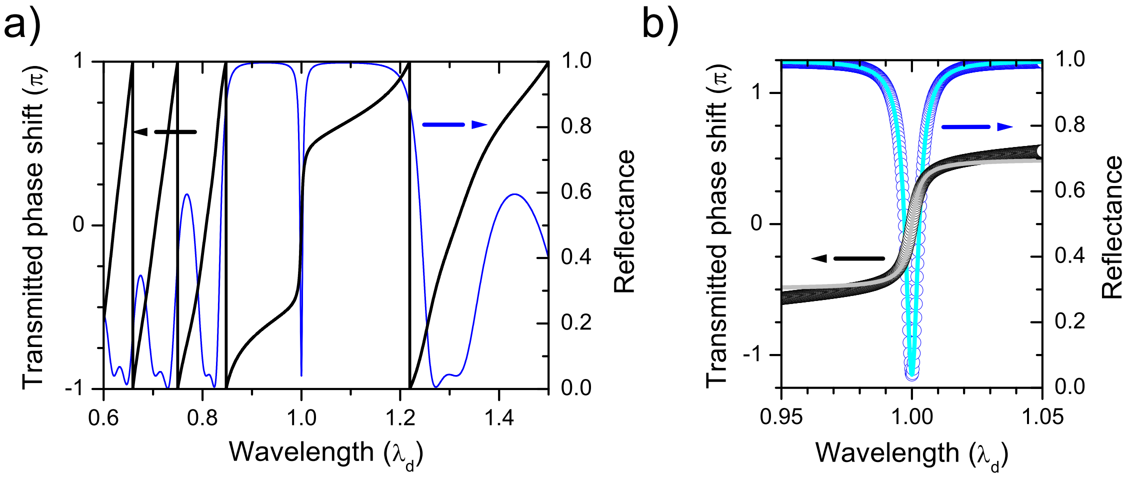

Figure 2.5: (a) The phase shift of transmitted light (black) and reflectance (blue) for a 19 layer microcavity ((H L)4 H 2L H (L H)4) consisting of dielectric media with the indices of refraction $n_0 = 1$, $n_s = 1.5$, $n_H = 2.2$ and $n_L = 1.45$ as a function of the design wavelength λ_d. (b) The reflectance (blue) and the transmission phase (black) of the cavity mode can be modeled by Lorentz function. Results from a transfer matrix calculation (open circles) are compared with the Lorentz model (lines).

A cavity mode, which includes the frequency dependent reflectance or transmittance as well as the phase shift, can be modeled by a single Lorentz oscillator with

$$t(\omega) = \sqrt{T(\omega)}\,\mathrm{e}^{-i\phi(\omega)} = t_0 + \frac{\mu}{\gamma_m + i(\omega - \omega_m)}. \tag{2.51}$$

Here, the phase transmission $t(\omega)$ has a maximum at the cavity mode frequency ω_m with a spectral width γ_m. Additionally, the Lorentz model includes an amplitude μ and a background transmission t_0. Figure 2.5 b depicts the result of modeling the cavity mode by a Lorentzian. For the reflectance curve ($R = 1 - T$) the model agrees with the transfer matrix calculation of a dielectric microcavity. The phase jump in transmission is also reproduced by the Lorentz model, whereas at off-resonance frequencies, the dispersion of the stack is stronger and the Lorentzian model deviates from the transfer matrix result. In case of strong absorption within the cavity layers, the Lorentz model cannot be applied in this simple manner and additional considerations have to be taken into account. The Lorentzian line shape is of special importance for the time dependence of the resonator and explains the exponential energy dissipation of the oscillator (q.v. Sec. A.1).

We have seen previously that in the resonance condition (Eq. 2.50) the cavity mode is influenced by the cavity layer and the mirror parameters. This is of special importance for cavities, which contain dielectric mirrors with a significant penetration depth L_D. Accounting for this, the cavity mode frequency ω_m is expressed by [20]

$$\omega_m = \frac{L_c \omega_c + L_D \omega_D}{L_{eff}}, \tag{2.52}$$

where $\omega_c = m\pi c / n_c L_c$ is the cavity frequency without a mirror phase delay. The integer number m accounts for the multiple of the optical half wave thickness of the cavity layer. The effective cavity length $L_{eff} = L_c + L_D$ is in the presence of DBRs greatly enhanced by their penetration depth and thus, the central frequency of the DBR ω_D mainly determines the cavity mode frequency.

In Fig. 2.6 we compare the electric field distribution in a microcavity and a DBR. In both structures, an oscillation of the amplitude is present. The envelope of the electric field amplitude decays exponentially in the DBR visualizing the penetration depth. By contrast, in the cavity the field is strongly amplified towards the cavity layer. Beside the large light intensity in the center of the structure, a considerable amount of energy is stored in the DBRs, which demonstrates the increase of the effective cavity thickness in comparison to the pure cavity layer. These electric field calculations are a solution of the transfer matrix algorithm and therefore only valid in the steady state. This means, only at continuously incident light the reflectance of a microcavity (Eq. 2.49) is reduced in comparison to a DBR (Eq. 2.42). If a light pulse enters a microcavity consisting of two high reflective DBRs, most of the light is reflected at the beginning. Only a small amount transmits through the first mirror and resonates in the cavity layer. In time, the amount of photons in the cavity increases until an equilibrium between incoming and absorbed or escaping photons is reached. Due to the phase shift in the cavity, the photons can only leave the cavity opposite to the side of incidence. As a results of the high reflectance of the DBRs, the photons in the microcavity perform a number of round trips and the electric field intensity is increased significantly. At the antinode position, the resonant cavity mode, for which all reflected waves are in phase, is enhanced by the factor Q', which can be calculated by applying the reflectances R_1 and R_2 of the

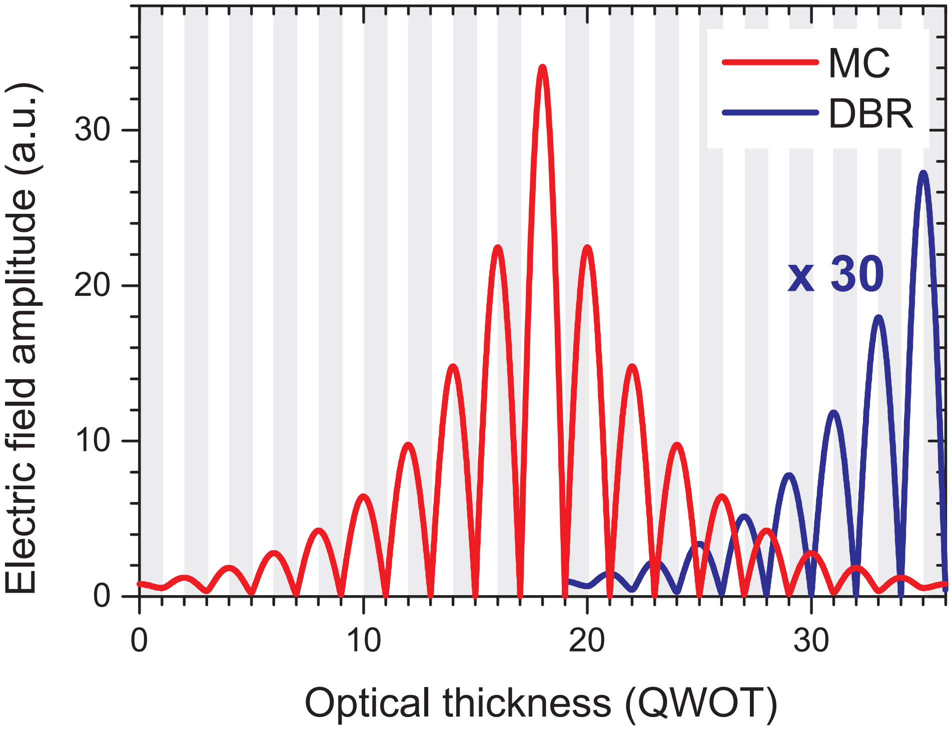

Figure 2.6: Comparison of the electric field amplitude in a DBR ((H L)8 H) (blue) and a microcavity ((H L)8 H 2L H (L H)8) (red) at the design wavelength. The structures consist of dielectric media with the indices of refraction $n_H = 2.2$ and $n_L = 1.45$ embedded in air ($n_0 = 1$) to the right and glass ($n_s = 1.5$) to the left . Light is incident from the right side with an amplitude of 1. The positions of high refractive index layers are emphasized by shaded areas. The amplitude of the DBR is increased 30 times for visualization.

surrounding mirrors 1 and 2 by [21]

$$Q' = \frac{(1+\sqrt[4]{R_1 R_2})^2}{1-\sqrt{R_1 R_2}}. \tag{2.53}$$

This internal electric field amplification is related to the quality factor Q of the cavity, which is defined as [22]

$$Q = 2\pi \frac{\text{stored energy}}{\text{energy lost in one cycle of oscillation}}. \tag{2.54}$$

The Q-factor is proportional to the cavity photon lifetime τ_c and is experimentally accessible by a measurement of the cavity mode wavelength λ and their corresponding linewidth $\Delta\lambda$:

$$Q = 2\pi \frac{c\,\tau_c}{\lambda} = \frac{\lambda}{\Delta\lambda}. \tag{2.55}$$

Every optical system consisting of thin films exhibits a polarization and angle dependence in reflection and transmission. This effect can be explained by the Fresnel reflection coefficients (Eqs. (2.14) and (2.21)) of each individual interface and the different phase matching at detuning, which both vary with angle of incidence and polarization. In real materials, absorption and dispersion additionally contribute to this behavior. Figure 2.7 depicts the angle dependent transmission of a microcavity for s- and p-polarization. For wavelengths around the design wavelength, the cavity mode is surrounded by the low transmission stop-band. With increasing angle of incidence, all modes shift to shorter wavelengths or higher energies. The p-polarized DBR modes, energetically located below the stop-band, shift stronger and the modes above weaker than the equivalent modes in s-polarization. As a consequence, the stop-band width increases in s-polarization and decreases in p-polarization with increasing angle of incidence.

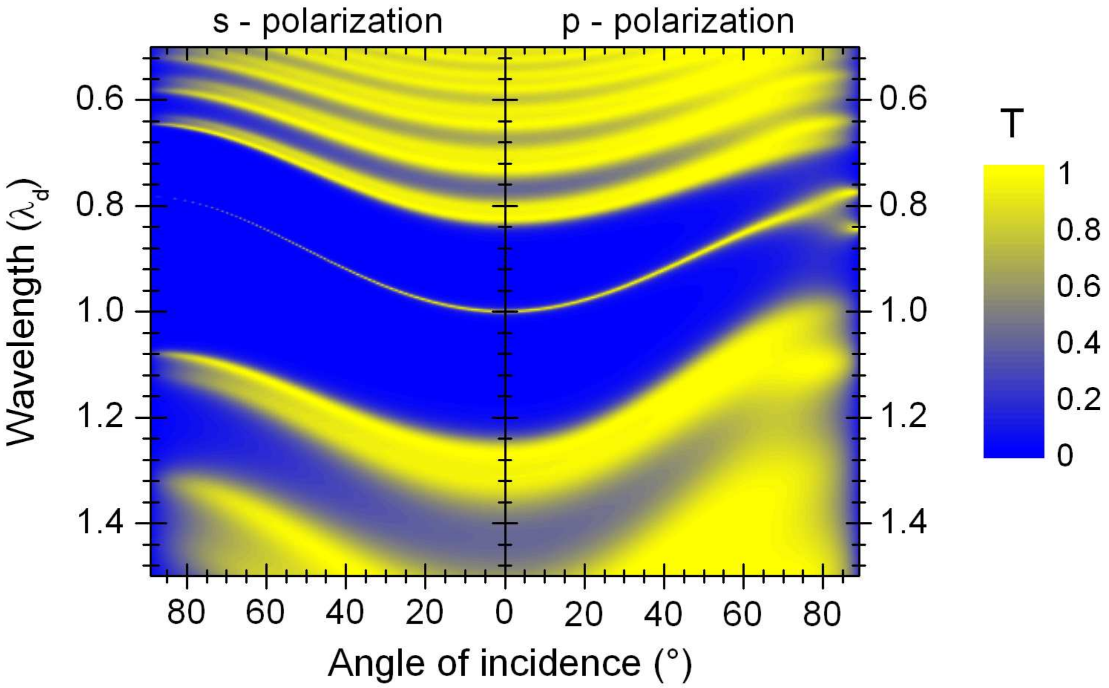

Figure 2.7: Calculated angle dependent transmission of a single microcavity for s- and p-polarization.

The blue shift of the resonant wavelengths with an increasing incident angle is counter-intuitive in the first view. With larger angles, the optical path inside a thin film increases as well, but the additional phase shift at the boundaries reduces the effective thickness. Neglecting an angle and polarization dependence of the phase shift at one boundary, the resonance wavelength λ' of a single thin film with the refractive index n_2 and the thickness d shifts with the angle of incidence θ as

$$\lambda' = 4\, n_2\, d \sqrt{1 - \left(\frac{n_1}{n_2} \sin\theta\right)^2}\,, \tag{2.56}$$

where n_1 is the index of refraction of the incident medium. From this equation, one obtains a blue shift of the resonant modes with increasing angle of incidence.

2.5 Coupled microcavity

2.5.1 Mode structure

Coupled microcavities are an extension of the concepts described in the former sections. They contain two or more resonator layers which are separated by additional mirrors. An interesting property of coupled cavities is the number of cavity modes, which is directly connected to the number of integrated resonators. The optical effects of coupled resonators cannot be derived from simple matrix manipulations as for the DBR or the single cavity. Additional mirrors inside the structure disturb the reflectance amplitude and phase behavior significantly. However, for cavity modes, the resonance condition has to be fulfilled for all resonators simultaneously. In the solutions, the penetration matrices of the cavity layers deviate from the simple form presented in Eq. 2.48. Therefore, we directly describe most properties of coupled microcavities on the basis of results from transfer matrix calculations.

By combining two identical single cavities, the two former isolated modes couple and the single mode is split into a mode pair. This splitting is caused by the central mirror, which disturbs the degeneracy of the single modes. We define the half-integer number of central mirror layer pairs as: $N_c + 1/2$. The splitting of the two frequencies ω of the coupled modes can be expressed by

$$\omega = \omega_m \pm C, \tag{2.57}$$

where ω_m is the central frequency of the unperturbed single cavities and C is the coupling parameter. This parameter can be written as [20]

$$C = \frac{c}{2 n_c L_{eff} \cos\theta_c} \arcsin\sqrt{1 - R_c}, \tag{2.58}$$

with the cavity layer refractive index n_c, the effective cavity thickness L_{eff}, the internal angle θ_c and the central mirror reflectance R_c. It can be seen that the central mirror has the strongest influence on the coupling strength between the two modes. In the $R_c \to 1$ case, the coupling vanishes and both modes have a frequency equal the uncoupled single mode. On the opposite, if the central mirror reflectivity vanishes, both modes are widely separated. The two modes are often referred to as symmetric and antisymmetric mode. The symmetric mode appears at the shorter wavelength, if N_c is even and the cavity layer consists of the low refractive index material. If one of the two constraints changes also the positions of the symmetric and the antisymmetric mode interchange.

Figure 2.8 exhibits the transmission and phase shift for a symmetric coupled cavity with a 5.5 pair central DBR. This transfer matrix simulation depicts two modes, which each deviate from the design wavelength by ± 1%. From Fig. 2.8 we can also see the phase difference between the two modes in transmission. Here, a phase difference of $\phi_S - \phi_{AS} = \pi$ occurs, which means a shift of both modes by $\pm\,\pi/2$ corresponding to the phase of the single modes (cf. Fig. 2.5).

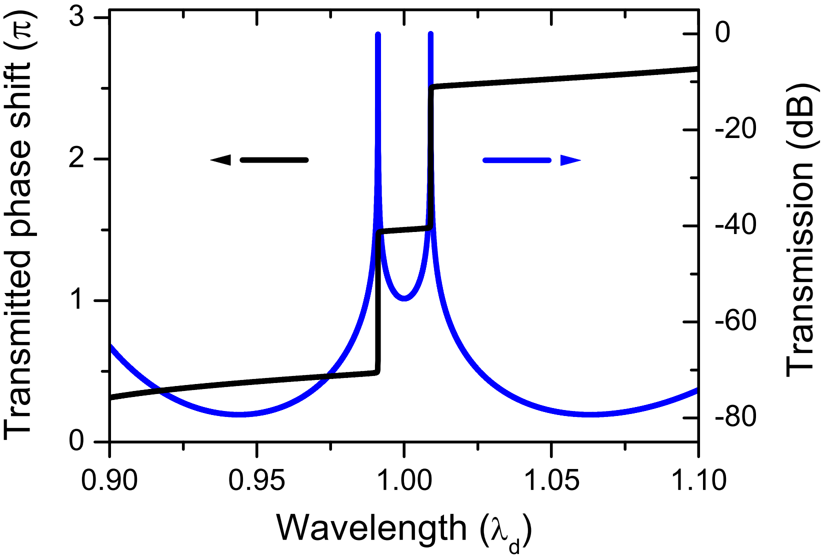

Figure 2.8: Calculated transmission and phase shift of a coupled microcavity with the design: (1H 1L)10 1H 2L 1H (1L 1H)5 2L (1H 1L)10 1H. The refractive indices are $n_H = 2.2$ for the high and $n_L = 1.45$ for the low index layer. The structure is surrounded by air ($n_0 = n_S = 1$).

For the following considerations, we have to remember some basic concepts of the transfer matrix algorithm. The electric field is as a part of an electromagnetic wave oscillating in time and in a layer calculated as the sum of the fields of a forward and backward traveling wave (Eq. 2.7 and Eq. 2.8). As a constraint in transfer matrix calculations, the incident light is assumed to have an equal and fixed phase for all wavelengths. The solution is therefore only representative for this phase. In other words, it is the stationary solution for the time, when the phases of all light frequencies are equal at the incident boundary. Regarding the wave behavior, the dynamics of the light in a layered system can be simulated with a knowledge of the electric field amplitude and the phase for a certain time.

Figure 2.9 presents the electric field distribution of two cavity modes within the same structure. For the plotted time, the two modes oscillate in phase in the left side of the structure and are out of phase in the resonator to the right. This demonstrates an energy concentration around one of the two resonators. Since both modes have a different wavelength and thus also a different frequency, their phases shift in time and a beating occurs. As a result, we obtain an oscillation of the light between the two cavity layers with the difference frequency of the two modes. One cannot directly detect this oscillation. However, in transmission or reflection measurements with coherent light, this internal oscillation generates a beating of the sum signal. For a design wavelength of 1000 nm, which corresponds to a frequency of nearly 300 THz, the beating frequency is for the sample in Fig. 2.8 approximately 6 THz.

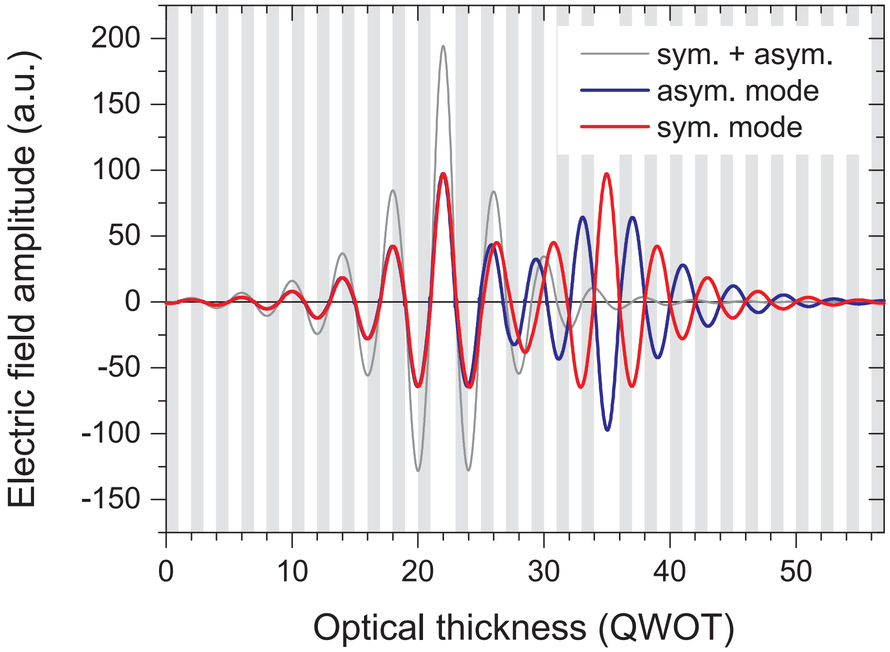

Figure 2.9: Simulation of the internal electric field in a coupled microcavity with the design (1H 1L)10 1H 2L 1H (1L 1H)5 2L (1H 1L)10 1H ($\lambda_d = 1000\,nm, n_H = 2.2, n_L = 1.45$). Light is incident from the right side with an amplitude of 1. The symmetric (red) and the antisymmetric (blue) mode are plotted as a function of the position within the sample (in units of quarter wave optical thickness). For the plotted time, the energy is concentrated in the left resonator and its surrounding layers, as denoted by the sum signal graph (gray line). High refractive index layers are denoted by the gray shaded areas.

The beating frequency is variable by the cavity design. As the central mirror influences the coupling between the two cavities, it also controls the beating frequency. An increasing central mirror reflectance reduces the coupling and therefore also the beating frequency. Figure 2.10 shows the strength of the mode splitting in dependence on the number of central DBR pairs. With 1.5 pairs a mode separation of about 30 THz is achieved, which is reduced to 2.5 THz in a sample with 7.5 pairs. In the limit of a totally reflective central mirror, both cavities are separated and no splitting will be observable. The two outer mirrors of a coupled cavity influence the photon lifetime within the complete structure. As in the single cavity, a high reflectance of these mirrors enables a high quality factor and a strong amplification of the internal electric field. This effect is accompanied by a narrowing of the transmission linewidths.

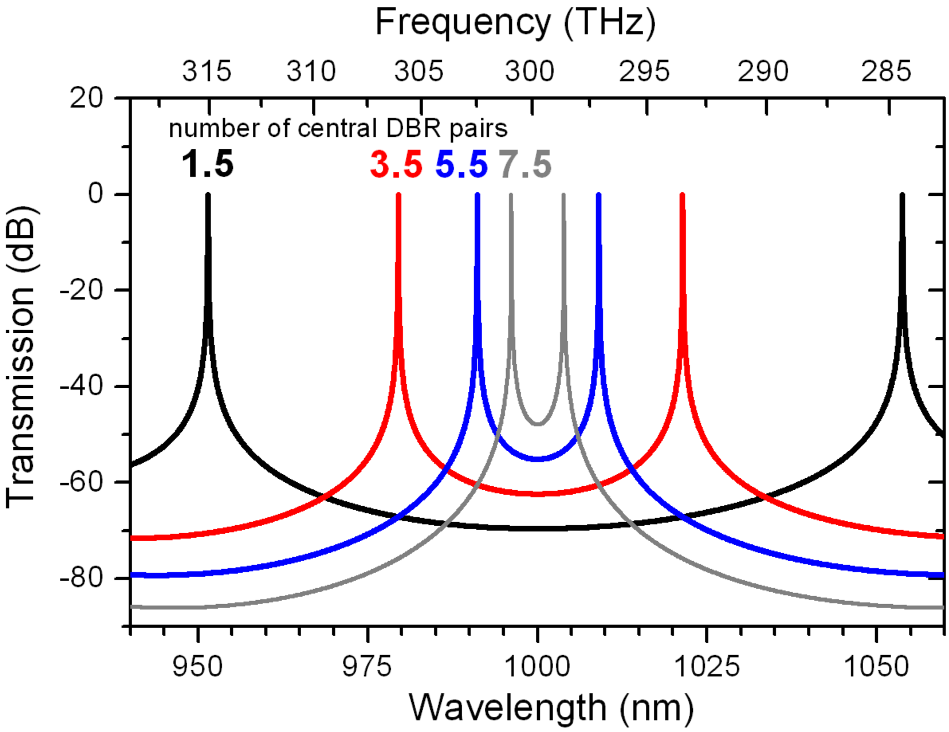

Figure 2.10: Calculated transmission of coupled microcavities with different number of central mirror pairs. The structure of (1H 1L)10 1H 2L 1H (1L 1H)$\mathbf{N}_c$ 2L (1H 1L)10 1H is designed for a wavelength of 1000 nm. The number of central mirror pairs N is chosen as 1,3,5 and 7. With increasing N_c, the coupling between the cavity modes and thus the spectral mode distance decreases.

2.5.2 Photonic Bloch oscillations

In research and technology coupled microcavities attract interest due to the mode splitting, the coupling of several modes, and the internal oscillation of light. First coupled microcavities have been investigated in 1994 by the application of a semiconductor structure grown by molecular beam epitaxy [23]. Later, this concept was applied in the fabrication of VCSELs with coupled cavity layers for optical [24, 25] and electrical pumping [26, 27]. All these devices exhibit single or dual mode laser emission. If the switching between single and dual mode operation would be controllable, a number of logical operations could be performed by such an optical device. Experimental and theoretical investigations have shown, that a coupled VCSEL with separately electrically excited active cavities can provide a controlled emission at either of the two modes or at both modes simultaneously [28]. The interaction of the photon modes and the two gain media in coupled VCSEL can also lead to a shortening of the laser pulse length, providing single pulses of only a few picoseconds [24]. In other configurations, coupled VCSELs demonstrate current dependent bistability with a high switching contrast [29] or Q-switching operation with gigahertz repetition rates [30].

Implementing identical quantum wells in both cavity layers of a coupled microcavity, whereas the quantum wells are in resonance with the photon mode of the isolated single cavities, the mode structure becomes even more curious. Such a system contains four oscillators, two of photonic and two of excitonic character. In resonance, these four oscillators couple and four cavity modes are generated. Such strongly-coupled microcavities provide an interaction between macroscopically separated quantum wells and enable the observation of excitonic states, which remain "dark" in single cavities [20, 31–33].

The internal oscillation of light in coupled microcavities is often referred as the optical analog of the electronic Bloch oscillation. Predicted in 1928, the Bloch oscillation describes the spatial oscillation of an electron in a periodic potential under a constant electric field [34]. The experimental confirmation of the theoretical prediction succeeded not before 1992, where the periodic movement of electrons in a semiconductor superlattice was detected by four-wave mixing [35–37] and by terahertz spectroscopy, which analyzes the radiation from the oscillating wave packet within this structure [38]. In optics, the analysis of Bloch oscillations is still under investigation. As with the fabrication of semiconductor superlattices for electronic oscillations, the first demonstration of coupled microcavities opened the door for the spatial oscillation of light with terahertz frequencies in layered structures. The introduction of a linear or exponential chirp of the refractive indices in a coupled microcavity with multiple resonator layers would resemble a Wannier-Stark ladder [39–41]. Another proposed superlattice design consists of a laterally confined DBR of porous silicon [42]. Here, the lateral confinement of the periodic structure simulates a continuous variation of the effective refractive index and the optical potential of the DBR has again the form of a Wannier-Stark ladder. In comparison to the chirped design, this setup with its three-dimensional confinement is even more complicated to fabricate.

In pioneering experiments, relying on two-dimensional waveguide structures, optical Bloch oscillations were firstly measured in 1999 [43]. By the application of layered systems, Bloch oscillations were demonstrated in a chirped coupled microcavity of porous silicon [44]. Within this optical Wannier-Stark ladder, the mode confinement in dependence on the refractive index gradient was shown by time resolved transmission experiments. Here, an increased gradient decreases the damping of the field oscillation. In another experiment on porous silicon coupled microcavities with a refractive index gradient, the linear transmission spectra are used for the determination of the oscillations [45]. The spectra are multiplied with a simulated femtosecond laser pulse. The Fourier transform of this product shows a beating of the electric field with a terahertz frequency. These results are indicated as an experimental confirmation of the Bloch oscillation. Unfortunately, the linear measurement gives no direct evidence for a temporal beating of the internal electric field.

In contrast to former experiments, we consider the local oscillation of light within unchirped coupled microcavities already as photonic Bloch oscillation. Indeed, a potential refractive index gradient in a coupled cavity gives an optical potential which is equivalent to its electric counterpart of a Wannier-Stark ladder. However, the external electric field, which accelerates the electron within a semiconductor has no direct analogy in optics. In conclusion, we apply the term Bloch oscillation for our observations of the internal oscillation of the electric field within unchirped coupled microcavities.

3 Light-matter interaction in microcavities

This Chapter is dedicated to the absorption and emission within optically confined structures. It explains the coupling of excitonic and optical properties under different conditions and develops a model for the calculation of an emission within a layered structure. A conclusion of the electronic properties of organic semiconductors leads to their application in organic microlasers.

3.1 Weak-coupling regime

In the weak-coupling regime, the spontaneous emission of an organic molecule and any other potential emitter is described by Fermi's Golden Rule:

$$\Gamma_{sp} = \tau_{sp}^{-1} = \frac{2\pi}{\hbar^2} |\langle|\hat{d} \cdot \hat{E}_{k,\sigma}^{\dagger}|\rangle|^2 \rho(\omega). \tag{3.1}$$

Here, the spontaneous emission rate Γ_{sp} and the inverse lifetime τ_{sp} are proportional to the density of states ρ. The Hamiltonian of the transition is given by the dipole operator $\hat{d}$ and the operator of the electric field $\hat{E}_{k,\sigma}$, where k is the plane wave vector and $\sigma = 1, 2$ gives the polarization index of the mode. In a microcavity, the mode structure is modified in comparison to the free space, which results in an alteration of the emission rate in the weak-coupling regime. For resonant k-vectors, the vacuum field fluctuations are enhanced and the spontaneous emission rate is increased. This enhancement is related to the Q-factor of the corresponding cavity mode and was first described in 1946 [46]. The so-called Purcell-factor of an emitter placed at the maximum position of the electric field and perfectly spectrally matched with the cavity mode has the form of

$$F_p = \frac{\tau_{free}}{\tau_{cav}} = \frac{3}{4\pi} \left(\frac{\lambda_c}{n}\right)^3 \frac{Q}{V_{eff}}. \tag{3.2}$$

This defines the ratio between the free space decay time τ_{free} and the emission decay time in cavity τ_{cav}, with knowledge about the refractive index n at the emitter position and the effective cavity volume V_{eff}. Purcell-factors of around 100 and higher have been achieved in high-Q cavities [47, 48]. At non-resonant frequencies, the emission is suppressed and the intensity is inversely proportional to the Q-factor. A microcavity in the weak-coupling regime redistributes the emission from a source. In comparison with a low-Q structure, more light can be emitted into the cavity mode in a high-Q microcavity, allowing the emission of light which would otherwise be trapped in the layered structure. This effect is used in the enhancement of the outcoupling efficiency in resonant cavity light emitting diodes (RCLEDs) [49–53] and the spontaneous emission into the laser mode of VCSELs [54–56].

3.2 Strong-coupling regime

In contrast to the weak-coupling regime, where the cavity mode and emission overlap, in the strong-coupling regime the cavity mode and the absorption of a dipole are in superposition. This coupling of a photon and an exciton creates a new quasiparticle - a polariton. A polariton can be understood as a state oscillating between being exciton and light. Cavity polaritons can be observed if the inequality [57]

$$\alpha L \gg 1 - \sqrt{R_1 R_2} \tag{3.3}$$

is fulfilled, where the product of the optical attenuation coefficient α and the cavity layer thickness L overcomes the losses of the resonator with the mirror reflectivities R_1 and R_2. With the gradual improvement of semiconductor microcavities and inorganic quantum well structures, the coupling between material and photons exceeded the decay rates of both. Cavity polaritons were first observed in 1992 in inorganic quantum well structures [5]. In the vicinity of the exciton resonance, the refractive index exhibits a pronounced change[1] resulting in a superposition with the Fabry-Perot mode at three different frequencies (Fig. 3.1 a). The central mode is destroyed by the high absorption of the exciton, giving the typical two peak structure in the transmission and reflection spectrum. Due to the angle dependence of the microcavity mode, a system non-resonant at normal incidence can be brought into the strong-coupling regime by turning the sample and creating an anticrossing at a larger angle of incidence (Fig. 3.1 b). At the anticrossing angle the two modes are separated by the Rabi energy $\hbar\Omega_{Rabi}$. Visualized, the Rabi frequency Ω_{Rabi} presents

---

[1] Real and imaginary part of the refractive index n are coupled, which is explained by the Kramers-Kronig relations. This effect is caused by the causality principle of electrodynamics and explained in Ref. [58].

the oscillation between the excitonic and the photonic state, giving a connection between the quantum physical phenomenon and the classical picture provided by the transfer matrix model. At low temperatures, inorganic semiconductor microcavities show a Rabi splitting energy of around 5 meV [59, 60]. This values have been strongly increased by the application of organic semiconductors in microcavities. J-aggregates, porphyrine and other dyes have been applied for mode coupling using their advantage of large oscillator strength (two orders of magnitude higher than III-IV semiconductor quantum wells) and narrow absorption linewidth [61–69]. Rabi splitting energies up to 430 meV have been achieved at room temperature in cavities with metal mirrors and thus relatively low Q-factors [70, 71] in comparison with their inorganic counterparts [72].

3.3 Spontaneous emission in layered structures

3.3.1 Plane-wave expansion

In the weak-coupling regime, where the dipole dephasing time and the cavity photon life time are much shorter than a Rabi oscillation, the spontaneous emission of a dipole is stimulated by the fluctuations of the vacuum field. This assumption is, beside others, one explanation of spontaneous emission. Optical resonators with their alteration of the mode structure have attracted interest due to the ability of focusing emitted light into selected channels with high efficiency. The strength of light emission in layered structures can be exactly calculated by the plane wave expansion method [51, 73–81].

In this method, the spontaneous emission is a result of a coupling between the emitters dipole moment and the electric field operator in dependence on the density of states, as it is represented by Fermi's Golden Rule (Eq. 3.1). Electric field operator and mode density depend on the cavity and therefore the model is only focussed on them. However, there exists no experiment where the electric field and the mode density influence on the emission can be separated. As a simplification, the influence on the emission rate can either be completely attributed to the electric field or to the density of states. Both views lead to the same results if analyzed properly. Here, an isotropic mode density is implied, which is not true in reality but in this model the density of states will be compensated by the electric field. Thus, the method is based on the calculation of the internal electric field in a layered structure [10,82], which can be obtained by the transfer matrix algorithm. The algorithm described below refers also to the transfer matrix method but is applicable for only one layer of a system. This approach results in an analytical solution for the electric field distribution and gives a more demonstrative insight than the matrix representation. By comparing

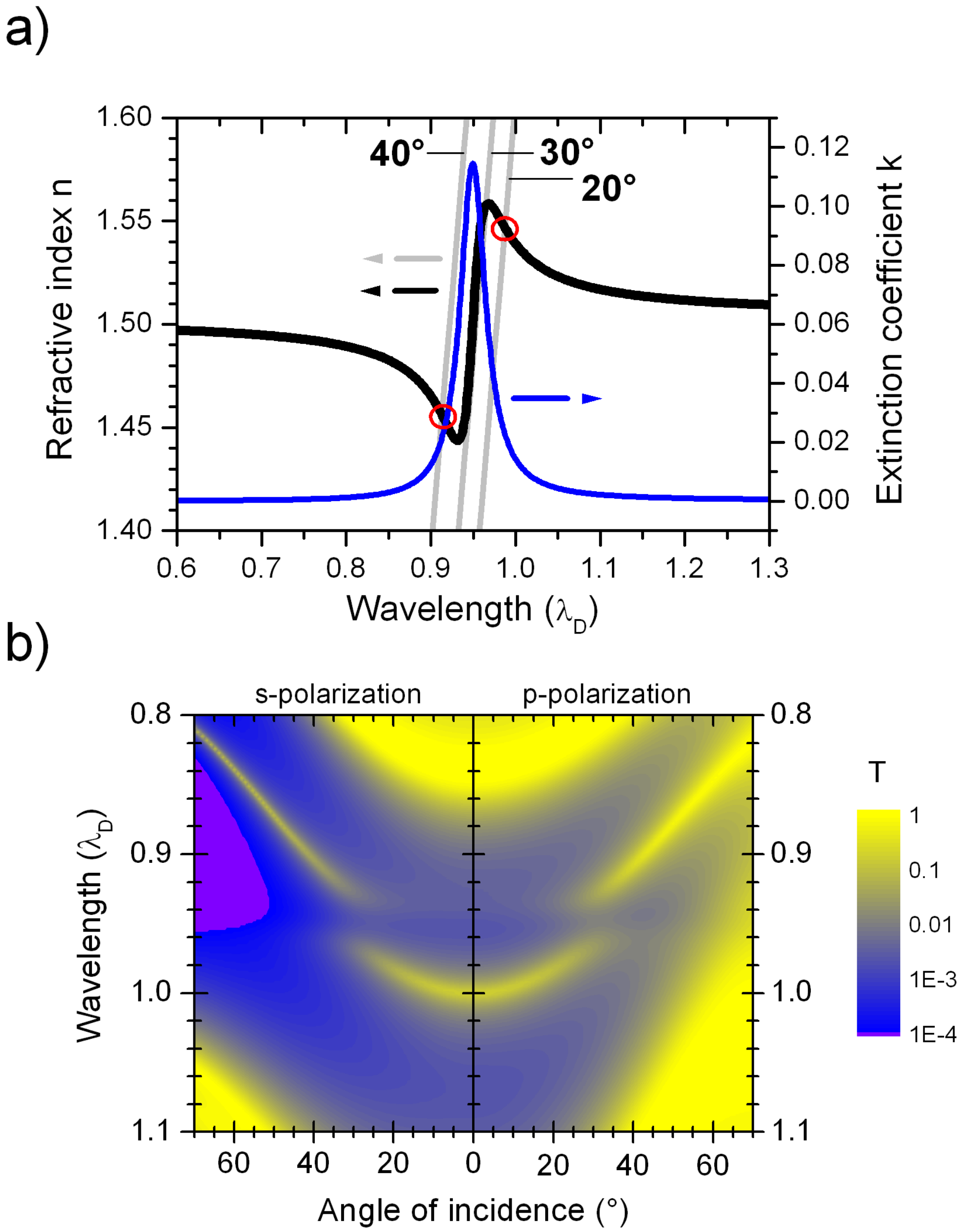

Figure 3.1: (a) The optical constants of an absorbing material modeled by a single Lorentz oscillator. The absorption with a center wavelength of 0.95 λ_d (blue) results in a change of the refractive index (blue). The cavity mode frequency (p-polarization) in dependence on the cavity layer refractive index is plotted for three angles around the resonance angle (grey) for a (H L)5 H 2C H (L H)5 microcavity. The cavity mode occurs at the crossing points (red) of the Fabry-Perot modes and the refractive index curve. (b) In the angle dependent transmission calculation strong-coupling is achieved at angles $\theta \approx 30°$ in s- and p-polarization. Refractive indices: $n_0 = 1$, $n_s = 1.5$, $n_H = 2.2$, $n_L = 1.45$ and $n_C(\infty) = 1.5$.

the strength of the internal electric field with the field outside the structure, a relative change and thus an enhancement or suppression factor of emission rate is received.

The model structure consists of two mirrors with the phase reflectivities r_1 and r_2 and the transmission t_2, which are defined as

$$r_1 = \sqrt{R_1}\,\mathrm{e}^{-i\phi_1},\ r_2 = \sqrt{R_2}\,\mathrm{e}^{-i\phi_2} \text{ and } t_2 = \sqrt{T_2}\,\mathrm{e}^{-i\phi}. \tag{3.4}$$

These complex values consist of the amplitude, given by the square root of the power reflectances R_1 and R_2, power transmittance T_2, and the corresponding phase shifts ϕ_1, ϕ_2 and ϕ. Between the mirrors, the layer of the thickness L with the refractive index n is located, which contains the emitting molecules. In this procedure light is incident from outside at the side of mirror 2. After the transmission through mirror 2, the light is entering the layer of interest and is completing a number of multiple reflections. For the emitter at the position z, the complex electric field $\mathcal{E}$ consists of a right and a left travelling wave $\mathcal{E}^-$ and $\mathcal{E}^+$. By Airy summation of the successive internal reflections, the electric field has the form of

$$\mathcal{E} = \mathcal{E}^- + \mathcal{E}^+ = \frac{t_2\,\mathrm{e}^{ik(L-z)} + t_2\,r_1\,\mathrm{e}^{ik(L+z)}}{1 - r_1\,r_2\,\mathrm{e}^{(2ikL)}} = \sqrt{E}\,\mathrm{e}^{i\Psi}. \tag{3.5}$$

The electric field consists of the intensity E and the phase Ψ that is dependent on the wave vector k. Here, the wave vector is defined as

$$k = \frac{2\pi n}{\lambda}\cos\theta, \tag{3.6}$$

where λ is the wavelength of the incident light and θ the angle of incidence. The electric field intensity E represents the enhancement factor of the spontaneous emission. In the case of a real refractive index of the emission layer, which is a realistic approximation for the most samples discussed within this thesis, the final formula for the emission enhancement becomes

$$E = \frac{T_2\left[1 + R_1 + 2\sqrt{R_1}\cos(-\phi_1 + \frac{4\pi n}{\lambda} z\cos\theta)\right]}{1 + R_1\,R_2 - 2\sqrt{R_1\,R_2}\cos(-\phi_1 - \phi_2 + \frac{4\pi n}{\lambda} L\cos\theta)}. \tag{3.7}$$

The bracket term in the numerator is also known as the antinode factor. It is maximized when the reflectivity R_1 and $\cos\theta$ are close and equal unity, respectively. It is especially dependent on the emitter position z with the strongest amplification at the antinode position of the electric field. Additionally, to obtain a strong enhancement of emission, the denominator which is characterized by the structure itself has to be minimized. This condition is fulfilled, if the resonance condition (2.50) is satisfied and the reflectivities R_1 and R_2 approach unity. The spectra obtained by this calculation coincide with the transmission and reflection mode structure of the microcavity. It is therefore demonstrated that the mode structure of internal emission

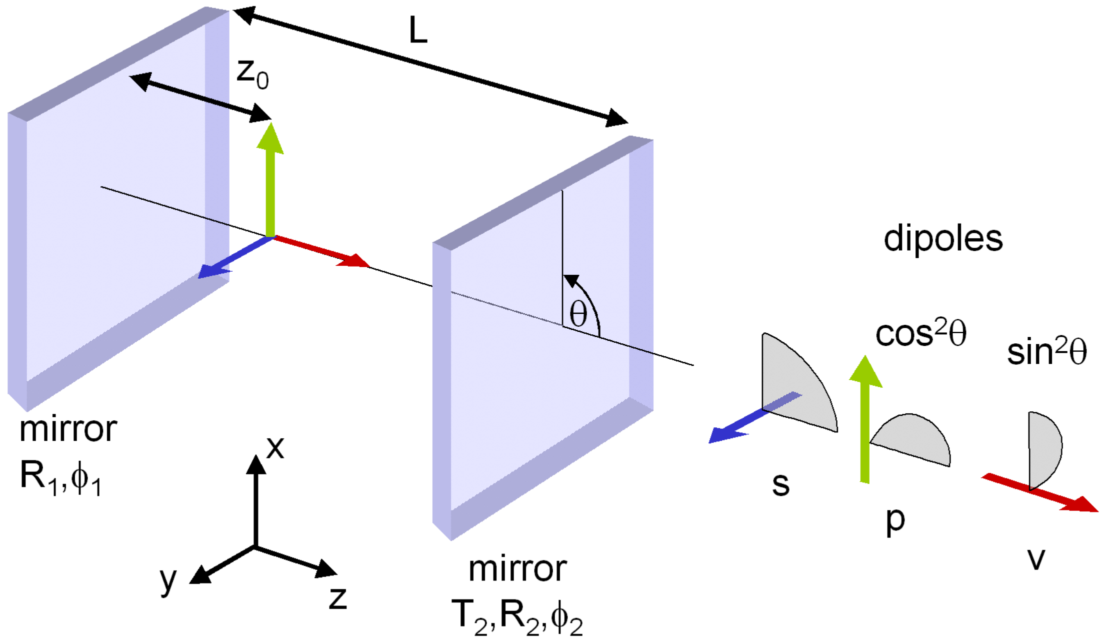

Figure 3.2: In the plane wave expansion model, a dipole at the position z_0 is situated in a cavity with the length L. The light is incident from the side of mirror 2 and the electric field at every dipole position is calculated by a superposition of a left and a right traveling wave. The interaction between the electric field and the p-polarized dipoles (horizontal p (green), vertical (red)) shows an angle dependence. However, the s-dipole (blue) emits with equal strength in all directions.

is directly related to the optical properties, which are observed from the outside. In accordance with DBR and microcavity properties, the enhancement factor is also influenced by the two polarizations at incident angles deviating from the normal.

For exact calculations of anisotropic emission layers, the active region is modeled by an orthogonal set of dipoles with the source terms

$$\Pi_s = \frac{3}{8\pi},\ \Pi_p = \frac{3}{8\pi}\cos^2\theta,\ \Pi_v = \frac{3}{8\pi}\sin^2\theta. \tag{3.8}$$

Here the source terms Π_s and Π_p represent the two planar dipoles parallel to the s- and p-polarization respectively and Π_v typifies the field of the out-of-plane vertical emitter. The emitted electric field of the vertical dipole is also p-polarized. The $\frac{3}{8\pi}$ term is a normalization constant. The final emission spectrum I_E of an active layer in a resonator is calculated by

$$I_E = (\alpha_s\,\Pi_s\,E^s + \alpha_p\,\Pi_p\,E^p + \alpha_v\,\Pi_v\,E^p)\,E_0. \tag{3.9}$$

The total emission consists of the contributions from the three dipoles. In an isotropic active medium all orientations have the same emission probability and

$\alpha_s = \alpha_p = \alpha_v = 1/3$. So the same amount of emitted light goes into s- and p-polarization and is influenced by the corresponding enhancement factors E^s and E^p. For quantum wells and epitaxially grown organic films the dipole distribution may become anisotropic, which gives $\alpha_s = \alpha_p = 1/2$ and $\alpha_v = 0$. Finally the enhancement terms are multiplied by the bulk emission spectrum E_0 of the active material.

For the calculation of the enhancement factor, the structure is divided at the active layer into two parts to determine the optical properties (see Eq. 3.4) of the two reflectors separately. In both transfer matrix simulations, the active layer is assumed as the ambient medium and the actual ambient medium is treated as the substrate for mirror 2. The advantage of having an analytical formula for the enhancement factor is hindered by the fact that transmission, reflections and phase shifts are easily accessible by a numerical calculation, only.

3.3.2 Internal mode structure

Equation (3.7) gives the exact formula for the calculation of the enhancement factors for modes, which can leave the layered structure into the ambient medium. By geometrical considerations, the ratio η of light emitted from the structure to the light bounded within is $\eta = 1 - \cos[\arcsin(n_0/n)]$, where n_0 and n are the refractive indices of the ambient and the active medium, respectively. The term $\arcsin(n_0/n)$ is also known as the critical angle θ_c of a medium. For angles larger than θ_c, total reflection occurs at the boundary to the ambience and the light is kept within the structure. From an active layer with $n = 1.7$, an usual value for organic materials, only a small amount of the totally emitted light can leave the optical system ($\eta \approx 17\%$). This is the main effect that limits the outcoupling efficiency of planar OLEDs, and necessitates more sophisticated device structures such as cavity designs [49, 51] or surface structuring [83–85].

Figure 3.3 depicts the mode distribution of a planar microcavity in k-space, with $k_z = k \cos\theta_{int}$ and θ_{int} as the internal angle in the active medium. For the simulation of the DBR reflectance and the emission enhancement factor, an organic material models the active medium ($n = 1.7$) and an infinite glass substrate ($n = 1.5$) is bounded to the back side. Only for larger k_z the DBRs are highly reflective, thus enabling the strong enhancement of the emission for the resonant cavity mode. With decreasing k_z and respectively increasing θ_{int}, the layered structure becomes transparent and light is penetrating nearly unaffected into the glass substrate. Starting from the outside critical angle, the light is totally reflected at the air-interface. Light propagating at such angles is forming leaky modes, which can propagate into the substrate but are not outcoupled to the surrounding air or a corresponding low re-

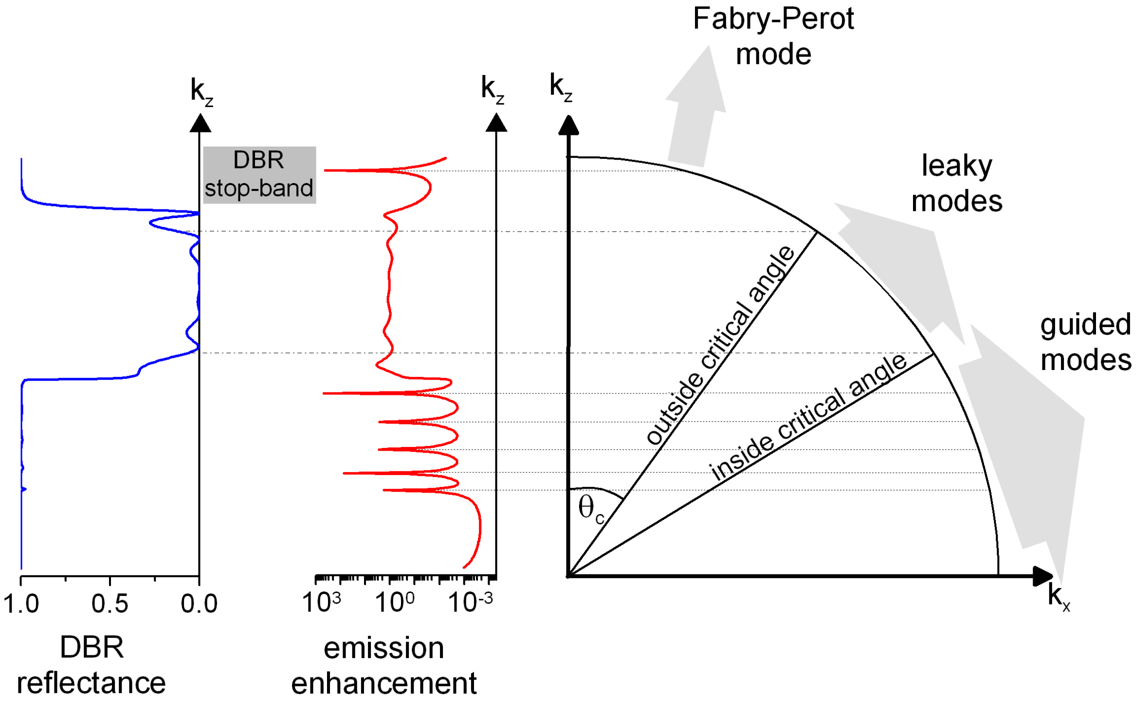

Figure 3.3: K-space plot of the emission modes of a Fabry-Perot microcavity compared to a DBR reflectance curve (left, blue) and the emission enhancement factor (center, red). Both spectra are calculated for a design wavelength of 800 nm and p-polarization. For the transfer matrix model, the layer structure (H L)10 H 2.2A H (L H)10 is embedded in an ambience of glass ($n_0 = n_S = 1.5$) on both sides, whereas the outside critical angle is given for an air-interface. The refractive indices of the layers are $n_A = 1.7 + i \cdot 10^{-4}$, $n_H = 2.2 + i \cdot 10^{-5}$ and $n_L = 1.45 + i \cdot 10^{-6}$.

fractive medium. The low DBR reflectivity leaves the emission of the active layer uninfluenced. Modes with internal angles larger than the inside critical angle are concentrated in the region around the active layer. At these high angles, the microcavity behaves as a slab waveguide due to the DBR layers with lower refractive indices compared to the emitter medium. Partially, the emission into these guided modes is as much enhanced as the emission of the resonant cavity mode. This demonstrates the numerous loss channels by guided modes for the emission of a potential light source based on planar microcavities. In contrast to guided modes, leaky modes create an evanescent field at the substrate-air interface and can therefore be extracted, for example, by surface structuring or scanning near field microscopy [86].

The enhancement factor is not defined by Eq. (3.7) for leaky and guided modes. To calculate the emission also for this angular region, two approaches are commonly used. In the first the whole structure is embedded in a high refractive index medium, with the lowest refractive index medium as the emitting layer. In this method, no leaky and guided modes occur and the total angular spectrum is accessible. The disadvantage here is the influence of the high refractive index medium on the mode

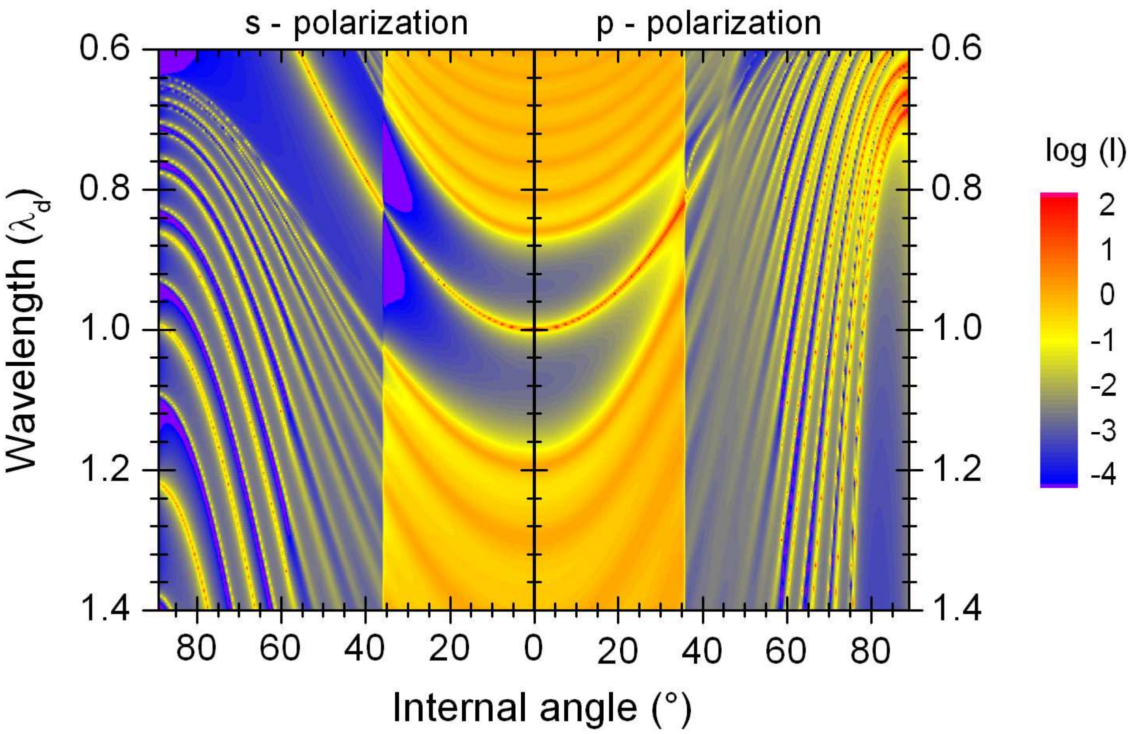

Figure 3.4: Calculated enhancement factor of an emitter in the center of a double-DBR microcavity for two polarizations towards the air surface. The layer structure (H L)10 H 2A H (L H)10 is attached to a semi-infinite substrate ($n_s = 1.5$) at the bottom side and covered by a semi-infinite ambience of air ($n_0 = 1$) at the top. The refractive indices of the layers are $n_A = 1.7,\ n_H = 2.2 + i \cdot 10^{-4}$ and $n_L = 1.45 + i \cdot 10^{-6}$.

structure and the amplitudes, which would deviate from a structure with a low refractive index ambience in reality as air or water. In the other approach, the transmission T_2 in the numerator of Eq. (3.7) is replaced by $1 - R_2$ and allows for the calculation of the leaky and guided mode structure, if an absorber is present within the system. The absorber is an essential constraint, since it prevents from the singularity in the equations numerator as it would be present for a dielectric layer stack, since R_2 would be equal unity.

The effect of emission into leaky and guided modes is not negligible for microcavity structures consisting of DBRs. As discussed in Sec. (2.3) and presented in Fig. 3.3, DBRs merely provide with the stop-band a spectrally limited region of high reflectance. Figure 3.4 presents the angle dependent spectrum of the enhancement factor within a planar high-Q microcavity. The calculation clearly shows the range of the extracted modes for angles smaller than $\theta_{crit} = 36°$. With increasing propagation angle all modes shift to the blue, but with a different strength dependent on the polarization and the wavelength position relative to the stop-band. In p-polarization, for example, the stop-band completely vanishes for the internal modes, due to the deviating shift of high and low energy DBR modes. However, in s-polarization, the stop-band possesses a nearly constant width also for the leaky modes. The transfer from leaky to guided modes is not pronounced. However, modes at angles larger than $\theta = 70^\circ$ can be assumed as guided modes and exhibit a strong polarization dependence. Thus, the p-polarized modes are the dominating emission channels for large angles and wavelengths shorter than the design wavelength, whereas at longer wavelengths the propagating light has mainly s-polarization.

In conclusion, we have demonstrated in Fig. 3.3 and 3.4 the applicability of the plane wave expansion method for the calculation of the internal emission enhancement of planar structures. It is shown that the strong amplification of the cavity mode emission is competing with the radiation into internal modes. This is a drawback of one-dimensional DBR microcavities, where a high DBR reflectivity enables extremely high Q-factors only for a small spectral and angular region. For a larger area of angles, the DBR structure does not alter the emission of an embedded active material, but guided modes enhance the emission into light waves with large angles of propagation.

3.4 Organic Semiconductors

Organic dyes combine a large oscillator strength with the infinite structural variability of organic chemistry. With the discovery of semiconducting properties in selected molecules, these materials entered also the field of electronics. Nowadays, a number of optoelectronic elements with active organic semiconductors have been developed and products have entered the market by applying their advantages of low cost fabrication and mechanical flexibility. The main disadvantage that have hindered organic materials from an earlier launch is their sensitivity to humidity and oxygen, especially in the excited state.

3.4.1 Electronic properties

The electrical and optical properties of organic semiconductors are mainly based on the electronic structure of the carbon atom. In unsaturated carbon molecules, e.g. benzene, a π-system is created by sp^2-hybridization, where the energy levels of the four valence electrons are adjusted (Fig. 3.5). In the plane of the benzene ring, three electrons of one carbon atom are linked by σ-bondings to their neighboring atoms. The six remaining electrons form dumbbell shaped orbitals perpendicularly oriented to the ring plane and are the basis for the resonantly generated delocalized π-electron system. The two rings of this electron system are aligned parallelly to the molecular plane. In contrast to the σ-system the binding energy is reduced and the gap between the highest occupied orbitals and the lowest unoccupied states is in the range of optical frequencies. This results in the characteristic absorption and emission spectra of organic dyes. Aromatic molecules, i.e. compounds of several benzene rings, show an increasing delocalization in the π-electron system with growing molecular size, which shifts the spectra towards longer wavelengths.

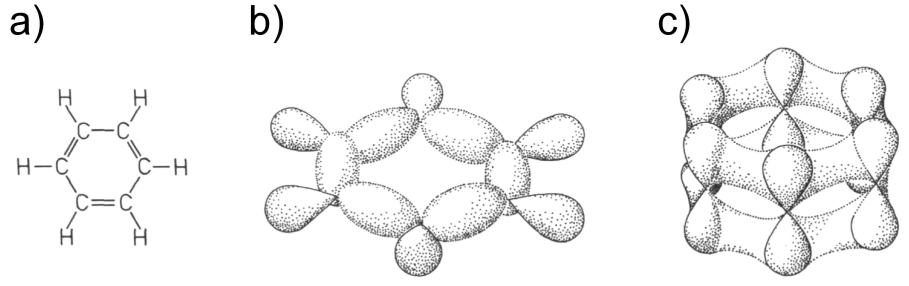

Figure 3.5: Benzene C_6H_6: (a) chemical structure, (b) electron density of σ-orbitals and (c) π-orbitals. [87]

The delocalized π-electron system, which is not restricted to aromatic molecules is the origin of the molecule's optical properties and present in all organic semiconductors. Its extension is sustainably influenced by additional atoms or atomic groups and furthermore dependent on the molecules environment, which results in different properties in the solid state, the liquid and gas phase.

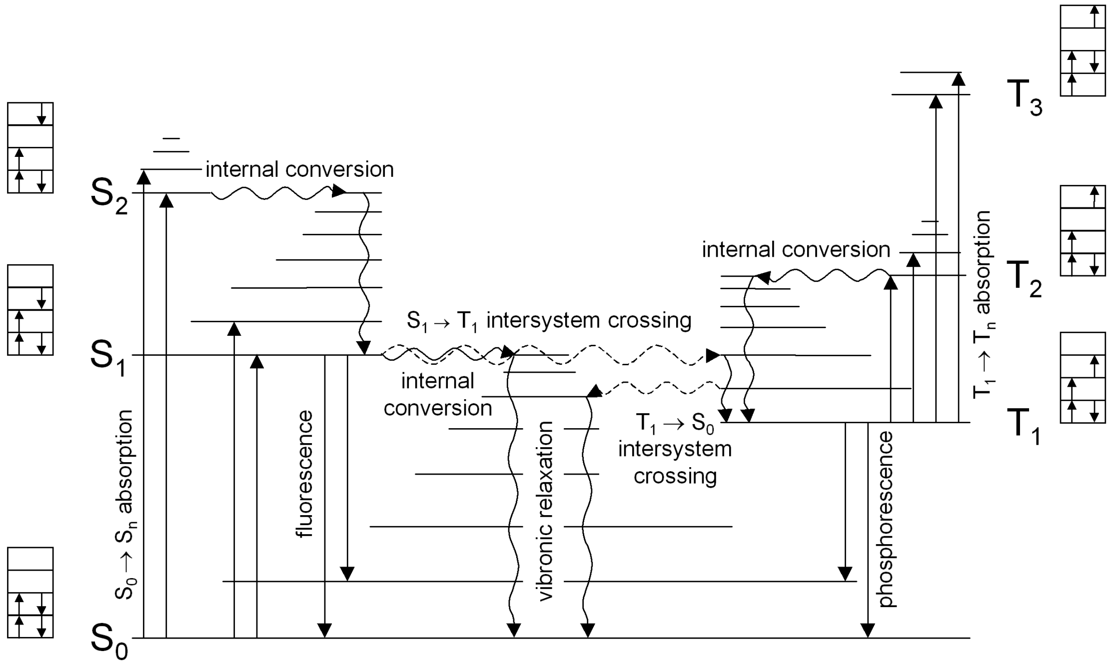

Figure 3.6: Jabłoński energy diagram of a molecule with radiative (straight) and non-radiative (corrugated) transfers. [88]

After external excitation of an organic molecule, either electrically or optically, the electronic charges are redistributed and the nuclei are shifted in their position as a result of the Coulomb interactions. The organic structure allows for a number of intramolecular transitions due to rotatory and vibronic levels, where rotations are only permitted in the gas phase (Fig. 3.6). Whenever a molecule is excited, it performs a number of radiative and non-radiative processes and returns to the ground state. Non-radiative relaxations in the excited state occur on very short time scales and result in the irreversible excitation of translations, vibrations and rotations (Tab. 3.1). In case of strong spin-orbit interaction, i.e in molecules with high atomic number nuclei, an irreversible intersystem crossing occurs between equal vibronic levels of the singlet and the triplet state. This behavior ends up in phosphorescence, the radiative transfer with low transfer rates. In the same way as the phosphorescence, the faster radiative fluorescence process in the singlet state can be initiated spontaneously by fluctuations of the vacuum field or stimulated externally by radiation with a photon energy matching the transfer gap.

process	lifetime (s)
absorption	10^{-15}
vibronic relaxation	$10^{-14} - 10^{-12}$
internal conversion	$10^{-2} - 10$
intersystem crossing	10^{-11}
fluorescence	$10^{-9} - 10^{-7}$
phosphorescence	$10^{-6} - 10^{2}$

Table 3.1: Lifetimes of photophysical processes [89].

3.4.2 Energy transfer

An energy transfer between two separated molecules may occur in three different ways. If the excitation is exchanged by radiation, the efficiency k decreases in free space with the distance r by $k \sim r^{-2}$. This transfer requires an overlap of emission and absorption spectra of the donor and acceptor molecules. Although it is not very prominent in standard organic thin films, its efficiency can be increased and the geometrical distance dependence can be overcome by the optical confinement of a microcavity [90]. For the investigations presented within the framework of this thesis, the radiative energy transfer plays only a marginal role.

Another non-radiative transfer mechanism is the short range Dexter transfer, which proceeds between particles with an overlap of their particular wave function [91]. Therefore, this process based on the exchange interaction is limited to short distances ($r < 2\,\mathrm{nm}$) and thus appears only between nearest neighbors in the solid state. The decay rate can be expressed by $k_D \sim J\exp(-2r/L)$, where J is the spectral overlap integral and L the orbital radius. The Dexter transfer obeys the spin conservation rules and is the dominant energy exchange process for triplet excitations.

The main transfer process for organic semiconductors applied in the experiments discussed within this work is the Förster resonant energy transfer [92, 93]. The Förster transfer is based on the Coulomb interaction and enables, relying on the conservation of spin multiplicity, singlet-singlet transfer only. It is also a near field process that has a greater range than the Dexter transfer and works for distances up to 10 nm. The Förster transfer rate for isotropically distributed dipoles is given by

$$k_F = \frac{1}{\tau_D}\left(\frac{R_0}{r}\right)^6 . \tag{3.10}$$

Here, the radiative lifetime of the donor in absence of an acceptor is given by τ_D. The Förster radius R_0 describes the spatial donor-acceptor distance, where the Förster transfer rate is equal to the radiative rate of the donor. It is of the order of $20-70\,\text{Å}$ for organic semiconductors and depends on the spectral overlap of donor and acceptor. As presented by Eq. 3.10, the transfer is very efficient but its probability decreases rapidly at distances which exceed the Förster radius.

3.5 Organic lasers

3.5.1 Microlasers

Since the first demonstration of a laser with an organic active material in liquid solution in 1966 [94] and in the solid state one year later [95], a large number of different dye laser systems have been developed. A few years later, they became a widely used instrument in research and industry [96]. To this day, all these systems have on crucial fact in common: they are not directly electrically pumped. The realization of this property approached with the verification of electroluminescence from organic thin films in 1987 [97]. Nowadays, OLEDs have left the stage of laboratory development, are applied in commercial products, and are a candidate for future displays. They combine the variety and attributes of organic compounds with the electric properties of semiconductors. Their extremely thin active layers of few hundred nanometers allow for a cost-effective fabrication on large and flexible substrates. Nevertheless, a number of electronic mechanisms compete with the luminescence [98, 99] and electrically generated laser emission from organic materials has not been demonstrated so far.

In comparison with inorganic semiconductor lasers, the gain of organic laser dyes is about one order of magnitude larger. This larger gain coefficient gives reasons to believe that the design of a potential organic laser diode may resemble an OLED structure in reference to the small active volume. Additionally to the gain, a laser requires a resonator, which in the simplest case consists of two mirrors [100]. Organic lasers with resonators based on total internal reflection are demonstrated in slab waveguides [101], microrings [102,103], microdiscs [103,104] and microdroplets [105]. Other lasers with organic thin films rely on DBR [104] and distributed feedback (DFB) designs [106–108].

Within this thesis, we have fabricated organic microcavity lasers. Such devices consist of two mirrors, which are directly attached to an active medium with usually sub-micrometer thickness [8, 54, 109–111]. These structures provide a vertical emission and, in principle, allow for the implementation of an OLED architecture. The disadvantage of the very thin gain medium has to be compensated by high mirror reflectivities. Although a single mode operation was achieved early, the laser threshold was significantly above that of other device architectures. With the substitution of the metal mirrors by higher reflective DBRs, the higher Q-factor increases the virtual gain length and the threshold is reduced drastically.

3.5.2 Basic concepts

In its simplest model, a laser is explained by an active medium in between two mirrors. As an active medium, any material can be used that amplifies light. For this purpose an external excitation generates a population inversion of excited states. Such a system must contain more than two levels, since in a two-level-system no inversion is achievable. Organic molecules are well explained by a four-level model (Fig. 3.7). This is supported by the fact that the relaxation processes in a certain excited state occur so fast that they are assumed as a single process. Therefore, a single excitation-emission cycle can be described by a model, which connects four electronic states by one corresponding transfer.

During the first transfer process, the pumping, electrons are lifted from the ground state (0) with the population N_0 to a higher vibronic level (3) of the first excited single state. By fast radiationless vibronic relaxations, the excited electrons populate the ground state 2 of the first excited state. The following transition from level (2) to level (1) is applied for the stimulated emission process. Due to the relatively long lifetime of the electrons in level (2) and the low initial population of level (1), a population inversion can easily be created, if there is no competing depletion path from level (3). The final transfer from level (1) to the ground state is again very fast, which allows an inversion also after the start of the stimulated emission process. In a true four-level laser system, level (1) is far above the ground state,

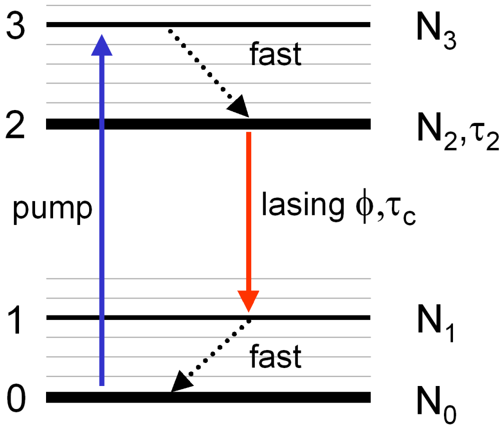

Figure 3.7: Energy levels and transitions in a 4-level laser system

which prevents a population by thermally excited electrons. The main advantage of the four-level system is that the transition of stimulated emission is decoupled from the ground state population. This increases the efficiency of the system in comparison to a three-level scheme, which does not contain the terminal laser level (1).

Laser operation will start if the gain created by the inversion overcomes the losses within the resonator. Thus, the oscillation condition for the laser wavelength λ_0 of a dye laser with an active organic medium of the thickness d between two mirrors with the reflectivities R can be written as

$$R(\lambda_0)\exp[(\sigma_{SE}(\lambda_0)N_2 - \sigma_a(\lambda_0)N_0)d] \geq 1. \tag{3.11}$$

Here, σ_{SE} represents the cross section of the absorption and σ_{SE} gives the stimulated emission cross section of the active medium. From this equation follows an amplification, when the gain, given by $\sigma_{SE}N_2$, overcomes the losses introduced by the limited reflectivities of the mirrors and the intrinsic absorption of the active medium. The stimulated emission cross section of an emitter with Gaussian spectral line shape is given by [112]

$$\sigma_{SE}(\lambda_0) = \frac{\lambda_0}{4\pi n^2 \tau_2 \Delta\nu}\sqrt{\frac{\ln 2}{\pi}}, \tag{3.12}$$

where n is the refractive index of the emitter, τ_2 represent the spontaneous emission lifetime of level (2) and $\Delta\nu$ is the spectral width of the transition from level (2) to level (1), which usually resembles the fluorescence spectrum of the emitting dye. Organic laser dyes exhibit a very high stimulated cross section of $\sigma_{SE} \approx 10^{-16}\,\mathrm{cm}^2$ [113], which is several orders of magnitude higher than in other solid state lasers (Ti:sapphire laser: $\sigma_{SE} \approx 4 \times 10^{-19}\,\mathrm{cm}^2$) [112]. These high values allow a very short gain length, which makes organic dyes a favorable active medium for microlasers. In VCSELs, the high reflectivity of dielectric mirrors can additionally reduce the length of the active zone. Another advantage of organic laser materials is the Stokes shift, which spectrally divides the absorption and emission bands. This effect significantly reduces the reabsorption of stimulated emitted light and therefore diminishes the losses within the laser medium. The disadvantage of organic dyes is the comparably short lifetime τ_2, which reduces the number of excited states N_2 in this level very quickly. This has to be overcome by a fast and intense pump mechanism, as for example with pulsed laser systems.

The dynamics of a coupled multilevel laser system is modeled by a set of differential equations [22]. In the simplest model, two rate equations describe the temporal behavior of the excited state population and the number of stimulated emitted photons of the laser by

$$\dot{N}_2 = R_p - B\phi N_2 - \frac{N_2}{\tau_2}, \tag{3.13}$$

$$\dot{\phi} = \Gamma B\phi N_2 - \frac{\phi}{\tau_c}. \tag{3.14}$$

In the first equation, the number of electrons in the excited laser level (2) is increased by an external pumping from the ground state via level (3) into level (2) with the rate R_p. This population decreases by two mechanisms: the spontaneous emission with a rate inverse proportional to the lifetime τ_3 of the electrons in level (3), and the stimulated emission, which depends linearly on the number of photons ϕ at the laser wavelength and the Einstein coefficient B for the stimulated laser transition. In the second equation, the same term is extended by the optical confinement factor Γ, which gives the fraction of stimulated emitted photons within the active medium. The first term describes the increase of the stimulated emitted photons in the cavity. A cavity photon lifetime τ_c is applied to describe the loss rate of the photons. This photon lifetime contains all loss mechanisms in the laser cavity as limited mirror reflectivity, absorption and scattering.

This simple rate equation set is the basis for the analysis of laser dynamics and has to be extended, if it should include, e.g., a time-dependent pump rate, spectrally broad spontaneous emission or saturation effects. Nevertheless, even in its simplest form, it describes a number of laser systems with reasonable precision.

4 Materials and experimental techniques

4.1 Sample preparation and characterization

4.1.1 High-vacuum layer deposition

Most of the samples investigated within this thesis are entirely fabricated in a high vacuum chamber[1] (Fig. 4.1). The dielectric layers are produced by reactive electron-beam evaporation. This technique is adaptable for a large number of metals and dielectric materials and is widely used in commercial optical thin film production. An electron-beam evaporator[2] with a four pocket crucible enables the exchange and thus the alternate deposition of different materials. Here, an electron-beam is accelerated by a high voltage of 8 kV and guided into the crucible, where a target is heated by absorbing the kinetic energy of the electrons. In the water-cooled crucible, target temperatures above 2000°C are achievable. Target temperatures and thus the evaporation rate of the source are controllable by the e-beam current. A deflection unit enables the adjustment of different beam patterns for a position dependent control of the evaporation. To obtain layers with a high optical quality, oxide layers are generally deposited with a low evaporation rate of 2 Å/s at an oxygen partial pressure of 2×10^{-4} mbar. At this O_2 pressure, the mean free path of the evaporant is equal to the crucible-substrate distance, which results in a reoxidation of monoxide and pure metal remnants. With this reactive process, the absorption especially of TiO_2 films is drastically reduced.

Optically polished 4 mm thick glass plates are used as standard substrates. For surface cleaning several approaches are evaluated. As the best procedure appears the ultrasonic bath in a water solution of the detergent Extran with subsequent drying under a nitrogen jet. Another cleaning method with the polymer OptiClean reduces the adhesion of optical films remarkably and is therefore no more applied. The layers

---

[1] LAB 500 EB by Leybold Optics GmbH

[2] ESV-14 by Leybold

are deposited at ambient substrate temperature, where the substrate is heated by the radiation from the evaporator only. During a fabrication cycle of a DBR, the glass temperature increases up to 150°C. Deposition rate and thickness control of the layers are performed by quartz crystal frequency measurements and an optical setup permitting in-situ reflectance detection for accurate optical thicknesses.

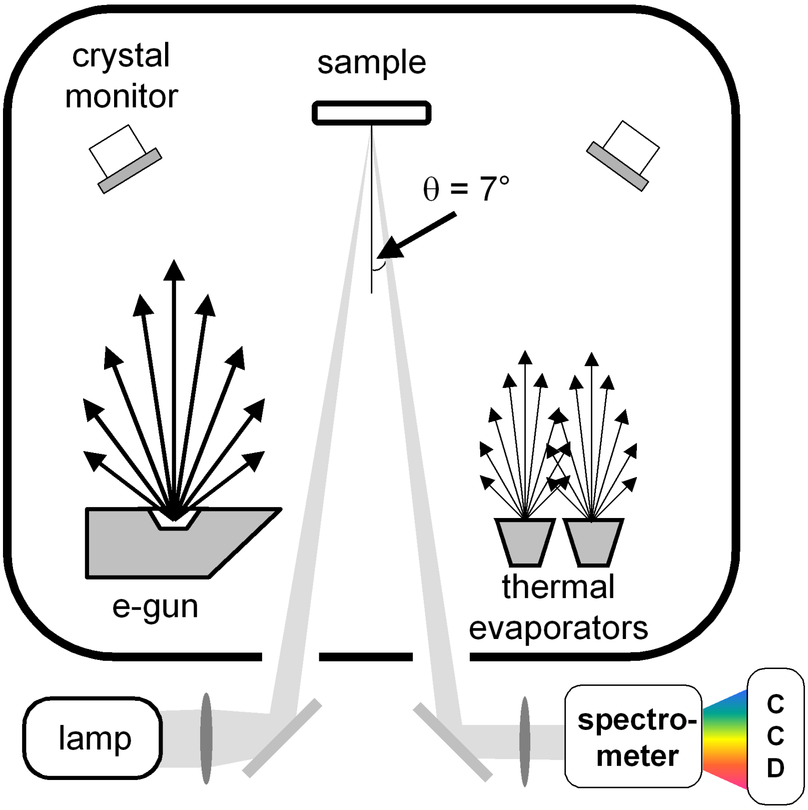

Figure 4.1: The vacuum chamber for the optical thin film fabrication. An electron-beam evaporator and several thermal sources are applied for the production of dielectric and organic films. Separate temperature and rate control enable the co-evaporation of different materials for mixed layers as solid state solutions of organic dyes in an oxide matrix or doped organic films. The evaporation rate and film thickness are controlled by quartz crystal monitors and an optical setup, which detects the sample reflection in-situ.

4.1.2 DBR materials SiO_2 and TiO_2

There exists a wide range of oxides, nitrides, fluorides and other materials that are used in optical thin film production [114]. The combination of SiO_2 and TiO_2[3] is preferred as it combines one of the largest achievable refractive index ratios $n_{TiO_2}/n_{SiO_2} = 1.5$ in the visible spectral range, with a low absorption, the main

---

[3] Prof. Feierabend GmbH Bochum, material purity: 99.997 % SiO_2, 99.9 % TiO_2

criterion for interference filter fabrication. Both materials allow a high optical quality with low porosity and absorption, good laser damage threshold, are compatible to e-beam evaporation, and cost-efficient.

The sublimation character of SiO_2 evaporation complicates the rate control and the thickness homogeneity due to a variable vapor distribution [114]. Figure 4.2 depicts the two mechanisms that reduce the process performance. With a variation of the electron-beam position, the distribution of the evaporant changes significantly. Such a periodic beam oscillation is unavoidable, since it keeps the surface of the SiO_2 target homogeneous during the evaporation process. Nevertheless, this technique produces grooves in the heated area, which influence the evaporation coil permanently. Exemplarily, a tunnel in the target results in an increase of the deposition rate directly above the crucible and a reduction for the other angles. This behavior is not observed in the TiO_2 evaporation, where a melting of the material provides a flat target surface resulting in uniform process conditions. Beside this disadvantage, the amorphously structured SiO_2 coatings exhibit only a slight variation in refractive index and absorption and a low sensitivity to parameters as, for example, oxygen pressure, substrate temperature, and process time. Because of this behavior, SiO_2 is in combination with a precise film thickness control a reasonable candidate for the low refractive index coating material.

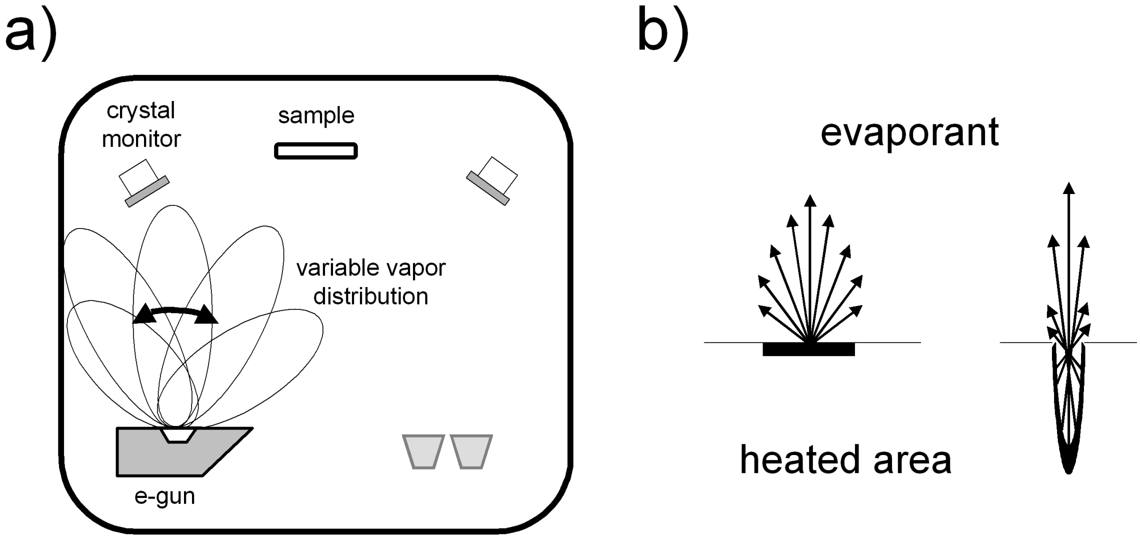

Figure 4.2: Mainly two effects hinder the homogeneous deposition of SiO_2 by electron-beam evaporation: the variation of the evaporant distribution with position of the e-beam (a) and a change in the target geometry with proceeding process time (b). [114]

A well-suited material for the high refractive index counterpart is TiO_2, featuring a higher melting point. In nature, TiO_2 appears in three different crystallographic phases: rutile, anatase, and brookite. Electron-beam evaporated films usually consist of the metastable anatase phase at process temperatures below 300°C with an increasing fraction of rutile in films grown at higher substrate temperatures [115–117]. In contrast to SiO_2, physical vapor deposited TiO_2 shows a refractive index variation during the deposition process even under constant conditions [115, 118]. Ellipsometric measurements on single layers yield an n_{TiO_2}-ascent of $10 - 15\%$ in the visual range within the first three evaporation cycles (Fig. 4.3). In further evaporations of the same starting material, the refractive index of the coatings stays constant. It is assumed that the target melt of TiO_2 needs a certain time until an equilibrium between the outgassing and reoxidation rate is achieved and stable results could be obtained. For this reason, we melt new target material under process conditions for a time of more than 10 minutes before applying this material in the sample production. As already mentioned, evaporated films of TiO_2 offer a number

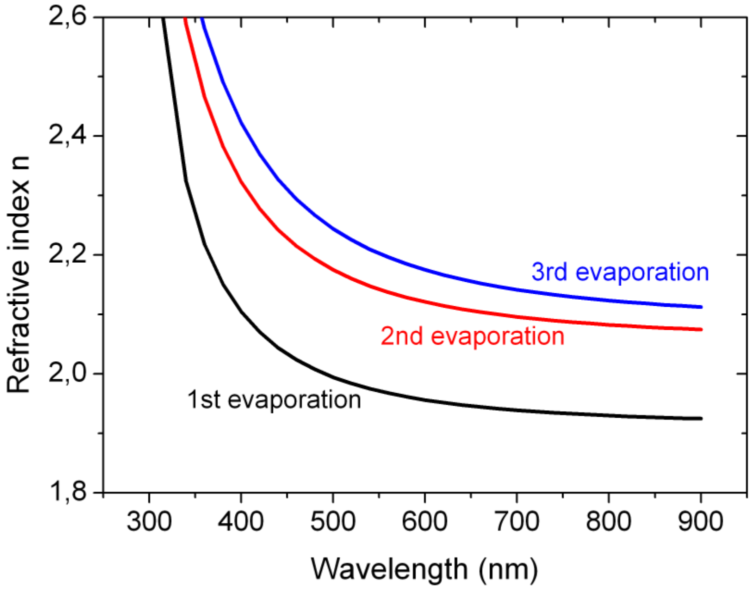

Figure 4.3: Refractive index variation of electron-beam evaporated TiO_2 with number of evaporation cycles.

of optical and structural advantages, which are desirable in interference filter coatings. In spite of this advantages, many process parameters influence the fabrication results. For instance, the refractive index of TiO_2 also depends on the starting material [115, 118–120], deposition technique [121, 122], sample position [120], O_2 partial pressure [115, 118, 120, 121, 123–128], substrate temperature [115, 119–121, 129], substrate material [124, 126], deposition rate [115, 120, 121, 125, 130], relative humidity [131], and annealing after preparation [128, 129, 132]. The dependence on numerous parameters requires an accurate control of the process variables. In order to guarantee a reasonable reproducibility, the parameters shall be kept constant. We have evaporated several layers with thicknesses between 50 and 200 nm on silicon substrates and investigated their optical properties with an ellipsometer in order to determine the optical constants of the fabricated films. Subsequently, the results are modeled by the Film Wizard thin film software. For the fitting procedure of the refractive index n and the extinction coefficient k, we apply the empirical Cauchy model for SiO_2, with

$$n = A_n + \frac{10^6 B_n}{\lambda^2} + \frac{10^{12} C_n}{\lambda^4} \tag{4.1}$$

$$k = A_k + \frac{10^6 B_k}{\lambda^2} + \frac{10^{12} C_k}{\lambda^4} \tag{4.2}$$

and the Cauchy exponential model for TiO_2, where n is again defined by Eq. 4.1 and

$$k = A'_k \cdot exp(B'_k(\frac{1239.8\,\mathrm{nm}}{\lambda} - C'_k)). \tag{4.3}$$

A_n, B_n and C_n are the Cauchy coefficients of the real and A_k, B_k, C_k, A'_k, B'_k and C'_k the Cauchy coefficients of the imaginary part of the refractive index. The dispersion curves and coefficients for the electron-beam evaporated SiO_2 and TiO_2 films are given in Fig. 4.4. Within this framework, these values are used in the transfer-matrix modeling of fabricated DBRs and microcavities.

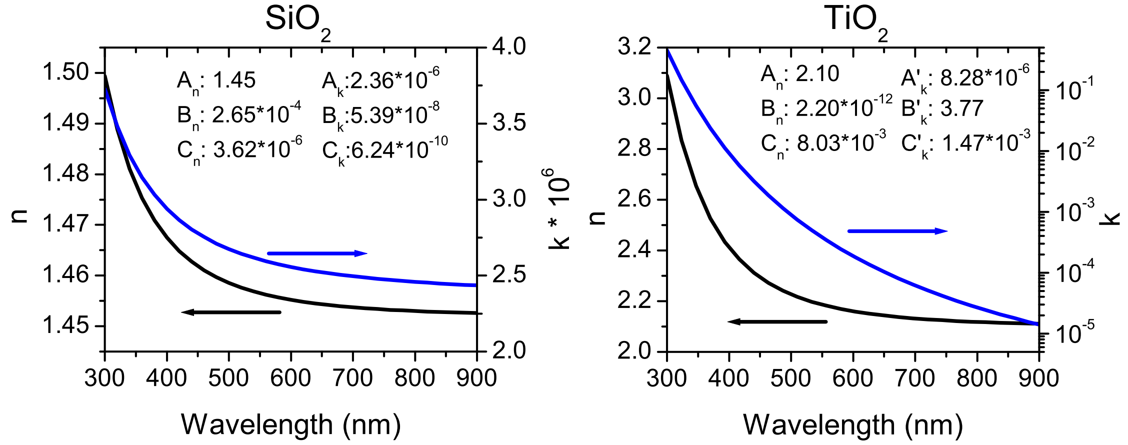

Figure 4.4: Dispersion curves of the real part n (black) and the imaginary part k (blue) of the refractive index for electron-beam evaporated SiO_2 and TiO_2 on Si as obtained by ellipsometry. Coefficients of the Cauchy fit for SiO_2 and exponential Cauchy fit for TiO_2 are given in the inset, respectively. Films deposited with 2 Å/s at 2×10^{-4} mbar O_2 pressure on ambient temperature silicon substrates

4.1.3 Layer thickness monitoring

The standard technique for thickness measurement in vacuum deposition processes is relying on the frequency change of oscillating quartz crystals. The eigenfrequency of the quartz, which is standardized to 5 or 6 MHz, decreases with film growth. With a knowledge of the film density, this variation gives an accurate value for the layer thickness. The error is given by the manufacturer with ± 0.5%. As described in Sec. 4.1.2, layer density and refractive index can vary during the fabrication process. Therefore, mass detection performed by a quartz crystal allows no conclusion about the optical thickness, which is the most important parameter of optical thin films.

In microcavity production, an accurate knowledge about the optical thickness is essential and cannot be provided by the quartz crystal method. In order to achieve exact QWOT in the DBRs and even-numbered multiples of QWOT in the cavity layer, an optical measurement is required. During the course of this work, an optical setup has been installed to measure in-situ the reflectance spectrum (Fig. 4.1). A halogen lamp spectrum is reflected by the growing layer, spectrally resolved by a monochromator, and recorded with a optical multichannel analyzer. Here, the detection of a spectrum justifies the higher expenses in comparison to a single wavelength system, consisting of a laser and a photo diode. Our optical system enables the fabrication control over a wide range of design wavelengths of the structure and is independent from an absolute measurement of the reflectance, since the spectral shape is monitored.

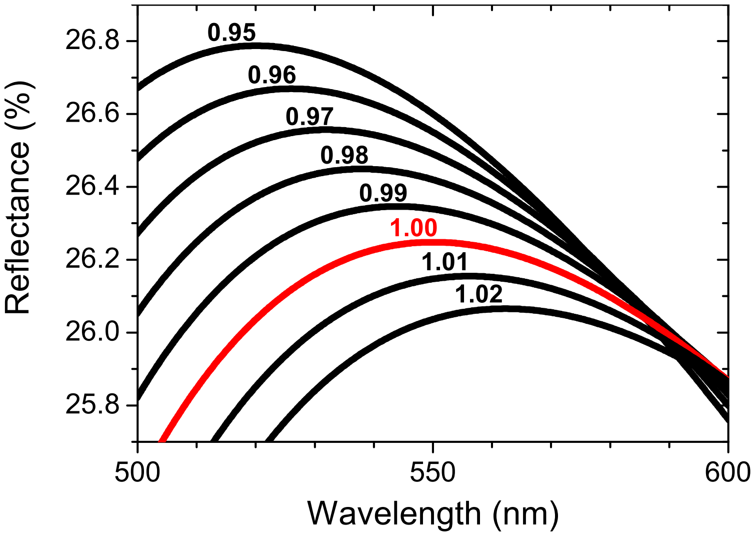

Figure 4.5: Reflectance calculation of a single layer of TiO_2 on glass with changing optical thickness. The design wavelength is 550 nm and the reflection angle 5°. Quarter wave optical thickness is varied from 0.95 to 1.02.

The setup records the differential reflectance $\Delta R/R$, which compares the reflection of the sample R and the substrate R_{sub} by

$$\frac{\Delta R}{R} = \frac{R - R_{Sub}}{R_{Sub}}. \tag{4.4}$$

The reflection spectra are compared with transfer matrix calculations in order to conclude the actual layer parameters. When depositing a higher index layer onto the substrate, high accuracy can be achieved by observing only the maximum wavelength of reflection. The position of the peak is moving towards longer wavelengths during the deposition. Fig. 4.5 shows the variation of the reflectance maximum for different QWOTs of TiO_2 on glass. The spectra exhibit a wavelength change of 40 nm at a QWOT variation from 0.95 to 1.02. A precision of ± 1 % in the QWOT can be obtained, since the setup provides a reading accuracy of ± 5 nm for the peak maximum wavelength. To keep this high precision when growing a multilayer stack for a DBR or a microcavity, it is favorable to measure the reflectance not directly on the sample, but on a separate interchangeable substrate. With increasing number of $\lambda/4$-layers, the reflectance behavior becomes more structured, the stop-band forms, and a position variation of the reflectance maximum is not observable anymore. Experiments and transfer matrix calculations show that after six $\lambda/4$-layers TiO_2/SiO_2 the sensor has to be replaced.

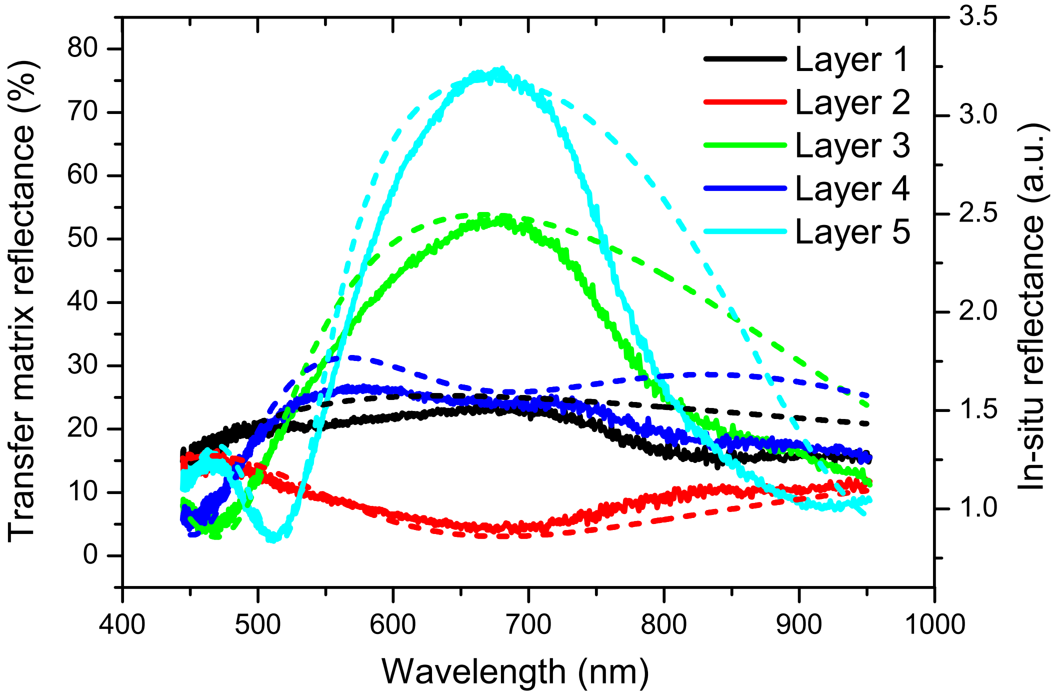

Figure 4.6: Comparison of reflectance calculation (dashed) and in situ measurement (solid) of a DBR designed for 630 nm and 7° angle of incidence. Plotted are the first 5 layers of the mirror starting with a $\lambda/4$-layer of TiO_2. With the growth of a high refractive index layer, the reflection around 630 nm increases, to decrease again with the following low index layer. During the fabrication process, the development of the maxima and minima around the design wavelength is observed. The deposition of one layer is stopped when these points coincide. As the figure depicts, the installed system provides a good coincidence with the simulation in the peak position and an acceptable overlap in the relative intensities.

Figure 4.6 shows measured reflectance spectra of first DBR layers in comparison with a transfer matrix calculation. In the range from 450 nm to 700 nm, experiment and model concide in spectral shape and intensity. The graph also depicts the oscillation in intensity at the design wavelength in dependence of the layer number. With the first high refractive index layer, the reflectance grows. The deposition of this layer is stopped when the peak position in the measurement achieves the calculated maximum wavelength. During the deposition of the next layer, low refractive SiO_2, a minimum enters the spectrum from the blue side of the spectrum and shifts towards longer wavelengths. Again, the process is finished, when the peaks coincide. After the coating with two alternating $\lambda/4$-layers, the reflectance at the design wavelength is below the value after the first layer. In the deposition of layer 3, the spectral behavior is similar to that in the first layer growth. However, with the fourth layer, the spectral behavior becomes complicated, since the reflectance changes are not as distinct as before.

After six layers, the reflectance spectrum looses its sensitivity to small thickness variations and the optical sensor has to be replaced. An exchange is easily performed by rotating the sensor holder, to turn a previously covered glass substrate into the detection beam. This technique allows for an optical thickness control in processes independent from the total number of single layers. During the optical thickness monitoring, the quartz oscillation method is used for evaporation rate control and provides an orientation for the film thickness. If the final layer thickness values from the quartz crystal stay constant over a number of evaporation cycles, the quartz crystal method can be used instead of the optical system. This procedure is allowed, since after about 10 or 15 cycles the process parameters approach a constant level and the ratio optical thickness/physical thickness stays equal.

4.1.4 Structural properties

The structure of optical thin films deposited by the process of thermal evaporation is almost always different from identical materials in bulk form. The properties are mostly sensitive to the process conditions and appear usually in the form of lower refractive index, higher losses, and reduced stability and durability [12].

A useful technique for studying the film structure is the electron microscopy. Already, early investigations have shown the tendency of columnar structure growth of physical vapor deposited films with columns in direction to the source [133–137]. The critical parameter for columnar growth is the substrate temperature, which is usually noticeably below the melting point of materials for optical films. The thermal energy of a molecule evaporated from an electron-beam melt is only about 0.1 eV. On a cold substrate, this energy is immediately lost and the particle rests at the point where it hits the sample. Thus, on substrates kept at room temperature, deposited films exhibit in the most cases a columnar structure [114, 138, 139]. The roughly cylindrically shaped columns grow with diameters from several tens of nanometers up to few micrometers in an approximately hexagonal formation. In TiO_2 films, the columns consist of rutil and anatase nanocrystals [117,140]. The presence of voids in between the columns reduces the film package density and leads to a reduction of the refractive index in comparison with bulk material. The packing density depends on the ratio between substrate temperature and material melting point T_m (Fig. 4.7). At low substrate temperatures, tapered crystallites grow, separated by voids. With increasing substrate temperature, the film density increases towards packed fibrous grains and columnar grains followed by a recrystalized grain structure [114,136,139]. In accordance with this model, for substrate temperatures from ambient to 300 °C, SiO_2 (T_{m,SiO_2}=1470 °C) and TiO_2 (T_{m,TiO_2}=1825 °C) layers may preferably grow in columnar structures with different densely packed grains. Due to the different melting points, the SiO_2 packing density exceeds the density of the titania films.

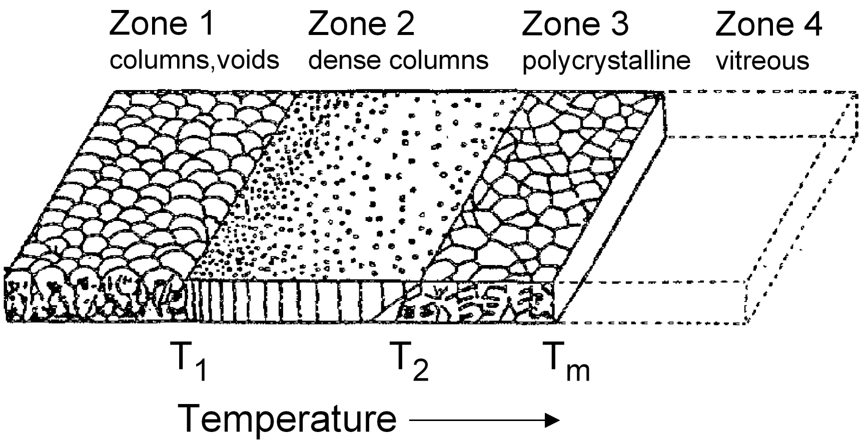

	Zone 1	Zone 2	Zone 3	Zone 4
metals	<0.3 T_m	0.3-0.45 T_m	>0.45 T_m	>T_m
oxides	<0.26 T_m	0.26-0.45 T_m	>0.45 T_m	

Figure 4.7: Coating structure as a function of the ratio of the substrate to melting temperature. Adapted from [139].

Oblique angle deposition of optical thin films forms an oblique columnar structure, where the columnar growth angle β depends on the vapor incident angle α often expressed by a tangent rule [137] (Fig. 4.8)

$$\tan\alpha = 2\tan\beta. \tag{4.5}$$

This formula is used as a handy expression and is successfully applied for samples

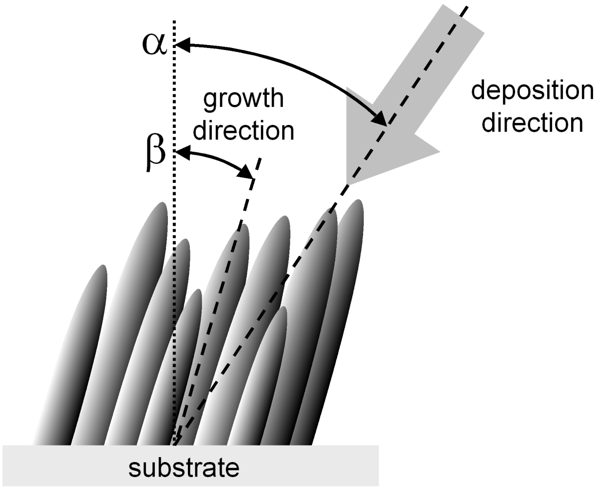

Figure 4.8: Illustration of the columnar growth under oblique angle deposition. The column angle is tunable by a variation of the deposition angle.

prepared with low evaporation rates and limited diffusion after deposition. More general theoretical approaches end up in the tangent rule as a special case [141–144]. In all models and experiments, the columnar angle is smaller than the angle of flux incidence. For conditions used in the experiments presented within this thesis, the tangent rule is sufficient to theoretically express the angle of columnar growth [145]. A three-dimensional simulation is performed with ballistic methods [146] and applied for the modeling of columnar structures, as grown under large flux angles by the method of glancing angle deposition (GLAD) [147, 148]. All models include self-shadowing effects, which means the presence of an at least weakly uneven substrate as a constraint for structural growth. In case of a flat substrate, the first layers of the film grow with an amorphous structure and columnar growth is prevented. This has been studied on TiO_2 grown on Si (001), where the first approximately 20 nm thick layer shows a much lower refractive index as following coatings [140].

In combination with columnar growth, an optical anisotropy is present in the deposited layers. Applying a simple geometrical model, which assumes equally sized columns, the cross section parallel to the substrate surface gives ellipsoids. Along the major and the minor axis of this ellipses, the layers exhibit a different refractive index leading to a birefringence. This model assumes an effective medium consisting of columns of bulk material and voids of low refractive index media as air, water or vacuum. It can thus be described as a metamaterial, since the column diameter is below 100 nm and thus significantly smaller than the wavelength of light. With an increasing columnar angle, the ratio between the axes of the ellipses becomes larger and the birefringence is more pronounced. The resulting angle dependence of the birefringence is experimentally confirmed for several metal oxides and deposition conditions [144, 149–153]. The refractive index along the columnar growth direction is also weakly influenced by the deposition angle and decreases with increasing flux angle [149–151]. A thin film consisting of oblique columns exhibits different refractive indices for all three spatial directions. As a consequence, the Fresnel formulas presented in Sec 2.1 for isotropic media are not valid. The formulas for p-polarization have to be replaced by more general expressions [150, 154] since the refractive indices for the normal and in-plane components contribute to the optical behavior for non-perpendicular angles of incidence.

4.1.5 Organic dye system Alq$_3$:DCM

The organic dye composite of tris-(8-hydroxyquinoline)-aluminum (Alq$_3$) molecularly doped with the laser dye 4-(dicyanomethylene)-2-methyl-6-[p-(dimethylamino)-styryl]-4H-pyran (DCM) was first applied in OLEDs as a doped electroluminescent layer [155] and later applied as one of the first active materials for organic solid state lasers [54, 104, 107, 156–162]. Because of its relatively low lasing threshold [158] in comparison to other dye compounds, it is still after 10 years a favorable laser system and under extensive investigation.

The chelate Alq$_3$ belongs to a stable class of organic metal complexes [163] and was therefore applied in the first OLED [97]. In connection with thermal and photostability, Alq$_3$ combines good electron transport properties with a high photoluminescence quantum efficiency of about 30% [164]. The maximum absorption of Alq$_3$ is located in the ultraviolet spectral range with one peak close to the visual range at around 400 nm (Fig. 4.9). In emission, it exhibits fluorescence as well as phosphorescence [165–167] with maximum peak positions at 530 nm and 730 nm, respectively. In thin films grown by physical vapor deposition, the molecules occur in two different geometrical isomers: the facial (fac) and the meridional (mer) which are defined by the configuration of the hydroxyquinoline ligands [168–170]. The mer-isomer is more stable and dominates in the layers, whereas the fac-phase shows a larger band gap with a slightly blue shifted emission. Four different crystalline phases have been observed so far, which explains the amorphous structure of evaporated films. It also accounts for the good performance and thermal stability, where recrystallization is retarded by the coexistence of several phases.

The dopant DCM is a very efficient arylidene laser dye and is preferably applied in liquid solution for organic lasers [113, 171, 172].

As observable in the absorption and emission spectra, the electronic properties of Alq$_3$ and DCM make them a favorable compound for the creation of a four level laser system. The Alq$_3$ emission and DCM absorption exhibit a large spectral overlap, which is a prerequisite for an efficient Förster energy transfer (also denoted

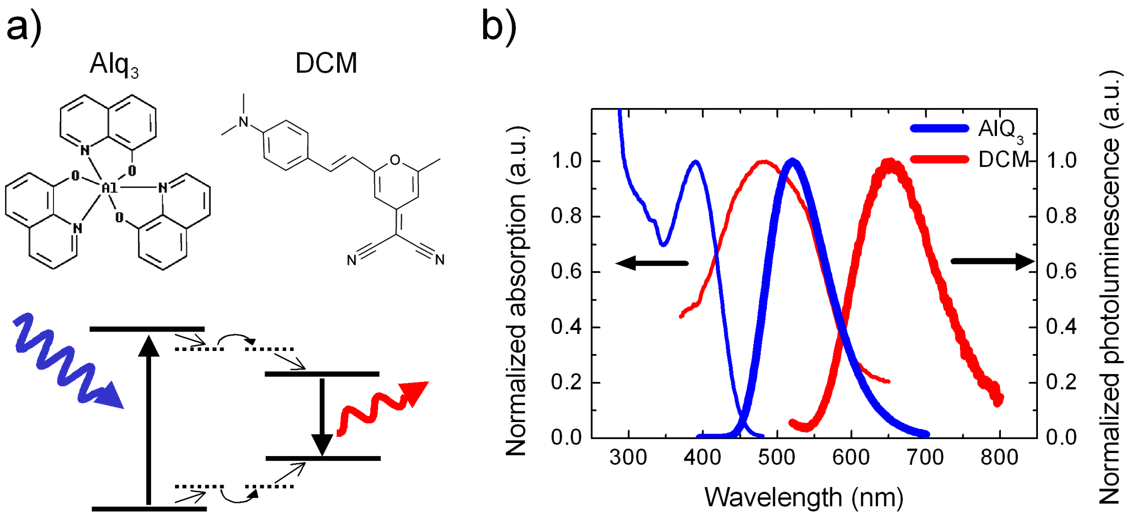

Figure 4.9: (a) The molecular structure of the organic dye molecules Alq_3 and DCM. A compound of both layers operates as a quasi 4-level system: blue light is absorbed by Alq_3 and transferred to DCM. At strong excitation, lasing may occur from DCM. (b) In optical spectroscopy, an overlap of the Alq_3 emission and the DCM absorption is measured, which is a prerequisite for an efficient Förster energy transfer.

as fluorescence resonant energy transfer - FRET). In the laser system, the Alq_3 is applied as the matrix material, which is excited at high energies. In our experiments, we preferably excite it at the absorption maximum at approximately 400 nm. The exciton is, after relaxation to the lowest vibronic level in the excited state, transferred to neighboring molecules via FRET. If the exciton is situated on a DCM molecule, it immediately (in picoseconds) relaxes to the lowest vibronic level of the excited state. In case of a low DCM concentration, where the Förster radius is larger than the distance between the DCM molecules, a further resonant energy transfer is impeded and the emission occurs on the DCM. Due to the long excitation lifetime of Alq_3 of circa 20 ns [155, 173–175], FRET is a very efficient process and nearly all excitons created on Alq_3 are rapidly (τ_{tr}=19 ps [56]) transferred to DCM. Independent studies yield a Förster radius for the transfer from Alq_3 to DCM of about 35 Å [176, 177], which corresponds to a doping ratio of 2 weight% DCM. At this concentration, the external quantum efficiency is maximized and the lowest lasing threshold at room temperature is observed [157].

The optical constants of the compound are mainly defined by the Alq_3 molecules. In the emission range of Alq_3 and DCM of 500-700 nm, the refractive index exhibits a slight dispersion and a weak dependence on the fabrication conditions [178, 179]. The experimental results of refractive index determinations vary in literature with $n_{\mathrm{Alq_3}} = 1.68\text{-}1.73$ [164, 180–183]. For the modeling of our laser structures, we use the value of $n_{\mathrm{Alq_3}} = 1.72$ in the transfer matrix calculation [184]. The addition of

2% DCM to the $\mathrm{Alq_3}$ matrix changes the refractive index due to the increased attenuation value k in the DCM maximum absorption region from 500 to 600 nm. Measurements at a mixed layer result in an index variation of the compound with $n_{\mathrm{Alq_3:DCM}} = 1.70\text{-}1.75$ at 500-700 nm [185]. Assuming this property, we model the compound with the same optical constants as the pure $\mathrm{Alq_3}$ film.

A main advantage for the microcavity fabrication is the high thermal and structural stability of $\mathrm{Alq_3}$ and DCM, which enables the fabrication of double-DBR resonators. Usually, organic dyes are sensitive to the high temperature deposition process of metal oxides by electron-beam evaporation [186]. This fabrication method leads normally to the loss of photoluminescence and electronic properties and is well known in OLED processing, where top contacts are made by the low temperature deposition of metals. The stability of $\mathrm{Alq_3}$:DCM is the basis for the generation of high-Q microcavities for organic VCSELs [56, 187, 188].

4.2 Optical sample characterization

4.2.1 Linear transmission, reflectance and fluorescence

Transmission - fluorescence setup

For angle dependent transmission and fluorescence measurements, we use among other commercial spectrometers a custom-built setup, which provides a high variability. In linear absorption measurements, a halogen lamp is used as light source. For fluorescence detection, different laser sources are available for the sample excitation, providing 532 nm (5 W, cw), 407 nm (3 mW, cw), or 390 nm (~ 50 mW, 80 MHz) wavelength. The sample is fixed on a three-axis stage, for horizonal and lateral movement with micrometer accuracy, and a rotation along the vertical axis. In both regimes, the sample is imaged onto a square slit. This restricts the sample area from which the transmitted light is collected to a small spot of about $100\times100\,\mu\mathrm{m}^2$. Thus, possible averaging due to lateral thickness variations is reduced. The transmitted beam is focused by a second lens onto the entrance slit of a 0.5 m monochromator[4] equipped with a 1200 lines/mm grating. The spectrum is dispersed onto an optical multichannel detector, a thermo-electrically cooled charge-coupled device with a 256×1024 pixel array[5]. The camera is read out by a controller[6] which forwards the spectral data to a computer.

---

[4] Model 500M from Jobin-Yvon

[5] TE/CCD-1024EM/UV detector from Princeton Instruments

[6] ST133 (16Bit) from Roper Scientific

Spectral photometer

In addition to the previously discussed setup, a commercial spectral photometer[7] is applied for the detection of the transmission and reflectance of optical thin films. In this spectrometer, two different light sources enable measurements from 200-3500 nm. The light is guided through a monochromator and split into two beams, where one is usually the sample beam and the other is kept empty as the reference beam. The detected sample area is dependent on the beam diameter and the selected slit width and is in a standard configuration of the order of several square millimeters. With a decreasing detection area, the spectral resolution is enhanced below 1 nm. In the investigation of samples with a position dependence in the optical properties, the large detection area reduces the accuracy of the measurement with a signal reduction and spectral broadening (see Sec. 5.1). Due to the configuration with a monochromator before the sample, also photoluminescence contributes to the signal, which should be considered and accordingly corrected for organic dyes with a high photoluminescence quantum yield.

Fluorescence spectrometer

Photoluminescence measurements which necessitate a high detection sensitivity are preformed by a fluorescence spectrometer[8]. The excitation light from a 150 W xenon lamp is spectrally selected in a Cerny-Turner-monochromator before illuminating the sample. The emission of the investigated material is guided through a second identical monochromator for a corresponding spectral analysis. Each monochromator is tunable from 200-900 nm enabling a spectral resolution of about 4 nm. In the standard configuration, the excitation beam is perpendicularly incident on the sample surface, whereas the emission is detected at an angle of 22.5°. The adequate selection of an edge filter suppresses the detection of excitation light in the photomultiplier tube[9].

For selected experiments with high excitation intensities, we use a He-Cd-laser, which provides emission wavelengths of 325 nm and 442 nm with a maximum output of 10 mW at 442 nm.

4.2.2 Time resolved transmission and emission

Optical experiments with temporal resolution in the picosecond range and faster are usually performed with an up-conversion technique (Fig. 4.10 a). This powerful method relies on the sum-frequency generation from a femtosecond laser pulse and a

---

[7] UV-2101/3101 PC from Shimadzu

[8] Fluoromax from SPEX

[9] R928P, Hamamatsu

second signal in a non-linear crystal. The femtosecond laser beam is therefore split into two beams, the gate and the pump beam. Depending on the experiments, the pump beam is either directly transmitted through the sample or frequency doubled beforehand to pump organic molecules. The temporal resolution results from a mechanical variation of the gate pulse path length and additionally depends on the pulse length. If the pump pulse and the sample signal overlap in space and time in the non-linear crystal the sum-frequency of both pulses is generated. As a consequence, the up-conversion signal is generally plotted as a function of the time delay τ (Fig. 4.10 b). Mathematically, it is the convolution of the sample signal and the gate pulse.

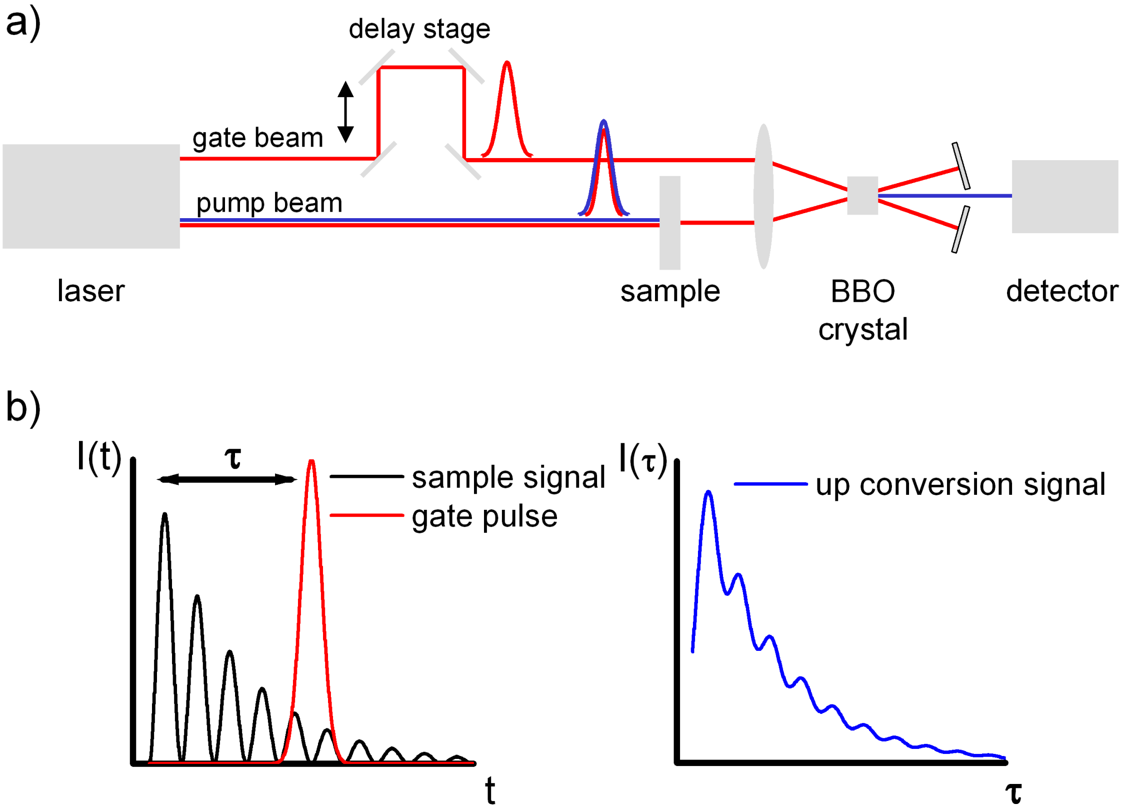

Figure 4.10: Experimental setup for time resolved transmission and luminescence measurements using the up-conversion technique (a). In a non-linear crystal the sample signal is superposed with the delayed gate pulse (b). The resulting up-conversion signal is the convolution of the gate and the sample pulse.

Ultrafast experiments with temporal resolution in the picosecond range are performed with two different laser setups. One system is specifically applied for photo mixing experiments of transmitted light through passive microcavities. By another setup the stimulated emission of organic active microcavities is investigated with lower repetition rate and high pulse power.

For time-resolved transmission measurements, near-infrared laser pulses are generated by a standard Kerr-lens modelocked Ti:Sapphire laser system (Tsunami, Spectra-Physics) which emits 782 nm pulses with a typical duration of around 150 fs and 7 nm linewidth at a repetition rate of 82 MHz. This laser is continuously pumped by a diode pumped Nd:YVO_4 laser (532 nm, 5 W) which is equipped with an intracavity second-harmonic-generation (Millennia, Spectra Physics). The up-conversion of the transmission and the gate pulse is performed by a 200 μm beta-BaB_2O_4 (BBO) non-linear crystal. For the signal detection, the same spectrometer/CCD configuration is applied as for the linear transmission measurements (see Sec. 4.2.1). Therefore this setup allows for the temporal and spectral analysis of the up-conversion signal.

Whereas high repetition rates and low pulse powers enable the successful investigation of passive structures, the analysis of active microcavities requires a different optical setup. The laser threshold of organic VCSELs demands relatively high pulse powers in combination with a low repetition rate, diminishing the bleaching of organic semiconductors. For this purpose an amplifier laser system is used. The light of a diode-pumped and frequency-doubled Nd:YVO_4-laser (Millennia, Spectra-Physics) with 2.2 W continuous-wave output power is used to pump a custom-built mode-locked Ti:Sapphire laser. This laser generates pulses of approximately 70 fs pulse length and 1 nJ pulse energy at a repetition rate of 80 MHz. Its emission is directed into the regenerative amplifier system (Spitfire) as a seeding laser. The amplifier is pumped by a Q-switched Nd:YLF laser (Merlin, SpectraPhysics) that provides 500 ns pulses at 1 kHz repetition rate of an energy of approximately 10 mJ. Finally, the emitted 800 nm amplifier pulses have an energy of 0.7 mJ at a rate of 1 kHz and 200 fs pulse length.

Before exciting the organic microcavity, the amplifier emission is divided in gate and pump beam. The frequency doubled pump light is focussed on the OVCSEL afterwards. After the sample, the emission is spectrally analyzed with a spectrometer/CCD combination with a spectral resolution of 0.05 nm or temporally investigated by up-conversion. The up-conversion signal of cavity luminescence and gate pulse is detected in a photomultiplier tube (R212, Hamamatsu) and electronically filtered by a laser triggered lock-in amplifier (SR 850).

4.3 Microcavity classification

The microcavities investigated within the framework of this thesis are separated into eight classes and can be described by three parameters (Fig 5.1). The first parameter divides the structures in passive and active structures, dependent on the material in the resonator layer. Here, passive microcavities consist of dielectrics and metals only and are investigated by transmission and reflection measurements. This means that all experiments are performed from outside the structure and the influence of the structure on incident light waves is studied. The term ”active” is applied for resonators which contain particles, here organic molecules, which interact with an external field by absorbing and emitting photons. In these cases, the source of the detected light is located inside the microcavity and allows for the investigation of their influence on the emission. The emission behavior is mainly studied in the weak coupling regime, where the cavity field strength is directly connected to the emission rate. Samples working in the strong-coupling regime and forming polaritons are preferably analyzed in transmission.

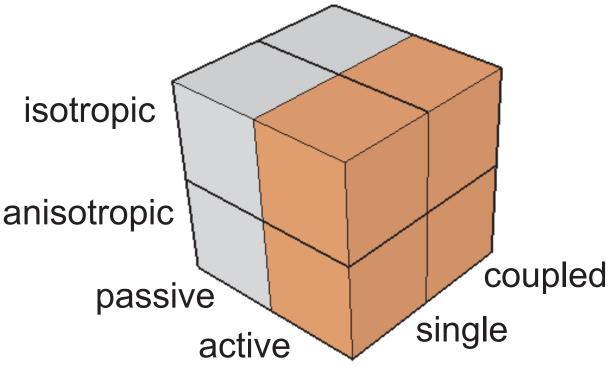

Figure 4.11: Schematic classification of investigated microcavities

A further parameter describes the cavities by the refractive index distribution within the optical thin films. If the layers are considered as isotropic, the optical properties are cylindrically symmetric and equal for every perpendicular incident polarization. Internal structures within the layers can lead to a birefringence and optical anisotropy and the former symmetry is invalid. As a result, resonator modes with different frequencies and orthogonal polarization appear even at normal angles of incidence.

The number of resonator layers within one structure defines the number of resonant modes within the stop band of a microcavity. In a single cavity, one observes only a single mode, whereas in coupled cavities, the number of resonant modes increases and is equal to the number of resonator layers. The number of structure layers is mainly limited by the fabrication process. Thus only coupled cavities with two or three resonators are produced and researched within this work. In coupled anisotropic microcavities with an inverted active resonator layer, four laser modes can be observed in emission.

In the following, the experimental part of this work consists of two Chapters: the first Chapter is focussed on passive structures, followed by a Chapter about active microcavities including organic cavity lasers.

5 Passive microcavities

This Chapter focuses on the results and discussions on passive microcavities. Here, the term "passive" is applied for structures that consist of dielectric layers only. To gain insight into the optical behavior, optical experiments are performed with a light source outside the devices. The influence of the microcavities on linear and time-resolved transmission and reflection measurements is discussed and compared to calculations with transfer matrix and Fourier transform based algorithms.

5.1 Sample uniformity and quality factor

As discussed in the previous Chapters, the main property of microcavities is the development of a resonance in an optically forbidden band. The strength of the resonance is described by the quality factor Q. One way to gain knowledge about the cavity grade is the measurement of the resonance position and linewidth and the following calculation of Q. Nevertheless, for high-Q devices this procedure requires an accurate setup with high spectral and spatial resolution, which is not provided by standard transmission spectrometers. The reasons for this are explained below. A more easily accessible measurement is the transmission or reflection in a wide spectral range around the cavity resonance. The resonance linewidth is a result of the quality of the reflectors, whereas the cavity mode position is mainly influenced by the cavity layer thickness. In contrast to the resonator layer, the modes outside this region are much more sensitive to layer thickness variations in the DBRs and an indicator measurable by low resolution setups. Figure 5.1 shows the transmission spectra of two high quality single and coupled microcavities obtained by the Shimadzu transmission spectrometer, where the spot size is several square millimeters. In the single cavity experiment, the Q-factor of 320 coincides with the theoretical value of the perfect design. A comparison of the peaks outside the stop-band in experiment and calculation exhibits a coincidence in most features as relative peak positions and heights for both the single and the coupled microcavities. Small deviations are caused by thickness or refractive index variations in the experiment or by small discrepancies in the refractive index models. It has to be stated that the calculations are not the result of spectral fittings, but are results of the modeling with the layer refractive index models presented in Sec. 4.1.2. This demonstrates the precise layer deposition of the investigated samples.

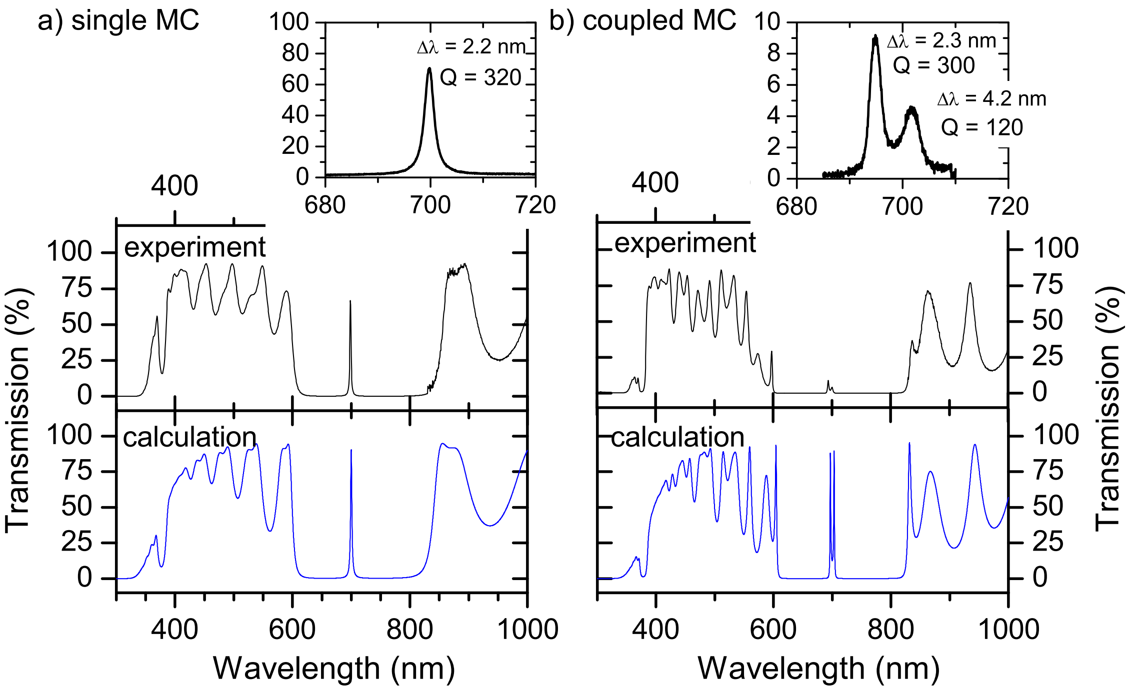

Figure 5.1: Comparison of high quality passive single (a) and coupled (b) microcavities. The designs are 4Gm (T S)5 T 2S T (S T)5 for the single cavity and 4Gm (T S)5 T 2S T (S T)7 2S T (S T)5 for the coupled cavity. The design wavelength is in both samples λ_d = 700 nm and the refractive index of the 4 mm thick substrate is $n_G = 1.52$. The calculation shows the transmission spectra for ideal samples with perfect layer thicknesses and refractive indices as obtained by ellipsometric measurements at single layers. Experimental transmission measurements are done with the Shimadzu spectrometer.

In the measurement of the coupled microcavity, the detected maximum transmission of the cavity modes is far below the expected value close to unity. This is in contradiction to the analogy of calculation and transmission spectra in the off-resonance regions of the spectra, which is a sign of an accurate sample structure. Here, the main reason is the strong dependence on the resonator layer adjustment. Both cavity modes have to be resonant in both $\lambda/2$-layers, a condition which is perturbed already by a small resonator thickness misalignment.

The spectroscopic analysis of the mode structure requires only a moderate spectral resolution in the transmission and reflection measurements. This changes when the determination of the Q-factor is the focus of interest. Its value can be obtained by the measurement of the spectral cavity mode linewidth or the decay time of emitted or transmitted light. As the Q-factor is a characteristic of the number of cavity round trips, it depends mainly on the reflectivities of the two mirrors and on the magnitude of internal losses by absorption and scattering. These losses lead to a homogeneous broadening of the Lorentzian transmission, here represented by the intensity $T(\omega)$ with

$$T(\omega) = \frac{\mu^2}{(\omega_c - \omega)^2 + \gamma^2}. \tag{5.1}$$

In this equation, the light frequency and the cavity mode central frequency are ω and ω_c, respectively, 2γ is the linewidth, and μ^2/γ^2 is the correction factor for the intensity. The Lorentzian signal is additionally broadened in the measurement process. This effect is for example caused by the spot size of the detection setup, where the diameter cannot be infinitely minimized. Material and thickness deviations within the detected area contribute to the broadening. Mathematically, the transmission experiment is described by a convolution of the signal, here $T(\omega)$, and the response function $R(\omega)$ resulting in the finally recorded transmission spectrum $\tilde{T}(\omega)$ by

$$\tilde{T}(\omega) = T(\omega) * R(\omega). \tag{5.2}$$

The choice of the particular response function depends on the experimental setup and the sample properties. During the fabrication process, geometrical deviations may form a wedge shaped structure with a linear change of film thickness or refractive index. In this case, a rectangular response function explains the resulting spectral blurring. For example, a linear thickness variation leads to a linear spectral line shift. As a consequence, Lorentzians with continuous spectral distribution contribute to the transmission process within a certain frequency range. In case of statistical variations in film thickness or refractive index, e.g. layer roughness, a Gaussian is the preferable response function. The influence of the response functions of a wedge shape cavity and of a statistically inhomogeneous system is compared in Fig. 5.2. In this model, the signal Lorentzian with a central frequency of $\omega_c = 1.77\,\text{eV}$ (700 nm) and a linewidth $\gamma = 10\,\text{meV}$ (4 nm) is convoluted with a rectangle function and Gaussian of equal half width (2 % of ω_c or 35 meV). For comparability, the response functions are normalized in order to keep the integrated intensities of the Lorentzian and the convolution result constant. In both models, the transmission modes are significantly broadened, accompanied by a reduction of the peak intensities. The differences in the line shapes are noticeably distinguishable and allow for a determination of the dominating broadening process in real structures.

The influence of different sample fabrication geometries in the same vacuum process is presented in Fig. 5.3. Here, the substrates are placed closest to each other on one sample holder. Then, a set of four coupled microcavities is off-axially produced in the vacuum chamber. This results in an oblique layer deposition and

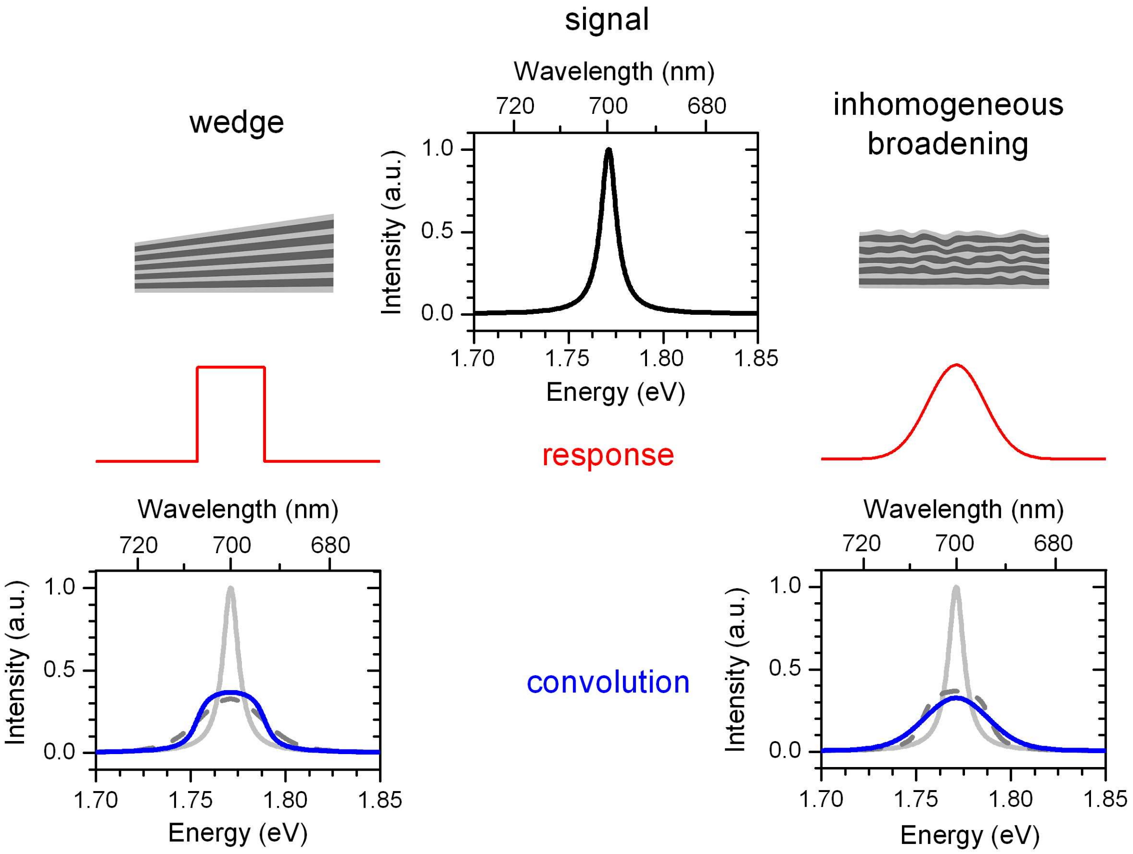

Figure 5.2: The two main effects for spectral broadening in transmission experiments. The local transmission curve is modeled by a Lorentzian (black) with a spectral width of 4 nm. The transmission experiment is explained by the convolution of the signal with a response function (red). In case of a wedge shaped layer distribution the response is a rectangle function. If the layers have statistically distributed thicknesses, the response is assumed to be a Gaussian. Here, the widths of both responses are 2 % of the resonance center frequency. The result of the convolution (blue) shows different spectral shapes and reduced maximum intensities for the two mechanisms.

decreasing layer thickness with increasing flux angle and distance (Fig. 5.3 inset), which is typical especially for electron beam evaporation of SiO_2 [114]. Although the substrates are mounted side by side, the cavity modes and thus the film thicknesses shift by around 10 % over a lateral distance of approximately 5 cm on the substrate holder. The resulting wedge shape in the thickness variation leads to the typical broadening discussed above. With increasing flux angle, the gradient in the thickness variation becomes larger, which is observed in the broadest transmission modes in sample #4. In principle, the real transmission mode $T(\omega)$ is accessible by a deconvolution of the measurement $\tilde{T}(\omega)$. The necessary values of either the linewidth 2γ or the maximum intensity μ^2/γ^2 can be modeled by transfer matrix calculations with small uncertainties for a single cavity. Unfortunately, in a coupled cavity, the mode intensity does not only depend on the system absorption. It is also sensitive on the adjustment of the two resonator layers. Therefore, the deconvolution approach is not applicable for the example presented in Fig. 5.3. Nevertheless, sample #2 exhibits a narrow linewidth and a nearly ideal shape. This indicates a homogeneous film thickness resulting in a measured quality factor of 560. In contrast to the simulations, the experimental cavity modes additionally show an asymmetry, which can be the result of a non-linear wedge gradient and different slopes in orthogonal lateral directions.

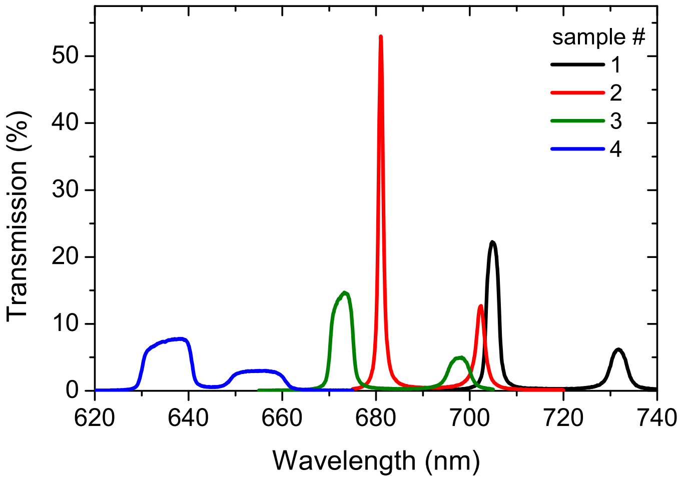

Figure 5.3: Experimental transmission spectra of coupled microcavities with different positions on the sample holder. Layer thickness and strength of the wedge depend on the distance from the evaporation source. The sample distance from the vaporator increases with the sample number. Measured with Shimadzu transmission spectrometer.

In experiments with comparably large spot sizes, the effect of a wedge shape is the dominating broadening process. Only for planar structures and small spot diameters, the Gaussian distribution in the layer parameters becomes the main broadening factor. In this case, the experimental curves have a Voigt function line shape. The strength of the Gaussian contribution is not strongly dependent on the fabrication geometry. In comparison with III-V nitride microcavities [189] the layer inhomogeneity is relatively small as confirmed by transmission measurements. It can be seen in the results of the single cavity in Fig. 5.1, where the experimental and theoretical linewidth agree. The spectral resolution in the experiment is not only connected to the quality of the detector but also to collimation and focus of the illuminant. Although quite extraordinary and not a standard device, a short pulse laser with its broad emission linewidth is the preferable light source [190]. By its coherence, a laser can be focussed into a much smaller spot size than a standard lamp. Achievable laser focus diameters are of the order of the light wavelength and thus at least one order of magnitude below the focal spot of a blackbody emitter.

At this point, it has to be stated that a high layer thickness uniformity is not the aim of this work. For research aspects, non-uniform and wedge shaped optical films have the advantage of a line shift by laterally scanning the sample at a normal angle of incidence. In comparison with the line shift by a variation of the light incidence angle, this technique avoids an offset of the light beam after transmission as it is mainly caused by an optical thick substrate. In reflection experiments, the cavity mode can be positioned within a certain spectral range, facilitating the setup by the fixed observation angle. This is successfully performed in experiments on strongly coupled organic microcavities [67, 68].

5.2 Transmission and angle dependence

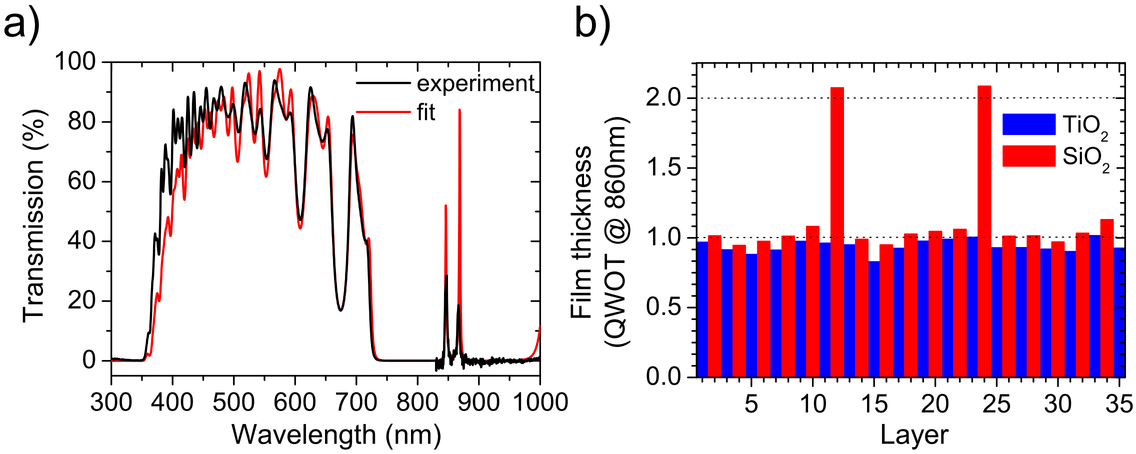

Figure 5.4: Comparison of experimental and fitted transmission of coupled microcavity (a). The sample design is (T S)5 T 2S (T S)5 T 2S (T S)5 T with the design wavelength of $\lambda_d = 860\,\mathrm{nm}$. The layer thickness distribution for the fit result shows small deviations from the perfect quarter and half wave optical thicknesses (b).

Data evaluation of optical experiments requires an accurate knowledge of the sample structure and the optical constants. As presented in Sec. 4.1, the refractive indices of the dielectric materials SiO_2 and TiO_2, determined by ellipsometric measurements, are the basis for the optical modeling. Thus, the remaining parameters are the layer thicknesses. Despite the usually high number of layers, one single optically measured spectrum is adequate for the thickness fitting, if the number of wavelength points exceeds the film number. The spectra are fitted by the Film Wizard thin film software using modified Levenberg-Marquardt and modified Simplex algorithms [191]. Global fitting methods of the respective models and varied starting parameters are applied in order to exclude thepresentation of local minima.

Figure 5.4 a shows the transmission spectrum and the corresponding fit for a 35 layer coupled microcavity. Fit and experiment exhibit a good overlap especially in the spectral range near the stop-band. At shorter wavelengths, the intensity deviates, probably due to differences in the imaginary parts of the refractive indices of the model and the real structure. Nevertheless, the most prominent features as peaks and minima are properly represented. In the specific sample, the high refractive index layers are slightly thinner than quarter wave optical thickness, whereas the resonator layers are thicker than one half wavelength (Fig. 5.4 b).

After fitting the layer thicknesses, the optical spectra of the structure can be calculated for all angles of incidence and both polarizations. Figure 5.5 compares angle and polarization dependent transmission data of the 35 layer coupled microcavity with transfer matrix calculations. It exhibits the typical shift of the mode structure towards higher energies with increasing angle of incidence. Additionally, with higher angles, the transmission intensity of the s-polarized modes is drastically reduced. This effect is also demonstrated in the experiment. For the largest angles, a superposition with p-polarized light transmitted through the polarizer hides the weak structure of the s-polarization. Neglecting this experimental artifact, experiment and theory coincide, which demonstrates the accuracy of the thickness fitting, the optical constants, and the transfer matrix method.

5.3 Time-dependent transmission of short laser pulses

Mathematically, the frequency spectrum of a signal allows for a direct reconstruction of the temporal dynamics of the signal generating system. This relation is usually described by a Fourier transform. The transmission and reflection spectra of a microcavity exhibit Lorentzian shaped resonances. By a Fourier transform of the cavity modes follows the property of a light trap (q.v. Eq. A.7 and A.8). The light is stored within the resonator and leaves the cavity statistically. An exponential intensity decay is observable in a time-dependent measurement. For a corresponding experiment a laser emitting ultrashort pulses is the preferable light source. It fulfills the constraints of coherence and a broad spectral width to excite one or more cavity modes including their wings. Normally, the spectra of ultrashort laser pulses are of Gaussian line shape with a consequential Gaussian temporal intensity evolution. The temporal development of the electric field reflected or transmitted by a structure

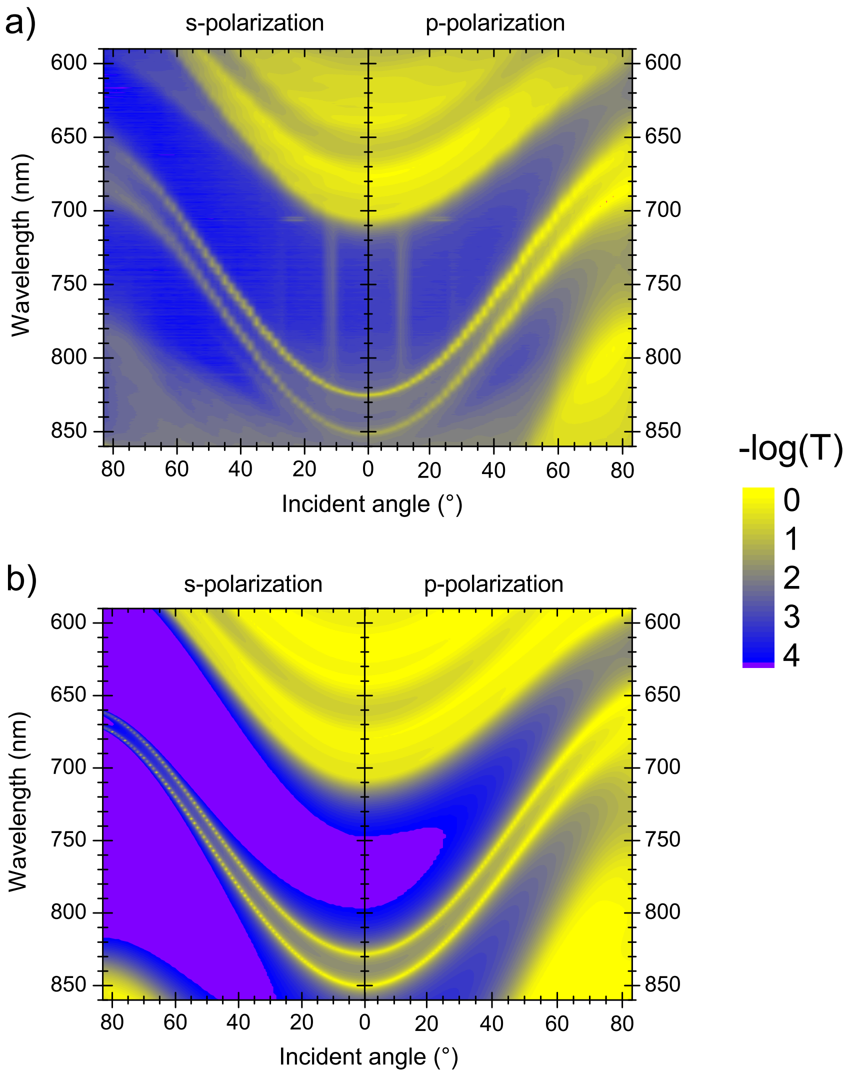

Figure 5.5: Angle dependent transmission of a coupled microcavity for s- and p-polarization. Experimental results (a) are compared to calculations (b) based on a design fit. Sample design as in Fig. 5.4 with different design wavelength due to a shift of the measured sample position.

is given by a Fourier transform with

$$E(t) = \int_{-\infty}^{\infty} \sqrt{I(\omega)L(\omega)}e^{i\phi(\omega)}d\omega. \tag{5.3}$$

Here, $L(\omega)$ is the intensity spectrum of the coherent light source, $I(\omega)$ is the power reflectance or power transmittance of the device, and $\phi(\omega)$ is the phase shift after reflection or transmission. For a planar film structure, $I(\omega)$ and $\phi(\omega)$ can be calculated by the transfer matrix algorithm or measured with a spectrometer and interferometer, respectively.

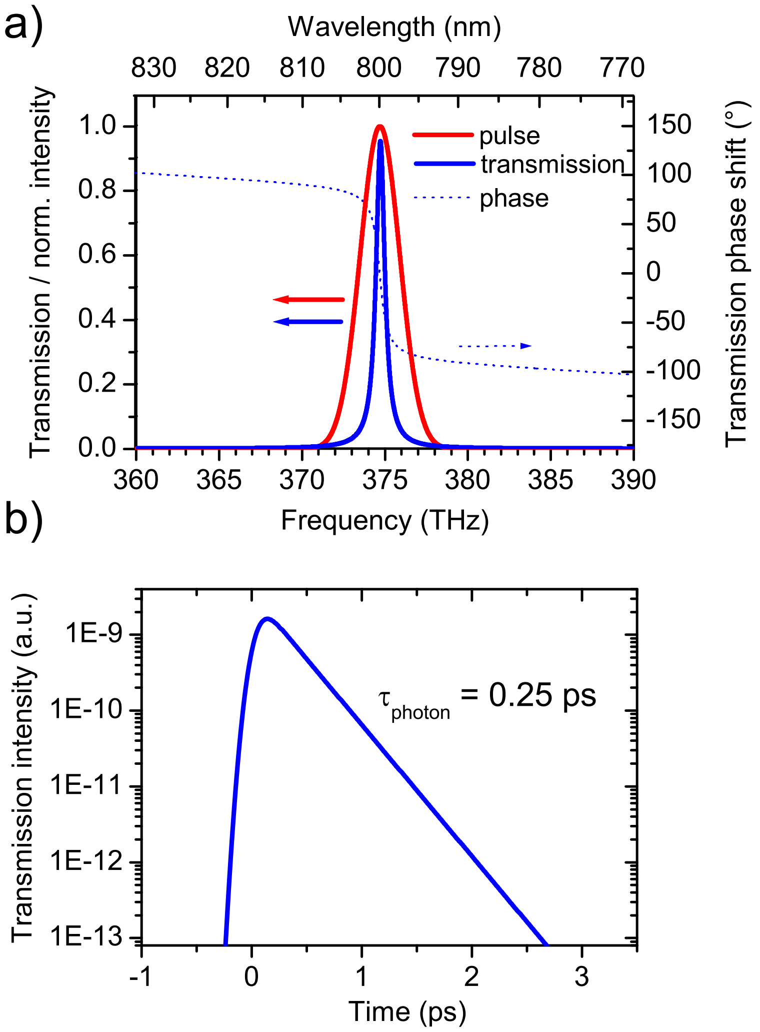

Figure 5.6: (a) Initial values for the calculated temporal transmission through a single microcavity with the structure (T S)6 T 2S (T S)6 and the design wavelength of 800 nm. A Gaussian laser pulse (red) is incident on the microcavity defined by its transmission (blue straight) and phase shift (dotted). (b) The Fourier transform exhibits an exponential decay which coincides with the cavity photon life time.

The Fourier transform approach provides correct results for pulses with several hundred femtoseconds pulse length. The application of a transfer matrix spectrum, which is the solution of continuously incident light, is supported by the penetration time of a DBR with few femtoseconds in metal oxide structures (q.v. Sec. 2.3). After the permeation of light into the cavity, the electric field intensity inside the resonator increases, the typical mode structure develops and the cavity becomes transparent at the cavity mode. For laser pulses that are temporally equal or shorter than the corresponding penetration time, a cavity appears high reflective. Even at the cavity mode frequency, the complete pulse is reflected with a phase delay time τ_r (Eq. 2.44).

Figure 5.6 presents a simulation for a realistic microcavity with a resonance at the design wavelength $\lambda_d = 800$ nm and a Q-factor of 590. Here, a 300 fs long Gaussian laser pulse with a corresponding FWHM of 6 nm at 800 nm wavelength is transmitted through the resonator. The transmitted light intensity increases with a Gaussian shape nearly resembling the temporal beam profile. The zero point in time designates the temporal intensity maximum of the incident pulse and coincides with the maximum of the Fourier transform of the pure pulse. Shortly after the transit of the pulse maximum, the transmission signal starts decaying. In accordance with this statistic process, the light intensity decreases with an exponential slope. The decay time of $\tau = 0.25$ ps coincides with the Q-factor of the cavity (Eq. 2.55).

Figure 5.7 a shows the transmission and phase shift spectra of coupled microcavities with two resonator layers and central DBRs with a different number of pairs. The design wavelength for all samples is again 800 nm and the spectral properties of the laser are the same as for the single cavity simulation. In dependence of the reflectivity of the central DBR, the two cavity modes of each structure are differentially separated. In the case of the strongest coupling between the resonator layers, both modes are widely separated. Therefore, in the thinnest sample, the mode distance is noticeably wider than the spectral laser width. In the Fourier transform of this sample appears a Gaussian time trace with low intensity (Fig. 5.7 b). Mainly, the incident light is reflected from the structure and the modes are not excited by the laser. With moderate coupling in the sample with 6.5 pairs in the central DBR, the outer wings of the laser spectrum enable an excitation of both cavity modes. As a consequence, the transmission decays exponentially with an additional beating. The beating frequency coincides with the spectral distance of the two modes of 5.2 THz. Before exponentially decaying, the intensity exhibits a Gaussian slope, which is based on the transmission of the spectral pulse maximum through the region between the two modes. This behavior also resembles the temporal pulse shape of the laser pulse. In contrast to the thinnest sample, the intensity of the transmitted light is higher since the reflectivity around 800 nm wavelength is reduced. In the spectra of the thickest sample with 9.5 central DBR pairs, the modes show the smallest separation and the laser excites both modes with a high intensity. In the Fourier transform of this structure, the transmission intensity directly exponentially decays after the maximum with a smaller beating frequency than in the former case.

The results of these simulations confirm the usability of the presented algorithm to the temporally model laser pulse transmission in a fast and simple manner. An-

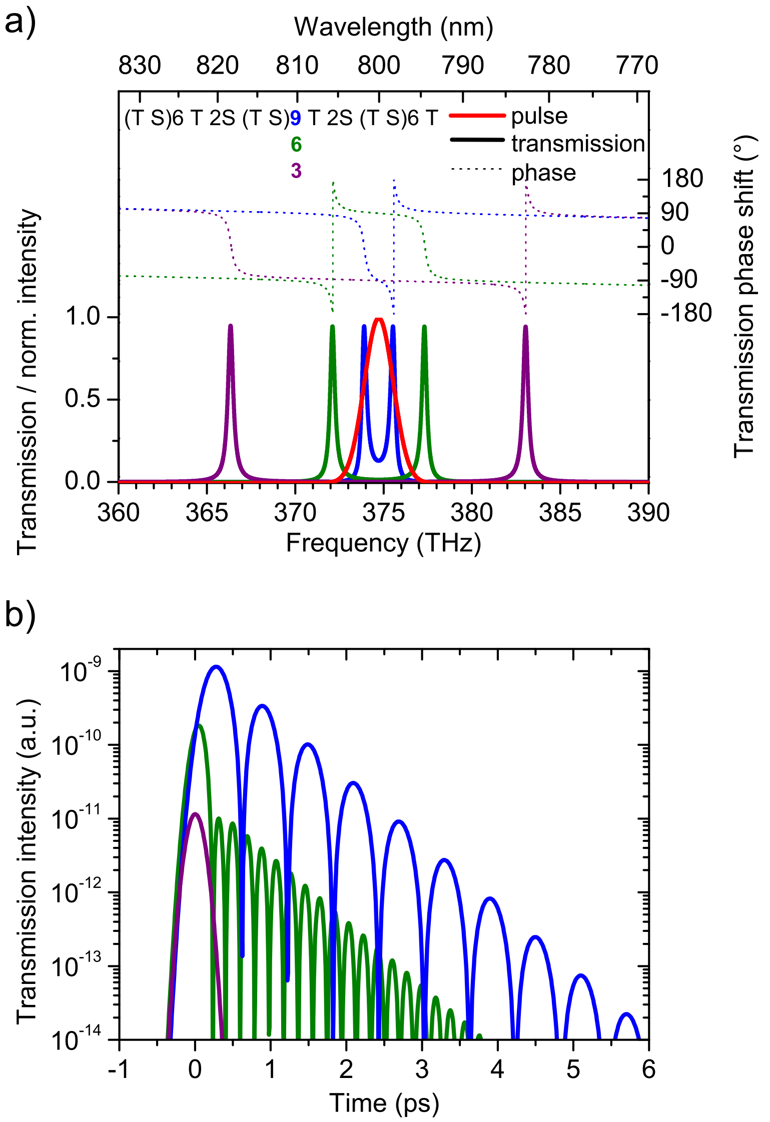

Figure 5.7: (a) Initial values for the calculation of temporal transmission through coupled microcavities with the structure (T S)6 T 2S (T S)n 2S (T S)6 (n = 3,6,9; n. . . number of central DBR pairs) at the design wavelength of 800 nm. The Gaussian laser pulse (red) excites two coupled cavities with their transmission power (straight) and phase shift (dotted). (b) The temporal behavior strongly depends on the central mirror thickness and coupling between the two modes. The Fourier transform exhibits the exponential decay which coincides with the cavities photon life time.

other approach is the finite difference time domain (FDTD) method [192]. Here, for the simulation the layer structure is divided by a grid in a number of isotropic regions. The Maxwell equations are solved time-dependent and separately for each region with dynamically changed boundary conditions. An accurate simulation requires a large number of areas and small temporal steps. This makes the procedure extremely time consuming. In a comparison with the transfer matrix and Fourier transform approach, the FDTD method exhibits comparable results, with a much longer processing time. The advantage of the FDTD algorithm is the application on arbitrary one-, two-, and three-dimensional structures, and the implementation of radiation sources into the device.

5.4 Photonic Bloch oscillations in coupled microcavities

The topic of the work in this Section is the observation of spatial oscillations of the internal electric field in a coupled microcavity. In Sec. 2.5, we have discussed the optical properties of coupled microcavities. In the presence of two and more adjusted cavity layers, the mode structure consists of a number of cavity modes equal to the number of resonators. The alignment of the cavity layers leads to symmetric and antisymmetric modes with different energy. In time, the electric fields of each mode oscillate with another frequency. The interference of the electric field vectors of waves with different frequencies results in a spatial oscillation of the light intensity. The light oscillates between the two cavities with a beating frequency identical to the frequency difference of the participating modes.

Two different designs of coupled microcavities are presented in order to perform time-resolved measurements, which indirectly verify the internal energy oscillation.

5.4.1 Precision requirements and fabrication

Coupled microcavities require a noticeably higher precision in fabrication than single cavities. This is due to the fact that only in symmetric structures, the resonator modes develop a symmetric or antisymmetric distribution of the electric field. In case of slight asymmetries, this behavior is disturbed. In asymmetric structures, the electric field intensity of the two modes is concentrated in opposite cavity layers. This reduces the amplitude of a potential beating, which means that an oscillation of the light between cavity modes is prevented, since both modes are located in another cavity layer and their respective electric fields do not interact.

A usual cavity deposited on a substrate is asymmetric since the ambient material and the substrate have a different refractive index. One can circumvent this problem by a design of the top DBR which deviates from an ordinary mirror with $\lambda/4$-layers. Additional adjusted layers may compensate the phase and amplitude shift from the substrate and the bottom mirror. For the samples presented within this thesis, this technique is not applied. It requires an exact knowledge of the optical parameters of

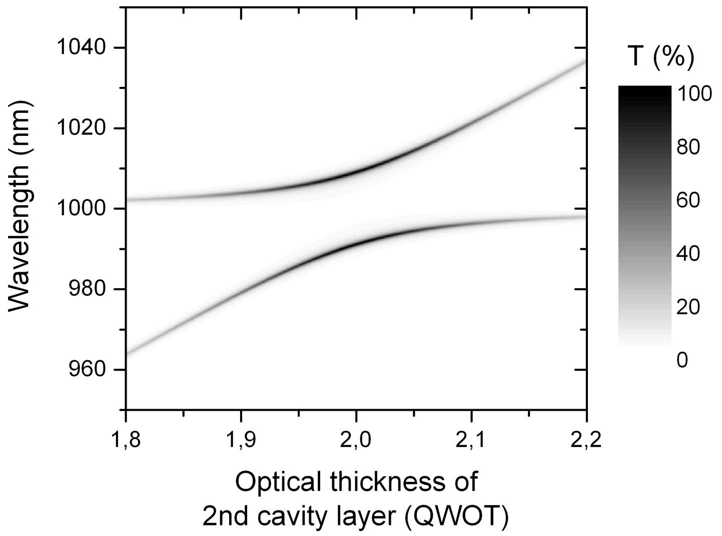

Figure 5.8: Thickness sensitivity of a coupled cavity on the resonator thickness adjustment. Plotted is the transmission of a coupled microcavity with the air embedded design (1H 1L)5 1H 2L 1H (1L 1H)5 2L (1H 1L)5 1H ($n_H = 2.2$, $n_L = 1.45$, $\lambda_d = 1000\,\mathrm{nm}$) in dependence on the optical thickness of the second cavity layer.

all layers, which is not provided by our fabrication method and sample characterization. Another important point for the symmetry is the alignment of the resonator layers. Figure 5.8 depicts the influence of the thickness of one resonator layer on the mode positions and intensities in an otherwise perfectly matched device. If the cavity layer has $\lambda/2$-thickness, the two modes exhibit the smallest mode separation and the largest coupling, which is demonstrated by a maximum transmission. With a variation of the resonator layer thickness, the cavity modes undergo an anticrossing. Already a 10 % thickness deviation from the perfect configuration drastically reduces the maximum transmission of the two cavity modes. This misalignment also doubles the splitting between the modes. In conclusion, a high precision is required in order to achieve the lowest beating frequency with the highest oscillation contrast.

5.4.2 Sample design

For the coupled cavity experiments, two different sample designs are applied. In the first design, the microcavity consists of two $\lambda/2$-layers of SiO_2, which are surrounded by three DBRs. The mode structure at normal angle of incidence is only weakly tunable. However, lateral thickness variations enable a shift of the cavity modes in this monolithic design. The investigated monolithic structure consists of three 5.5 pair DBRs at a design wavelength of about 800 nm.

In a second sample structure, two cavities are directly attached with their surfaces

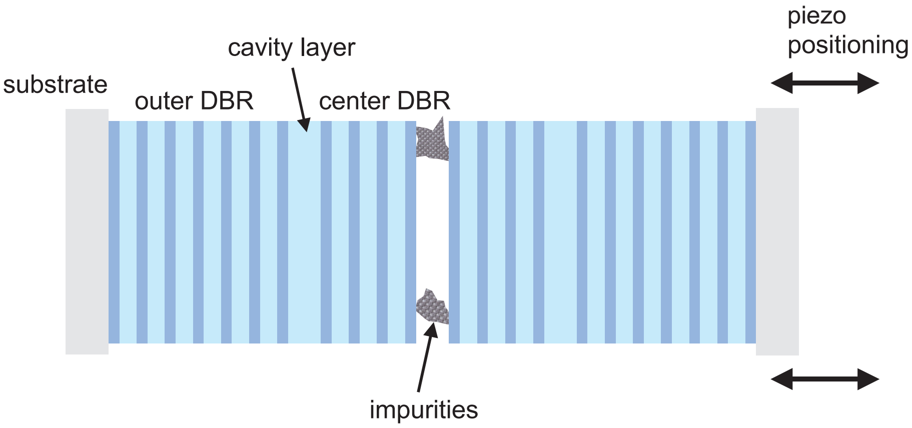

Figure 5.9: Formation of a coupled cavity by direct attachment of two single microcavities. The double-monolithic design allows a mode tuning by piezo motors with submicrometer precision.

(Fig. 5.9). Both cavities are produced in the same fabrication cycle. Therefore, they have nearly identical optical properties. One of the cavities is fixed in the sample mount, whereas the other sample is movable by three piezo motors with submicrometer precision. Both cavities are separated by an air gap that is caused by dust particles located at the surfaces. These particles can have sizes up to about hundred micrometers and limit the minimum distance between both samples. If both parts are aligned, the sample symmetry results in a triple cavity. The two $\lambda/2$-layers of SiO_2 act as cavity layers. Additionally, the two $\lambda/4$-layers of TiO_2 atop the single cavities and the air gap form a third cavity layer.

In the transmission experiments, two cavities with 7.5 pairs in the bottom DBR and 2.5 pairs in the top DBR are directly attached. The mode structure of the double-monolithic design is strongly dependent on the spatial distance of the two parts. Figure 5.10 plots the calculated positions of the cavity modes in dependence on the size of the air gap. In the simulation, either two or three cavity modes contribute to the internal electric field oscillation at gap thicknesses around 1μm. With more realistic distances around $100\,\mu$m, the number of modes is increased and the mode distance is reduced to around 1.3 THz.

5.4.3 Terahertz oscillation

First, we discuss the experiments with the monolithic design. Figure 5.11 depicts the transmission spectrum of the monolithic cavity illuminated by a Ti:sapphire laser. In this experiment, the laser provides an emission line at 818 nm with a spectral width of 15 nm. Two modes are measured after transmission of the laser light through the coupled cavity. With their corresponding spectral positions at 820.3 nm (365.5 THz)

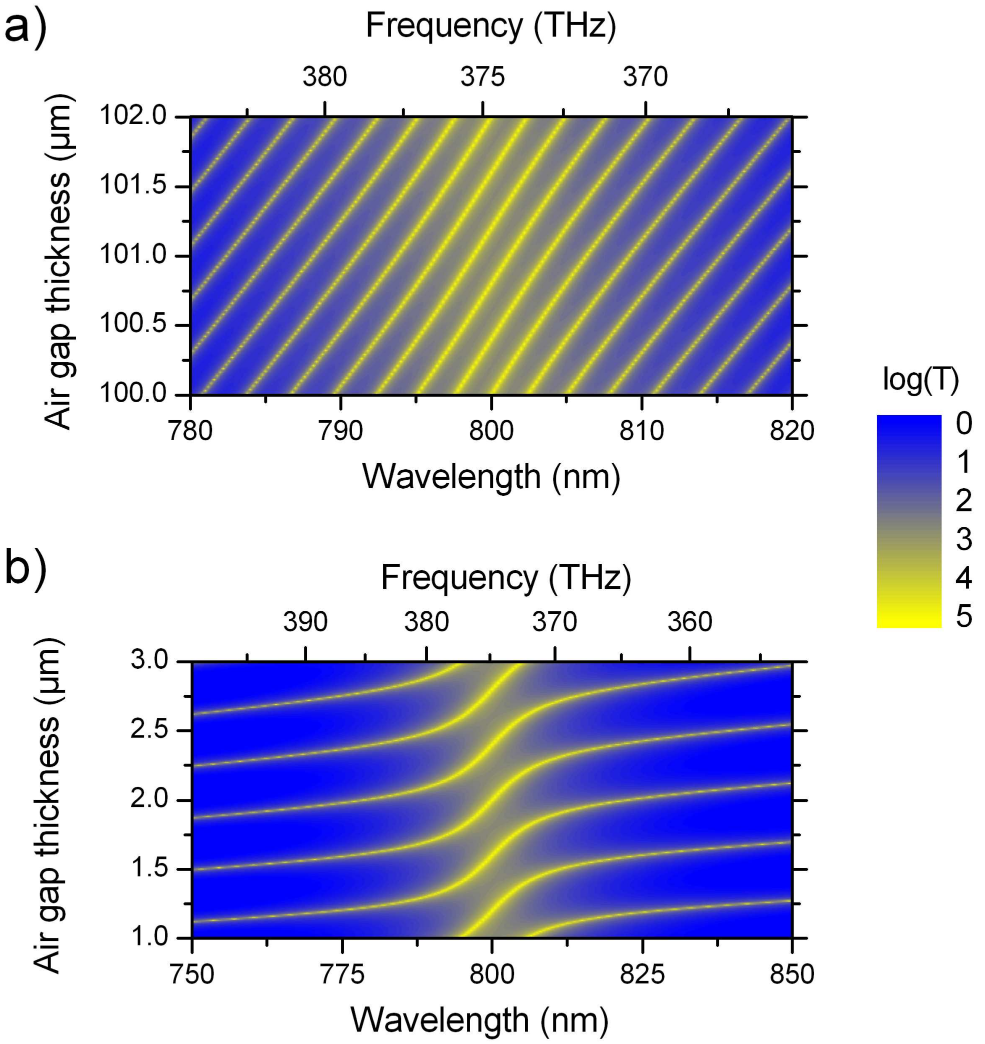

Figure 5.10: Calculated cavity mode positions of a double-monolithic microcavity in dependence of the air gap. The structure (1T 1S)7 1T 2S 1T (1S 1T)2 Air (1T 1S)2 1T 2S 1T (1S 1T)7 is designed for 800 nm. The influence of thickness variations around air gap sizes of 100 μm (a) and 1 μm (b) are demonstrated for the mode positions around the design wavelength. With increasing thickness of the cavity distance the number of cavity modes increases with a reduced mode splitting.

and 812.9 nm (368.8 THz), they exhibit a mode splitting of 3.3 THz.

The time-dependent transmission of the coupled microcavities is investigated by an optical gating experiment. A short laser pulse with a broad Gaussian spectral shape is transmitted by the cavity modes and guided into a non-linear crystal. In the crystal, a time-delayed gate pulse from the same laser is up-converting the transmission signal. The sum-frequency signal is detected spectrally resolved with a CCD array. By changing the light path of the gate beam, the delay time is varied and thus the temporal evolution of the transmitted light is evaluated.

Figure 5.12 a presents the up-conversion signal of the laser pulse transmission

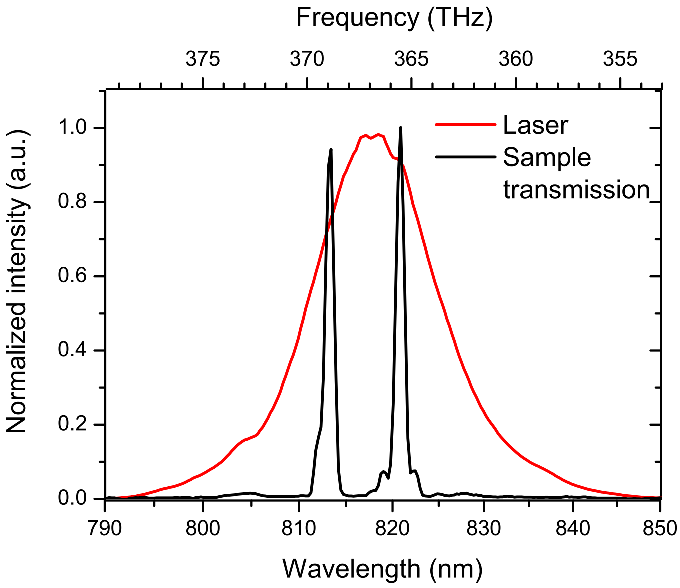

Figure 5.11: Laser spectrum and transmission spectrum of the monolithic microcavity. The laser excites both cavity modes - the basis for an oscillation of the internal electric field.

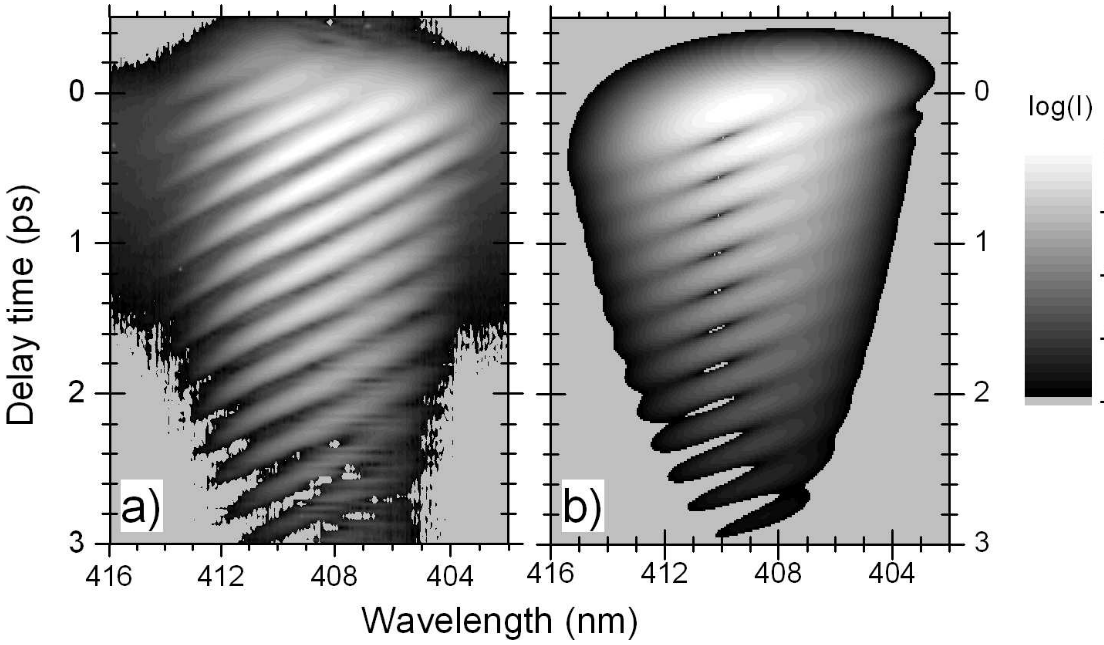

Figure 5.12: Measured (a) and calculated (b) up-conversion signal of a transmitted laser pulse through a monolithic coupled microcavity. The transmission shows a beating of 3.5 THz with tilting of the wavefront originating from a laser chirp.

through the monolithic coupled microcavity. After a fast signal rise, the intensity decreases exponentially with a longer decay time. The most prominent feature in the experiment is the beating of the transmission signal with a frequency of about

3.5 THz. This beating corresponds directly to the spectral distance of the two cavity modes. A slight difference is caused by a shift of the investigated area between the linear transmission and the up-conversion experiment. An additional feature in the measurement is the tilting of the wavefront. This behavior is attributed to a chirp of the laser pulses.

The up-conversion signal $|U(\omega,\tau)|^2$ is modeled by an analytical approach with the final formula:

$$\begin{aligned} U(\omega,\tau) &= \sum_{j=1}^{2}(-1)^j\sqrt{-2i\beta+\Gamma^2}\pi\mu_j \ \mathrm{Erfc}\left[-\frac{-2\gamma_j-(+2i\beta-\Gamma^2)\tau+i(\omega-2\omega_j)}{2\sqrt{-2i\beta+\Gamma^2}}\right] \\ &\times \ \exp\left\{-\frac{-2\gamma_j^2+\omega^2+2\gamma_j[(-2i\beta+\Gamma^2)\tau+i(\omega-2\omega_j)]}{2(-2i\beta+\Gamma^2)}\right\} \\ &\times \ \exp\left\{-\frac{-(4\beta+2i\Gamma^2)\tau(\omega-\omega_j)-2\omega\omega_j+2\omega_j^2-2\omega\omega_L+2\omega_L^2}{2(-2i\beta+\Gamma^2)}\right\}. \end{aligned} \tag{5.4}$$

A derivation of this equation can be found in the Appendix A.2. Laser and cavity parameters are both taken into account. The Gaussian laser pulse is described by a linewidth Γ with a linear chirp β and a center wavelength ω_L. The cavity modes $j = 1, 2$ are assumed to have Lorentzian line shape with a center wavelength ω_j, a linewidth γ_j, and an amplitude μ_j. The signal is calculated as a function of the up-conversion frequency ω and the gate laser delay time τ.

The calculation results are plotted in Fig. 5.12 b. The parameters are selected to yield a good correspondence with the measured transmission: $\hbar\omega_1 = 1526.5$ meV (812.2 nm), $\hbar\omega_2 = 1510$ meV (821.1 nm), $\mu_1 = \mu_2$, $\hbar\gamma_1 = \hbar\gamma_2 = 1.1$ meV, $\hbar\Gamma = 4.8$ meV, $\beta = 30$, and $\hbar\omega_L = 1520.4$ meV (815.5 nm). The cavity mode frequencies differ slightly from the linear transmission spectra, as already seen in the deviation of the beating frequency. However, the calculation reproduces the signal shape, the decay, the beating, and the spectral tilting of the oscillation maxima. In the simulation, the tilting is completely attributed to the laser chirp, which is introduced by the set of Γ and β that fit the experiment best. An influence of the cavity on the temporal evolution of the wavefront cannot be excluded. Naturally, the cavity modes and especially the phase shifts slightly deviate from the Lorentz model. However, an influence of the microcavity phase shift and the material dispersion on a potential tilting is not demonstrated in numerical transfer matrix calculations. In this model, the transmission of an unchirped Gaussian laser pulse is simulated and subsequently twofold Fourier transformed. The results of this numerical approach coincide with the analytic model without a laser chirp.

Applying the same optical gating experiment, the temporal evolution in a double monolithic coupled microcavity has been investigated. Figure 5.13 a depicts the temporal evolution of a transmitted laser pulse. After a fast signal increase, the transmission signal again decays exponentially. The mechanical composition of two single cavities results in a higher Q-factor since the ratio of stored energy and losses per oscillation cycle is enhanced by the air gap. Therefore, one can experimentally observe the up-conversion signal longer than 25 ps. In the double-monolithic sample, a smaller spectral mode distance results in a reduced beating frequency of 1.2 THz. The oscillation maxima of the transmission are again shifted in time.

Figure 5.13 b shows a calculated curve for the up-conversion experiment of the double-monolithic microcavity applying Eq. 5.4. The coupled microcavity is represented by two cavity modes with the following parameters: $\hbar\omega_1 = 1525$ meV (813.0 nm), $\hbar\omega_2 = 1520$ meV (815.7 nm), $\mu_1 = \mu_2$, and $\hbar\gamma_1 = \hbar\gamma_2 = 0.11$ meV. The laser is modeled by $\hbar\Gamma = 2$ meV, $\hbar\omega_L = 1522$ meV (814.6 nm), and $\beta = 20$. Also for the double microcavity, the model enables an accurate simulation of the spectral shape and the intensity in time. Additionally, the beating and the laser chirp are reproducible. In the experiment, the chirps increases with the delay time, which is not included in the model. Therefore at short delays, the model does not fit the experimental chirp accurately.

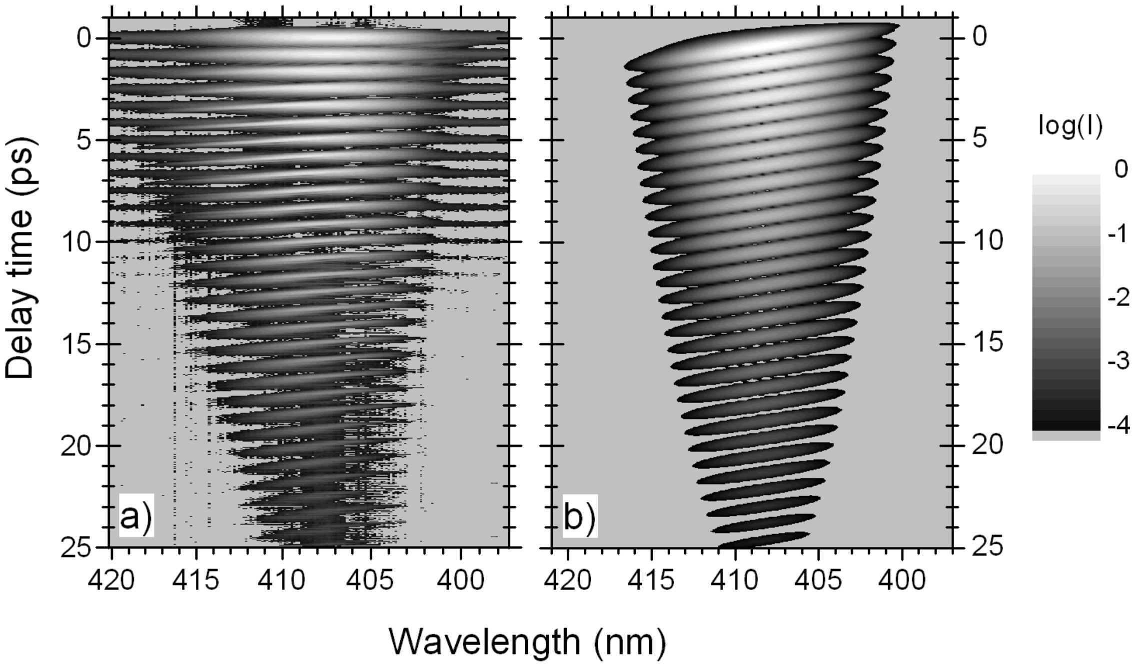

Figure 5.13: Measured (a) and calculated (b) up-conversion signal of a transmitted laser pulse through a double-monolithic coupled microcavity. The transmission shows a beating of 1.2 THz with a slight tilting of the maxima originating from a laser chirp.

In both experiments, the monolithic and the double monolithic coupled microcavities generate a terahertz beating of the transmission signal in time. This beating is a consequence of an internal oscillation of the electric field between the cavity layers. A number of indicators support this assumption. Two cavity modes with equal polarization contribute to the beating. A single laser pulse is exciting these two modes, i.e. the electric field of both modes oscillates in the same position. Since the two modes have different frequencies but equal polarization, the internal oscillation in time results also in a spatial oscillation of light between the coupled cavity layers. In accordance with the Q-factor, a certain amount of light escapes from the cavity per round-trip and performs the exponential intensity decay. However, due to the spatial oscillation, the light is concentrated in either cavity layer. Thus, light can leave the cavity only by the outer mirror at the respective side of light concentration.

The excitation pulse of the laser with its temporal length below 1 ps is much shorter than the cavity photon lifetime. Therefore, internally oscillating light cannot interfere with incident light. As a consequence, the oscillating photons can leave the cavity at both sides. Due to the spatial oscillation, the light emission at both sides shows an intensity variation corresponding to the beating frequency. Additionally, the signal from the opposite sides is out of phase.

In conclusion, the optical gating experiments at coupled microcavities indicate the spatial oscillation of a photon wave packet in an optically confined structure. A similar oscillation of electrons in periodic potentials is known as Bloch oscillation. Therefore, the beating in coupled microcavities can be referred as the optical analogon of the electronic Bloch oscillation. The experiments presented before are not a direct observation of the internal spatial oscillation. Nevertheless, the signal beating of a single transmitted laser pulse from a coupled microcavity with equally polarized modes is a direct consequence of the photonic Bloch oscillation. This assumptions are supported by transfer matrix calculations and FDTD modeling, which both allow for a theoretical simulation of the periodic electric field variation.

5.5 Anisotropic microcavities

5.5.1 Film anisotropy and birefringence

In Section 4.1.4, the optical anisotropy caused by an oblique angle deposition of thin films is discussed. Anisotropic optical films allow for an extension of thin film applications due to a higher degree of freedom in the design of the layer refractive index distribution [154] and thus the optical properties. Multilayer structures with large birefringence have been demonstrated with polymers [154] and by glancing angle deposition of dielectric materials [193]. With these techniques, refractive index differences between the normal and in-plane direction of around 10 % and higher have been achieved. In contrast to this results, the application of layer deposition at smaller angles of incidence leads to a lower contrast of birefringence. The samples presented within this work are fabricated under deposition angles from 0° to 30°. As demonstrated for electron beam evaporated TiO_2 films, the difference of the indices of refraction is significantly below 10% [150].

Investigations of cleaved microcavities with scanning electron microscopy show the columnar grain structure of the deposited films (Fig. 5.14). Both microcavity materials TiO_2 and SiO_2 exhibit an anisotropic structure with no clear voids. In the micrographs, the TiO_2 layers appear brighter due to their higher conductivity. A relatively high substrate temperature prevents from the growth of clearly separated columns. The formation of a comparably dense and stable substructure agrees with the substrate temperature dependent model of the layer morphology by GUENTHER [139]. For both materials, the substrate temperature is about 25% of the corresponding melting point, which results in the growth of densely packed columns. Therefore, the strength of a potential anisotropy is distinctly reduced in comparison with pure columnar structures. Cracks penetrating through the complete structure demonstrate the propagation of the anisotropy from layer to layer. The carbon coated sample in Fig. 5.14 d shows a substructure especially visible in the TiO_2 layers. Grain sizes from approximately 50 - 150 nm are in coincidence with the results for TiO_2 nanocrystals created during the fabrication process as demonstrated in Ref. [116, 117, 194].

The above microscopic analysis of microcavities grown by an oblique angle deposition technique demonstrates the generation of anisotropic and therefore birefringent films. Typically, in such devices the optical axes do not coincide with the normal axis of the structure. This results in the particular property of a single anisotropic microcavity, where two energetically different modes with perpendicular polarization are observable. Whereas in isotropic structures s- and p-polarization are treated independently, this is not allowed for anisotropic structures. Here, at the interface an incident wave produces waves with different polarization. This leads to a mode coupling within the microcavity and the energy is mutually converted between the two polarizations. For an exact calculation of the optical properties of a layered anisotropic structure, the transfer matrix model has to be extended into a 4×4 matrix formulation. In this method the transfer matrix consists of s- and p-polarization components simultaneously [10, 195].

5.5.2 Polarization splitting and terahertz beating

Optically anisotropic microcavities exhibit two perpendicular axes with different optical properties. Perpendicularly polarized light oscillating along these directions are in resonance with the cavity for unequal energies. This polarization splitting is a direct consequence of the refractive index variation and the identical resonator

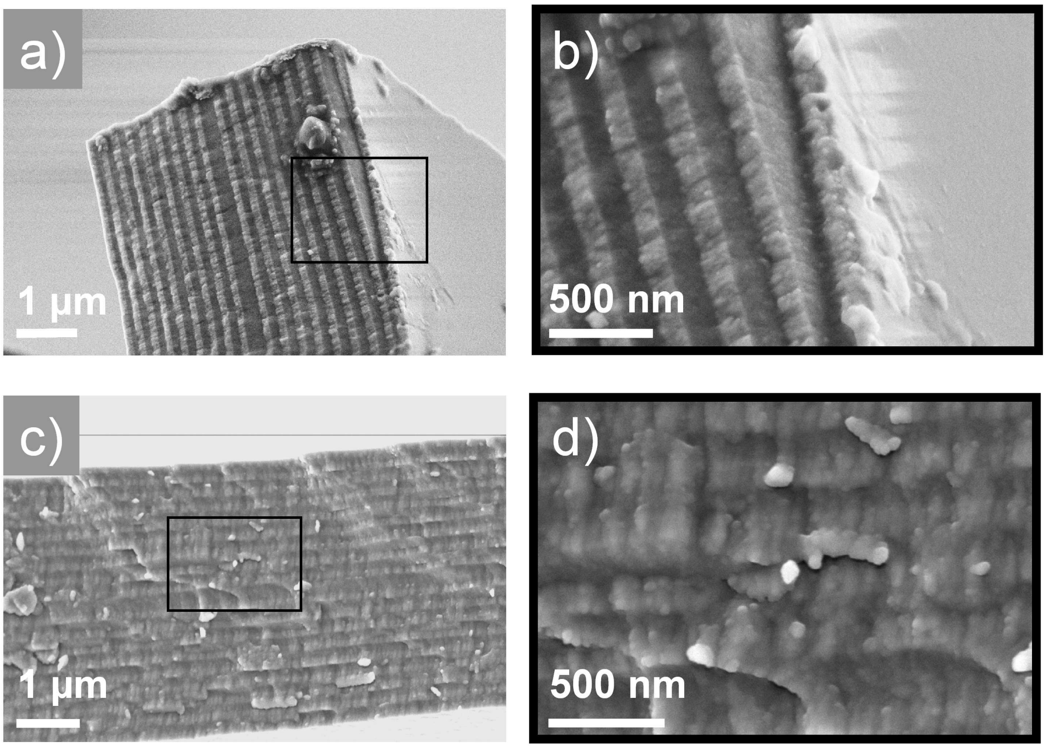

Figure 5.14: Scanning electron microscope graphs of cleaved microcavity. Bright layers are TiO_2 and dark films consist of SiO_2. The graphs (a) and (c) exhibit the columnar grains in the total structure. Selected areas with larger magnification show the anisotropic density in both materials (b, d) . The samples in Fig. c and d are coated with a 3 - 10 nm carbon film to enhance the conductivity. Instrument: SEM Gemini 1530 (Zeiss), U = 2 - 5 kV, I_s = 60 pA

thickness for both planes. The magnitude of birefringence depends on the columnar angle of the internal layer structure and is therefore variable by changing the angle of deposition.

Figure 5.15 a presents the transmission spectra of an anisotropic single microcavity grown by oblique angle deposition. The passive structure exhibits two modes at 782 nm and 779.5 nm with perpendicular polarization. The linewidth of about $\Delta\lambda = 0.6$ nm results in a quality factor of $Q = 1300$. The spectral distance corresponds to a difference in frequency of 1.25 THz. Simulations by a 2×2 transfer matrix model, where the polarizations for simplicity are treated independently, imply a refractive index difference of the order of 10^{-3} between the two resonances (Fig. 5.15 b). In this model, a set of dispersion free optical constants is chosen. The ordinary mode at 782.0 nm is modeled with a refractive index $n_{o,\mathrm{SiO_2}} = 1.45$ and the imaginary index of refraction $k_{o,\mathrm{SiO_2}} = 2 \times 10^{-6}$ for SiO_2. As the high refractive index layer, the optical constants for TiO_2 are assumed as $n_{o,\mathrm{TiO_2}} = 2.17$ and $k_{o,\mathrm{TiO_2}} = 1 \times 10^{-4}$. These optical constants coincide with the values from the ellipsometric measurements of

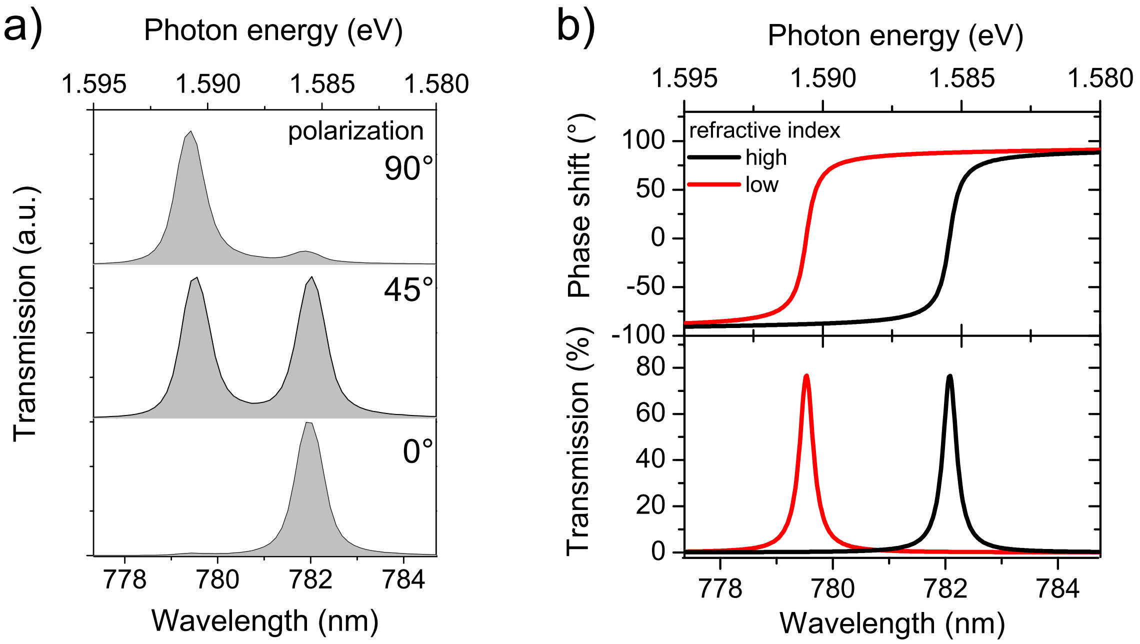

Figure 5.15: (a) Polarization dependent transmission of a passive microcavity. The structure design is (T S)8 T 2S T (S T)8 with a design wavelength of 781 nm. (b) Results of transfer matrix calculations for two different sets of refractive indices. The refractive index of the blue shifted mode is reduced by 0.33 % with respect to the low energy mode.

dielectric films evaporated at right angle. The whole stack consists of $\lambda/4$-layers at the design wavelength of 782.0 nm and is grown on a 4 mm thick glass substrate ($n_{\mathrm{Sub}} = 1.52$). The extraordinary blue shifted mode at 779.5 nm is modeled with the same physical layer thicknesses but reduced refractive indices. It is assumed that the refractive indices for both dielectric materials decrease with the same factor. An optimal value of the reduction factor is determined as 0.99675, resulting in $n_{e,\mathrm{SiO_2}} = 1.445$ and $n_{e,\mathrm{TiO_2}} = 2.163$. The calculated transmission intensities and phase shifts of the ordinary and extraordinary modes are shown in Fig. 5.15 b.

Transmitting coherent light through an anisotropic cavity implicates a number of interesting effects, which are discussed in the following. The transmitted light consists of two modes with their corresponding energies E_1 and E_2. By the coherence of the light both modes are phase related and develop a beating with the frequency $f_b = |E_1 - E_2|/h$ with h as Planck's constant. Since the energetic difference between both modes is relatively small, the wave train can be assumed as constantly coupled for several neighboring oscillations (Fig. 5.16 a-c). At a certain position of the train, maxima and minima of the two modes coincide and the resulting polarization is linear. Afterwards, this polarization becomes elliptical and a quarter beating period later the resulting mode is circularly polarized. In one complete beating period the resulting polarization vector changes between linear, elliptical and circular oscillation

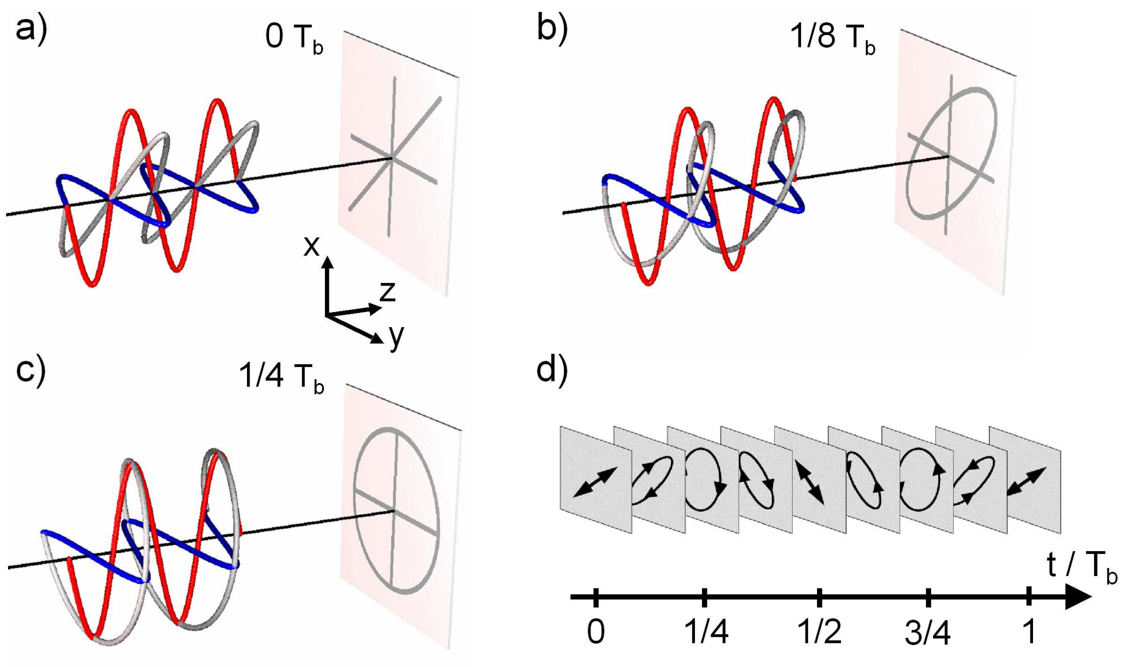

Figure 5.16: Effective polarization following transmission through an anisotropic microcavity. At the time 0, the perpendicularly polarized transmission modes (red, blue) are in phase and the resulting E-field (gray) is linearly polarized (a). An eighth (b) and a quarter (b) beating period later the light is elliptically and circularly polarized, respectively. During one beating period the resulting polarization is particulary linearly, elliptically and circularly polarized (d).

(Fig. 5.16 d). By selecting a certain polarization plane with a polarizer, a beating of the two cavity modes becomes observable.

The dynamics of the transmission through the anisotropic microcavity is experimentally studied with the up-conversion technique (Sec. 4.2.2). The pump light from the laser source is polarized with 45° in order to have electric field components in the polarizations of the two cavity modes. Energetically, the femtosecond pulse of the laser system is covering both modes. The transmission is focussed on a BBO crystal and up-converted with the time delayed gate pulse. Since the up-conversion process is also polarization dependent, the rotation of the pump or gate beam by a $\lambda/2$-plate allows for the selection of one or two modes of the cavity transmission for the investigation. Figure 5.17 demonstrates the spectrally resolved transmission of a femtosecond laser pulse recorded by the up-conversion method.

Due to the frequency-doubling mechanism, the cavity mode position is shifted from around 780 nm to 390 nm wavelength. The signal of the single mode experiment at 0° polarization shows two distinct spectral features with different temporal behavior. The dominating part with the highest intensity is the up-conversion signal of the light transmitted by the cavity mode. This particular signal, which shows a

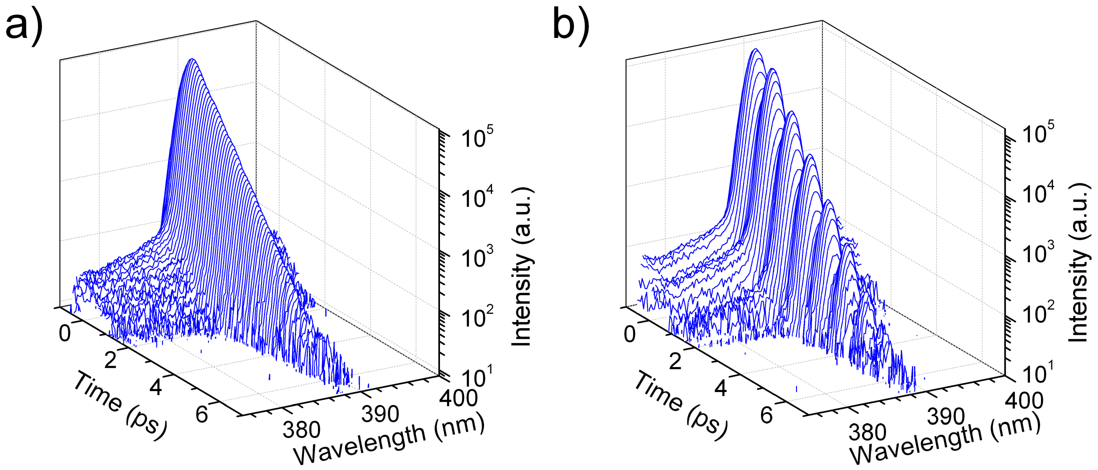

Figure 5.17: Experimental up-conversion results of an anisotropic single microcavity for one (a) and two (b) contributing modes. The beating frequency for two modes is 1.25 THz.

Gaussian spectral behavior, decays exponentially as expected from the theoretical predictions in Sec. 5.3. The exponential decay is well explained by the resonator properties with its light accumulation and subsequent statistical emission of photons. Mathematically it is modeled by the Fourier transform of the Lorentzian line shape. Such a typical resonator transmission decay allows the determination of the cavity photon lifetime. The slope of the central part of the signal yields a decay time τ_p of 0.65 ps in an exponential fit. The cavity photon lifetime is directly proportional to the quality factor by $Q = 2\pi c \tau_p / \lambda$ resulting in $Q = 1600$. This result agrees with the linear transmission measurements ($Q = 1300$).

The second contributing part of the up-conversion signal is orders of magnitudes weaker, much broader, and has a mainly Lorentzian spectral contribution. This signal originates from off-resonantly transmitted laser light. Thus, it is weakly influenced in time by the resonator properties of the microcavity and strongly suppressed in intensity by the high DBR reflectivities. The temporal decay is dominated by the laser pulse itself. As a result, a Gaussian intensity decrease in time of the off-resonantly transmitted light is observed.

A selective rotation of the laser polarization enables the investigation of the sum signal of the two perpendicularly polarized modes (Fig. 5.17 b). The up-conversion signal shows the same spectral and temporal features as the single mode with an additional intensity modulation. This oscillation frequency of 1.25 THz corresponds exactly to the frequency difference between the two cavity modes. The beating is also observable in the wings of the spectrum having a Gaussian decay. The slight beating frequency deviation between the transmission and up-conversion experiments results from the different setup for the linear and non-linear experiments, where different sample spots were investigated. Due to sample inhomogeneities, the cavity mode wavelength and the spectral separation vary over a certain range.

The up-conversion transmission experiment is explained by a similar analytical approach as used for the coupled microcavities in Sec. 5.4. The formula has been simplified by the assumption of a transmitted temporal δ-pulse with infinite spectral width. However, the delayed gate pulse is still assumed to be of Gaussian shape in frequency and time domain. It is defined by the central laser frequency ω_L and the spectral width Γ and delayed by the time τ. A Lorentzian is modeling the optical properties of the two cavity modes with their amplitudes μ_j, widths γ_j, and their central frequencies ω_j. To obtain the detected up-conversion signal $|U(\omega,\tau)|^2$, the following formula for the amplitude is applied:

$$U(\omega,\tau) \propto \sum_{j=1}^{2} \mu_j \operatorname{Erfc}\left[\mathrm{i}\tfrac{\omega_j+\omega_L-\omega}{\sqrt{2}\Gamma_L} - \tfrac{\Gamma_L}{\sqrt{2}}\left(\tau - \tfrac{\gamma_j}{\Gamma_L^2}\right)\right] \times$$
$$\exp\left\{-\tfrac{[\omega-(\omega_j+\omega_L)]^2}{2\Gamma_L^2} + \mathrm{i}[\omega-(\omega_j+\omega_L)]\left[\tau-\tfrac{\gamma_j}{\Gamma_L^2}\right] + [\mathrm{i}\omega_L - \gamma_j]\tau\right\}. \tag{5.5}$$

The results of calculations with this model are presented in Fig. 5.18. An optimized set of parameters is chosen to fit the experimental results of Fig. 5.17. This values deviate from the results of the linear measurement since, as described above, sample inhomogeneities prevent from an exact reproduction in the time-resolved experiment. In the model, the cavity modes at $\hbar\omega_1 = 1596.2\,\mathrm{meV}$ (776.8 nm) and $\hbar\omega_2 = 1590.9\,\mathrm{meV}$ (779.4 nm) are excited by the laser with a central wavelength of $\hbar\omega_L = 1584.9\,\mathrm{meV}$ (782.3 nm) and a width of $\hbar\Gamma = 12.8\,\mathrm{meV}$ (6.3 nm). From the spectral distance of the two cavity modes, a beating period of 0.80 ps (1.25 THz) results. The Lorentzians of the two cavity modes are modeled with the same amplitudes ($\mu_1 = \mu_2$) and widths of $\hbar\gamma_1 = \hbar\gamma_2 = 0.48\,\mathrm{meV}$ (0.23 nm) .

Both the simulations of the single and two mode sum frequency signal reproduce the main features of the experiment. The signal at the resonance has in both cases a Gaussian spectral shape and is decaying exponentially. Additionally, the beating of the up-conversion signal in the two mode experiment can be simulated. Only in the off-resonant spectral range the simulation deviates from the experiment. Mainly, this is caused by the δ-pulse shape of the transmitted pulse in the calculation, which is spectrally broader and temporally shorter than the laser pulse in the experiment.

In summary, a new method for the generation of terahertz beating has been demonstrated. The nature of this beating differs significantly from coupled microcavities, where a spatial oscillation is the origin of the transmission intensity variation. In anisotropic cavities, the birefringence of the optical thin films creates two perpendicularly polarized modes with different resonance frequencies. By the application of a polarizer, these modes can be mixed and a beating can be detected,

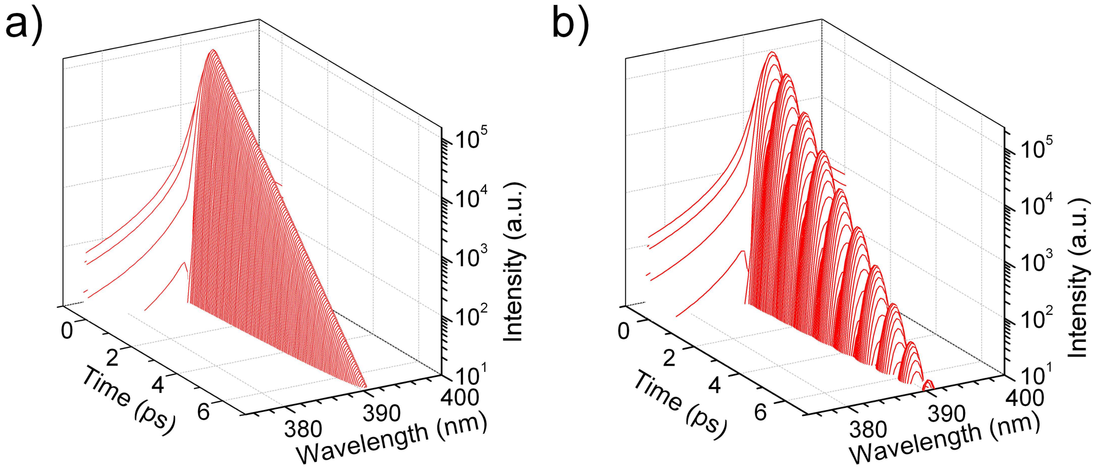

Figure 5.18: Modeling of the up-conversion experiment presented in Fig 5.17 for one (a) and two (b) contributing modes. Parameters are chosen to fit the experimental data.

if the used light source is emitting coherent light. The main advantage of such a structure is the requirement of only a single cavity layer, which simplifies the fabrication process drastically. With the implementation of a position dependent change of the columnar angle in the layers, the splitting of the two modes can be varied. In fact, such a gradient is already produced by the current fabrication method. It allows a tuning of the terahertz beating frequency by a simple lateral shift of the microcavity in the up-conversion setup. This concept enables a continuous variation of the beating frequency from 0 to 2 THz and higher, which could be of interest for future applications in terahertz generation by photomixing.

The combination of anisotropic films and coupled microcavities would additionally increase the number of cavity modes. This is of great interest, if the beating signal should consist of short pulses. In standard solid state lasers, 10^3-10^4 modes oscillate and generate fs-pulses in the mode-locking regime [22]. In a coupled anisotropic microcavity with two resonator layers, the four cavity modes can be used to create pulses with length of about 100 fs, if the amplitudes and the spectral distances are well aligned.

In the next Chapter on active microcavities, it will be demonstrated that anisotropic mirrors can lead to a mode splitting even in presence of an isotropic cavity layer. In an organic VCSEL, the polarization splitting is applied for the generation of two laser modes and a terahertz beating in stimulated emission is shown.

6 Active Microcavities

This Chapter discusses the influence of a strong one-dimensional optical confinement on the light emission from organic molecules. In the first part, the emission mode structure in planar cavities is studied. A Section on microcavities in the strong-coupling regime - a collaboration with the group of David Lidzey from Sheffield University - follows. In the last Section, the stimulated emission in high-Q organic microcavities is investigated. Two laser modes are generated by an optical anisotropy in the DBRs, which show a mode-coupling applicable for a terahertz beating in a photomixing experiment. The results of the last Section are based on up-conversion experiments of Marco Koschorreck (single mode emission) [56] and Marko Swoboda (coupled mode emission) [187]. The rate equation set for the laser modeling is also developed by M.K.

6.1 Emission mode structure and leaky modes

In active microcavities, the light source is positioned within the resonator and therefore directly influenced by the internal electric field (see Sec. 3.3). The emission rate is thereby influenced by the electric field strength and the corresponding wave vector. Optical microcavities enhance and suppress the internal electric field in dependence on the resonance wavelengths. At resonance, the spontaneous emission rate of one molecule can be enhanced by orders of magnitude. At the same time, it will be suppressed for off-resonant frequencies and propagation angles.

Figure 6.1 depicts transmission and emission spectra of a microcavity containing the host-guest system Alq_3:DCM with a cavity mode at 650 nm. The transmission spectrum shows a number of modes which indicates that the structure is different from an ideal structure with $\lambda/4$-layers in the DBRs. Therefore, transmission and reflection spectra of this device are used for a fitting of the individual layer thicknesses. The calculation of the final fitted structure overlaps very well with the experiment. The parameters of the two mirrors are applied in the following for the calculation of the spontaneous emission of the organic film. This analysis is based on the plane wave expansion algorithm presented in Sec. 3.3. In the experimental spec-

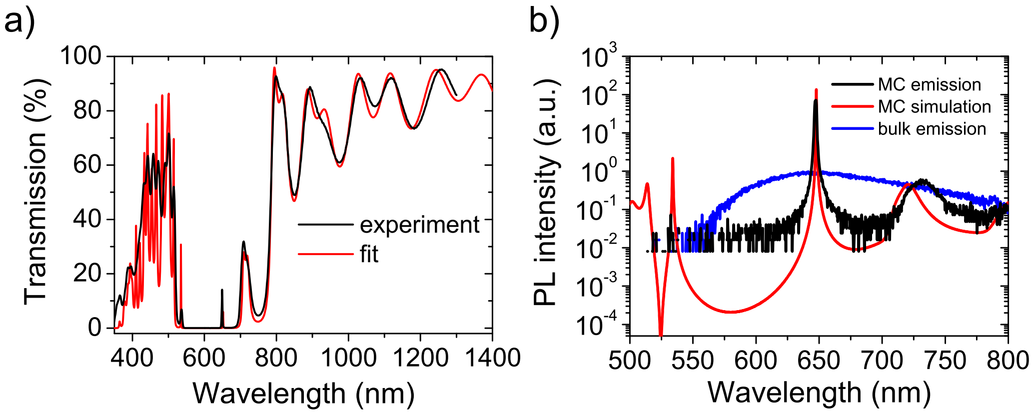

Figure 6.1: Transmission and photoluminescence spectra of a microcavity with an active cavity layer of Alq_3:DCM. The structure design is (T S)8 T 2A T (S T)8 at a design wavelength of 650 nm. (a) The transmission measurement is compared to calculation of a structure with fitted layer thicknesses. (b) Simulation and measurement of the spontaneous emission coincide in mode position and intensity. At the resonance frequency, the photoluminescence exceeds the bulk emission without cavity by a factor of 100.

trum of the cavity emission, an enhancement of about 100 times at the resonance frequency is observable in comparison with an equal film without cavity (Fig. 6.1 b). Off-resonantly, the photoluminescence is inhibited by approximately the same factor. The simulation even provides a stronger suppression, which is not detectable due to the finite noise of the CCD detector. In the best case, the detector dark current limits the experimentally accessible dynamic range to four orders of magnitude. However, the simulation demonstrates an intensity variation over more than six orders of magnitude. At 740 nm, an additional mode shows an enhanced emission, which is less pronounced. This is mainly caused by a lower quality factor of the mode and thus a weaker electric field amplification. It is the first mode outside the stop-band and a so-called DBR mode. The electric field of such a side mode is mainly concentrated in the DBR layers with higher field intensities in the mirrors than in the cavity layer. The deviation of the mode position in experiment and model is caused by the different sample positions in the transmission experiment, which was applied for the structure fit, and the photoluminescence measurement. Nevertheless, the model reproduces the emission linewidth and intensity.

A typical property for the emission in planar structures is the presence of internal modes and the limited light emission into the ambience. As discussed in Sec. 3.3.2, one can divide the light emission in a microcavity in three different classes of modes (Fig. 6.2). The light detectable outside the device is the Fabry-Perot mode, which

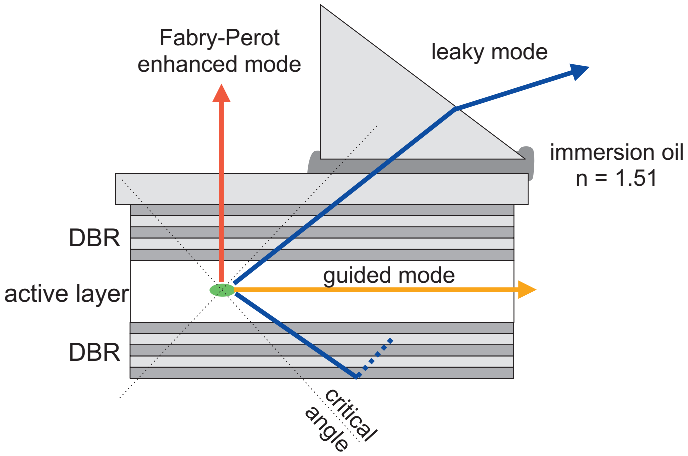

Figure 6.2: Experimental configuration for the detection of leaky mode emission. Leaky modes are propagating with angles larger than the critical angle (~ 35° for Alq_3) through the DBR. The total reflection of the leaky modes is overcome by the attachment of a glass prism.

is usually amplified as discussed before. Another class is trapped within the active region and a result of a waveguide structure. This is caused by layers with lower refractive indices surrounding the emissive material. Without a structuring of the active region, it is impossible to couple this light out so that guided modes are a loss channel for the external efficiency. The third group of modes is normally also lost, but propagates to the ambient boundary. Due to total internal reflection, this light becomes evanescent at the surface. By attaching a prism to this surface, the light can propagate further and is detectable. These modes are the leaky modes, which penetrate the DBRs at larger propagation angles outside the mirror stop-band. They are the result of the limited stop-band width of real structures, which in turn is based on the limited refractive index contrast of the dielectric materials.

The largest internal angle for the propagation of Fabry-Perot modes is the critical angle which is given by Snell's law with $\theta_{crit} = \arcsin(n_0/n)$. This angle becomes larger with smaller ratio between the refractive of the ambient medium n_0 and the refractive index of the emission layer n is. Excluding any cavity effects concerning a change of the emission rate, the critical angle defines also the outcoupling efficiency η of a planar structure by $\eta \sim 1/2n^2$ [75]. For an organic film with $n = 1.7$, the critical angle of $\theta_{crit} = 36°$ only allows an extraction efficiency of 17%.

By varying the surface angle, light propagating in leaky modes can be outcoupled. Figure 6.2 demonstrates the technique applied for this purpose. Here, a glass prism is attached to the planar substrate surface using an immersion oil to enable an optical contact. With a refractive index of $n_{\text{oil}} = 1.51$, the leaky modes are only weakly influenced at the substrate-oil-prism boundary and can penetrate into the prism.

At the prism-air interface, the angle of incidence is different in comparison to the substrate-air surface and the former leaky modes couple to the ambient medium.

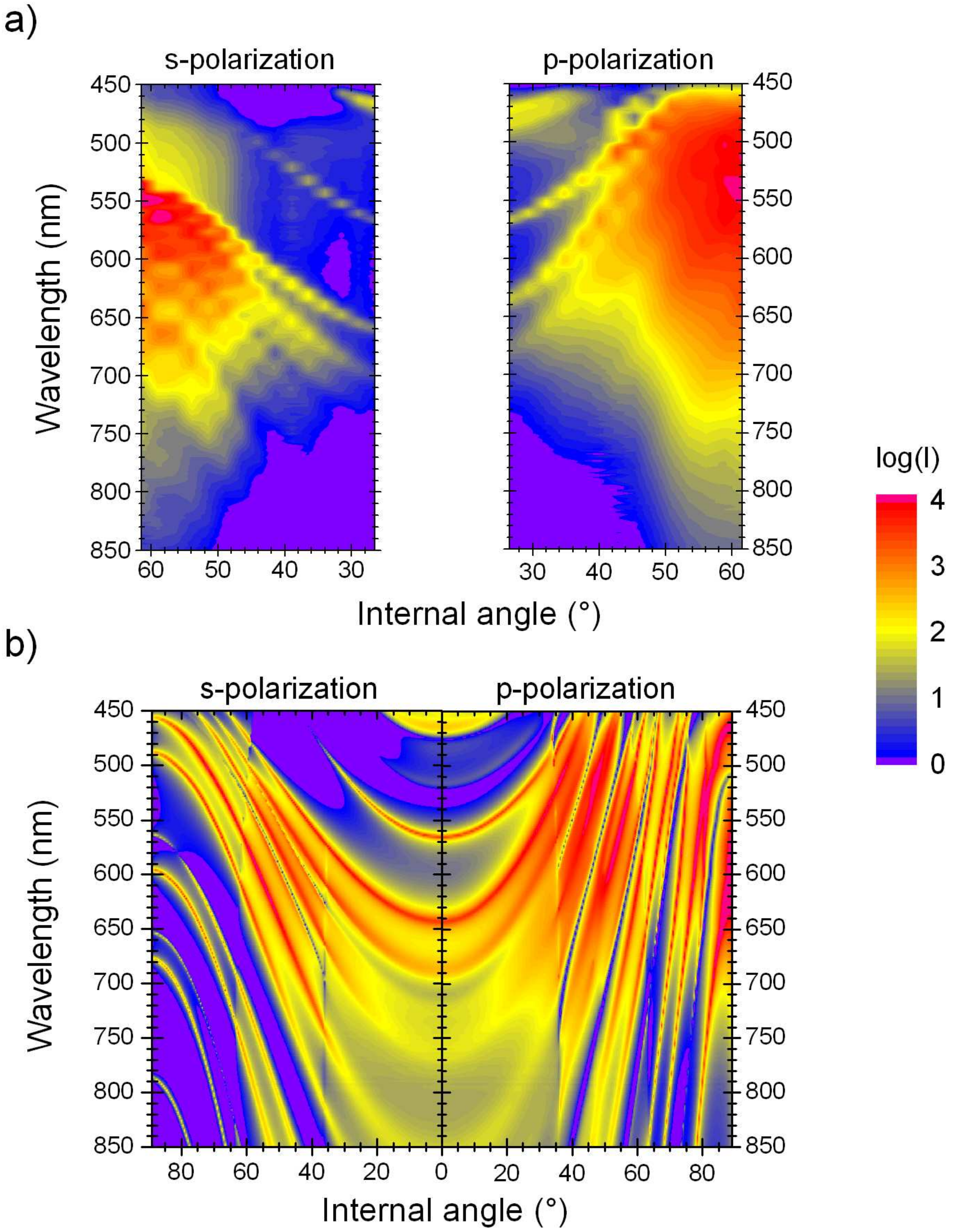

Figure 6.3: Light emission of Alq_3 in a planar microcavity with the design (T S)10 T 2A T (S T)5 at 550 nm. Comparison of experimental (a) leaky mode emission and plane wave expansion calculation (b). The enhanced emission in p-polarization is a result of the Brewster-type polarization filtering at around 50°.

The leaky mode structure of an active microcavity with an organic layer of Alq_3

is studied in a fluorescence spectrometer (Fig. 6.3 a). Due to experimental limitations, only the angular range between 26° and 62° is detectable. This configuration therefore prevents a direct comparison of the light intensity emitted by the microcavity into directly outcoupled modes and the amount of light radiated into the leaky modes. The experiment is performed for both polarizations separately. A stronger intensity of p-polarized emission is the result of the disappearance of the stop-band at internal angles between 40° and 60°. This effect is related to the Brewster angle of $\theta_{Brewster} = \arctan(n_2/n_1)$ with n_1 as the refractive index of the incident medium, here Alq_3, and n_2 as the index of refraction of the ambient medium, here glass. With $n_1 = n_{\mathrm{Alq_3}} = 1.7$ and $n_2 = n_{\mathrm{glass}} = 1.5$, the Brewster angle becomes approximately 50°. In the experiment, the mode structure vanishes and the emission resembles the bulk photoluminescence of Alq_3 with a maximum at 530 nm. In s-polarization, the stop-band influences the luminescence in the complete measured angular range and the internal mode structure is also visible for all investigated angles.

The data of the leaky mode experiment are compared to a simulation presented in Fig. 6.3 b. The applied algorithm is also based on the plane wave expansion algorithm. Before calculating, transmission and reflection spectra are fitted relating the individual thicknesses of the cavity layers. These values are used for the simulation of the DBRs optical properties. At the emission side, the structure is assumed to be embedded in a semi-infinite ambience of glass ($n_{\mathrm{glass}} = 1.5$), which resembles the glass prism. On the reverse side, the semi-infinite medium is air ($n_{\mathrm{air}} = 1$). In s-polarization, the model depicts all modes from the experiment. For the perpendicular polarization, the calculation also shows the measured modes but exhibits additionally a mode structure in the area of high emission intensities around 50°. At the angles of 35° and 65°, the simulation yields some steps in the intensity. These are the angles of total internal reflection. The former one is the angle for the boundary to the air and the later the critical angle between Alq_3 and SiO_2. Both angles therefore mark the ranges of the three different mode types. Up to 35°, one observes the Fabry-Perot enhanced modes, which emit into air. From 35° to 65°, the leaky modes propagate within the structure and for all larger angles the emission is guided within the active layer of Alq_3. Since the critical angles are dependent on the materials refractive indices, they exhibit also a dispersion and decrease slightly with decreasing wavelength.

6.2 Emission in the strong-coupling regime

The results of the following Section are developed in close collaboration with Liam Connolly, Jakub Wenus, and David Lidzey from the University of Sheffield. Within the European Union financed HYTEC network, our two groups investigated the optical properties of J-aggregates in microcavities. The J-aggregates and a part of the microcavities are provided by the Sheffield group. The double-DBR microcavities and the optical investigations presented here were done in Dresden.

6.2.1 Metal-DBR structures

During the last decade, a number of experiments have demonstrated the strong-coupling in microcavities containing organic semiconductors as active material (see Sec. 3.2). Six years after the first demonstration of photon-exciton-coupling in inorganic structures [5], hybridization was also achieved in organic devices containing a porphyrin dye [61]. The large oscillator strength of these organic molecules not only allows for a strong optical coupling at room temperature, but also provides a large Rabi splitting in low-Q cavities. Another class of materials that combines the constraint of a narrow absorption line with a large oscillator strength are J-aggregates or Scheibe-aggregates [196]. Exceeding a certain concentration in a liquid solution, e.g. cyanine dyes arrange in chains with head-to-tail alignment. The resulting delocalized exciton state creates the typical single, narrow and intense absorption and emission line as depicted in Fig. 6.4 for a cyanine dye solution in polyvinyl alcohol (PVA). Here, the spectra are dominated by a narrow line in emission and absorption at about 1.85 eV with a very small Stokes shift. Although the peak absorption provided by the J-aggregates is dominating the spectrum, a noticeable absorption intensity at higher energies is related to single cyanine molecules in the solution. These dye among other cyanines has been successfully applied for strongly coupled microcavities [62, 63, 71, 197–201].

The samples provided by the Sheffield group consist of a bottom DBR formed by 9 pairs of silicon dioxide ($n_{SiO_2} = 1.45$) and silicon nitride ($n_{Si_3N_4} = 1.95$) with a 120 nm layer spin-coated cyanine dye dissolved in a PVA matrix atop. Finally, the sample is coated by a 300 nm silver mirror. In this configuration, the microcavity provides a quality factor of $Q = 35$. The organic layer thickness is aligned to give a cavity mode position at a normal angle of incidence 150 meV below the J-aggregate exciton. This enables a strong-coupling at angles of 35°.

In a first experiment, the microcavities are optically excited by the 442 nm line of a 30 mW cw HeCd laser from the substrate side. The angle dependent emission is recorded in the Fluoromax fluorescence spectrometer from the same side separately for s- and p-polarization (Fig. 6.5). A number of different modes is visable in this experiment. At high energies, the emission is dominated by the modes transmitted through the DBR outside the stop-band. Observing at a normal angle of incidence, these modes range from 450 nm to 650 nm. The J-aggregate emission line is detected at 670 nm and does not shift with the angle of incidence. Cavity mode normal

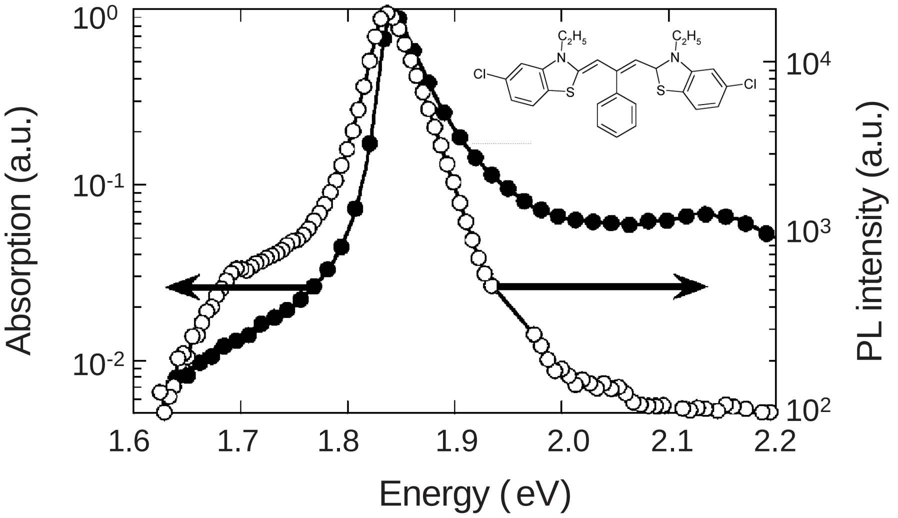

Figure 6.4: Relative absorption and photoluminescence intensity of the cyanine dye dissolved in a PVA matrix as applied for strong-coupling in a microcavity. The chemical structure of the dye is shown as a inset. Adapted from [198].

emission is visible at 725 nm and a low energy DBR mode can be seen at 850 nm. Except the J-aggregate emission line, all modes show the typical angle dependent line shift with a stronger shift for the high energy DBR modes in s-polarization and a larger shift of the low energy modes in p-polarization. Both different shifts result in a reduced stop-band width in p-polarization in comparison to the emission of s-polarized light.

A energetically broad emission as observed here with a rather high intensity from 450 nm to 850 nm cannot be expected from the spectra of the isolated film (Fig. 6.4). It is assumed that a longer storage time of the sample leads to a reorganization of the cyanine molecules with an increasing number of single molecules. Single molecules provide a naturally broader linewidth than J-aggregates [196]. An additionally enhanced photoluminescence quantum yield of the solid solution of single molecules may also contribute to the high intensity of the cavity and DBR modes.

The emission of the J-aggregate even at frequencies which do not coincide with the cavity mode is probably caused by scattering at sample inhomogeneities and the non-zero transmission of the DBR. At around 35°, the cavity mode crosses the J-aggregate exciton line, which leads to the strong-coupling observable in both polarizations. Although they are not identical, the small Stokes shift and the limited spectral resolution prevent from a distinction of J-aggregate emission from the absorption. In both polarizations, the emission in the lower polariton branch (LPB) exceeds the luminescence into the upper polariton branch (UPB). This results from the fast relaxation processes, which lead to a depletion of the upper mode. Former experiments have shown an active Raman mode in this cyanine dye [198,202]. With an energy of 73.4 meV, this Raman mode provides a transition channel between the two branches by emitting a phonon. The width of the polariton branches and the Rabi splitting in the same order support this assumption.

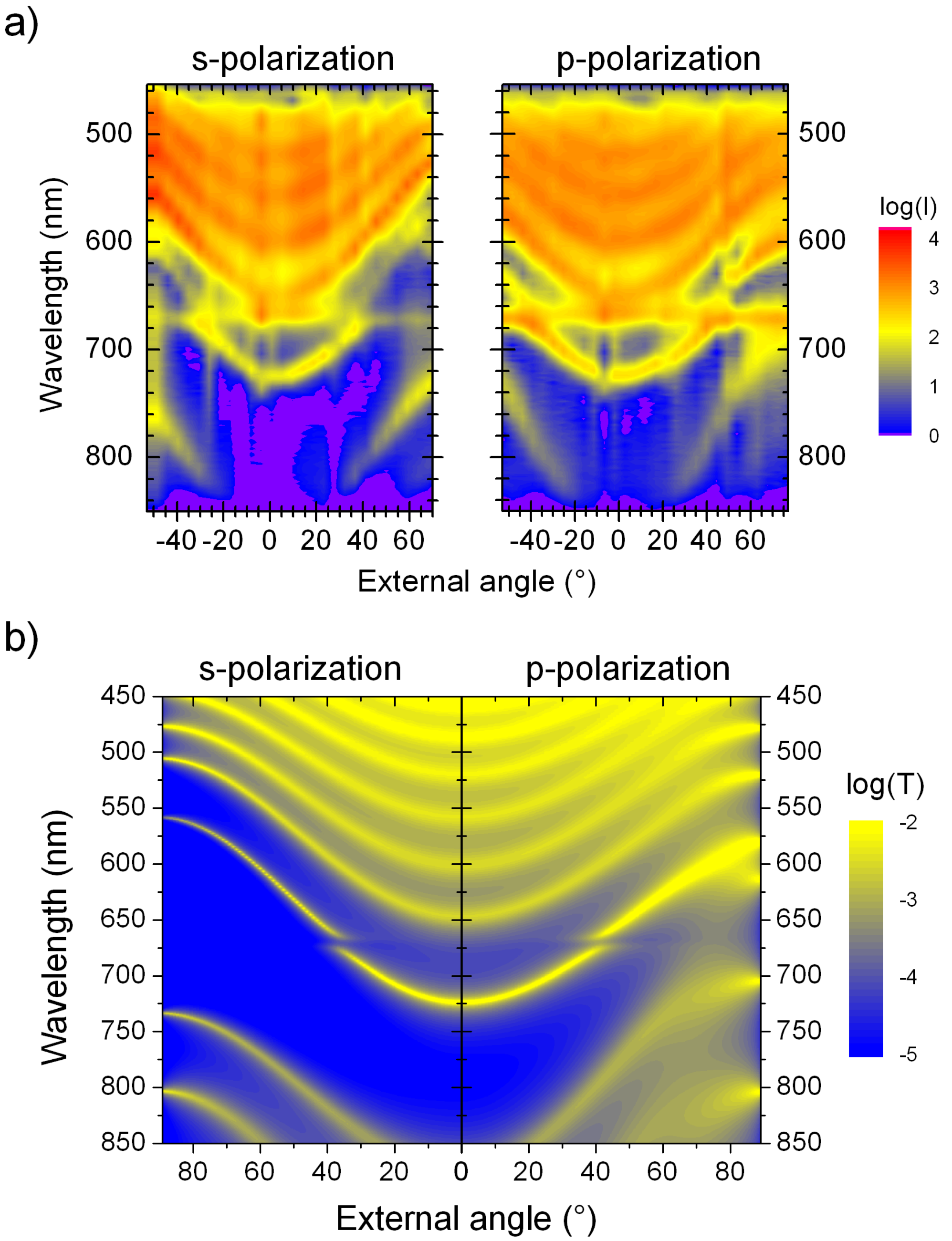

Figure 6.5: Experimentally measured photoluminescence intensity (a) and transmission calculation (b) of an organic microcavity for s- and p-polarization and varying angle of observation. The transmission was calculated using a transfer-matrix model with a Lorentz oscillator medium between the silver mirror and the DBR. The parameters of the Lorentz oscillator are: $\epsilon_\infty = 2.37$, $E_{center} = 1.85\,eV$, $A = 0.08\,eV$, $\nu = 0.025\,eV$.

Based on the absorption measurements depicted in Fig. 6.4, the dispersion of the dielectric constant ϵ of the cyanine is modeled by the following Lorentz equation:

$$\epsilon(E) = \epsilon_\infty \left(1 + \frac{A^2}{E_{center}^2 - E + iE\nu}\right). \tag{6.1}$$

Here, ϵ_∞ represents the high frequency dielectric constant, E_{center} the center energy of the oscillator and ν the vibrational energy width. With these J-aggregate parameters and the optical constants of the mirror materials, the transmission spectra are calculated, where the J-aggregate layer thickness was optimized to fit the experimental results. Finally, the transmission spectrum exhibits the mode structure as observed in the photoluminescence measurement. Cavity and DBR mode positions and stop-band width are reproduced successfully.

6.2.2 Double-DBR structures

A high reflectivity and low losses are the main advantages of DBRs. Among other physical effects, double-DBR microcavities allow the investigation in transmission, which makes them preferable candidates for laser experiments on ultrashort timescales. As we have seen in the fundamentals Chapter, high mirror reflectivities are a necessary condition for a high quality microcavity. Nevertheless, our first strong-coupling experiments with organic samples are performed with organic films coated on a DBR and covered by a metal mirror. This method is preferred due to the lower thermal stress introduced by the fast deposition of a metal film with relatively low evaporation temperature. In organic microcavities, the high oscillator strength allows for the polariton generation in devices with two metal mirrors and Q-factors as low as 10 [71]. In microcavities with low mirror losses, the polariton lifetime, which is approximately twice the photon lifetime, is significantly increased leading to a higher polariton population density. Such macroscopic densities may allow for a observation of stimulated polariton scattering at room temperature as already documented for inorganic structures [203, 204]. Organic microcavities have been demonstrated with porphyrin dyes and deposited DBR [64] and in laminated structures with J-aggregates [67, 68]. Q-factors ranging from 110 for the laminated structures up to 625 for the deposited devices have been achieved by these techniques.

Our goal is the fabrication of organic microcavities with deposited DBRs on the bottom and top side. In a first step, the application of a spin-coated gelatine film as the cavity layer is evaluated. It is important to investigate the possibility, if a gelatine film is able to form the resonator layer of a high-Q cavity, since it is the matrix material for the applied J-aggregates. Figure 6.6 presents the transmission spectra of a microcavity containing a cavity layer of gelatine ($n_G = 1.52$). The DBRs are designed for a wavelength of 600 nm and a cavity mode occurs at 675 nm.

A compound of 10.5 pairs of TiO_2 and SiO_2 guarantees for a maximum reflectivity significantly above 99%. Although noticeably off-resonant, the cavity mode exhibits a Q-factor of 650, thus forming a high-Q organic microcavity. In the measured polarization dependent transmission spectrum, a polarization splitting occurs (Fig. 6.6 inset). As already discussed in the experimental Chapter of the passive microcavities, this effect is attributed to the anisotropy of the evaporated SiO_2 and TiO_2 films (see Sec. 5.5). The prominent feature in this sample is the gelatine layer, which can be assumed as structurally and optically isotropic. From this follows that the polarization splitting is caused by the anisotropic mirrors only, a fact that is not obvious but supported by transfer matrix calculations.

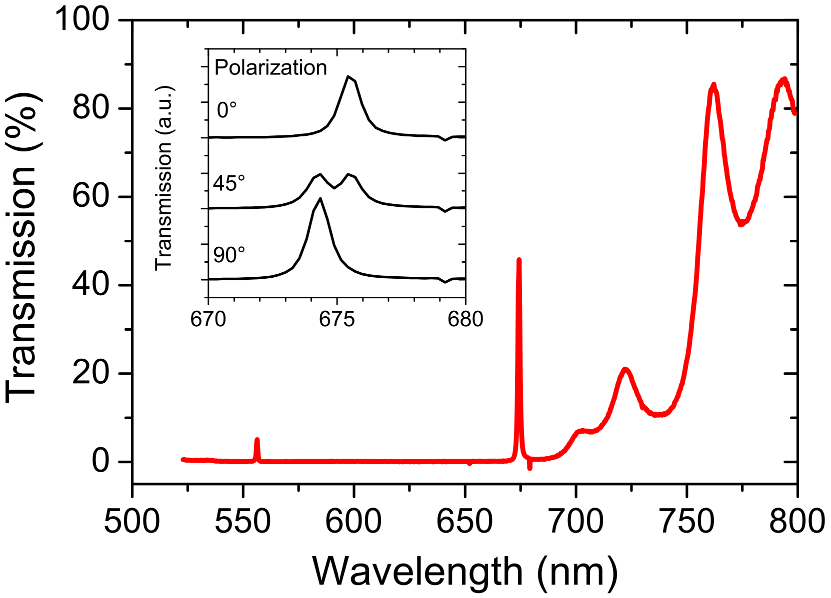

Figure 6.6: Transmission of a microcavity containing a spin-coated gelatine layer as cavity layer. The design is (T S)10 T 2.9G T (S T)10 for a design wavelength of 600 nm. From the linewidth of the cavity mode at 675 nm a Q-factor of 650 is calculated. Polarization dependent transmission at normal angle of incidence exhibit a polarization splitting (inset).

For the fabrication of strongly-coupled organic microcavities, the two cyanine dyes H2 and H4 [68] are provided by the Sheffield group. In a first experiment, the stability of both dyes against the electron beam evaporation of SiO_2 and TiO_2 is proved. Because of their structural and spectral similarity, only the dye H2[1] is chosen for further investigations (Fig. 6.7 a). Dissolved in a gelatine matrix, the H2 molecules arrange in J-aggregates forming a narrow absorption line at 635 nm. A very small Stokes shift of 15 meV results in a photoluminescence peak at 640 nm. The optical constants of the H2-gelatine compound are fitted by a Lorentz oscillator

---

[1] (5-chloro-2-[3-[5-chloro-3(3-sulfopropyl)-2(3H)-benzothiazolylidene]-2-methyl-1-propenyl]-3-(3-sulfopropyl)-benzothiazolium hydroxide)

using the data from the transmission measurement of a single film with known thickness. The fitting results are depicted in Fig. 6.7 b. They are the basis for the transfer matrix modeling of the strongly-coupled H2 microcavities.

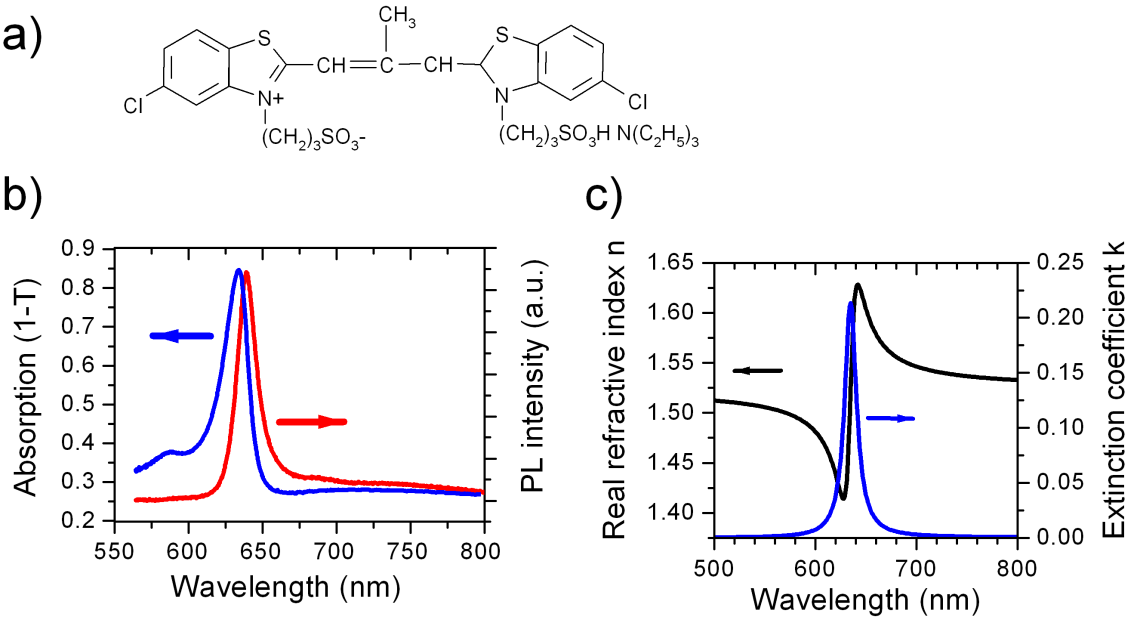

Figure 6.7: Chemical structure of the cyanine dye H2 that forms J-aggregates when dissolved in gelatine (a). Absorption and photoluminescence of the J-aggregates of the cyanine dye H2 dissolved in a gelatine matrix with a layer thickness of 230 nm (b). H2 chemical structure as inset. A Lorentz oscillator is applied for the modeling of the optical constants of the H2-gelatine compound (c). The Lorentz parameters are: $\epsilon_{\infty} = 2.31$, $E_{center} = 1.95\,eV$, $A = 0.15\,eV$, $\nu = 0.04\,eV$.

Transfer matrix calculations demonstrate a strong influence of the DBR pair number on the transmission intensity of the two polariton branches. With increasing layer number, the maximum transmission drops from around 50% for 2.5 pairs per DBR to 10^{-3} for 10.5 pairs per DBR. As a compromise between high Q-factor and reasonable transmission intensity, a pair number of 5.5 is chosen for the double-DBR microcavities with H2.

In linear transmission experiments, a sample containing H2 with a $\lambda/2$-layer thickness at the right design wavelength exhibits an anticrossing of the cavity mode and the exciton absorption. Strong-coupling can be observed at 45° angle of incidence with a Rabi-splitting energy of 110 meV (Fig. 6.8). Transfer matrix calculations with the parameters of the Lorentz fit of H2 (Fig. 6.7) support the measured peak positions of the two polariton branches. The peak intensities, especially of the lower polariton branch at small angles of incidence, cannot be described by our model. Losses due to scattering at sample inhomogeneities and absorption in the cavity layer may contribute to this effect.

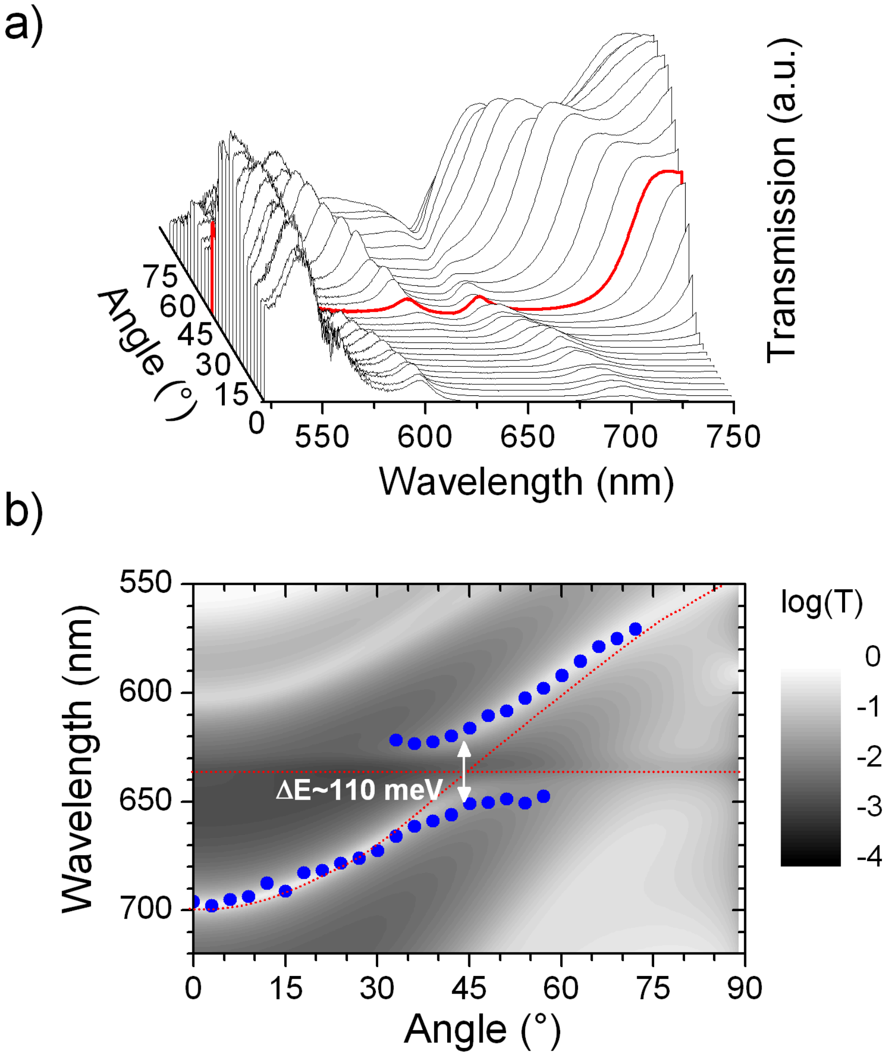

Figure 6.8: (a) Measured angle dependent transmission of a microcavity containing the J-aggregate H2 (linear scale). (b) The experimental peak positions (blue) of the two polariton branches coincide with the transfer matrix model. Strong-coupling occurs at an incident angle of 45° with a Rabi splitting of 110 meV. Exciton and cavity mode position of an unaffected cavity are shown for comparison (red).

Photoluminescence measurements are performed by exciting the samples with the unfocussed, continuous wave, p-polarized 532 nm emission of a Nd:YAG laser at an output power of approximately 100 mW. Before every single measurement, the sample is shifted by a few microns to avoid an influence of the fast degradation of the organic molecules on the following exposures. Figure 6.9 presents the emission of an uncovered H2 film and a microcavity filled with the J-aggregate. For the cavity, the excitation wavelength is far above resonance and can penetrate the DBRs at minimal tuning angles outside their stop-band. In the plot, one can see that emission is totally suppressed in the UPB. The highest intensity is detected in the LPB in the angular range from 40° to 20°. At lower energies and smaller tuning angles, the luminescence is decreasing remarkably. A small fraction of emission is scattered within the cavity and is not coupled into the cavity modes. This emission with a constant peak wavelength of 640 nm coincides with the pure H2 film photoluminescence. Its intensity distribution overlaps with the angular range of the polariton emission. An enhancement of the emission into the LPB has been observed in organic microcavities before [68, 71, 198, 200, 202]. The explanation of this effect is based on the emission of a phonon, which enables the interbranch energy transfer. In Ref. [202], a Raman active mode of 74 meV is reported for another J-aggregate. This may explain the UPB depletion in a cavity with a Rabi-splitting of the same order [198]. Spectral Raman analysis of H2 has not been performed so far. Thus the polariton relaxation and the interbranch energy transfer is not confirmed for this material in a microcavity. A possible phonon in H2 would have an energy of the order of the Rabi-splitting of 110 meV. The large difference in UPB and LPB photoluminescence is supported by the high Q-factor due to the two DBRs. Explicit calculations of transfer rates in a low-Q microcavity ($Q = 90$) in [198] result in a photon lifetime exceeding the polariton transfer time by a factor of 2. Our structure is assumed to have an even higher Q-factor, which would increase this factor. In conclusion, this may explain the efficient energy transfer between the polariton branches and pure LPB emission.

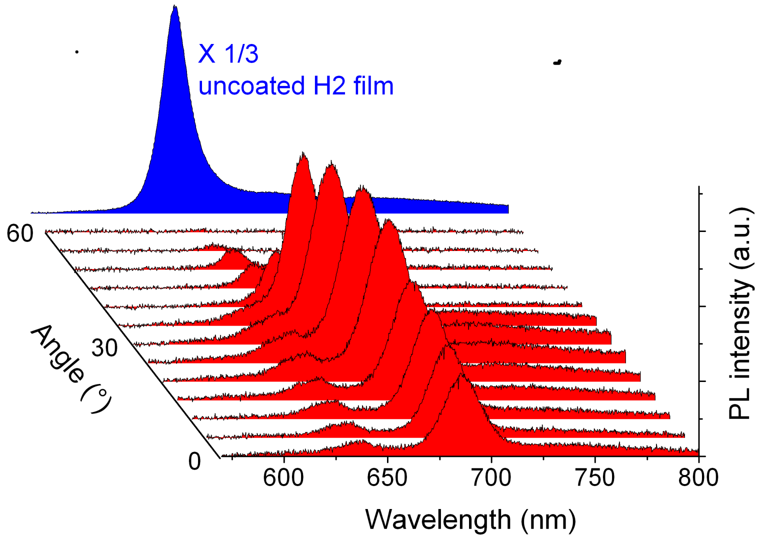

Figure 6.9: Angle dependent photoluminescence of a microcavity with an active cavity layer of the J-aggregate H2. The sample is excited by p-polarized 532 nm laser light (cw) and detected in s-polarization. Strong emission is only visible in the LPB with a maximum at 30°. An emission spectrum of an uncoated H2 film is included for comparison. At angles from 0° to 30° scattered light of H2 molecules contributes to the spectrum with a signal at 640 nm.

6.3 Organic VCSEL

6.3.1 Sample structure and linear transmission

The results presented in this Section are based on one fabrication series of high-Q organic microcavities. Here, two DBRs made by reactive electron-beam evaporation of SiO_2 and TiO_2 guarantee for a high reflection within the cavity with a maximum reflectance $R_{max} > 99.6\%$ of each single mirror. To obtain equal reflectance from both sides, the bottom mirror at the substrate side and the top mirror at the air interface consist of 10.5 and 9.5 layer pairs respectively (Fig. 6.10 a). The DBR design wavelength is with 690 nm slightly above the optimum that is given by the gain maximum of DCM at 615 nm [185]. Accounting for this deviation, the organic film of Alq_3 doped with 2% DCM is evaporated with a thickness of 670 nm. With an assumed refractive index of the compound of $n_{\mathrm{Alq_3:DCM}} = n_{\mathrm{Alq_3}} = 1.72$, the optical thickness reads $3.7\lambda/2$ for the wavelength $\lambda = 625\,\mathrm{nm}$. This odd-numbered optical thickness results in the generation of two modes in the DBR stop-band, one at about 625 nm and another at circa 710 nm (Fig. 6.10 b). The higher energy mode is applied for lasing as it overlaps with the DCM gain after strong optical pumping. A comparison with a transfer matrix calculation exhibits the presence of two spectrally separated cavity modes and strong transmission suppression within the stop-band that is hidden by the noise of the detector. The deviations between model and experiment in mode positions and intensities are mainly due to thickness variations in the DBRs from the ideal quarter wave optical thickness. In linear transmission experiments with a halogen lamp, the laser mode possesses a Q-factor of approximately 780. By applying the collimated white light laser beam from the amplifier system, the measured Q-factor increases up to 4500 in an extrapolation of the data to a zero spot size [190].

6.3.2 Threshold and emission characteristic

The organic dye composite of Alq_3 doped with 2% DCM is a small molecule solid state laser systems with one of the lowest lasing threshold. Nevertheless, very high optical excitation densities are necessary to achieve a gain that overcomes the losses in the system. This requires a pulsed light source with high pulse energy, short pulse length, and a low repetition rate to limit the molecular degradation on a short timescale. For this purpose, we use an amplifier laser system, which generates 200 fs long pulses at 400 nm with a repetition rate of 1 kHz (Sec. 4.2.2). Here, the laser wavelength is located at a maximum of the Alq_3 absorption and transmitted through the DBR. It uses the advantage of the DBR dispersion, which provides a stop-band of very high reflectance around the design wavelength and broad bands

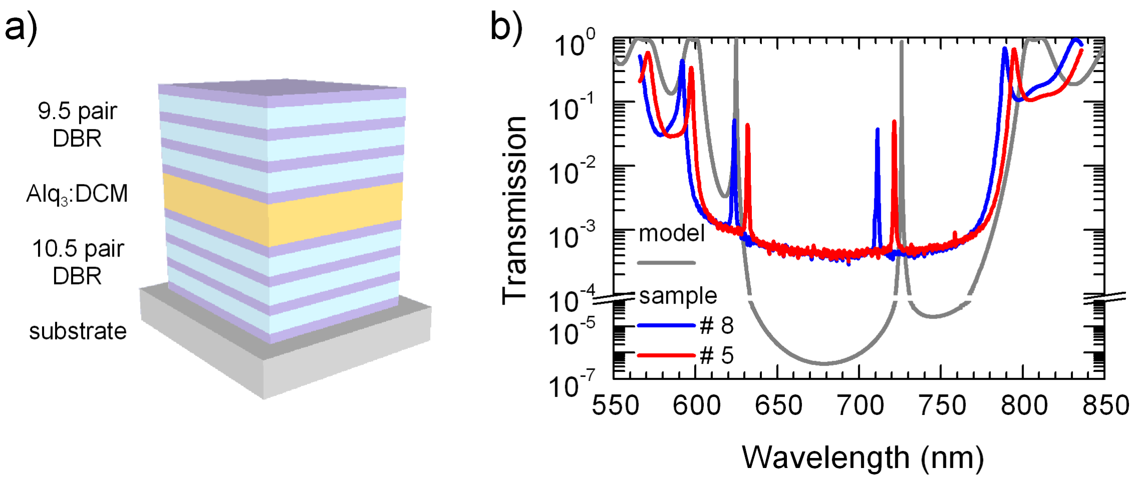

Figure 6.10: (a) Two TiO_2/SiO_2 DBRs surround the organic laser dye composite to form a high-Q organic VCSEL. (b) In transmission two modes appear in the stop-band, where the mode at the shorter wavelengths of around 625 nm is the laser mode. The spectra of two different samples produced in the same cycle show a mode shift due to thickness variations (blue and red). The measurements are compared to a transfer matrix calculation of a structure with a DBR design wavelength of 690 nm and an organic layer thickness of 670 nm (grey).

with high transmission at off-resonant wavelengths. Within the organic layer, the pump laser spot size is around 50 μm. The comparison of the incident intensity with the transmission and reflectance yields an energy storage in the microcavity of 90%. From these two values, we calculate the pump pulse excitation densities.

Figure 6.11 shows the input-output characteristics of the organic laser. At low excitation intensities, the microcavity emission increases linearly with the pump power. At a certain level, this linear behavior is superseded by an exponential output increase, which again goes into a linear regime at high excitation densities. The start of the emission outburst marks the threshold of the laser and thus the excitation level, where the gain in the organic material overcomes the losses within the complete structure. In the low excitation regime, the output is dominated by spontaneously emitted photons. In this mode, we observe a spectral linewidth of about 0.3 nm, which corresponds to a Q-factor of the microcavity of $Q = 2100$ (Fig. 6.12). The exact Q determination is limited by the wedge shape of the microcavity and the pump laser spot size of 50 μm. Both parameters in connection result in a broadening of the zero spot size diameter. A maximum Q-factor of $Q = 4500$ is approximated by a variation of the spot size and a subsequent extrapolation of the data. This enables the calculation of the cavity photon lifetime τ_{cav} by $Q = 2\pi c\tau_{cav}/\lambda$ with the emission wavelength λ as $\tau_{cav} = 1.5$ ps.

When increasing the pump power above the lasing threshold, a narrowing of the emission line is observed (Fig. 6.12). In spontaneous emission, all molecules

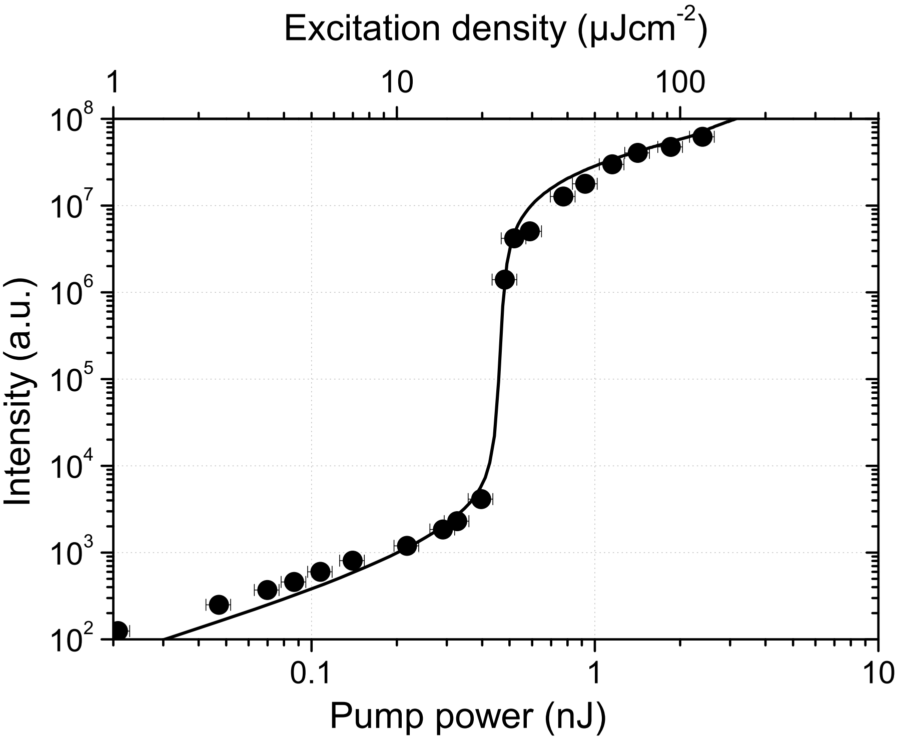

Figure 6.11: Organic VCSEL peak intensities as a function of the pump pulse power and density. The measurement (circles) is compared to rate equation model (line). From this plot, the laser threshold is determined as 0.4 nJ and 20 μJ/cm^2, respectively.

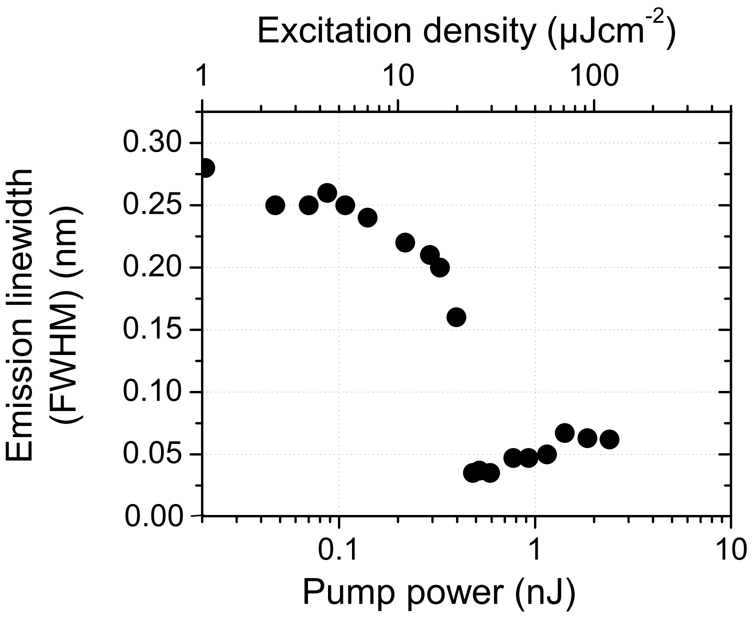

Figure 6.12: Linewidth of the microcavity below and above lasing threshold. Values above the lasing threshold are limited by the spectrometer resolution of 0.025 nm.

emit photons with arbitrary phase at the resonant mode. Position and linewidth are defined by the cavity only. After switching to the laser regime, most photons are emitted by a stimulation from photons that already oscillate in the laser mode. The amplification following is limited to a small spectral region, and in addition to the phase coupling, this results in a distinct mode narrowing. In our setup, the spectral resolution of the monochromator limits the exact determination of the laser linewidth. The measured 0.05 nm FWHM are therefore only the upper limit of the laser mode line width.

An additional feature of our laser is the directed emission normal to the surface of the microcavity. Due to this observation, the structure is referred to as an organic VCSEL. The origin of the small divergence is explained by the laterally limited inversion region. An amplification of the stimulated emission requires a number of photon round trips in the active medium. Only photons propagating in the vertical direction pass the active medium without leaving the excited zone. Light that is emitted in oblique directions is lost after few cycles in the laser area and does not contribute to the lasing process. In the near field, the electric field intensity of the laser mode can be expressed by a Gaussian function

$$E = E_0 \exp\left[-\frac{1}{2}\left(\frac{x}{D}\right)^2\right], \tag{6.2}$$

with the maximum electric field intensity E_0, the spot diameter D, and the lateral coordinate x. The near field distribution as the Fourier transform of the far field allows for the calculation of the spreading angle θ of the laser mode at the wavelength λ by

$$\theta = \arctan\left(\frac{\lambda}{2\pi D}\right). \tag{6.3}$$

If one assumes for our sample a gain region with a diameter of $D = 10\,\mu\text{m}$ at the laser wavelength of 625 nm, the spreading angle is calculated as $\theta = 0.6°$. Thus, in a distance of 30 cm, the laser beam has a diameter of 6 mm. This coincides with the observations and is a hint towards a lateral laser mode extension significantly smaller than the pumped area of 50 μm spot size.

6.3.3 Dynamics

The temporal development of the emitted laser pulses above threshold is investigated in an up-conversion experiment (Sec. 4.2.2). For this experiment, the 800 nm pulse of the amplifier is split in two laser beams. One beam is frequency doubled and used as the pump beam of the organic microcavity. The VCSEL emission is guided into another non-linear crystal and is added with the second beam, the gate beam, from the amplifier. Its temporal arrival can be varied by a delay stage in a range of approximately 500 ps. The time resolution of this experiment is given by the gate pulse length of about 200 fs.

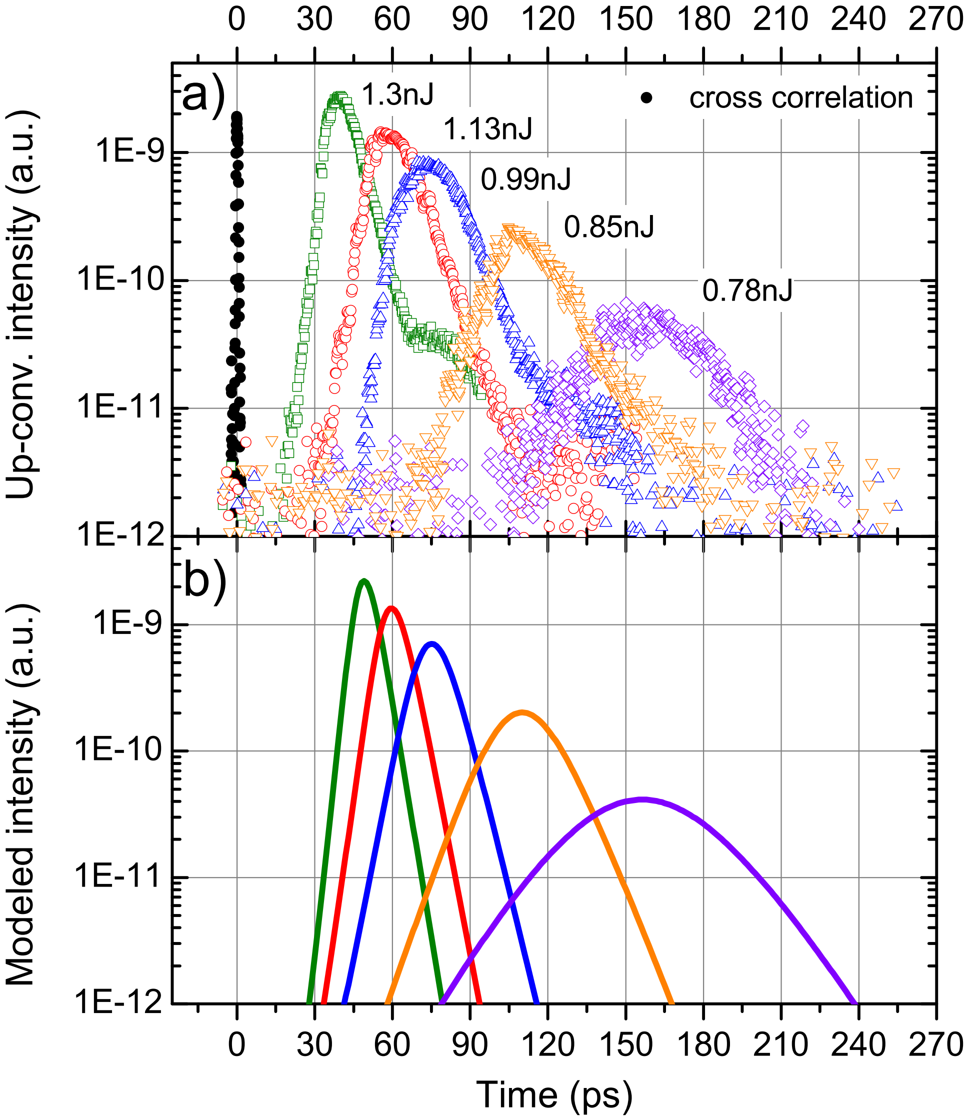

Figure 6.13: (a) Time-resolved organic VCSEL emission as measured by an up-conversion technique for pump powers above threshold. (b) The laser output is modeled by a set of rate equations for the different excitation energies.

Figure 6.13 a presents five time traces of the organic laser for different pump powers above threshold. At the lowest recorded pump pulse power of 0.78 nJ, the maximum output occurs about 150 ps after the arrival of the pump pulse with a pulse width of 60 ps. With increasing power, the VCSEL pulse appears earlier and exhibits a narrower temporal width. After a nearly doubling of the excitation power to 1.3 nJ, the organic laser shows the highest output 40 ps after pump pulse incidence with a reduced width of 14 ps. This temporal behavior is described as gain switching [205, 206], since the active medium is excited by a femtosecond pulse and the threshold is overcome nearly instantaneously for a short time in the picosecond range. The existence of the gain switched state is much shorter than the natural lifetime of the excited state as observed by the spontaneous emission lifetime. An additional requirement for gain switching is a short photon lifetime which is also fulfilled by $\tau_{cav} = 1.5\,\mathrm{ps}$. In our experiment, a 400 fs pump pulse excites a large number of Alq$_3$ molecules, which have a comparably long radiative lifetime of about $\tau_{\mathrm{Alq_3}} = 20\,\mathrm{ns}$. The excitation is non-radiatively transferred to the DCM molecules with a lifetime of $\tau_{\mathrm{DCM}} = 5\,\mathrm{ns}$. As the up-conversion data show, the laser emission occurs after several picoseconds and thus appears sufficiently earlier than the spontaneous emission.

With a delay of 40-70 ps after the maximum, a second peak appears in the up-conversion traces. This output with an intensity two orders of magnitude lower than the maximum is observed about 80 ps after pumping with 1.3 nJ and is also visible in other graphs. Probably, it is related to relaxation oscillations, where the upper laser level is increasing its population again when the photon number is below lasing threshold. In our sample, the main part of the excited states contribute to the first output laser pulse since the most excitons are transferred to the DCM before the first laser emission occurs.

The dynamics of the organic VCSEL are modeled by a set of rate equations. The first equation is attributed to the time dependence of the excited Alq$_3$ molecules, which present the reservoir of the organic laser. The evolution of the exciton population $N_a(t)$ in the lowest level of the first excited Alq$_3$ state is given by

$$\frac{dN_a}{dt} = -k_a N_a(t) - k_{tr} N_a(t). \tag{6.4}$$

Here, the depopulation is explained by the laser loss channel in the Alq$_3$ with the rate k_a and the transfer rate to the DCM molecules with the rate k_{tr}. Including radiative and nonradiative decays, k_a is approximated with $(16\,\mathrm{ns})^{-1}$. In a second equation, the dynamics of the excited DCM molecules N is described:

$$\frac{dN}{dt} = k_{tr} N_a(t) - k_e N(t) - c\sigma_{\mathrm{SE}} q(t) N(t). \tag{6.5}$$

The DCM state is filled by the transfer from the Alq$_3$ reservoir and the number of DCM excitons decreases with the rate $k_e = k_{e,r} + k_{e,nr}$ given by sum of radiative ($k_{e,r} = (5\,\mathrm{ns})^{-1}$) and non-radiative processes ($k_{e,nr}$ is a fit parameter), and via stimulated emission. This emission term is described by the current number of photons in the laser mode $q(t)$, the stimulated emission cross section σ_{SE}, and the vacuum speed of light c. The last rate equation considers the number of photons in the laser mode. First, its number is increased by the fraction β of spontaneously emitted photons in the laser mode with the rate $k_{e,r}$. The portion of the laser mode photons that is in the active medium at the same time is expressed by the confinement factor Γ. By the dominant process of stimulated emission, the photon number is amplified in dependence on Γ, c, $N(t)$, and $q(t)$. The photon lifetime in the cavity is given by $(k_{cav})^{-1}$ and the evolution of the photon number reads finally as

$$\frac{dq}{dt} = (c\Gamma\sigma_{\mathrm{SE}}N(t) - k_{cav})q(t) + \Gamma k_{e,r}\beta N(t). \tag{6.6}$$

For a concluding analysis, the rate equations are simplified to reduce the final number of coupled equations. From the solution of Eq. 6.4 $N_a(t) = N_{a,0}e^{(k_a+k_{tr})t}$, one can determine the pumping rate by $R(t) = k_{tr}N(t)$. The initial population is expressed by $N_{a,0} = A\frac{E_{pump}}{h\nu V}$ with the absorbed fraction $A = 0.9$ of the incident pump power E_{pump} at the pump laser frequency ν and the excited volume V. Unfortunately, the application of an initial population in the rate equation set prevents from a modeling of the relaxation oscillations. In Eqs. 6.5 and 6.6, a threshold density $N_{thr}(t) = \frac{k_{cav}}{c\Gamma\sigma_{\mathrm{SE}}}$ is applied for a redraft of the terms. The threshold density from the laser input/outout measurements is approximated with $N_{thr} = 5.5\times10^{17}\mathrm{cm}^{-3}$. The newly arranged formulas read now

$$\begin{aligned} \frac{dN}{dt} &= R(t) - k_eN(t) - \frac{k_{cav}N(t)}{\Gamma N_{thr}}, && (6.7)\\ \frac{dq}{dt} &= k_{cav}\left(\frac{N(t)}{N_{thr}} - 1\right)q(t) + \Gamma k_{e,r}\beta N(t). && (6.8) \end{aligned}$$

The rate equation set is solved by a numerical algorithm, where the remaining parameters $k_e = 1.3\,\mathrm{ns}$, $\Gamma = 0.31$ and, $k_{e,r}$ and $k_{tr} = 19\,\mathrm{ps}$ are applied as fit values of the up-conversion traces. The fraction of spontaneously emitted photons in the laser mode $\beta = 6\times10^{-4}$ is chosen to match the characteristics of the threshold curve. The final results of the calculated pulse shapes are presented in Fig. 6.13 b and the calculated threshold curve is directly compared to the measurements in Fig. 6.11. At this point, one has to add that this set of parameters, although it models the experiment accurately, is not necessarily the correct solution of the rate equation given. As extensively discussed in Ref. [207], it is not possible to find the optimal solution of the equations by an automatical fit procedure. By the manual fitting approach used here, the global minimum of the fitting parameter deviation can easily be missed. Additionally, the determination of the initial excitation density $N_{a,0}$ is of crucial importance for the final fitting values and potential inaccuracies will lead to incorrect estimates.

In summary, the results of the rate equation modeling should be taken with caution. Nevertheless, the results of the experiments and simulation will be discussed in the following Sections.

6.3.4 Threshold comparison

For the application of a certain laser design, a knowledge of the laser threshold is essential. It defines the pump power necessary to start lasing from the active medium. A low threshold is of special interest for organic solid state lasers. The limited photostability of organic dyes requires a low pump power for a long time operation. This is important since the medium is not circulating as in standard dye lasers that apply liquid solutions. Currently, much effort is made to create an organic laser diode. Up to now, such a device has not been demonstrated, which is mainly due to the high losses that occur to electric charges at high densities [99].

Lasing from the organic dye system Alq$_3$:DCM has been studied in several resonator configurations. This allows for a comparison of our results with other systems (Tab. 6.1). As a general feature, the threshold of lateral resonators is smaller than that of the VCSEL designs. Mainly, this fact is based on the excitation of a long stripe on the sample. The much larger gain length in these devices overcompensates the smaller optical confinement. Among the VCSELs, our design provides the lowest threshold. This is attributed to the higher Q-factor. Both other designs contain a silver mirror, which we replace by a DBR. This increase of the Q-factor from 420 [54] to 4500 [56] leads to a laser threshold decreased by one order of magnitude.

design	pulse energy (nJ)	pulse density (μJ cm^{-2})	reference
slab waveguide	1	1	Kozlov et.al. [208]
heterostructure	<1	1	Kozlov et.al. [156]
DFB	2	4	Riechel et.al. [107]
	n/a	10	Schneider et.al. [108]
VCSEL	40	300	Bulovic et.al. [54]
	n/a	400	Liu et.al. [55]
	0.4	20	Koschorreck et.al. [56]

Table 6.1: Laser threshold pulse intensities and densities of different sample architectures with the same active medium Alq$_3$:DCM. The sample of the author is shown in the last row.

For an estimation of the threshold injection current j_{thr} of a potential organic

VCSEL diode, one can use the expression:

$$j_{thr} = \frac{N_{thr}\, d\, e\, k_e}{\kappa}. \tag{6.9}$$

The current density depends on the threshold density N_{thr} in the active medium with the thickness d, the radiative decay rate k_e of DCM, the fraction of radiative excitons $\kappa = 1/4$, and the elementary charge e. Since it neglects any charge losses, this approximation gives only a lower limit of the current density. Assuming $N_{thr} = 10^{-17}\mathrm{cm}^{-3}$ and $d = 1\,\mu\mathrm{m}$, the threshold current density of $j_{thr} = 5\,\mathrm{kAcm}^{-2}$ exceeds a realistic value for an electrically pumped organic laser. Therefore, an enhanced design is needed in order to reduce the necessary pump power. One possible way is the reduction of the active volume by lateral structuring. By the formation of photonic dots in micropillars [209–211] and buried heterostructures [212,213], the mode volume and the laser threshold have been reduced in comparison with planar microcavities [214]. Up to now, only one experiment has been published with lateral structuring of organic microcavities [215]. This opens a new field for extended investigations on laterally structured organic VCSELs.

In the following, we discuss two parameters of the VCSEL that have an impact on the threshold: the confinement factor Γ and the spontaneous emission coupling factor β.

6.3.5 Confinement factor Γ

One of the fitting parameters in the laser rate equations describes the ratio of the resonant light in the active medium to the total light intensity of the laser mode. In an ideal laser, this confinement factor Γ equals unity. However, especially in microlasers with DBRs, the penetration depth into the mirrors reduces the amount of radiation in the active medium and thus Γ. From the fitting of the temporal output pulse shapes at different pump intensities, a confinement factor of $\Gamma = 0.31$ is obtained. Another approach for the determination of the confinement factor is the calculation of the internal electric field of the laser mode by a transfer matrix model.

Figure 6.14 presents the calculation of the electric field intensity for the laser mode in a model structure. The DBRs consist of $\lambda/4$-layers of SiO_2 and TiO_2 at the design wavelength of 690 nm. An organic film thickness of 670 nm results in two cavity modes, with the laser mode at 624.8 nm (Fig. 6.10 b). The electric field calculation shows the concentration of light in the active medium, but also the penetration of light into the DBRs. Fortunately, the light in the DBRs has the highest intensities in the less absorbing SiO_2 layers. The confinement factor

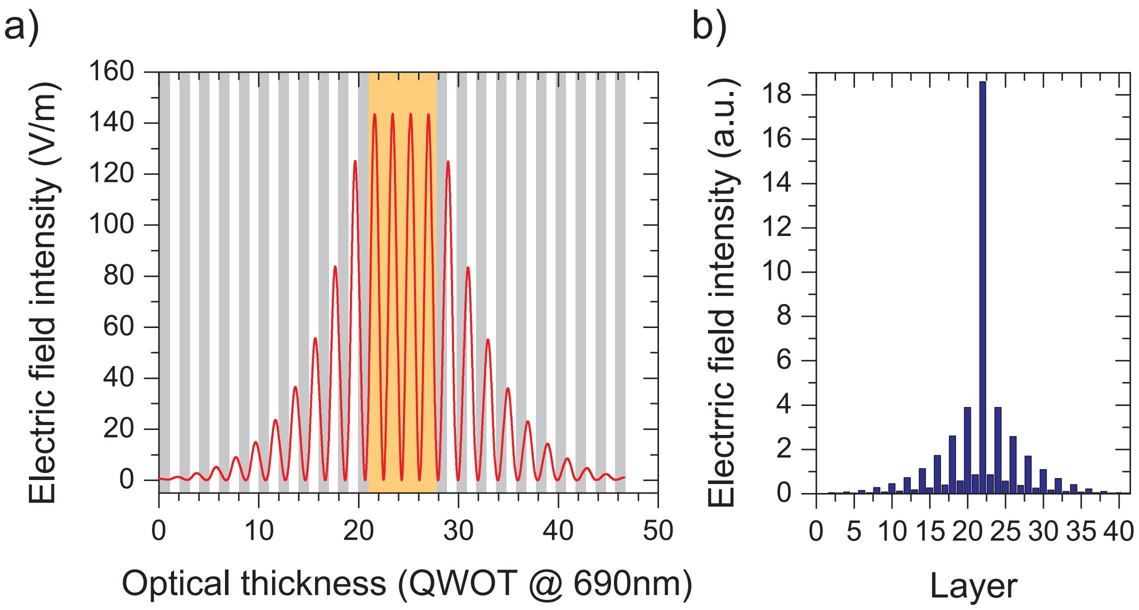

Figure 6.14: (a) Calculated electric field intensity of the laser mode in the investigated OVCSEL. The calculation is performed for the 624.8 nm mode for the structure shown in Fig. 6.10 with the design (1T 1S)10 1T 6.6A (1T 1S)9 1T. Light is incident from the right side and the optical thickness is plotted for the DBR design wavelength of 690 nm. Positions of high refractive TiO_2 layers (grey) and the active Alq_3:DCM layer (orange) are shown in the background. (b) In a plot of the electric field per layer, the concentration of the light in the active zone is demonstrated - a consequence of the 670 nm thick organic layer. As a further advantage, the light in the DBRs is mainly stored in the low absorbing SiO_2 films.

from this transfer matrix approach is $\Gamma_{TM} = 0.41$, which is higher than in the rate equation fit. It has to be commented that in the transfer matrix calculation a perfect layer match in the DBRs is assumed. This and other variations between model and real structure can constitute the different results.

Since Γ is one of the factors which enhance the stimulated emission in a laser, this value should be maximized in order to reduce the laser threshold. The simplest method to achieve this goal is the enlargement of the active medium. This can be done in two ways. As the most effective appears the maximization of the organic film between the two mirrors, where the electric field and the interaction between laser mode and inverted molecules is highest. In fact, a rather large organic film thickness is required in this approach. From another point of view, this thickness increase seems not very promising as already 90% of the pump light is absorbed in the current film with approximately 2λ optical thickness. The second way is based on the varying electric field distribution in the DBRs. As demonstrated in Fig. 6.14, most light is concentrated in the lower refractive index layer in the mirrors. A replacement of the SiO_2 layers by Alq_3:DCM would bring another low index layer and active material in positions of a high electric field. With this method, the thickness of the active medium between the mirrors needs no further increase. A threshold reduction of 30% has already been demonstrated by this method with active DBRs [216]. Due to the inverse proportionality of threshold and Γ, the minimum laser excitation density can be reduced by a factor 3 with an optimization of our VCSEL design.

6.3.6 Spontaneous emission coupling factor β

In the organic VCSEL presented, the external pumping of $\mathrm{Alq_3}$ and the subsequent relaxation and transfer of the energy to DCM create an inverted system. Lasing will occur from the inverted system, when the emission is stimulated and amplified by photons propagating in the laser mode. The only process that generates this photons is the spontaneous emission of excited DCM molecules. In a microcavity, the spontaneous emission is enhanced for a number of modes. For a laser, the fraction of spontaneously emitted photons that contribute to lasing is defined by the coupling factor β with

$$\beta = \frac{\text{spontaneously emitted photons into laser mode}}{\text{total amount of spontaneous emission}}. \tag{6.10}$$

A coupling factor equal to unity would create an ideal thresholdless laser [217]. This is difficult to achieve. In standard lasers, β is usually several orders of magnitude smaller. This means that the number of excited states is reduced drastically before the amplified stimulated emission starts in a pulsed regime. As a consequence, the pump intensity has to be increased to overcome the losses and to exceed the laser threshold. The influence of β on the input-output characteristic of microcavity lasers has been studied by rate equation modeling [207,217]. Whether inorganic or organic VCSEL, the threshold increases approximately inversely proportional to β.

The fitting of the temporal emission traces leads to $\beta = 6 \times 10^{-4}$. This low value is confirmed by the modeling of the same measurement with a different set of rate equations [207]. There exist several approaches for the theoretical calculation of the coupling factor. The analytical formulas presented in Ref. [218] give an insight into the relations on the cavity linewidth and the emission linewidth of the excited molecule. Unfortunately, they are not easily applicable to our or system with an inhomogeneously broadened emission spectrum. Another method is the calculation of the overall emission by the plane wave expansion method (Sec. 3.3). It enables also the determination of the spontaneous emission into the laser mode. The disadvantage of this method is the approximated mode intensity for internally propagating waves (Sec. 3.3.2) and the assumption of an infinitely laterally extended pump region. Nevertheless, the results of a simulation of our structure allow an approximation with $\beta \ll 10^{-3}$.

A further approach relies on an extended mode counting [219, 220]. Here, the β-dependence on the lateral size and the emission linewidth is analyzed. The results of $\beta \approx 10^{-4}$ coincide also with our fitting value. All approaches demonstrate that the broad emission spectrum of DCM ($\Delta\lambda_{\mathrm{DCM}}$ =130 nm) and the one-dimensional optical confinement reduce the coupling factor β. Therefore, a lateral confinement of the active regions seems essential for the reduction of the laser threshold. In current experiments, β-factors of β up to 0.28 have been demonstrated in inorganic micropillar cavities [214]. This value is orders of magnitude above the value of our organic VCSEL and shows the potential of lateral dimensioning.

6.3.7 Anisotropic mirrors and polarization splitting

Besides the already discussed laser parameters of threshold, linewidth, vertically collimated emission, and temporal behavior, the polarization of a laser is an additional device characteristic. In a perfect VCSEL that offers a radial symmetry along the emission direction, no preferred polarization exists. This typical problem of a VCSEL results in an arbitrary polarization of the emission with two competing orthogonally polarized modes [221–223]. Usually, this instability is overcome by the introduction of an asymmetry in the laser structure. The asymmetry of very different nature can be included, for example, by external strain [224], oxide apertures [225], asymmetric geometries [226], quantum wires [227], or a tilted pillar structure [228].

In our structure, the asymmetry is created by an oblique deposition angle of about 15° during the DBR fabrication. This leads to an anisotropic distribution of material on the substrate. Under these conditions, the dielectrics form columnar structures inclined at a certain angle with respect to the deposition angle. As discussed in Sec. 4.1.4 and 5.5, dielectric mirrors consisting of such anisotropic layers contribute to the formation of two perpendicularly polarized cavity modes in microcavity structures. Thus, by varying the deposition angle, the spectral distance of the two modes can be tuned over a certain range. In contrast to the anisotropic passive microcavities, the organic cavity layer of the VCSEL is most likely isotropic. This means that only the anisotropic mirrors influence the polarization dependence of the laser mode structure. Therefore, the mode splitting is smaller than in the passive structures with an anisotropic cavity layer.

Figure 6.15 presents the two mode emission following optical pumping with 400 nm radiation above the laser threshold of 0.7 nJ pump pulse energy. The modes are spectrally positioned at 612.46 nm and 612.69 nm, with linewidths of 0.056 nm (45 GHz) and 0.05 nm (40 GHz) FWHM, which is on the order of the spectrometer resolution. Both laser lines exhibit an apparent line splitting of 0.23 nm or 180.6

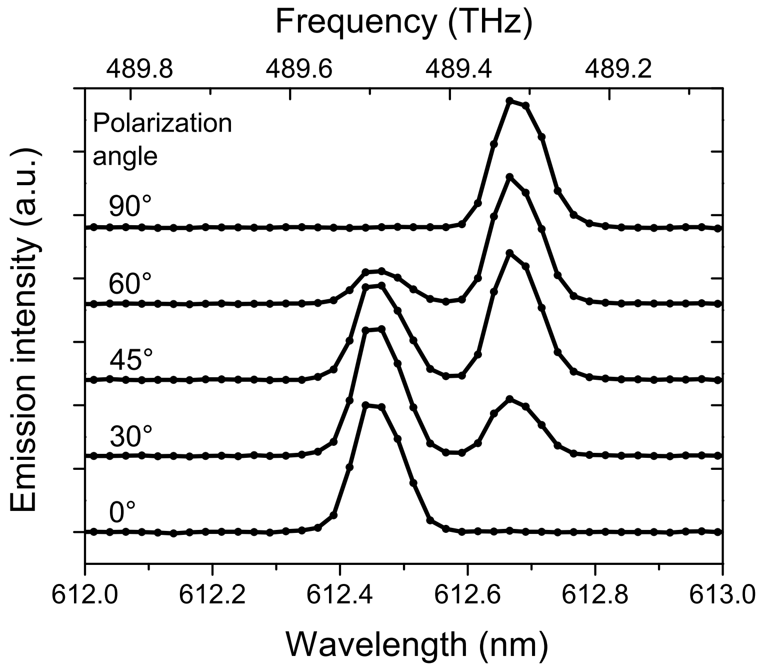

Figure 6.15: Normalized microcavity laser emission spectra in dependence of the polarizer angle. Two laser lines are observed, with either maximum at 90° and 0°. Both modes are spectrally separated by $\Delta\lambda = 0.23\,\mathrm{nm}$ or $0.18\,\mathrm{THz}$

GHz. Additionally, they are perpendicularly polarized with a particular polarization ratio above 100:1.

The influence of the anisotropic mirrors on the mode structure can be analyzed by the transfer matrix method. It is applied to the calculation of the resonance wavelength and the phase shift of the two polarizations. We have already discussed that the mode positions in transmission and internal emission are equal. However, for the phase behavior one has to include additional assumptions. In the transfer matrix model, the light source is positioned at the substrate interface of the bottom DBR. The light of this source has an equal phase for all wavelengths. After the transmission through the first DBR, this behavior is only slightly influenced. A DBR provides only a weak phase dispersion around the design wavelength, as discussed in Sec. 2.3. A phase shift of 180° for the transmitted light at frequencies around the design wavelength follows. In contrast to the DBR, a complete microcavity shows a 180° jump in the phase shift at the cavity resonance (Sec. 2.4). Since the DBRs provide only a weak phase dispersion, the jump is attributed to the cavity layer. This means that the light enters the cavity layer with equal phase and during the oscillation inside the cavity, the phase is differently shifted. After the transmission through the total structure, the light with wavelengths above the resonance is 180° shifted with respect to the light below the resonance wavelength.

Therefore, a reversal of the light path results in a phase jump of the emitted light. A light source inside the cavity layer, which emits without a phase dispersion, provides a jump of the phase shift outside the structure. With this assumption, the transmission phase shift of the organic VCSEL is calculated and subsequently transferred to emission. This model is supported by own extensions of the plane wave expansion method (Sec. 3.3) to the phase of emitted radiation.

For the simulation of the anisotropic laser device, two structures with same layer thicknesses, but different refractive indices are used for the DBR-layers. In the model, the light source is situated at the substrate-DBR border and the transmitted phase is calculated for the DBR-air interface. The dispersion of the optical constants is neglected. This is justified by the narrow spectral region of the laser emission. The optical constants of the dielectric materials are taken from the ellipsometric measurements of films deposited at right angle (Sec. 4.1.2). The real refractive index value for TiO_2 is in the model $n_{1,\mathrm{TiO_2}} = 2.17$ with an additional extinction coefficient of $k_{1,\mathrm{TiO_2}} = 1 \times 10^{-4}$. For SiO_2, the values determined are $n_{1,\mathrm{SiO_2}} = 1.45$ and $k_{1,\mathrm{SiO_2}} = 2 \times 10^{-6}$. The design wavelength for the mirrors is chosen to be 680 nm and all DBR layer thicknesses are $\lambda/4$. The active layer of Alq_3 and DCM is modeled with the refractive index $n_{\mathrm{Alq_3}} = 1.72$ with the imaginary part $k_{\mathrm{Alq_3}} = 1 \times 10^{-4}$. The absorption-free substrate is modeled with $n_{\mathrm{Sub}} = 1.52$. To obtain a mode at 612.46 nm, an organic layer thickness of 655.49 nm is required. This layer thickness then represents approximately $3.7\lambda/2$.

To model perpendicular polarization, the refractive indices of the DBR layers are shifted such that the cavity mode is located at 612.69 nm. As a further constraint, the ratio of the two material refractive indices are kept constant. This assumption is supported by considering the columnar growth of both materials as equal. The resulting values are $n_{2,\mathrm{TiO_2}} = 2.1715$ and $n_{2,\mathrm{SiO_2}} = 1.4510$. This demonstrates that a refractive index variation of the order of 10^{-4} can explain the polarization splitting.

The results for the transmission phases $\phi_m(\omega)$ of each mode m are presented in Figure 6.16 b. The emission intensities $I_m(\omega)$ are obtained from the measured emission spectrum (Fig. 6.15) and fitted with a Gaussian function (Fig. 6.16 a). Their positions are 2024.38 meV ($\lambda_1 = 612.46$ nm) and 2023.62 meV ($\lambda_2 = 612.69$ nm), with an equal width (FWHM) of 0.26 meV (0.08 nm) and a maximum intensity ratio of 0.76.

6.3.8 Terahertz beating and mode coupling

The dynamics of the laser emission from the anisotropic VCSEL are studied by the same up-conversion technique as for the single mode (Sec. 6.3.3). As an additional optical element, a $\lambda/2$-plate is installed to rotate the polarization axis of the VCSEL emission. Since the up-conversion process requires the same polarization of gate and

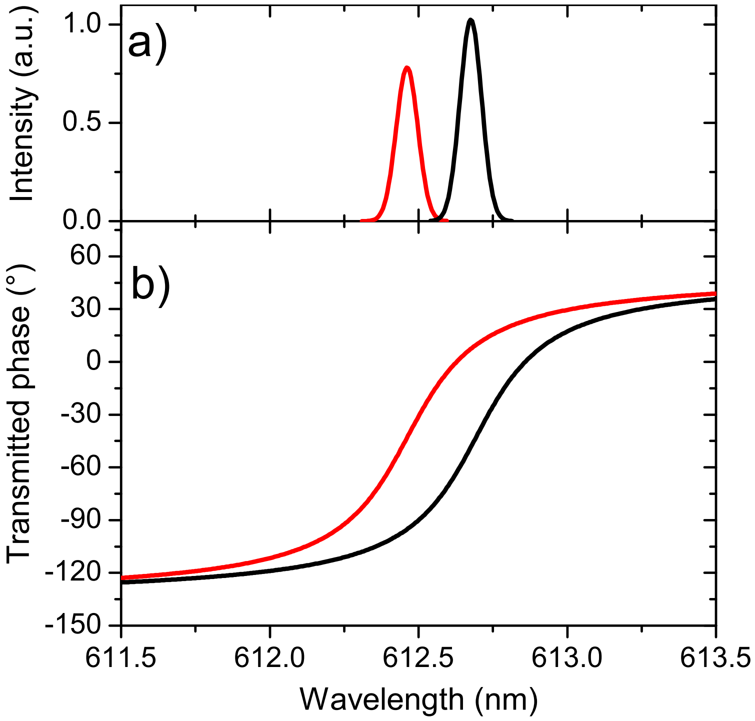

Figure 6.16: The fitted intensities (a) and the corresponding calculated phases (b) of the two emitted laser modes as used for the Fourier transform model. The two Gaussian lines represent the two emission modes. The phases of transmitted light for two microcavities with corresponding resonance frequencies. Around the resonance wavelength a phase shift of ∼ 150° occurs.

signal pulse, the $\lambda/2$-plate enables the selection between one or two contributing laser modes to this process. By this method, the two modes can either be studied independently or their sum signal is analyzed with a variability of their respective amplitudes.

Figure 6.17 depicts the up-conversion signal of a single mode and the sum signal of both laser lines from the organic microcavity. The single mode exhibits the typical time dependence of single pulse emission. By a 45° rotation of the polarization of the emission, the up-conversion pulse shows an intensity modulation in time. The frequency of this beating corresponds with the mode splitting of 0.18 THz.

Every data point of the up-conversion experiment is the result of the signal integration over several seconds. At a laser repetition rate of 1 kHz, thousands of single pulses contribute to each point of the temporal spectrum. The sum signal detects the interference phenomena of the two modes that do not average out. Further, every pump pulse newly excites a totally relaxed electronic Alq_3:DCM system. Nevertheless, there occur intensity minima and maxima at certain delay times. This implies that the phases of both modes are reproducibly coupled. Would this not be the case, the averaged sum signal should look like the single mode signal.

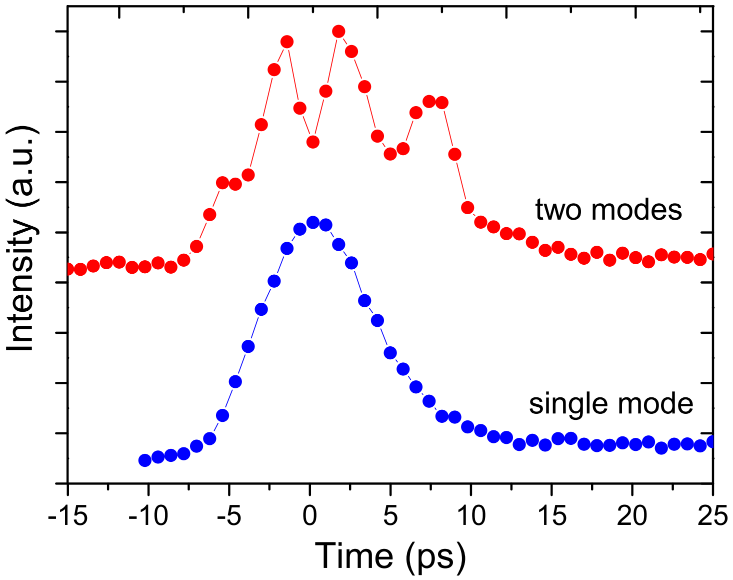

Figure 6.17: Measured up-conversion with two laser modes (top) contributing to the up-conversion signal with clearly visible interference oscillation at 5.5 ps period time, and with one mode (bottom). Each dot represents a single up-conversion measurement over several thousand pulses.

For the analysis of the up-conversion results, two models are used. The first approach applies an extended formulation of the rate equations presented in Sec. 6.3.3. Another simulation is based on the Fourier transform of the measured emission and the spectral phase shift of the laser.

In the extended rate equation model, the electrical field is reconstructed by a sum of two perpendicular polarized single pulses, considering their temporal phase. The time-dependent sum signal of the up-conversion experiment $E(t)$ reads now as

$$E(t) = \sum_{m=1}^{2} \sqrt{I(t)} A_m \cos\theta_m \mathrm{e}^{i(\omega_m t + \phi_m)}, \tag{6.11}$$

where ω_m is the mode angular frequency, θ_m is the angle of the mode electric field with respect to the polarization plane of observation and $I(t)$ is the single mode photon number function. The angle θ_m accounts for the oscillation contrast. With $\theta_1 = \theta_2 + 90°$, one obtains maximum contrast at $\theta_1 = -\theta_2 = 45°$. A_m is an amplitude factor. In the calculations, A_2 and ϕ_2 are considered as fit parameters and $A_1 = 1, \phi_1 = 0$. Mode wavelength and splitting frequency are taken from the laser emission spectrum in Fig. 6.15. Spectrum and fitting procedure yield $A_2 = 0.2$, $\phi_2 = 0$, $\hbar\omega_1 = 2024.37\,\mathrm{meV}$ ($\lambda_1 = 612.46\,\mathrm{nm}$), $\hbar\omega_2 = 2023.62\,\mathrm{meV}$ ($\lambda_2 = 612.69\,\mathrm{nm}$). The amplitude square of the resulting electric field is plotted in Fig. 6.18.

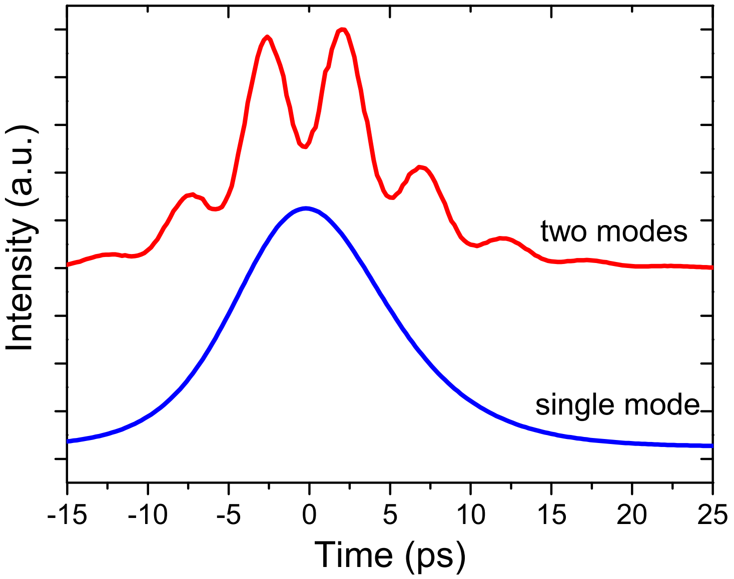

Figure 6.18: Results of rate equation based model for one (bottom) and two (top) contributing laser modes to the up-conversion signal.

In the rate equation approach, the experimental results are reasonably reproduced. Oscillation frequency and pulse length can be derived. Unfortunately, the initial phase of the emission is a fitting parameter and therefore postulated. In the Fourier transform approach following, the emission intensity and the phase results from the previous Section are included (Fig. 6.16).

Both fields with their corresponding phase can be added up as they are emitted at the same time with a defined phase relation. Having constructed an electric field including spectral phase allows then to perform a Fourier transform

$$E(t) = \int_{-\infty}^{\infty} \sum_{m=1}^{2} \sqrt{I_m(\omega)} e^{i\phi_m(\omega)} d\omega, \tag{6.12}$$

to find the expected temporal behavior $E(t)$ of the system.

The results of the following Fourier transform are depicted in Fig. 6.19. The approach reproduces the characteristic occurrence of four major peaks at a periodicity corresponding to the spectral distance of the two peaks, with a Gaussian envelope with 11 ps duration. The results also show that it is indeed possible to model the cavity behavior with a Fourier transform approach based on the transmitted phase. Two calculations for equal initial phases and a phase difference of

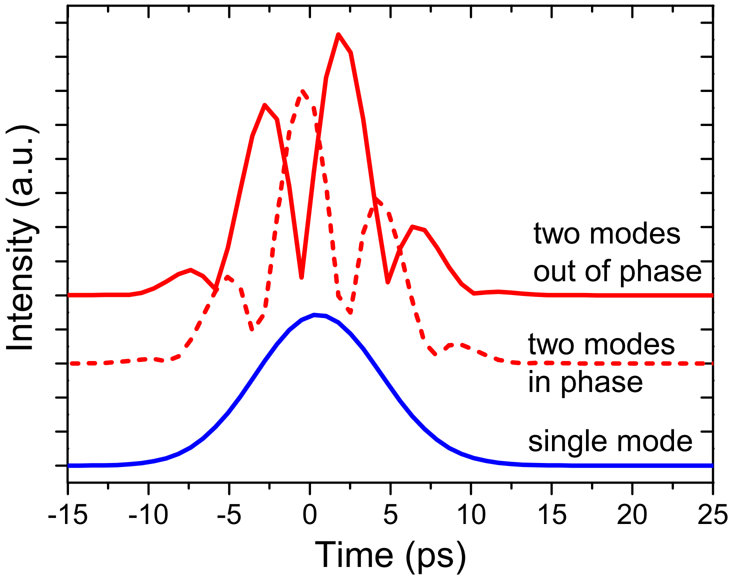

Figure 6.19: Fourier transform of one (bottom) and two contributing laser modes with Gaussian spectral shape. The temporal behavior shows a dependence on the initial phase relation. In the out of phase signal (top) the beating pulse with the maximum intensity occurs later than in the in phase transformation (middle).

$\Delta\phi = \pi$ are compared with the experiment in order to demonstrate the influence of this parameter. However, the coincidence between the experimental results and the Fourier transform including a π-phase difference allows no conclusion about the initial phase relation. In the up-conversion experiment, the phase relation between the two VCSEL modes at the position of the non-linear crystal is measured. With a frequency of 0.18 THz, the sum-frequency signal has a wavelength of 1.7 mm. A position variation of the non-linear crystal over this distance would cover all possible phase differences for a certain detected delay time.

The calculations by the rate equation approach and the Fourier transform based model represent the intensity of the sum-frequency signal at the position of emission. This position is not accessible in the up-conversion experiment, which therefore allows no detection of the initial phase relation.

For the explanation of the mode-coupling mechanism, a model based on the coupled-mode theory [229] is applied in Ref. [190]. Here, the coupling is attributed to the anisotropic DBRs, which have optical properties similar to Šolc-filters that rotate the polarization of the modes, during the propagation in the DBR. The response in the dielectric materials on the two oscillating optical fields is driving the coupling of previously perpendicularly polarized modes.

In this work, another description of the coupling mechanism is suggested. The main difference to the former model is the assumption that the coupling occurs mainly in the active material. As demonstrated in the experiments on passive and active microcavities in the previous Sections, the anisotropy in the refractive index of the DBRs is resulting in two perpendicularly polarized modes traveling along the normal axis of the sample. In laser emission, these two modes have a Gaussian spectral shape (Fig. 6.15) that weakly overlap. After pumping above laser threshold and energy transfer to the DCM molecules, spontaneous emission into the normal modes starts the lasing process. Excited DCM molecules with a dipole moment deviating from the polarization of the two laser modes can be stimulated to emit in either of the two modes. With higher probability, the photon is emitted into the mode of stimulation. However, a small amount of modes is afterwards propagating in the perpendicularly polarized mode.

If the modes have different Q-factors, lasing will start in the mode with the highest Q-factor. By the coupling, this additionally initiates the amplified stimulated emission in the other mode with a certain temporal delay. Since lasing is started in both modes by the same photons, the emission of the two laser lines is coupled in phase. Later, when the photon population is strongly increased in both modes, the modes are synchronized by the strong internal electric field. The electric field vector as the sum of both orthogonal fields is oscillating in time and changing between linear, elliptical and circular polarization (see description in Sec. 5.5 and Fig. 5.16). As the emission process into the laser modes is driven by the electric field oscillating with the same frequency, the laser process in both modes is coupled by a periodic variation of the internal field.

In summary, a number of new effects have been investigated in the experiments on the organic VCSEL. First, a gain-switching mechanism has been demonstrated that leads to an emission of laser pulses with a length of approximately 10 ps with a wavelength of around 630 nm after optical pumping with a femtosecond laser system. In this device, a high Q-factor of the cavity modes combines a low laser threshold ($0.7\,\mathrm{nJ}/\,20\,\mu\mathrm{Jcm}^{-2}$) with a very narrow linewidth of about 0.05 nm and a small beam divergence with $\theta < 1^\circ$. By the application of a rate equation model, the dynamics of the photon number evolution is successfully explained. Furthermore, an optical anisotropy in the DBRs leads to two orthogonally polarized laser modes with different wavelengths. This behavior stabilizes the polarization of the organic VCSEL and additionally leads to an optical beating of the sum-frequency signal. As demonstrated in an up-conversion experiment, the two perpendicularly polarized modes are phase coupled. Therefore, the spectral distance of the coupled laser modes allows the generation of a signal beating with terahertz frequencies. This oscillation can be reproduced in the pulsed excitation regime of the organic laser. A potential continuously emitting VCSEL with anisotropic mirrors would be a stable light source for the generation of highly monochromatic terahertz emission by a photomixing process. The beating frequency is widely tunable by the anisotropy in the DBRs and thus the fabrication conditions, which make this device a promising candidate for the application in terahertz spectroscopy.

7 Conclusion and outlook

This thesis is focussed on the development of novel planar microcavities, their design, fabrication, and experimental as well as theoretical analysis. The combination of standard evaporation techniques and optical measurements provides new insights into the unique linear and ultrafast processes related to this attractive class of micro devices. High quality microcavities, whose fabrication is enabled by the implementation of an optical setup for in-situ layer thickness measurement are successfully applied for the confinement of incident and internally generated light. In transmission measurements with pulsed laser light, the storage of electromagnetic waves for a resonant cavity mode is demonstrated by an optical gating experiment. By applying an additional technique to the standard linear transmission measurements, the photon lifetime is verified in a different and more direct manner.

With an oblique angle deposition technique, a slight optical anisotropy, tunable by the process conditions, is introduced into the dielectric layers. Conventional microcavity with a single resonator layer provide only a single mode. A single cavity with anisotropic layers shows two modes with different resonance frequencies and orthogonal polarization. With a spectrally aligned pulsed laser source, both modes can be excited simultaneously and a beating of the transmission signal is observable in a photomixing experiment. By a variation of the anisotropy within the cavity forming optical films, the spectral mode distance is widely tunable and the beating frequency is variable typically in the terahertz range.

Following the passive cavity experiments, the properties of organic dyes within such optical resonators are investigated. It is demonstrated that organic semiconductors, whose optical properties were extensively studied in free space and bulk material for decades, are subject to drastic changes after their implementation into microcavities. Their formally broad spectral emission is narrowed and accompanied by a shortening of the radiative lifetime in the weak-coupling regime. Laser emission from an organic dye compound is recorded with an extremely narrow linewidth, small beam divergence, and picosecond output pulse duration after high power pulsed laser excitation. A reduced threshold is obtained by high quality dielectric layer stacks in comparison with similar layer designs. By a further improvement of the layer fabrication, an additional reduction of the laser threshold can be expected even in one-dimensional designs. The high accuracy and low complexity of the vertical layer fabrication process make organic vertical cavity surface emitting lasers a competing candidate for electrically pumped organic lasers. In cavity lasers with birefringent mirrors, stimulated emission at two perpendicular modes is observed with a strong phase correlation. With this design, which is not restricted to organic cavity lasers, a new way for the generation of terahertz light based on sum-frequency mixing is opened. Applied in cavity lasers, with either organic or inorganic active media, a micrometer sized device creates pulses with terahertz beating usually demonstrated in macroscopically extended resonator configurations. Additionally, this new cavity assembly prevents the spontaneous polarization switching typically observed in cylindrical symmetric lasers. An utilization of anisotropic dielectric mirrors in standard lasers with long cavities is also conceivable.

In further experiments, coupled microcavities are investigated with respect to their multimode transmission and emission qualities. In contrast to anisotropic single cavities, a design with two coupled resonators provides two modes with equal polarization, thus allowing for optical Bloch oscillations within the structure. Optical Bloch oscillations with terahertz beating are verified with the same setup utilized for the terahertz generation in anisotropic cavities.

All experiments are accompanied by various theoretical models. Linear transmission, reflection, and absorption properties are described by the transfer matrix algorithm, which also enables the determination of the materials optical constants as well as the layer thicknesses, in-situ and ex-situ. The transfer matrix method extended by a plane wave expansion approach is the basis for the analytical explanation of the cavity photoluminescence in the weak-coupling regime. The temporal emission evolutions of the lasers is described by a set of rate equations. A model for the calculation of time resolved transmission and optical beating traces is demonstrated by a combination of transfer matrix and Fourier transform analysis. Furthermore, time resolved spectroscopy measurements are explained by an extended Fourier transform algorithm providing insights into beforehand non perspicuous physical properties.

After completion of this work, a number of open questions remain leaving tasks for future projects. At the moment, best efforts are made to create organic laser diodes. The presented VCSEL structure is only one possible configuration. As demonstrated within this work, the laser threshold of an organic VCSEL is comparable with other designs. However, it is far away from the requirements for an electrically driven laser, which is at least three orders of magnitude below the current value. One possible way for a threshold decrease is lateral structuring of planar microcavities in order to further reduce the number of modes [215, 230]. This approach increases the spontaneous emission coupling factor β of the laser. A different way to gain a lower laser threshold is the increase of optical confinement factor Γ, which gives the fraction of the mode volume in the active medium. For example, the implementation of active media in the DBRs can increase Γ significantly.

A completely different concept of coherent light generation is the polariton laser [231–233]. In this device, a dense degenerated Bose gas of polaritons is formed in a microcavity. In optically pumped systems, a laser threshold decrease of two order of magnitude has been demonstrated in comparison with a conventional photon laser. The application of the polariton laser concept in electrically driven systems can be realized by hybrid structures [234, 235]. In such a device, inorganic quantum wells can provide polaritons after electrically pumping and transfer the quasi-particles to organic layers. Afterwards, the polariton population in the organic material can be used to create stimulated emission with a low laser threshold.

The reduction of the laser threshold is not the only option on the road to the electrically pumped organic laser. Currently, a low threshold is required by the limited photostability and conductivity of organic materials. The photostability is improvable by an enhanced encapsulation that prevents from an interaction with oxygen and water. In an organic VCSEL, this can be realized by the implementation of encapsulation layers in the DBRs. Already the microcavity lasers presented within this thesis provide a higher photostability in comparison with bare organic films.

The applicable maximum current density for the operation of an organic diode is limited by the conductivity of the total structure. At the present time, losses and annihilation processes limit the generation of high carrier densities and lead to a material deterioration. Further investigations are required in order to understand the internal electrical processes, their relations, and limitations. At the same time, new concepts of carrier transport and layer arrangement have to be proven. New designs of organic transport layers and recombination zones that differ from a standard OLED may reduce the path length of electrons and holes and may overcome the conductivity limitations. In summary, the realization of an organic laser diode requires a parallel improvement of the laser threshold and on the opposite an enhancement of photostability and conductivity.

Within this thesis, a terahertz pulsing of laser emission has been demonstrated. By the coupling of two energetically different modes in an organic VCSEL with anisotropic mirrors, laser pulses with a length below 3 ps have been demonstrated. This pulse length can be further reduced, if the number of coupled modes is increased. A possible design for this purpose are coupled microcavities. Coupled microcavities with two resonator layers and anisotropic DBRs provide four modes. If all modes are equidistant in energy and properly coupled, pulse length below one picosecond are achievable. By the application of wedge shaped cavity layers, triple cavities can be fabricated with low requirements on the layer thickness accuracy. A possible number of six coupled laser modes may further reduce the pulse length. Beside the challenging fabrication of coupled microcavity lasers, a deeper understanding of the phase-coupling mechanism is essential. The two approaches presented so far for the anisotropic organic VCSEL cannot describe all observations. Furthermore, a rate equation model that considers the phases of contributing laser modes has to be developed.

A challenging project for the improvement of dielectric mirrors is the application of rugate filter designs [12, 236, 237]. In rugate filters, the refractive index is varied continuously or gradually in contrast to the step-like change in standard DBRs with $\lambda/4$-layers. The additional degree of freedom in the structure design enables the customization of the optical properties. For example, mirrors with high reflectance stop-bands and spectrally broad bands of high transmission can be realized. This is an alternative for optically driven devices, where currently a certain amount of the incident light is reflected by reflectance modes outside the stop-band.

The present work demonstrated that even a century after its invention, the simple planar resonator design is still applicable for the investigation of new optical effects. Applications relying on effects investigated within this work are imaginable for coherent light sources as organic lasers or terahertz modulators for distance measurement, sensors, and optical computers.

Appendix

A.1 Fourier transform

The Fourier transform $\mathcal{F}$ is an integral transform that connects a continuous function $f(t)$ with its corresponding function $F(\omega)$ in the frequency domain. The Fourier transform to the frequency domain is given by

$$F(\omega) = \int_{-\infty}^{\infty} f(t)\, \mathrm{e}^{-i\omega t} dt = \mathcal{F}\{f(t)\} \tag{A.1}$$

and its inverse Fourier transform is defined as

$$f(t) = \frac{1}{2\pi} \int_{-\infty}^{\infty} F(\omega)\, \mathrm{e}^{i\omega t} d\omega = \mathcal{F}^{-1}\{F(\omega)\}. \tag{A.2}$$

After introducing the definitions of the transform some rules for the calculation with Fourier transforms should be discussed.

Linearity. The transform of the sum of two functions is the sum of the respective transforms

$$\mathcal{F}\{\alpha f(t) + \beta g(t)\} = \alpha\{F(\omega)\} + \beta\{G(\omega)\}. \tag{A.3}$$

Convolution. The product of two Fourier transforms is the transform of their convolution

$$\mathcal{F}\{f(t) * g(t)\} = F(\omega) \cdot G(\omega). \tag{A.4}$$

Similarity. The compression of the coordinate in one domain elongates the adequate coordinate in the other

$$\mathcal{F}\{f(t/\alpha)\} = |\alpha| F(\alpha\omega). \tag{A.5}$$

Shifting. A shift in the coordinate in one domain results in a frequency shift in the other.

$$\begin{aligned} \mathcal{F}\{f(\alpha t + t_0)\} &= (1/\alpha)\, \mathrm{e}^{it_0\omega/\alpha} F(\omega/\alpha) \qquad \text{(A.6)} \\ \mathcal{F}^{-1}\{F(\omega + \omega_0)\} &= \mathrm{e}^{-i\omega_0 t} f(t). \end{aligned}$$

Two examples are of importance for the analysis presented within this thesis.

Lorentzian

For a given exponential function with the time decay constant $-\alpha$

$$f(t) = \begin{cases} \mathrm{e}^{-(\alpha - i\omega_0)t} & (t \geq 0) \\ 0 & (t < 0), \end{cases} \tag{A.7}$$

the contributing Fourier transform is a complex Lorentzian with the frequency linewidth α

$$F(\omega) = \frac{1}{\alpha + i(\omega - \omega_0)}. \tag{A.8}$$

This result explains for example the temporal transmission of a microcavity. Since a cavity mode can be modeled by a Lorentz function in the frequency domain, the time decay of the transmission is exponential. This is also a typical behavior of the harmonic oscillator and presents the relation between the line spectrum and its temporal properties.

Gaussian

Assuming a Gaussian function

$$f(t) = \mathrm{e}^{-\alpha t^2} \tag{A.9}$$

the corresponding linewidth (FWHM) in time is $\delta t = 2\sqrt{\frac{\ln 2}{\alpha}}$. The Fourier transform is again a Gaussian function with

$$F(\omega) = \sqrt{\frac{\pi}{\alpha}}\,\mathrm{e}^{-\frac{\omega^2}{4\alpha}} \tag{A.10}$$

and results in a linewidth (FWHM) in frequency of $\delta\omega = 4\sqrt{\alpha \ln 2}$. The relation between Gaussian spectra and time traces occurs for example in laser spectroscopy, where ultrashort laser pulses with pulse length in the picosecond range and below have Gaussian temporal shape and thus also Gaussian spectra. The linewidth in time and frequency are inverse proportional so that shorter Fourier transform limited laser pulses have a broader spectral width. As an example, a 800 nm laser ($\nu = 375\,\mathrm{THz}$) with a 100 fs pulse length has a spectral width of about 20 nm.

A.2 Reconstruction of the transmission up-conversion signal

In the optical gating experiments on microcavities, the temporal evolution of a transmitted laser pulse is investigated. This work is focused on the behavior of the cavity resonances only. In the standard approach, transmission linewidth and phase shift of a cavity mode $T(\omega)$ are modeled by a Lorentzian, with

$$T(\omega) = \frac{\mu}{\gamma + i(\omega - \omega_0)}. \tag{A.11}$$

Here, μ is the amplitude, γ describes the corresponding linewidth and ω is the center frequency of the resonance. In the present model, the electric field $E_L(\omega)$ of a laser pulse is approximated by a Gaussian function:

$$E_L(\omega) = \mathrm{e}^{-\frac{(\omega-\omega_L)^2}{2\Gamma^2}}, \tag{A.12}$$

with the spectral width Γ and the central frequency ω_L.

Before passing the microcavity, the laser beam is split in sample and gate beam. Therefore, sample and gate pulse have an equal spectrum and can be explained by the same Gaussian. The spectrum of the transmitted light $E_T(\omega) = T(\omega)E_L(\omega)$ is guided into the non-linear crystal. In the crystal, the transmitted light is up-converted by the temporally delayed gate pulse. Finally, the up-conversion signal is detected spectrally resolved in dependence on the delay time τ.

The amplitude $U(\omega, \tau)$ of the up-conversion signal can be expressed by a threefold Fourier transform, with

$$\begin{aligned} U(\omega,\tau) \;=\; & \int_{-\infty}^{\infty} \left[\int_{-\infty}^{\infty} \underbrace{\sum_{j=1}^{n} \frac{\mu_j}{i(\omega'-\omega_j)+\gamma_j}}_{\text{cavity modes}} \; \underbrace{\mathrm{e}^{\frac{-(\omega'-\omega_L)^2}{2\Gamma^2}}}_{\text{incident laser}} \; \mathrm{e}^{i\omega' t}\mathrm{d}\omega' \right] \\ & \times \left[\int_{-\infty}^{\infty} \underbrace{\mathrm{e}^{\frac{-(\omega''-\omega_L)^2}{2\Gamma^2} - i\omega''(t-\tau)}}_{\text{gate laser}} \,\mathrm{d}\omega'' \right] \mathrm{e}^{i\omega t}\mathrm{d}t. \end{aligned} \tag{A.13}$$

The Fourier transforms in the brackets separately convert the transmission signal and the gate pulse from frequency domain into time domain. The up-conversion signal as the product of both Fourier transforms is finally reconverted into frequency domain by a third Fourier transform. This equation demonstrates the complete process in an descriptive way and enables a numerical calculation of the detected signal.

In the following, an approach for an analytical solution of the problem is given. First, we only consider the transmission of one cavity mode with the center frequency ω_0, and at the end present the result as a sum of several modes.

By the application of the convolution theorem (A.4), the up-conversion signal can be rewritten as the convolution integral of the transmission and the delay pulse by

$$U(\omega,\tau) = \int_{-\infty}^{\infty} \mu \frac{\mathrm{e}^{\frac{(\omega-\omega_L-\omega'')^2}{2\Gamma^2} - \frac{(-\omega_L+\omega'')^2}{2\Gamma^2} - i\tau\omega''}}{\gamma + i(\omega-\omega_0-\omega'')} d\omega''. \tag{A.14}$$

This equation is rearranged by a number of substitutions to

$$U(\omega,\tau) = \frac{\Gamma}{i} \int_{-\infty}^{\infty} \mu \frac{\mathrm{e}^{-k^2 - \frac{-2z^2+\omega^2-2\omega\omega_L+2\omega_L^2}{2\Gamma^2}}}{k-a} dk \tag{A.15}$$

with

$$z = \frac{-i\Gamma^2\tau + \omega}{2}, \quad k = \frac{(z-\omega'')}{\Gamma}, \text{ and } a = \frac{z + i\gamma - \omega + \omega_0}{\Gamma}. \tag{A.16}$$

In the following, a tabulated formula [238] is applied for the determination of the integral:

$$\frac{i}{\pi} \int_{-\infty}^{\infty} \frac{\mathrm{e}^{-k^2}}{-k+a} dk = \mathrm{e}^{-a^2} \mathrm{Erfc}(-ia). \tag{A.17}$$

By the introduction of the complementary error function Erfc, the up-conversion amplitude has the analytical form of

$$U(\omega,\tau) = -\Gamma\pi\mu \mathrm{e}^{-a^2 - \frac{-2z^2+\omega^2-2\omega\omega_L+2\omega_L^2}{2\Gamma^2}} \mathrm{Erfc}(-ia). \tag{A.18}$$

In a next step, the substitutions are replaced and we get the final formula for the up-conversion signal amplitude of a single mode:

$$\begin{aligned} U(\omega,\tau) &= -\Gamma\pi\mu \exp\left\{ -\frac{-2\gamma^2 + \omega^2 + 2\gamma(\Gamma^2\tau + i(\omega - 2\omega_0))}{2\Gamma^2} \right\} \\ &\times \exp\left\{ -\frac{-2i\Gamma^2\tau(\omega-\omega_0) - 2\omega\omega_0 + 2\omega_0^2 - 2\omega\omega_L + 2\omega_L^2}{2\Gamma^2} \right\} \\ &\times \mathrm{Erfc}\left[-\frac{-2\gamma + \Gamma^2\tau + i(\omega - 2\omega_0)}{2\Gamma} \right] \end{aligned} \tag{A.19}$$

The analytical formula enables a precise description of the up-conversion signal dynamics and the influence of every single parameter. When several modes of a microcavity contribute to the transmission of the laser pulse, the amplitudes $U(\omega, \tau)$ of each mode can be added with respect of their corresponding phase. For non-coupled modes, as for example in the transmission of anisotropic single cavities, the amplitudes are simply added. In coupled microcavities, the phase shifts at the mode resonances deviate by 180° and either the sum or difference of the amplitudes models the detected signal accurately.

A.3 Optical thin film nomenclature

In thin film optics, a special nomenclature is used to express a thin film structure in a short form. A capital letter denotes the material, which is defined by its optical constants. Frequently used expression are H and L for high and low refractive index material, respectively, T for titanium dioxide and S for silicon dioxide. The thickness type is given by a small letter 'm' for massive (no phase shift), 'p' for physical and 'o' for optical. In the case of an absent small letter the layer thickness is also optical and given in quarter wavelengths at the design wavelength.
The following examples illustrate the convention:

2.2H	high index material with an optical thickness of 2.2 quarter wavelengths
500Sp	500 nm thick silicon dioxide layer
4Tm	4 mm thick titanium dioxide layer

Additionally, repetitions of layers may be combined into groups using parentheses. The design

1T 1S 1T 1S 1T 2S 1T 1S 1T 1S 1T

could also be written for example as

(T S)2 T 2S T (S T)2 or (T S)3 (S T)3.

As an additional convention, a layer stack is oriented with the semi-infinite substrate attached to the left and the semi-infinite ambient medium connected to the right side. This defines the incidence of the light from the right side and the reflectance calculation at the right border. The values calculated for transmission are valid for the left edge of the layer structure.

List of Abbreviations

Alq_3	tris-(8-hydroxyquinoline)- aluminum
BBO	beta-BaB_2O_4
CCD	charge coupled device
cw	continuous wave
DBR	distributed Bragg reflector
DCM	4-(dicyanomethylene)-2-methyl-6-[p-(dimethylamino)styryl]-4H-pyran
DFB	distributed feedback
FDTD	finite difference time domian
FRET	Förster/fluorescence resonance energy transfer
FWHM	full width at half maximum
GLAD	glancing angle deposition
H2	5-chloro-2-[3-[5-chloro-3(3-sulfopropyl)-2(3H)-benzothiazolylidene]-2-methyl-1-propenyl]-3-(3-sulfopropyl) benzothiazolium hydroxide
LPB	lower polariton branch
MC	microcavity
OLED	organic light emitting diode
OVCSEL	organic vertical cavity surface emitting laser
PL	photoluminescence
PVA	polyvinyl alcohol
QWOT	quarter wave optical thickness
RCLED	resonant cavity light emitting diode
SiO_2	silicon dioxide
TE	transversal electric
TiO_2	titanium dioxide
TM	transversal magnetic
UPB	upper polariton branch
VCSEL	vertical cavity surface emitting laser

Bibliography

[1] J. Niehoff and T. Pearsall, eds., *Consolidated European Photonics Research Initiative - Photonics for the 21st Century*, VDI - The Association of German Engineers, 2005.

[2] K. J. Vahala, "Optical microcavities," *Nature* **424**, 839, 2003.

[3] H. Li and K. Iga, *Vertical-Cavity Surface-Emitting Laser Devices*, Springer-Verlag Berlin Heidelberg New York, 2003.

[4] S. Pau, G. Björk, J. Jacobson, H. Cao, and Y. Yamamoto, "Stimulated emission of a microcavity dressed exciton and suppression of phonon scattering," *Phys. Rev. B* **51**, 7090, 1995.

[5] C. Weisbuch, M. Nishioka, A. Ishikawa, and Y. Arakawa, "Observation of the coupled exciton-photon mode splitting in a semiconductor quantum microcavity," *Phys. Rev. Lett.* **69**, 3314, 1992.

[6] D. G. Lidzey, D. D. C. Bradley, M. S. Skolnick, T. Virgili, S. Walker, and D. M. Whittaker, "Strong exciton-photon coupling in an organic semiconductor microcavity," *Nature* **395**, 53, 1998.

[7] F. Hide, B. J. Schwartz, M. A. DiazGarcia, and A. J. Heeger, "Laser emission from solutions and films containing semiconducting polymer and titanium dioxide nanocrystals," *Chem. Phys. Lett.* **256**, 424, 1996.

[8] N. Tessler, G. J. Denton, and R. H. Friend, "Lasing from conjugated-polymer microcavities," *Nature* **382**, 695, 1996.

[9] M. Born and E. Wolf, *Principles of Optics*, Cambridge University Press, Cambridge, 7th ed., 1999.

[10] P. Yeh, *Optical Waves in Layered Media*, John Wiley & Sons, Inc., Hoboken, New Jersey, 2005.

[11] M. Gerken, “Transfer-matrix-methode,” *http://www.lti.uni-karlsruhe.de/-rd_download/EOB_TransfermatrixMethode.pdf* , 2006.

[12] H. A. Macleod, *Thin-Film Optical Filters*, Institute of Physics Publishing, Bristol, Philadelphia, 3rd ed., 2001.

[13] E. Hecht, *Optik*, Oldenbourg, München, 4th ed., 2005.

[14] C. C. Katsidis and D. I. Siapkas, “General transfer-matrix method for optical multilayer systems with coherent, partially coherent, and incoherent interference,” *Appl. Opt.* **41**, 3978, 2002.

[15] K. Busch, S. Lölkes, R. B. Wehrspohn, and H. Föll, eds., *Photonic Crystals - Advances in Design, Fabrication, and Characterization*, Wiley-VCH, Weinheim, 2004.

[16] D. I. Babic and S. W. Corzine, “Analytic expression for the reflection delay, penetration depth, and absorptance of quater-wave dielectric mirrors,” *IEEE J. Quantum Electr.* **28**, 514, 1992.

[17] C. Fabry and A. Perot, “Sur les franges des lames minces argentées et leur application à la mesure de petites épaisseurs d’air,” *Ann. Chim. Phys.* **12**, 459, 1897.

[18] C. Fabry and A. Perot, “Théorie et applications d’une nouvelle méthode de spectroscopie interférentielle,” *Ann. Chim. Phys.* **16**, 115, 1899.

[19] J. F. Mulligan, “Who were Fabry and Perot?,” *Am. J. Phys.* **66**, 797, 1998.

[20] G. Panzarini, L. C. Andreani, A. Armitage, D. Baxter, M. S. Skolnick, V. N. Astratov, J. S. Roberts, A. V. Kavokin, M. R. Vladimirova, and M. A. Kaliteevski, “Exciton-light coupling in single and coupled semiconductor microcavities: Polariton dispersion and polarization splitting,” *Phys. Rev. B* **59**, 5082, 1999.

[21] C. Weisbuch, R. Houdre, and R. P. Stanley, “Microcavities and semiconductors: The strong-coupling regime,” in *Spontaneous Emission and Laser Oscillation in Microcavities*, H. Yokoyama and K. Ujihara, eds., ch. 4, 109, CRC Press, Boca Raton, 1995.

[22] O. Svelto, *Principles of Lasers*, Plenum Press, New York, 4th ed., 1998.

[23] R. P. Stanley, R. Houdre, U. Oesterle, M. Ilegems, and C. Weisbuch, “Coupled semiconductor microcavities,” *Appl. Phys. Lett.* **65**, 2093, 1994.

[24] P. Michler, M. Hilpert, and G. Reiner, "Dynamics of dual-wavelength emission from a coupled semiconductor microcavity laser," *Appl. Phys. Lett.* **70**, 2073, 1997.

[25] P. Pellandini, R. P. Stanley, R. Houdre, U. Oesterle, M. Ilegems, and C. Weisbuch, "Dual-wavelength laser emission from a coupled semiconductor microcavity," *Appl. Phys. Lett.* **71**, 864, 1997.

[26] J. F. Carlin, R. P. Stanley, P. Pellandini, U. Oesterle, and M. Ilegems, "The dual wavelength bi-vertical cavity surface-emitting laser," *Appl. Phys. Lett.* **75**, 908, 1999.

[27] A. J. Fischer, K. D. Choquette, W. W. Chow, H. Q. Hou, and K. M. Geib, "Coupled resonator vertical-cavity laser diode," *Appl. Phys. Lett.* **75**, 3020, 1999.

[28] V. Badilita, J.-F. Carlin, M. Ilegems, and K. Panajotov, "Rate-equation model for coupled-cavity surface-emitting lasers," *IEEE J. Quantum. Electron.* **40**, 1646, 2004.

[29] A. J. Fischer, K. D. Choquette, W. W. Chow, A. A. Allerman, and K. M. Geib, "Bistable output from a coupled-resonator vertical-cavity laser diode," *Appl. Phys. Lett.* **77**, 3319, 2000.

[30] A. J. Fischer, W. W. Chow, K. D. Choquette, A. A. Allerman, and K. M. Geib, "Q-switched operation of a coupled-resonator vertical-cavity laser diode," *Appl. Phys. Lett.* **76**, 1975, 2000.

[31] A. Armitage, M. S. Skolnick, V. N. Astratov, D. M. Whittaker, G. Panzarini, L. C. Andreani, T. A. Fisher, J. S. Roberts, A. V. Kavokin, M. A. Kaliteevski, A. F. Ioffe, and M. R. Vladimirova, "Optically induced splitting of bright excitonic states in coupled quantum microcavities," *Phys. Rev. B* **57**, 14877, 1998.

[32] G. Panzarini, L. C. Andreani, A. Armitage, D. Baxter, M. S. Skolnick, V. N. Astratov, J. S. Roberts, A. V. Kavokin, M. R. Vladimirova, and M. A. Kaliteevski, "Cavity-polariton dispersion and polarization splitting in single and coupled semiconductor microcavities," *Phys. Solid State* **41**, 1223, 1999.

[33] M. Emam-Ismail, V. N. Astratov, M. S. Skolnick, D. M. Whittaker, and J. S. Roberts, "Asymmetric photoluminescence spectra from excitons in a coupled microcavity," *Phys. Rev. B* **62**, 1552, 2000.

[34] F. Bloch, "Über die Quantenmechanik der Elektronen in Kristallgittern," *Z. Physik* **52**, 555, 1928.

[35] J. Feldmann, K. Leo, J. Shah, D. A. B. Miller, J. E. Cunningham, T. Meier, G. von Plessen, A. Schulze, P. Thomas, and S. Schmitt-Rink, "Optical investigation of Bloch oscillations in a semiconductor superlattice," *Phys. Rev. B* **46**, 7252, 1992.

[36] K. Leo, P. H. Bolivar, F. Brüggemann, R. Schwedler, and K. Köhler, "Observation of Bloch oscillations in a semiconductor superlattice," *Solid State Commun.* **84**, 943, 1992.

[37] K. Leo, "Interband optical investigation of Bloch oscillations in semiconductor superlattices," *Semicond. Sci. Technol.* **13**, 837, 1998.

[38] C. Waschke, H. G. Roskos, R. Schwedler, K. Leo, H. Kurz, and K. Köhler, "Coherent submillimeter-wave emission from Bloch oscillations in a semiconductor superlattice," *Phys. Rev. Lett.* **70**, 3319, 1993.

[39] G. Malpuech, A. Kavokin, G. Panzarini, and A. Di Carlo, "Theory of photon Bloch oscillations in photonic crystals," *Phys. Rev. B* **63**, 035108, 2001.

[40] P. B. Wilkinson, "Photonic Bloch oscillations and Wannier-Stark ladders in exponentially chirped Bragg gratings," *Phys. Rev. E* **65**, 056616, 2002.

[41] V. Lousse and S. Fan, "Tunable terahertz Bloch oscillations in chirped photonic crystals," *Phys. Rev. B* **72**, 075119, 2005.

[42] G. Malpuech and A. Kavokin, "Picosecond beats in coherent optical spectra of semiconductor heterostructures: photonic Bloch and exciton-polariton oscillations," *Semicond. Sci. Technol.* **16**, R1, 2001.

[43] T. Pertsch, P. Dannberg, W. Elflein, A. Bräuer, and F. Lederer, "Optical Bloch oscillations in temperature tuned waveguide arrays," *Phys. Rev. Lett.* **83**, 4752, 1999.

[44] R. Sapienza, P. Costantino, D. Wiersma, M. Ghulinyan, C. Oton, and L. Pavesi, "Optical analogue of electronic Bloch oscillations," *Phys. Rev. Lett.* **91**, 263902, 2003.

[45] V. Agarwal, J. D. Rio, G. Malpuech, M. Zamfirescu, A. Kavokin, D. Coquillat, D. Scalbert, M. Vladimirova, and B. Gil, "Photon Bloch oscillations in porous silicon optical superlattices," *Phys. Rev. Lett.* **92**, 97401, 2004.

[46] E. M. Purcell, “Spontaneous emission probabilities at radio frequencies,” *Phys. Rev.* **69**, 681, 1946.

[47] A. M. Vredenberg, N. E. J. Hunt, E. F. Schubert, D. C. Jacobson, J. M. Poate, and G. J. Zydzik, “Controlled atomic spontaneous emission from Er^{3+} in a transparent $\mathsf{Si/SiO_2}$ microcavity,” *Phys. Rev. Lett.* **71**, 517, 1993.

[48] J.-M. Gerard and B. Gayral, “Strong Purcell effect for InAs quantum boxes in three-dimensional solid-state microcavities,” *J. of Lightwave Technology* **17**, 2089, 1999.

[49] R. H. Jordan, L. J. Rothberg, A. Dodabalapur, and R. E. Slusher, “Efficiency enhancement of microcavity organic light emitting diodes,” *Appl. Phys. Lett.* **69**, 1997, 1996.

[50] A. Dodabalapur, L. J. Rothberg, R. H. Jordan, T. M. Miller, R. E. Slusher, and J. M. Phillips, “Physics and applications of organic microcavity light emitting diodes,” *J. Appl. Phys.* **80**, 6954, 1996.

[51] H. Benisty, H. D. Neve, and C. Weisbuch, “Impact of planar microcavity effects on light extraction part II: Selected exact simulations and role of photon recycling,” *IEEE J. Quantum Electronics* **34**, 1632, 1998.

[52] P. K. H. Ho, D. S. Thomas, R. H. Friend, and N. Tessler, “All-polymer optolectronic devices,” *Science* **285**, 233, 1999.

[53] D. Delbeke, R. Bockstaele, P. Bienstman, R. Baets, and H. Benisty, “High-efficiency semiconductor resonant-cavity light-emitting diodes: A review,” *IEEE J. Sel. Top. Quantum Electron.* **8**, 189, 2002.

[54] V. Bulovic, V. G. Kozlov, V. B. Khalfin, and S. R. Forrest, “Transform-limited, narrow-linewidth lasing action in organic semiconductor microcavities,” *Science* **279**, 553, 1998.

[55] X. Liu, D. Poitras, Y. Tao, and C. Py, “Optically pumped lasing from organic microcavity,” *Can. J. Phys.* **82**, 481, 2004.

[56] M. Koschorreck, R. Gehlhaar, V. G. Lyssenko, M. Swoboda, M. Hoffmann, and K. Leo, “Dynamics of a high-Q vertical cavity organic laser,” *Appl. Phys. Lett.* **87**, 181108, 2005.

[57] Y. Zhu, D. J. Gauthier, S. E. Morin, Q. Wu, H. J. Carmichael, and T. W. Mossberg, “Vacuum rabi splitting as a feature of linear-dispersion theory: Analysis and experimental observations,” *Phys. Rev. Lett.* **64**, 2499, 1990.

[58] J. S. Toll, “Causality and the dispersion relation: Logical foundations,” *Phys. Rev.* **104**, 1760, 1956.

[59] M. S. Skolnick, T. A. Fisher, and D. M. Whittaker, “Strong coupling phenomena in quantum microcavity structures,” *Semicond. Sci. Technol.* **13**, 645, 1998.

[60] G. Khitrova, H. M. Gibbs, F. Jahnke, M. Kira, and S. W. Koch, “Nonlinear optics of normal-mode-coupling semiconductor microcavities,” *Rev. Mod. Phys.* **71**, 1591, 1999.

[61] D. G. Lidzey, D. D. C. Bradley, M. S. Skolnick, T. Virgili, S. Walker, and D. M. Whittaker, “Strong exciton-photon coupling in an organic semiconductor microcavity,” *Nature* **395**, 53, 1998.

[62] D. G. Lidzey, D. D. C. Bradley, T. Virgili, A. Armitage, M. S. Skolnick, and S. Walker, “Room temperature polariton emission from strongly coupled organic semiconductor microcavities,” *Phys. Rev. Lett.* **82**, 3316, 1999.

[63] D. G. Lidzey, D. D. C. Bradley, A. Armitage, S. Walker, and M. S. Skolnick, “Photon-mediated hybridization of Frenkel excitons in organic semiconductor microcavities,” *Science* **288**, 1620, 2000.

[64] L. G. Connolly, D. G. Lidzey, R. Butte, A. M. Adawi, D. M. Whittaker, M. S. Skolnick, and R. Airey, “Strong coupling in high-finesse organic semiconductor microcavities,” *Appl. Phys. Lett.* **83**, 5377, 2003.

[65] D. G. Lidzey, “Strong optical coupling in organic semiconductor microcavities,” in *Electronic Excitations in Organic Based Nanostructures*, V. M. Agranovich and G. F. Bassani, eds., ch. 8, 355, Elsevier, Amsterdam, 2003.

[66] R. J. Holmes and S. R. Forrest, “Strong exciton-photon coupling and exciton hybridization in a thermally evaporated polycrystalline film of an organic small molecule,” *Phys. Rev. Lett.* **93**, 186404, 2004.

[67] J. Wenus, L. G. Connolly, D. M. Whittaker, M. S. Skolnick, and D. G. Lidzey, “Tuning the exciton-photon coupling in a strongly coupled organic microcavity containing an optical wedge,” *Appl. Phys. Lett.* **85**, 5848, 2004.

[68] J. Wenus, L. G. Connolly, and D. G. Lidzey, “New organic materials and microcavity structures for strong exciton-photon coupling,” *Phys. Stat. Sol. (c)* **2**, 3899, 2005.

[69] R. J. Holmes and S. R. Forrest, “Exciton-photon coupling in organic materials with large intersystem crossing rates and strong excited-state molecular relaxation,” *Phys. Rev. B* **71**, 235203, 2005.

[70] N. Takada, T. Kamata, and D. D. C. Bradley, “Polariton emission from polysilane-based organic microcavities,” *Appl. Phys. Lett.* **82**, 1812, 2003.

[71] P. A. Hobson, W. L. Barnes, D. G. Lidzey, G. A. Gehring, D. M. Whittaker, M. S. Skolnick, and S. Walker, “Strong exciton-photon coupling in a low-Q all-metall mirror microcavity,” *Appl. Phys. Lett.* **81**, 3519, 2002.

[72] R. P. Stanley, R. Houdre, U. Oesterle, M. Gailhanou, and M. Ilegems, “Ultrahigh finesse microcavity with distributed Bragg reflectors,” *Appl. Phys. Lett.* **65**, 1883, 1994.

[73] W. Lukosz, “Theory of optical-environment-dependent spontaneous-emission rates for emitters in thin layers,” *Phys. Rev. B* **22**, 3030, 1980.

[74] G. Björk and Y. Yamamoto, “Spontaneous emission in dielectric planar microcavities,” in *Spontaneous Emission and Laser Oscillation in Microcavities*, H. Yokoyama and K. Ujihara, eds., ch. 6, 189, CRC Press, Boca Raton, 1995.

[75] H. Benisty, H. D. Neve, and C. Weisbuch, “Impact of planar microcavity effects on light extraction-part I: Basic concepts and analytical trends,” *IEEE J. Quantum Electronics* **34**, 1612, 1998.

[76] H. Benisty, R. Stanley, and M. Mayer, “Method of source terms for dipole emission modification in modes of arbitrary planar structures,” *J. Opt. Soc. Am. A* **15**, 1192, 1998.

[77] P. Royo, R. P. Stanley, and M. Ilegems, “Planar dielectric microcavity light-emitting diodes: Analytical analysis of the extraction efficiency,” *J. Appl. Phys.* **90**, 283, 2001.

[78] P. Royo, R. P. Stanley, and M. Ilegems, “Analytical calculation of the extraction efficiency of microcavity light-emitting diodes for display and fiber coupling applications,” *IEEE J. Sel. Top. Quantum Electronics* **8**, 207, 2002.

[79] G. Björk, S. Machida, Y. Yamamoto, and K. Igeta, “Modification of spontaneous emission rate in planar dielectric microcavity structures,” *Phys. Rev. A* **44**, 669, 1991.

[80] D. Ochoa, R. Houdre, M. Ilegems, C. Hanke, and B. Borchert, “Microcavity light emitting diodes as efficient planar light emitters for telecommunication applications,” *C. R. Physique* **3**, 3, 2002.

[81] T. Shiga, H. Fujikawa, and Y. Taga, “Design of multiwavelength resonant cavities for white organic light-emitting diodes,” *J. Appl. Phys.* **93**, 19, 2003.

[82] M. A. Muriel and A. Carballar, “Internal field distributions in fiber Bragg gratings,” *IEEE Photonics Technol. Lett.* **9**, 955, 1997.

[83] K. Neyts, “Microcavity effects and the outcoupling of light in displays and lighting applications based on thin emitting films,” *Appl. Surf. Sci.* **244**, 517, 2005.

[84] S. Möller and S. R. Forrest, “Improved light out-coupling in organic light emitting diodes employing ordered microlens arrays,” *J. Appl. Phys.* **91**, 3324, 2002.

[85] J. Lim, S. S. Oh, D. Y. Kim, S. H. Cho, I. T. Kim, S. H. Han, H. Takezoe, E. H. Choi, G. S. Cho, Y. H. Seo, S. O. Kang, and B. Park, “Enhanced out-coupling factor of microcavity organic light-emitting devices with irregular microlens array,” *Opt. Express* **14**, 6564, 2006.

[86] D. W. Pohl, W. Denk, and M. Lanz, “Optical stethoscopy: Image recording with resolution $\lambda/20$,” *Appl. Phys. Lett.* **44**, 651, 1984.

[87] H. Haken and H. C. Wolf, *Molekülphysik und Quantenchemie*, Springer-Verlag, Berlin, 3rd ed., 1998.

[88] J. B. Birks, *Organic Molecular Photophysics, Vol. 2*, John Wiley and Sons, London, 1975.

[89] B. M. Krasovitskii and B. M. Bolotin, *Organic Luminescent Materials*, VCH Weinheim, 1988.

[90] D. M. Basko, F. Bassani, G. C.La Rocca, and V. M. Agranovich, “Electronic energy transfer in a microcavity,” *Phys. Rev. B* **62**, 15962, 2000.

[91] D. L. Dexter, “A theory of sensitized luminescence in solids,” *J. Chem. Phys.* **21**, 836, 1953.

[92] T. Förster, “Zwischenmolekulare Energiewanderung und Fluoreszenz,” *Ann. Physik* **6**, 55, 1948.

[93] T. Förster, “Transfer mechanisms of electronic excitation,” *Discuss. Faraday Soc.* **27**, 7, 1959.

[94] P. P. Sorokin and J. R. Lankard, “Stimulated emission observed from an organic dye chloro-aluminum phthalocyanine,” *IBM J. Res. Develop.* **10**, 162, 1966.

[95] B. H. Soffer and B. B. McFarland, “Continuously tunable narrow-band organic dye lasers,” *Appl. Phys. Lett.* **10**, 266, 1967.

[96] F. P. Schäfer, ed., *Dye Lasers*, Springer-Verlag, Berlin, 1973.

[97] C. W. Tang and S. A. van Slyke, “Organic electroluminescent diodes,” *Appl. Phys. Lett.* **51**, 913, 1987.

[98] G. J. Denton, N. Tessler, N. T. Harrison, and R. H. Friend, “Factors influencing stimulated emission from poly(p-phenylenevinylene),” *Phys. Rev. Lett.* **78**, 733, 1997.

[99] M. A. Baldo, R. J. Holmes, and S. R. Forrest, “Prospects for electrically pumped organic lasers,” *Phys. Rev. B* **66**, 35321, 2002.

[100] A. Schülzgen, C. Spiegelberg, M. M. Morrell, S. B. Mendes, B. Kippelen, N. Peyghambarian, M. F. Nabor, E. A. Mash, and P. M. Allemand, “Near diffraction-limited laser emission from a polymer in a high finesse planar cavity,” *Appl. Phys. Lett.* **72**, 269, 1998.

[101] V. G. Kozlov, G. Parthasarathy, P. E. Burrows, S. R. Forrest, Y. You, and M. E. Thompson, “Optically pumped blue organic semiconductor lasers,” *Appl. Phys. Lett.* **72**, 144, 1998.

[102] Y. Kawabe, C. Spiegelberg, A. Schülzgen, M. F. Nabor, B. Kippelen, E. A. Mash, P. M. Allemand, M. Kuwata-Gonokami, K. Takeda, and N. Peyghambarian, “Whispering-gallery-mode microring laser using a conjugated polymer,” *Appl. Phys. Lett.* **72**, 141, 1998.

[103] S. V. Frolov, A. Fuji, D. Chinn, M. Hirohata, R. Hidayat, M. Taraguchi, T. Masuda, K. Yoshino, and Z. V. Vardeny, “Microlasers and Micro-LEDs from disubstituted polyacetylene,” *Adv. Mat.* **10**, 869, 1998.

[104] M. Berggren, A. Dodabalapur, and R. E. Slusher, “Stimulated emission and lasing in dye-doped organic thin films with Forster transfer,” *Appl. Phys. Lett.* **71**, 2230, 1997.

[105] H. Taniguchi, T. Fujiwara, H. Yamada, S. Tanosaki, and M. Baba, “Whispering-gallery-mode dye lasers in blue, green, and orange regions using dye-doped, solid, small spheres,” *Appl. Phys. Lett.* **62**, 2155, 1993.

[106] S. Riechel, C. Kallinger, U. Lemmer, J. Feldmann, A. Gombert, V. Wittwer, and U. Scherf, "A nearly diffraction limited surface emitting conjugated polymer laser utilizing a two-dimensional photonic band structure," *Appl. Phys. Lett.* **77**, 2310, 2000.

[107] S. Riechel, U. Lemmer, J. Feldmann, S. Berleb, A. G. Mückl, W. Brütting, A. Gombert, and V. Wittwer, "Very compact tunable solid-state laser utilizing a thin-film organic semiconductor," *Opt. Lett.* **26**, 593, 2001.

[108] D. Schneider, S. Hartmann, T. Benstem, T. Dobbertin, D. H. A. Metzdorf, E. Becker, T. Riedl, H.-H. Johannes, W. Kowalsky, T. Weimann, J.Wang, and P. Hinze, "Wavelength-tunable organic solid-state distributed-feedback laser," *Appl. Phys. B* **77**, 399, 2003.

[109] M. A. Diaz-Garcia, F. Hide, B. J. Schwartz, M. D. McGehee, M. R. Andersson, and A. J. Heeger, "Plastic lasers: Comparison of gain narrowing with a soluble semiconducting polymer in waveguides and microcavities," *Appl. Phys. Lett.* **70**, 3191, 1997.

[110] S. E. Burns, G. Denton, N. Tessler, M. A. Stevens, F. Cacialli, and R. H. Friend, "High finesse organic microcavities," *Opt. Mat.* **9**, 18, 1998.

[111] T. Granlund, M. Theander, M. Berggren, M. Andersson, A. Ruzeckas, V. Sundström, G. Björk, M. Granström, and O. Inganäs, "A polythiophene microcavity laser," *Chem. Phys. Lett.* **288**, 879, 1998.

[112] W. Koechner, *Solid-State Laser Engineering*, Springer, Berlin, 4th ed., 1996.

[113] U. Brackmann, *Lambdachrome Laser Dyes*, Lambda Physik AG, Göttingen, Germany, 3rd ed., 2000.

[114] R. R. Willey, *Practical Design and Production of Optical Thin Films*, Marcel Dekker, Inc., New York, Basel, 2002.

[115] H. K. Pulker, G. Paesold, and E. Ritter, "Refractive indices of TiO_2 films produced by reactive evaporation of various titanium-oxygen phases," *Appl. Opt.* **15**, 2986, 1976.

[116] J. V. Grahn, M. Linder, and E. Fredriksson, "In situ growth of evaporated TiO_2 thin films using oxygen radicals: Effect of deposition temperature," *J. Vac. Sci. Technol. A* **16**, 2495, 1998.

[117] H. K. Jang, S. W. Whangbo, H. B. Kim, K. Y. Im, Y. S. Lee, I. W. Lyo, C. N. Whang, G. Kim, H.-S. Lee, and J. M. Lee, "Titanium oxide films on Si (100)

deposited by electron-beam evaporation at 250°C," *J. Vac. Sci. Technol. A* **18**, 917, 2000.

[118] S. C. Chiao, B. G. Bovard, and H. A. Macleod, "Repeatability of the composition of titanium oxide films produced by evaporation of Ti_2O_3," *Appl. Opt.* **37**, 5284, 1998.

[119] F. Waibel, E. Ritter, and R. Linsbod, "Properties of TiO_x films prepared by electron-beam evaporation of titanium and titanium suboxides," *Appl. Opt.* **42**, 4590, 2003.

[120] H. W. Lehmann and K. Frick, "Optimizing deposition parameters of electron beam evaporated TiO_2 films," *Appl. Opt.* **27**, 4920, 1988.

[121] J. M. Bennett, E. Pelletier, G. Albrand, J. P. Borgogno, B. Lazarides, C. K. Carniglia, R. A. Schmell, T. H. Allen, T. Tuttlehart, K. H. Guenther, and A. Saxer, "Comparison of the properties of titanium dioxide films prepared by various techniques," *Appl. Opt.* **28**, 3303, 1989.

[122] C. R. Ottermann and K. Bange, "Correlation between the density of TiO_2 films and their properties," *Thin Solid Films* **286**, 32, 1996.

[123] E. Ritter, "Deposition of oxide films by reactive evaporation," *J. Vac. Sci. Technol.* **3**, 225, 1966.

[124] J. S. Chen, S. Chao, J. S. Kao, G. R. Lai, and W. H. Wang, "Substrate-dependent optical absorption characteristics of titanium dioxide thin films," *Appl. Opt.* **36**, 4403, 1997.

[125] D. Mergel, D. Buschendorf, S. Eggert, R. Grammes, and B. Samset, "Density and refractive index of TiO_2 films prepared by reactive evaporation," *Thin Solid Films* **371**, 218, 2000.

[126] H. Selhofer and R. Müller, "Comparison of pure and mixed coating materials for AR coatings for use by reactive evaporation on glass and plastic lenses," *Thin Solid Films* **351**, 180, 1999.

[127] K. V. Rottkay, T. Richardson, M. Rubin, J. Slack, and L. Kullman, "Influence of stoichiometry on electrochromic cerium-titanium oxide compounds," *Solid State Ionics* **115**, 425, 1998.

[128] J. C. Hsu and C. C. Lee, "Single- and dual-ion-beam sputter deposition of titanium oxide films," *Appl. Opt.* **37**, 1171, 1998.

[129] M. H. Suhail, G. M. Rao, and S. Mohan, "dc reactive magnetron sputtering of titanium-structural and optical characterization of TiO_2 films," *J. Appl. Phys.* **71**, 1421, 1992.

[130] R. Linsbod, E. Ritter, and K. Leitner, "Evaluation of the oxidation of TiO_2 films during reactive evaporation of Ti_3O_5 and during exposure of the films to the atmosphere," *Appl. Opt.* **42**, 4580, 2003.

[131] A. Alvarez-Herrero, A. J. Fort, H. Guerrero, and E. Bernabeu, "Ellipsometric characterization and influence of relative humidity on TiO_2 layers optical properties," *Thin Solid Films* **349**, 212, 1999.

[132] M. Wiggins, M. Nelson, and C. Aita, "Phase development in sputter deposited titanium dioxide," *J. Vac. Sci. Technol. A* **14**, 772, 1996.

[133] D. O. Smith, M. S. Cohen, and G. P. Weiss, "Oblique-incidence anisotropy in evaporated permalloy films," *J. Appl. Phys.* **31**, 1755, 1960.

[134] H. K. Pulker and E. Jung, "Correlation between film structure and sorption behaviour of vapour deposited ZnS, Cryolite and MgF_2 films," *Thin Solid Films* **9**, 7, 1971.

[135] N. G. Nakhodkin and A. I. Shaldervan, "Effect of vapour incidence angles on profile and properties of condensed films," *Thin Solid Films* **10**, 109, 1972.

[136] J. A. Thornton, "Influence of apparatus geometry and deposition conditions on structure and topography of thick sputtered coatings," *J. Vac. Sci. Tec.* **11**, 666, 1974.

[137] A. G. Dirks and H. J. Leamy, "Columnar microstructure in vapor-deposited thin films," *Thin Solid Films* **47**, 219, 1977.

[138] H. A. Macleod, "Structure-related optical properties of thin films,"*J. Vac. Sci. Technol. A* **4**, 418, 1986.

[139] K. H. Guenther, B. Loo, D. Burns, J. Edgell, D. Windham, and K. H. Müller, "Microstructure analysis of thin-films deposited by reactive evaporation and by reactive ion plating," *J. Vac. Sci. Technol. A* **7**, 1436, 1989.

[140] L. Sun and P. Hou, "Spectroscopic ellipsometry study on e-beam deposited titanium dioxide films," *Thin Solid Films* **455-456**, 525, 2004.

[141] S. Lichter and J. Chen, "Model for columnar microstructure of thin solid films," *Phys. Rev. Lett* **56**, 1396, 1986.

[142] R. N. Tait, T. Smy, and M. J. Brett, “Modelling and characterization of columnar growth in evaporated films,” *Thin Solid Films* **226**, 196, 1993.

[143] R. Fiedler and G. Schirmer, “Säulenwachstum bei aufgedampften Schichten,” *Thin Solid Films* **167**, 281, 1988.

[144] I. Hodgkinson, Q. H. Wu, and J. Hazel, “Empirical equations for the principal refractive indices and column angle of obliquely deposited films of tantalum oxide, titanium oxide, and zirconium oxide,” *Appl. Opt.* **37**, 2653, 1998.

[145] G. K. Kiema, M. J. Colgan, and M. J. Brett, “Dye sensitized solar cells incorporating obliquely deposited titanium oxide layers,” *Sol. Energy Mat. and Sol. Cells* **85**, 321, 2005.

[146] T. Smy, D. Vick, M. J. Brett, S. K. Dew, A. T. Wu, J. C. Sit, and K. D. Harris, “Three-dimensional simulation of film microstructure produced by glancing angle deposition,” *J. Vac. Sci. Technol. A* **18**, 2507, 2000.

[147] K. Robbie, M. J. Brett, and A. Lakhtakia, “Chiral sculptured thin films,” *Nature* **384**, 616, 1996.

[148] K. Robbie and M. J. Brett, “Sculptured thin films and glancing angle deposition: Growth mechanics and applications,” *J. Vac. Sci. Technol. A* **15**, 1460, 1997.

[149] E. Pelletier, F. Flory, and Y. Hu, “Optical characterization of thin films by guided waves,” *Appl. Opt.* **28**, 2918, 1989.

[150] F. Flory, D. Endelema, E. Pelletier, and I. Hodgkinson, “Anisotropy in thin films: Modeling and measurement of guided and nonguided optical properties: Application to TiO_2 films,” *Appl. Opt.* **32**, 5649, 1993.

[151] H. Wang, “Assessment of optical constants of multilayer thin films with columnar-structure-induced anisotropy,” *J. Phys. D: Appl. Phys.* **28**, 571, 1995.

[152] M. Levichkova, V. Mankov, N. Starbov, D. Karashanova, B. Mednikarov, and K. Starbova, “Structure and properties of nanosized electron beam deposited zirconia thin films,” *Surf. Coat. Technol.* **141**, 70, 2001.

[153] S.-H. Woo and C. K. Hwangbo, “Optical anisotropy of microstructure-controlled TiO_2 films fabricated by glancing-angle deposition (GLAD),” *J. Korean Phys. Soc.* **48**, 1199, 2006.

[154] M. F. Weber, C. A. Stover, L. R. Gilbert, T. J. Nevitt, and A. J. Ouderkirk, "Giant birefringent optics in multilayer polymer mirrors," *Science* **287**, 2451, 2000.

[155] C. W. Tang, S. A. VanSlyke, and C. H. Chen, "Electroluminescence of doped organic thin films," *J. Appl. Phys.* **65**, 3610, 1989.

[156] V. G. Kozlov, V. Bulovic, P. E. Burrows, and S. R. Forrest, "Laser action in organic semiconductor waveguide and double-heterostructure devices," *Nature* **389**, 362, 1997.

[157] V. G. Kozlov, V. Bulovic, and S. R. Forrest, "Temperature independent performance of organic semiconductor lasers," *Appl. Phys. Lett.* **71**, 2575, 1997.

[158] V. G. Kozlov, V. Bulovic, P. E. Burrows, M. Baldo, V. B. Khalfin, G. Parthasarathy, S. R. Forrest, Y. You, and M. E. Thompson, "Study of lasing action based on Förster energy transfer in optically pumped organic semiconductor thin films," *J. Appl. Phys.* **84**, 4096, 1998.

[159] M. Berggren, A. Dodabalapur, R. E. Slusher, A. Timko, and O. Nalamasu, "Organic solid-state lasers with imprinted gratings on plastic substrates," *Appl. Phys. Lett.* **72**, 410, 1998.

[160] V. G. Kozlov, P. E. Burrows, G. Parthasarathy, and S. R. Forrest, "Optical properties of molecular organic semiconductor thin films under intense electrical excitation," *Appl. Phys. Lett.* **74**, 1057, 1999.

[161] V. G. Kozlov, G. Parthasarathy, P. E. Burrows, V. B. Khalfin, J. Wang, S. Y. Chou, and S. R. Forrest, "Structures for organic diode lasers and optical properties of organic semiconductors under intense optical and electrical excitations," *IEEE J. Quantum El.* **36**, 18, 2000.

[162] J. Jakabovic, O. Lengyel, J. Kovac, T. C. Wong, C. S. Lee, and S. T. Lee, "Properties of 4-dicyanomethylene-2-methyl-6-(p-dimethyl-aminostyryl)-4H-pyran-doped Alq layers as optically pumped lasers," *Appl. Phys. Lett.* **83**, 1295, 2003.

[163] D. C. Freeman and C. E. White, "The structure and characteristics of the fluorescent metal chelates of o,o'-dihydroxyazo compounds," *J. Am. Chem. Soc.* **78**, 2678, 1956.

[164] D. Z. Garbuzov, V. Bulovic, P. E. Burrows, and S. R. Forrest, "Photoluminescence efficiency and absorption of aluminum-tris-quinolate (Alq_3) thin films," *Chem. Phys. Lett.* **249**, 433, 1996.

[165] M. Cölle and C. Gärditz, “Phosphorescence of aluminum tris(quinoline-8-olate),” *Appl. Phys. Lett.* **84**, 3160, 2004.

[166] M. Cölle and C. Gärditz, “Delayed fluorescence and phosphorescence of tris-(8-hydroxyquinoline)aluminum (Alq_3) and their temperature dependence,” *J. Lum.* **110**, 200, 2004.

[167] C. Gärditz, A. G. Mückl, and M. Cölle, “Influence of an external magnetic field on the singlet and triplet emissions of tris-(8-hydroxyquinoline)aluminum(III) (Alq_3),” *J. Appl. Phys.* **98**, 104507, 2005.

[168] A. Curioni, M. Boero, and W. Andreoni, “Alq_3: ab initio calculations of its structural and electronic properties in neutral and charged states,” *Chem. Phys. Lett.* **294**, 263, 1998.

[169] M. Cölle, R. E. Dinnebier, and W. Brütting, “The structure of the blue luminescent δ-phase of tris(8-hydroxyquinoline)aluminium(iii) (Alq_3),” *Chem. Commun.* , 2908, 2002.

[170] M. Cölle, S. Forero-Lenger, J. Gmeiner, and W. Brütting, “Vibrational analysis of different crystalline phases of the organic electroluminescent material aluminium tris(quinoline-8-olate) (Alq_3),” *Phys. Chem. Chem. Phys.,* **5**, 2958, 2003.

[171] P. R. Hammond, “Laser-dye DCM, its special properties, synthesis and comparison with other dyes in the red,” *Opt. Comm.* **29**, 331, 1979.

[172] B. J. Jung, C. B. Yoon, H. K. Shim, L. M. Do, and T. Zyung, “Pure-red dye for organic electroluminescent devices: Bis-condensed DCM derivatives,” *Adv. Func. Mat.* **11**, 430, 2001.

[173] I. Sokolik, R. Priestley, A. Walser, R. Dorsinville, and C. Tang, “Bimolecular reactions of singlet excitons in tris(8-hydroxyquinoline) aluminum,” *Appl. Phys. Lett.* **69**, 4168, 1996.

[174] K.-C. Tang, P.-W. Cheng, V. U. Chien, C. P. Cheng, P.-Y. Cheng, and I.-C. Chen, “Fluorescence life time of tris-(8-hydroquinoline) aluminum thin film and solution,” *J. Chin. Chem. Soc.* **47**, 875, 2000.

[175] V. V. N. Ravi Kishore, K. L. Narasimhan, and N. Periasamy, “On the radiative lifetime, quantum yield and fluorescence decay of Alq in thin films,” *Phys. Chem. Chem. Phys.,* **5**, 1386, 2003.

[176] R. S. Deshpande, V. Bulovic, and S. R. Forrest, “White-light-emitting organic electroluminescent devices based on interlayer sequential energy transfer,” *Appl. Phys. Lett.* **75**, 888, 1999.

[177] Y. Wu, H. R. Wu, Y. C. Zhou, Y. Q. Zhan, J. Zhou, X. M. Ding, and X. Y. Hou, “Excitation energy transfer between tris-(8-hydroxyquinoline) aluminum and a red dye,” *Appl. Phys. Lett.* **88**, 123512, 2006.

[178] A. B. Djurisic, C. Y. Kwong, W. L. Guo, T. W. Lau, E. H. Li, Z. T. Liu, H. S. Kwok, L. S. M. Lam, and W. K. Chan, “Spectroscopic ellipsometry of the optical functions of tris (8-hydroxyquinoline) aluminum (Alq$_3$),” *Thin Solid Films* **416**, 233, 2002.

[179] A. B. Djurisic, C. Y. Kwong, T. W. Lau, E. H. Li, Z. T. Liu, H. S. Kwok, L. S. M. Lam, and W. K. Chan, “Optical functions of tris (8-hydroxyquinoline) aluminum (Alq$_3$) by spectroscopic ellipsometry,” *Appl. Phys. A* **76**, 219, 2003.

[180] D. Z. Garbuzov, S. R. Forrest, A. G. Tsekoun, P. E. Burrows, V. Bulovic, and M. E. Thompson, “Organic films deposited on Si p-n junctions: Accurate measurements of fluorescence internal efficiency, and application to luminescent antireflection coatings,” *J. Appl. Phys.* **80**, 4644, 1996.

[181] B. Masenelli, S. Callard, A. Gagnaire, and J. Joseph, “Fabrication and characterization of organic semiconductor-based microcavities,” *Thin Solid Films* **364**, 264, 2000.

[182] P. Dalasinski, Z. Lukasiak, M. Rebarz, M. Wojdyla, A. Bratkowski, and W. Bala, “Photoluminescence, optical transmission and reflection of Alq$_3$ layers obtained by thermal evaporation deposition,” *Opto-Electron. Rev.* **12**, 429, 2004.

[183] S. Kumar, V. K. Shukla, and A. Tripathi, “Ellipsometric investigations on the light induced effects on tris(8-hydroxyquinoline) aluminum (Alq$_3$),” *Thin Solid Films* **477**, 240, 2005.

[184] B. Masenelli, A. Gagnaire, L. Berthelot, J. Tardy, and J. Joseph, “Controlled spontaneous emission of a tri(8-hydroxyquinoline) aluminum layer in a microcavity,” *J. Appl. Phys.* **85**, 3032, 1999.

[185] S. Riechel, *Organic Semiconductor Lasers with Two-Dimensional Distributed Feedback.* PhD thesis, Ludwig-Maximilians-Universität München, 2002.

[186] R. Gehlhaar, “Untersuchungen an Festkörperlösungen organischer Farbstoff-Moleküle,” Diploma thesis, Technische Universität Dresden, 2002.

[187] M. Swoboda, R. Gehlhaar, M. Sudzius, M. Hoffmann, H. Fröb, V. G. Lyssenko, and K. Leo, "Terahertz beating of laser emission from an organic microcavity," *Appl. Phys. Lett.* **89**, 121110, 2006.

[188] R. Gehlhaar, M. Swoboda, M. Sudzius, M. Hoffmann, H. Fröb, V. G. Lyssenko, and K. Leo, "Dual-wavelength laser emission from an organic microcavity with terahertz beating," *Appl. Phys. B* **86**, 413, 2007.

[189] G. Christmann, D. Simeonov, R. Butté, E. Feltin, J.-F. Carlin, and N. Grandjean, "Impact of disorder on high quality factor III-V nitride microcavities," *Appl. Phys. Lett.* **89**, 261101, 2006.

[190] M. Swoboda, "Time-resolved laser emission from organic microcavities," Diploma thesis, Technische Universität Dresden, 2006.

[191] SCI Scientific Computing International, Carlsbad, USA, *Film Wizard Thin Film Software, Getting Started Manual, Professional Version*, 2003.

[192] A. Taflove and S. C. Hagness, *Computational Electrodynamics*, Artech House, Boston, London, 2nd ed., 2000.

[193] K. Kaminska and K. Robbie, "Birefringent omnidirectional reflector," *Appl. Opt.* **43**, 1570, 2004.

[194] B. Karunagaran, R. T. Rajendra Kumar, D. Mangalaraj, S. K. Narayandass, and G. M. Rao, "Influence of thermal annealing on the composition and structural parameters of DC magnetron sputtered titanium dioxide thin films," *Cryst. Res. Technol.* **37**, 1285, 2002.

[195] P. Yeh, "Electromagnetic propagation in birefringent layered media," *J. Opt. Soc. Am.,* **69**, 742, 1979.

[196] D. Möbius, "Scheibe aggregates," *Adv. Mat.* **7**, 437, 1995.

[197] D. G. Lidzey, D. D. C. Bradley, M. S. Skolnick, and S. Walker, "Optical coupling of Frenkel excitons in organic semiconductor micocavities," *Synth. Met.* **124**, 37, 2001.

[198] D. G. Lidzey, A. M. Fox, M. D. Rahn, M. S. Skolnick, V. M. Agranovich, and S. Walker, "Experimental study of light emission from strongly coupled organic semiconductor microcavities following nonresonant laser excitation," *Phys. Rev. B* **65**, 195312, 2002.

[199] D. G. Lidzey, A. I. Tartakovskii, M. Emam-Ismail, M. S. Skolnick, and S. Walker, “Enhanced Raman scattering in a strongly coupled microcavity containing J-aggregates,” *Synth. Met.* **127**, 151, 2002.

[200] R. Gehlhaar, R. Schüppel, M. Koschorreck, T. Fritz, H. Fröb, M. Hoffmann, V. G. Lyssenko, K. Leo, L. Connolly, J. Wenus, and D. G. Lidzey, “Time-resolved and cw photoluminescence from strongly-coupled organic microcavities,” *J. Lum.* **110**, 354, 2004.

[201] D. G. Lidzey, J. Wenus, D. M. Whittaker, G. Itskos, P. N. Stavrinou, D. D. C. Bradley, and R. Murray, “Hybrid polaritons in strongly coupled microcavities: experiments and models,” *J. Lum.* **110**, 347, 2004.

[202] A. I. Tartakovskii, M. Emam-Ismail, D. G. Lidzey, M. S. Skolnick, D. D. C. Bradley, S. Walker, and V. M. Agranovich, “Raman scattering in strongly coupled organic semiconductor microcavities,” *Phys. Rev. B* **63**, 121302(R), 2001.

[203] R. M. Stevenson, V. N. Astratov, M. S. Skolnick, D. M. Whittaker, M. Emam-Ismail, A. I. Tartakovskii, P. G. Savvidis, J. J. Baumberg, and J. S. Roberts, “Continuous wave observation of massive polariton redistribution by stimulated scattering in semiconductor microcavities,” *Phys. Rev. Lett.* **85**, 3680, 2000.

[204] A. I. Tartakovskii, D. N. Krizhanovskii, D. A. Kurysh, V. D. Kulakovskii, M. S. Skolnick, and J. S. Roberts, “Polariton parametric scattering processes in semiconductor microcavities observed in continuous wave experiments,” *Phys. Rev. B* **65**, 081308(R), 2002.

[205] M. Demokan and A. Nacaroglu, “An analysis of gain-switched semiconductor lasers generating pulse-code-modulated light with a high bit rate,” *IEEE J. Quantum. Electr.* **20**, 1016, 1984.

[206] L. G. Melcer, J. R. Karin, R. Nagarajan, and J. E. Bowers, “Picosecond dynamics of optical gain switching in vertical cavity emitting lasers,” *IEEE J. Quantum Electr.* **27**, 1417, 1991.

[207] P. Schneeweiß, “Stimulated emission from organic microcavities under sub-ps excitation,” Diploma thesis, Technische Universität Dresden, 2006.

[208] V. Kozlov and S. Forrest, “Lasing action in organic semiconductor thin films,” *Curr. Op. in Sol. St. and Mat. Sci.* **4**, 203, 1999.

[209] J. M. Gerard, D. Barrier, J. Y. Marzin, R. Kuszelewicz, L. Manin, E. Costard, V. Thierry-Mieg, and T. Rivera, "Quantum boxes as active probes for photonic microstructures: The pillar microcavity case," *Appl. Phys. Lett.* **69**, 449, 1996.

[210] M. Röhner, J. P. Reithmaier, A. Forchel, F. Schäfer, and H. Zull, "Laser emission from photonic dots," *Appl. Phys. Lett.* **71**, 488, 1997.

[211] H. Lohmeyer, K. Sebald, C. Kruse, R. Kröger, J. Gutowski, D. Hommel, J. Wiersig, N. Baer, and F. Jahnke, "Confined optical modes in monolithic II-VI pillar microcavities," *Appl. Phys. Lett.* **88**, 051101, 2006.

[212] A. Muller, C.-K. Shiha, J. Ahn, D. Lu, D. Gazula, and D. G. Deppe, "High Q (33 000) all-epitaxial microcavity for quantum dot vertical-cavity surface-emitting lasers and quantum light sources," *Appl. Phys. Lett.* **88**, 031107, 2006.

[213] A. Muller, D. Lu, J. Ahn, D. Gazula, S. Quadery, S. Freisem, D. G. Deppe, and C. K. Shih, "Self-aligned all-epitaxial microcavity for cavity QED with quantum dots," *Nano Lett.* **6**, 2920, 2006.

[214] S. Reitzenstein, A. Bazhenov, A. Gorbunov, C. Hofmann, S. Münch, A. Löffler, M. Kamp, J. P. Reithmaier, V. D. Kulakovskii, and A. Forchel, "Lasing in high-Q quantum-dot micropillar cavities," *Appl. Phys. Lett.* **89**, 051107, 2006.

[215] A. M. Adawi, A. Cadby, L. G. Connolly, W.-C. Hung, R. Dean, A. Tahraoui, A. M. Fox, A. G. Cullis, D. Sanvitto, M. S. Skolnick, and D. G. Lidzey, "Spontaneous emission control in micropillar cavities containing a fluorescent molecular dye," *Adv. Mat.* **18**, 742, 2006.

[216] H. Sakata, H. Takeuchi, K. Natsume, and S. Suzuki, "Vertical-cavity organic lasers with distributed-feedback structures based on active Bragg reflectors," *Opt. Express* **14**, 11681, 2006.

[217] Y. Yamamoto, S. Machida, and G. Björk, "Microcavity semiconductor laser with enhanced spontaneous emission," *Phys. Rev. A* **44**, 657, 1991.

[218] M. P. van Exter, G. Nienhuis, and J. P. Woerdman, "Two simple expressions for the spontaneous emission factor β," *Phys. Rev. A* **54**, 3553, 1996.

[219] T. Baba, T. Hamano, F. Koyama, and K. Iga, "Spontaneous emission factor of a microcavity DBR surface-emitting laser," *IEEE J. Quantum Elec.* **27**, 1347, 1991.

[220] T. Baba, T. Hamano, F. Koyama, and K. Iga, "Spontaneous emission factor of a microcavity DBR surface-emitting laser (II) - effects of electron quantum confinement," *IEEE J. Quantum Elec.* **28**, 1310, 1992.

[221] C. J. Chang-Hasnain, J. P. Harbison, G. Hasnain, A. C. Von Lehmen, L. T. Florez, and N. G. Stoffel, "Dynamic, polarization, and transverse mode characteristics of vertical cavity surface emitting lasers," *IEEE J. Quantum Electron.* **27**, 1402, 1991.

[222] D. Burak, J. V. Moloney, and R. Binder, "Microscopic theory of polarization properties of optically anisotropic vertical-cavity surface-emitting lasers," *Phys. Rev. A* **61**, 053809, 2000.

[223] N. A. Loiko and I. V. Babushkin, "Competition of orthogonally polarized transverse Fourier modes in a VCSEL," *J. Opt. B: Quantum Semiclass. Opt.* **3**, 234, 2001.

[224] K. Panajotov, B. Nagler, G. Verschaffelt, A. Georgievski, H. Thienpont, J. Danckaert, and I. Veretennicoff, "Impact of in-plane anisotropic strain on the polarization behavior of vertical-cavity surface-emitting lasers," *Appl. Phys. Lett.* **77**, 1590, 2000.

[225] C. L. Chua, R. L. Thornton, D. W. Treat, and R. M. Donaldson, "Anisotropic apertures for polarization-stable laterally oxidized vertical-cavity lasers," *Appl. Phys. Lett.* **73**, 1631, 1998.

[226] K. D. Choquette and R. E. Leibenguth, "Control of vertical-cavity laser polarization with anisotropic transverse cavity geometries," *IEEE Photonics Technol. Lett.* **6**, 40, 1994.

[227] A. Chavez-Pirson, H. Ando, H. Saito, and H. Kanbe, "Quantum wire microcavity laser made from GaAs fractional layer superlattices," *Appl. Phys. Lett.* **64**, 1759, 1994.

[228] H. Y. Chu, B.-S. Yoo, M. S. Park, and H.-H. Park, "Polarization characteristics of index-guided surface-emitting lasers with tilted pillar structure," *IEEE Photonics Technol. Lett.* **9**, 1066, 1997.

[229] A. Yariv and P. Yeh, *Optical Waves in Crystals : Propagation and Control of Laser Radiation*, John Wiley and Sons, Inc., 2003.

[230] C. Schriever, "Untersuchung und Beeinflussung des Energietransfers zwischen Farbstoffmolekülen in Mikroresonatoren," Diploma thesis, Technische Universität Dresden, 2007.

[231] H. Deng, G. Weihs, C. Santori, J. Bloch, and Y. Yamamoto, "Condensation of semiconductor microcavity exciton polaritons," *Science* **298**, 199, 2002.

[232] G. Weihs, H. Deng, R. Huang, M. Sugite, F. Tassone, and Y. Yamamoto, "Exciton-polariton lasing in a microcavity," *Semicond. Sci. Technol.* **18**, S386, 2003.

[233] H. Deng, G. Weihs, D. Snoke, J. Bloch, and Y. Yamamoto, "Polariton lasing vs. photon lasing in a semiconductor microcavity," *PNAS (Proc. of the Nat. Academy of Sciences)* **100**, 15318, 2003.

[234] R. J. Holmes, S. Kéna-Cohen, V. M. Menon, and S. R. Forrest, "Strong coupling and hybridization of Frenkel and Wannier-Mott excitons in an organic-inorganic optical microcavity," *Phys. Rev. B* **74**, 235211, 2006.

[235] J. Wenus, R. Parashkov, S. Ceccarelli, A. Brehier, J.-S. Lauret, M. S. Skolnick, E. Deleporte, and D. G. Lidzey, "Hybrid organic-inorganic exciton-polaritons in a strongly coupled microcavity," *Phys. Rev. B* **74**, 235212, 2006.

[236] Q. Tang, H. Matsuda, K. Kikuchi, and S. Ogura, "Fabrication and characteristics of rugate filters deposited by the TSH reactive sputtering method," *J. Vac. Sci. Technol. A* **16**, 3384, 1998.

[237] X. Wang, H. Masumoto, Y. Someno, L. Chen, and T. Hirai, "Design and preparation of a 33-layer optical reflection filter of TiO_2-SiO_2 system," *J. Vac. Sci. Technol. A* **18**, 933, 2000.

[238] M. Abramowitz and I. A. Stegun, *Handbook of Mathematical Functions*, Dover Publications, New York, 10th ed., p.297, 1972.

List of publications

Scientific articles

Time-resolved and cw photoluminescence from strongly-coupled organic microcavities
R. Gehlhaar, M. Koschorreck, R. Schüppel, T. Fritz, H. Fröb, M. Hoffmann, V. G. Lyssenko, K. Leo, L. Connolly, J. Wenus, and D. G. Lidzey, *J. Lumin.* **110**, 354 (2004)

Dynamics of a high-Q vertical-cavity organic laser
M. Koschorreck, R. Gehlhaar, V. G. Lyssenko, M. Swoboda, M. Hoffmann, and K. Leo, *Appl. Phys. Lett.* **87**, 181108 (2005)

Polarization splitting and terahertz oscillations from a single planar Fabry-Pérot microcavity
R. Gehlhaar, M. Swoboda, M. Sudzius, M. Hoffmann, H. Fröb, V. G. Lyssenko, K. Leo, and H. Wendrock, *Appl. Phys. Lett.* **88**, 091121 (2006)
also published in *Virt. J. Ultrafast Sci.* **5** (4) (2006)

THz oscillations from organic microcavity laser emission
M. Swoboda, R. Gehlhaar, M. Sudzius, V. G. Lyssenko, M. Hoffmann, and K. Leo, *Proc. SPIE* **6192**, 61920F (2006)

Terahertz beating of laser emission from an organic microcavity
M. Swoboda, R. Gehlhaar, M. Sudzius, M. Hoffmann, H. Fröb, V. G. Lyssenko, and K. Leo, *Appl. Phys. Lett.* **89**, 121110 (2006)
also published in *Virt. J. Ultrafast Sci.* **5** (10) (2006)

THz oscillations from optically anisotropic planar microcavities and organic microcavity lasers
R. Gehlhaar, M. Swoboda, M. Sudzius, M. Hoffmann, H. Fröb, V. G. Lyssenko, and K. Leo, *Proc. SPIE* **6368**, 63680P (2006)

Dual-wavelength laser emission from an organic microcavity with terahertz beating
R. Gehlhaar, M. Swoboda, M. Sudzius, M. Hoffmann, H. Fröb, V. G. Lyssenko, and K. Leo, *Appl. Phys. B* **86**, 413 (2007) *invited paper*

Conference contributions

Time-resolved and cw photoluminescence properties of organic microcavities
R. Gehlhaar, M. Koschorreck, R. Schüppel, T. Fritz, H. Fröb, M. Hoffmann, V. G. Lyssenko, K. Leo, L. Connolly, J. Wenus, M. S. Skolnick, and D. G. Lidzey, 325th WE-Heraeus-Seminar "Organic molecular solids: Excited electronic states and optical properties", Bad Honnef (2004)

Photoluminescence of organic microcavities
R. Gehlhaar, V. G. Lyssenko, R. Schüppel, M.Hoffmann, H. Fröb, T. Fritz and K. Leo, HYTEC meeting, Hersonnisos (2004)

Design, preparation and optical characterization of high finesse organic microcavities
R. Gehlhaar, M. Koschorreck, V. G. Lyssenko, H. Fröb, M. Hoffmann, and K. Leo, Frühjahrstagung der Deutschen Physikalische Gesellschaft, Berlin (2005)

Gain switching as lasing mechanism in organic microcavities
M. Koschorreck, R. Gehlhaar, V. G. Lyssenko, M. Hoffmann, and K. Leo, Frühjahrstagung der Deutschen Physikalische Gesellschaft, Berlin (2005)

Vacuum deposited composite films for luminescence conversion
M. Levichkova, J. Assa, H. Fröb, R. Gehlhaar, and K. Leo, Frühjahrstagung der Deutschen Physikalische Gesellschaft, Berlin (2005)

Fabrication and optical characterization of high finesse organic microcavities
R. Gehlhaar, M. Levichkova, M. Koschorreck, V. G. Lyssenko, M. Hoffmann, H. Fröb, T. Fritz, and K. Leo, HYTEC meeting, Dresden (2005)

Doping of vacuum deposited AlQ_3 films - a trend for higher quantum efficiency
M. Levichkova, J. Assa, H. Fröb, R. Gehlhaar, and K. Leo, 3rd International Symposium on Irradiation Induced Phenomena in Chalcogenide, Oxide and Organic Thin Films, Tryavna (2005)

Terahertz-modulated emission from an organic VCSEL
M. Swoboda, M. Koschorreck, R. Gehlhaar, V. G. Lyssenko, M. Sudzius, H. Fröb, M. Hoffmann, and K. Leo, Frühjahrstagung der Deutschen Physikalische Gesellschaft, Frankfurt (2006)

Design, fabrication and characterization of microcavity OLED structures
H. Gothe, R. Gehlhaar, H. Fröb, V. G. Lyssenko, and K. Leo, Frühjahrstagung der Deutschen Physikalische Gesellschaft, Dresden (2006)

Polarization splitting and terahertz oscillations from a single planar Fabry-Perot microcavity
R. Gehlhaar, M. Swoboda, M. Sudzius, H. Wendrock, M. Hoffmann, H. Fröb, V. G. Lyssenko, and K. Leo, Frühjahrstagung der Deutschen Physikalische Gesellschaft, Dresden (2006)

Dynamics of optical wavepackets in coupled microcavities
M. Sudzius, V. G. Lyssenko, R. Gehlhaar, M. Swoboda, M. Hoffmann, and K. Leo, Frühjahrstagung der Deutschen Physikalische Gesellschaft, Dresden (2006)

Lasing from optically structured organic microcavities
P. Schneeweiss, M. Swoboda, R. Gehlhaar, V. G. Lyssenko, M. Hoffmann, and K. Leo, Frühjahrstagung der Deutschen Physikalische Gesellschaft, Dresden (2006)

THz oscillations from organic microcavity laser emission
M. Swoboda, R. Gehlhaar, M. Sudzius, V. G. Lyssenko, M. Hoffmann, and K. Leo, SPIE Photonics Europe, Strasbourg (2006)

Strong-coupling in double-DBR microcavities
R. Gehlhaar, M. Langner, M. Swoboda, M. Sudzius, M. Hoffmann, H. Fröb, V. G. Lyssenko, and K. Leo, HYTEC meeting, Hersonnisos (2006)

Terahertz beating in transmission and stimulated emission of anisotropic planar microcavities
R. Gehlhaar, M. Swoboda, M. Sudzius, M. Hoffmann, H. Fröb, V. G. Lyssenko, and K. Leo, DPG Physics School "Photonic Crystals and Metamaterials", Bad Honnef (2006)

THz oscillations from optically anisotropic planar microcavities and organic microcavity lasers
R. Gehlhaar, M. Swoboda, M. Sudzius, M. Hoffmann, H. Fröb, V. G. Lyssenko, and K. Leo, SPIE Optics East, Boston (2006)

Multimode spontaneous emission of optically confined organic photonic dots
M. Langner, C. Schriever, R. Gehlhaar, H. Fröb, V. G. Lyssenko, and K. Leo, Frühjahrstagung der Deutschen Physikalische Gesellschaft, Regensburg (2007)

Spontaneous emission confinement in organic photonic dots
R. Gehlhaar, M. Langner, H. Fröb, V. G. Lyssenko, and K. Leo, HYTEC meeting, Cachan (2007)

Patents

Transparent light emitting element
K. Leo, V. G. Lyssenko, R. Gehlhaar, EP 1 727 221, (2006)

Transparent light emitting element
K. Leo, R. Gehlhaar, V. G. Lyssenko, EP 1 727 222, (2006)

Mikroresonator für Anordnungen zur Intensitätsmodulation von Strahlung mit Frequenzen im Terahertz-Bereich
V. G. Lyssenko, R. Gehlhaar, H. Fröb, K. Leo, K. Schmidt, German patent application number 10 2005 042 952.1-54, (2007)

Acknowledgements

It is a pleasure for me to thank all the people, who have contributed to my scientific work.

Prof. Karl Leo as the head of the institute has supervised and constantly supported me during the thesis. His first skepticism about the new field changed into a growing interest, which was a great motivation for me in continuing the work. In all respects, he provides an outstanding infrastructure and atmosphere that lifts the research far above the level of standard work. A constant financial support enabled this work and the participation in international conferences and workshops.

Prof. Vadim Lyssenko initiated the work with his inexhaustible reservoir of new, crazy, wild, and sometimes revolutionary ideas. Based on his outstanding practical and theoretical knowledge, he has immediately begun to reconstruct my crude building of physical understanding. With great carefulness and patience, he did not fix all the loose parts, he started again from the fundament. Later, we had endless and always interesting discussions about our research and, tried together to understand the strangeness of life and nature in general and light in particular.
Thank you Vadim for your guidance, your motivation, your total decline of mountaineering and, especially, for being a friend!

I wish to thank my coworkers Marco Koschorreck and Marko Swoboda for their invaluable contributions in the organic laser work. With enormous patience and sensitiveness, they managed the amplifier laser system and the up-conversion setup. Their experimental results in combination with the optical modeling are one of the main parts of this thesis. With the beginning of his scientific career, Maik Langner produced excellent J-aggregate microcavities. During the past year we shared the same enthusiasm and interest in optical confinement. Many thanks to the three Ms for your teamwork and comradeship!

Further, I want to thank the members of the groups, I collaborated with: Dr. Hartmut Fröb, Dr. Michael Hoffmann, Dr. Jakub Assa, Dr. Torsten Fritz, Marieta Levichkova, Dr. Markas Sudzius, Kai Schmidt, Hannes Gothe, Clemens Schriever, and Rico Schüppel. Without their experimental, theoretical and spiritual contributions, this research would not have been finished or even exist.

Our first investigated microcavity was provided by Prof. David Lidzey and his coworkers Liam Connolly and Dr. Jakub Wenus from the University of Sheffield. As a pioneer in the field of organic microcavities, David Lidzey continuously promoted our work. As the head of the HYTEC research project of the European Union, he installed an international scientific network. We and all other participants have benefited a lot from this collaboration and the periodic meetings.

Dr. Horst Wendrock from the Institut für Werkstoffwissenschaften (IFW) in Dresden performed the scanning electron microscopy, which gave us a detailed insight into the structural properties of our samples. I am grateful to him for his diligence, effort and humor in preparing and analyzing our sensitive offsprings.

Michael Falz of Vakuum Technik Dresden has given important details for the fabrication of high quality dielectric mirrors and microcavities.

Dr. Bernd Schmidt and Jarka Potfajova from the Forschungszentrum Dresden in Rossendorf (FZD) provided the essential ellipsometric data that are the basis of the theoretical modeling of our optical experiments.

At the end, I want to acknowledge all the members of the Institut für Angewandte Photophysik, who made the work during my PhD thesis a pleasure.

Versicherung

Hiermit versichere ich, dass ich die vorliegende Arbeit ohne unzulässige Hilfe Dritter und ohne Benutzung anderer als der angegebenen Hilfsmittel angefertigt habe. Gedanken, die aus fremden Quellen direkt oder indirekt übernommen wurden, sind als solche kenntlich gemacht. Die Arbeit wurde bisher weder im Inland noch im Ausland in gleicher oder ähnlicher Form einer anderen Prüfungsbehörde vorgelegt. Ich erkenne die Promotionsordnung der Technischen Universität Dresden an.

Diese Arbeit wurde am Institut für Angewandte Photophysik der Technischen Universität Dresden unter der wissenschaftlichen Betreuung von Prof. Dr. Karl Leo angefertigt.

Dresden, den 17.04.2007

Robert Gehlhaar